Journal of Magnetic Resonance **151,** 153–227 (2001)
doi:10.1006/jmre.2001.2336, available online at http://www.idealibrary.com on IDEAL®

ADVANCES IN MAGNETIC RESONANCE

High-Resolution ^{1}H NMR Spectroscopy in the Solid State: Very Fast Sample Rotation and Multiple-Quantum Coherences

Ingo Schnell and Hans Wolfgang Spiess

Max-Planck-Institut für Polymerforschung, Postfach 3148, D-55021 Mainz, Germany

E-mail: schnelli@mpip-mainz.mpg.de; spiess@mpip-mainz.mpg.de

Received May 19, 2000

In the past few years, solid-state ^{1}H NMR spectroscopy under fast magic-angle spinning (MAS) has developed into a versatile tool for elucidating structure and dynamics. Dipolar multiple-quantum (MQ), in particular double-quantum (DQ), MAS spectroscopy has been applied to a variety of materials and provided unique insight, e.g., into the structure of hydrogen-bonded systems. This review intends to present solid-state ^{1}H DQ and MQ MAS spectroscopy in a systematic fashion with a particular emphasis on methodological aspects, followed by an overview of applications. © 2001 Academic Press

Key Words: **proton solid-state NMR; fast magic-angle spinning; multiple-quantum spectroscopy.**

1. INTRODUCTION

Their ubiquity in organic and inorganic materials, coupled with their high magnetogyric ratio, makes protons very important and valuable nuclei for NMR spectroscopy. In solution state, ^{1}H NMR spectroscopy therefore belongs to the standard methods routinely applied for material characterization. In the solid state, however, the combination of high spin density and high magnetogyric ratio, which is advantageous as far as sensitivity is concerned, turns into a disadvantage, because the spectra are dominated by strong homonuclear dipolar interactions. In solution, these interactions are averaged out by the rapid isotropic motion of the molecules; however, in solids, dipolar couplings with effective strengths of up to 50 kHz severely broaden the resonance lines. At such strengths, the dipolar interaction surpasses, by about one order of magnitude, all ^{1}H chemical shielding effects which are of vital importance for the identification of typical molecular building blocks (like aromatic rings, CH_2, CH_3, etc.) and, in general, for substance characterization. Up to now, this problem has prevented ^{1}H NMR spectroscopy from being widely applied to solids. Therefore, new solid-state ^{1}H NMR methods must, on the one hand, aim at the reduction of dipolar interactions, in order to reveal at least partially the chemical shift information, while, on the other hand, one would like to preserve the valuable information about *intra*- and *inter*molecular proton–proton proximities and hence about the structure and the dynamics of the sample inherent to the proton–proton dipolar couplings. Consequently, the ideal approach will combine information about the identity of a molecular building block from the chemical shift with the spatial distance and orientation information from dipolar interactions.

The standard approaches for resonance-line narrowing in solid-state NMR are based on *coherent averaging* (*51*), the most widely used method being magic-angle sample spinning (MAS) (*4, 5, 71*). This, in principle, allows the removal of all anisotropic interactions whose spatial parts can be represented as second-rank tensors and contribute to the NMR frequency in first order only (*1*). Referring to the effect of MAS on anisotropic broadenings, Maricq and Waugh distinguished between "homogeneous" and "inhomogeneous" interactions (*72*): under MAS, an inhomogeneously broadened line splits spontaneously into a pattern of sharp spinning sidebands, while homogeneously broadened lines successively narrow with increasing MAS frequencies, allowing the observation of the underlying spinning-sideband pattern only if the lines are sufficiently resolved. To date, MAS has not been widely applied to rigid and dense ^{1}H systems, because the homogeneous character of multispin homonuclear dipolar interactions seemed to necessitate MAS frequencies well above the effective coupling strength, which is, in most cases, still beyond the current state-of-the-art technology.

A NMR approach, which instead of fighting the dipolar interaction makes use of strongly dipolar-coupled networks, is dipolar multiple-quantum (MQ) spectroscopy. The first MQ NMR experiments performed on rigid ^{1}H systems were so-called spin-counting experiments, which do not aim at resolving different ^{1}H species in the spectrum, but rather at determining the size of dipolar-coupled spin clusters by exciting higher-order MQ coherences (*112, 8, 9, 101*). In static samples, without requiring spectral resolution, the intensity distribution over the different MQ orders allows the cluster size to be extracted (*77, 80, 76*).

1090-7807/01 $35.00

Spectral site resolution can be achieved, at least in the final detection period of the experiment, by combining the spin-counting experiment with cross polarization to ^{13}C (*7*) or with MAS (*40*). Moreover, introducing a MQ evolution period under fast MAS conditions between the excitation and reconversion periods of the experiment allows resonance lines to be spectrally resolved and, hence, to be assigned to MQ coherences (*42*). Limiting the MQ order or, equivalently, the minimum number of coupled spins to 2, leads to DQ spectroscopy, by use of which dipolar-coupled networks can be analyzed in a pairwise manner with respect to the chemical shifts of the involved nuclei.

In order to interpret the first experimental DQ NMR results under fast MAS conditions, Gottwald *et al.* proposed a spin-pair approach which describes the evolution of dipolar-coupled multispin systems approximately in the so-called "short time limit" (*46, 41*). Following the first applications to ^1H spin-pair model systems, ^{31}P DQ MAS experiments were subsequently performed on polycrystalline phosphates (*32, 33, 24, 39, 6*) and phosphate glasses (*34, 116*). In addition, analogous ^{29}Si DQ MAS experiments have also been performed on silicate glasses (*44*). Moreover, mobile systems have been investigated, with, e.g., the chain order and dynamics in polymers and elastomers having been quantified by homonuclear ^{13}C and ^1H DQ methods (*48–50*). Focusing on methyl groups, triple-quantum (TQ) spectroscopy was introduced (*38*) and, proceeding with the method beyond purely homonuclear systems, dipolar MQ NMR has been extended to heteronuclear ^1H–^{13}C pairs (*103, 91, 92*).

Recently available MAS equipment, allowing MAS to be performed at spinning frequencies of up to 35 kHz, has had major impact on the development of dipolar MQ methods. Besides providing a significant and vital resolution enhancement in ^1H spectroscopy (*98*), it allowed the experimental verification of a full theoretical treatment of dipolar-coupled multispin systems under fast MAS (*35, 36*). Based on a Floquet approach coupled with Rayleigh–Schrödinger perturbation theory, the analytical treatment considers the evolution of a ^1H multispin system, which is subject to both MAS and homonuclear dipolar interactions (*35*). It turns out that such a system develops successively two-, three- and higher spin correlations, while MAS suppresses the formation of these correlations with increasing efficiency as more spins become involved (*36*). In the limit of fast MAS, the multispin system can therefore be considered to decompose into a superposition of two-spin correlations, the latter being of inhomogeneous character (*72*). This dominant role of two-spin correlations provides the basis for the spectroscopy of spin pairs, i.e., DQ spectroscopy.

This review intends to present solid-state ^1H MQ MAS spectroscopy in a systematic fashion with a particular emphasis on methodological aspects: It considers the experimental excitation and the properties of MQ coherences as well as the origin of MQ MAS spinning sideband patterns (*46, 41, 37*). The information content of spectral features like signal intensities or MAS sideband patterns is discussed, paying particular attention to the influence of perturbing spins. The physical insight provided by this analysis is illustrated by first applications, which concentrate on the elucidation of phenomena inducing supramolecular order, namely hydrogen bonds and π–π interactions between aromatic systems (*97, 18*). In addition to addressing structural problems, MQ MAS experiments are, due to their inherent multidimensional form, particularly well suited to investigations of molecular dynamics, which are expected to be of major interest for further NMR method developments as well as future applications.

2. DIPOLAR-COUPLED SPIN SYSTEMS UNDER MAS

In this opening section, the dominant internal interactions present in ^1H multispin systems, i.e., dipolar couplings and isotropic chemical shielding effects, as well as some analytical formalisms necessary for describing the NMR experiments will be introduced. Since the technique of magic-angle spinning is essential for ^1H NMR experiments in the solid state, we will consider its effect on the internal interactions and, in particular, present a theoretical approach which describes its decoupling effect on a dense network of dipolar-coupled spins. The results form the basis for ^1H MQ MAS spectroscopy, which will be the topic of Section 3.

2.1. The Dipolar and Quadrupolar Interactions

Due to the negligible overlap of the nuclear wavefunctions, the *direct* spin–spin interactions between two nuclei with spin $I^{(i,j)} \neq 0$ are limited to the dipolar interaction, the Hamiltonian for which can be written as

$$\hat{\boldsymbol{H}}_D^{(ij)} = \hat{\boldsymbol{I}}^{(i)} \cdot \boldsymbol{D}^{(ij)} \cdot \hat{\boldsymbol{I}}^{(j)}, \qquad [1]$$

using a coupling tensor $\boldsymbol{D}^{(ij)}$ which is, in the principal axes system (PAS) of the interaction, always of symmetrical form

$$\boldsymbol{D}^{(ij)} = -2D^{(ij)} \cdot \begin{pmatrix} -\frac{1}{2} & 0 & 0 \\ 0 & -\frac{1}{2} & 0 \\ 0 & 0 & 1 \end{pmatrix}. \qquad [2]$$

The dipolar coupling constant is given by

$$D^{(ij)} = -\frac{\mu_0 \hbar \gamma_i \gamma_j}{4\pi r_{ij}^3}, \qquad [3]$$

where μ_0 denotes the vacuum permeability, and $\gamma_{i,j}$ are the magnetogyric ratios of the interacting nuclei i and j, and r_{ij} is their distance. Transformation into the laboratory frame (LAB) with the z-direction defined by the external magnetic field, B_0, i.e., $\boldsymbol{B}_0 \| z$, results in

$$\hat{\boldsymbol{H}}_D^{(ij)} = -\frac{\mu_0 \hbar \gamma_i \gamma_j}{4\pi} \cdot \left[\frac{3(\hat{\boldsymbol{I}}^{(i)} \cdot \boldsymbol{r}_{ij})(\hat{\boldsymbol{I}}^{(j)} \cdot \boldsymbol{r}_{ij})}{r_{ij}^5} - \frac{\hat{\boldsymbol{I}}^{(i)} \cdot \hat{\boldsymbol{I}}^{(j)}}{r_{ij}^3} \right]$$
$$= D^{(ij)} \cdot [A + B + C + D + E + F], \qquad [4]$$

where the so-called "dipolar alphabet" (*1*) is given by

$$\begin{aligned} A &= (1-3\cos^2\theta)\hat{\boldsymbol{I}}_z^{(i)}\cdot\hat{\boldsymbol{I}}_z^{(j)} \\ B &= \frac{1}{2}(1-3\cos^2\theta)\big(\hat{\boldsymbol{I}}_z^{(i)}\cdot\hat{\boldsymbol{I}}_z^{(j)}-\hat{\boldsymbol{I}}^{(i)}\cdot\hat{\boldsymbol{I}}^{(j)}\big) \\ C &= -\frac{3}{2}\sin\theta\cos\theta e^{-i\phi}\big(\hat{\boldsymbol{I}}_z^{(i)}\cdot\hat{\boldsymbol{I}}_+^{(j)}+\hat{\boldsymbol{I}}_+^{(i)}\cdot\hat{\boldsymbol{I}}_z^{(j)}\big) \\ D &= -\frac{3}{2}\sin\theta\cos\theta e^{i\phi}\big(\hat{\boldsymbol{I}}_z^{(i)}\cdot\hat{\boldsymbol{I}}_-^{(j)}+\hat{\boldsymbol{I}}_-^{(i)}\cdot\hat{\boldsymbol{I}}_z^{(j)}\big) \\ E &= -\frac{3}{4}\sin^2\theta e^{-2i\phi}\hat{\boldsymbol{I}}_+^{(i)}\cdot\hat{\boldsymbol{I}}_+^{(j)} \\ F &= -\frac{3}{4}\sin^2\theta e^{2i\phi}\hat{\boldsymbol{I}}_-^{(i)}\cdot\hat{\boldsymbol{I}}_-^{(j)}. \end{aligned} \quad [5]$$

The vector $\boldsymbol{r}_{ij}$ connects the coupled spins i and j. In the dipolar alphabet, $\boldsymbol{r}_{ij}$ is expressed in terms of its polar coordinates (r_{ij},θ,ϕ), describing the orientation of $\boldsymbol{r}_{ij}$ with respect to the laboratory frame. The raising and lowering operators $\hat{\boldsymbol{I}}_\pm$ are defined as $\hat{\boldsymbol{I}}_\pm=\frac{1}{\sqrt{2}}(\hat{\boldsymbol{I}}_x\pm i\hat{\boldsymbol{I}}_y)$.

Nuclei with spin $I\geq 1$ possess an electric quadrupole moment, Q, which interacts with the electric field gradient, $\boldsymbol{V}$, at the nucleus. The later can be represented by a tensor with the components

$$(V)_{\alpha\beta}=\frac{\partial^2\Phi}{\partial\alpha\partial\beta}, \quad [6]$$

where $\alpha,\beta=x,y,z$, and Φ denotes the electric potential. Using this gradient $\boldsymbol{V}$, the quadrupolar coupling tensor, $\boldsymbol{Q}$, is then given by

$$\boldsymbol{Q}=\frac{eQ}{2I(2I-1)\hbar}\cdot\boldsymbol{V}, \quad [7]$$

with I and eQ denoting the nuclear spin and the product of the elementary charge e and quadrupole moment Q, respectively. Using the coupling tensor, $\boldsymbol{Q}$, the quadrupolar interaction can be written in the form

$$\hat{\boldsymbol{H}}_Q=\hat{\boldsymbol{I}}\cdot\boldsymbol{Q}\cdot\hat{\boldsymbol{I}}, \quad [8]$$

where Q, in the principal axes system of the interaction, is given by

$$\boldsymbol{Q}=\delta\cdot\begin{pmatrix}-\frac{1+\eta}{2} & 0 & 0\\ 0 & -\frac{1-\eta}{2} & 0\\ 0 & 0 & 1\end{pmatrix}. \quad [9]$$

η and δ reflect the asymmetry and the anisotropy, respectively, of the interaction, with the latter given by

$$\delta=\frac{e^2qQ}{2I(2I-1)\hbar}. \quad [10]$$

The formal analogy of the dipolar and the quadrupolar interaction (Eqs. [1], [2] and [8], [9]) opens up the possibility of using the latter as an *intra*nuclear analogue to the *inter*nuclear dipolar interaction. Hence, from an experimental point of view, it can be envisaged that certain quadrupolar systems will be well suited to serve as models for small dipolar-coupled spin systems. Since the dipolar interaction is always symmetric, this model approach requires the field gradient tensor to be symmetric, i.e., $\eta=0$, and, additionally, both interactions to be of the same order of magnitude with respect to the dominating Zeeman interaction. Dipolar systems virtually never exceed coupling strengths of about 50 kHz and, hence, a first-order secular approximation is valid throughout, so that an analogous treatment of dipolar and quadrupolar interactions is, from the outset, restricted to first-order quadrupolar systems. Therefore, the discussions of quadrupolar systems are, in this review, limited to weak and symmetric couplings.

For the dipolar interaction, the secular part can be easily derived from the dipolar alphabet using the fundamental secular commutator $[\hat{\boldsymbol{H}}_Z,\hat{\boldsymbol{H}}_{D,\mathrm{sec}}]=0$. The secular part is obviously given by the terms A and B, because the terms C to F contain operators $\hat{\boldsymbol{I}}_\pm$, which do not commute with $\hat{\boldsymbol{I}}_z$ of the Zeeman interaction:

$$\begin{aligned} \hat{\boldsymbol{H}}_{D,\mathrm{sec}}^{(ij)} &= D^{(ij)}\cdot\frac{1}{2}(1-3\cos^2\theta)\cdot\big(3\hat{\boldsymbol{I}}_z^{(i)}\cdot\hat{\boldsymbol{I}}_z^{(j)}-\hat{\boldsymbol{I}}^{(i)}\cdot\hat{\boldsymbol{I}}^{(j)}\big) \\ &= D^{(ij)}\cdot\frac{1}{2}(1-3\cos^2\theta)\cdot\big[2\hat{\boldsymbol{I}}_z^{(i)}\cdot\hat{\boldsymbol{I}}_z^{(j)} \\ &\quad -\big(\hat{\boldsymbol{I}}_+^{(i)}\cdot\hat{\boldsymbol{I}}_-^{(j)}+\hat{\boldsymbol{I}}_+^{(j)}\cdot\hat{\boldsymbol{I}}_-^{(i)}\big)\big], \end{aligned} \quad [11]$$

(After this introductory section, the notation "sec" indicating the secular part of a Hamiltonian will be dropped for reasons of simplicity.) In this way, the dipolar interaction can be divided into a static term $\propto\hat{\boldsymbol{I}}_z^{(i)}\cdot\hat{\boldsymbol{I}}_z^{(j)}$ and an exchange term $\propto(\hat{\boldsymbol{I}}_+^{(i)}\cdot\hat{\boldsymbol{I}}_-^{(j)}+\hat{\boldsymbol{I}}_+^{(j)}\cdot\hat{\boldsymbol{I}}_-^{(i)})$ (*79*). The static term can be viewed as the interaction of a spin $\hat{\boldsymbol{I}}^{(i)}$ with the dipolar field of another spin $\hat{\boldsymbol{I}}_z^{(j)}$. Depending on the orientation, i.e., $+z$ or $-z$, of the second spin, two energy levels can be distinguished, which means that the static term gives rise to a doublet splitting. The exchange term combines states which differ only in the polarization of the spins. If the energy difference is negligibly small compared to the coupling, the dipolar field of one spin can "flip" the magnetic moment of the second spin in a resonance process, conserving the magnetic spin-quantum number M of the system and hence its energy, though both spins change the sign of their states. Once the precession frequencies of both nuclei are sufficiently different, this so-called "flip-flop" mechanism is energetically suppressed, and the system approaches the weak coupling limit. In

homonuclear systems, such a situation can be accomplished by chemical shift differences which exceed the dipolar couplings. In the case of heteronuclear dipolar couplings, the difference between the Larmor frequencies of both nuclei is, in general, several orders of magnitude larger than the dipolar coupling, so that the heteronuclear dipolar Hamiltonian is given by

$$\hat{\boldsymbol{H}}^{(IS)}_{D,\mathrm{sec}} = D^{(IS)} \cdot (1 - 3\cos^2\theta)(\hat{\boldsymbol{I}}_z \cdot \hat{\boldsymbol{S}}_z), \qquad [12]$$

with the exchange term being dropped and, for distinction, the two different spins being written as $\hat{\boldsymbol{I}}^{(i)} = \hat{\boldsymbol{I}}$ and $\hat{\boldsymbol{I}}^{(j)} = \hat{\boldsymbol{S}}$.

In analogy to the homonuclear dipolar case, the first-order secular part of the quadrupolar Hamiltonian is given by

$$\hat{\boldsymbol{H}}_{Q,\mathrm{sec}} = \frac{e^2qQ}{2I(2I-1)\cdot\hbar} \cdot \frac{1}{2}(1 - 3\cos^2\theta) \cdot (3\hat{\boldsymbol{I}}_z \cdot \hat{\boldsymbol{I}}_z - \hat{\boldsymbol{I}} \cdot \hat{\boldsymbol{I}}). \qquad [13]$$

2.2. The Spherical Representation of Interaction Tensors

For the theoretical description of NMR phenomena, it is advantageous to divide the Hamiltonians into a space part $\mathcal{A}$ and a spin part $\mathcal{T}$:

$$\hat{\boldsymbol{H}} = \hat{\boldsymbol{\mathcal{A}}} \cdot \hat{\boldsymbol{\mathcal{T}}}. \qquad [14]$$

In the secular approach, the reference frame is given by the LAB frame, whose z-axis is parallel to the quantization axis along $\boldsymbol{B}_0$. Consequently, all interactions have to be transformed from their principal axes frames, defined by the relative arrangement of the interacting nuclei, into the LAB frame, as has been done for the dipolar and first-order quadrupolar interactions in the previous section. Although these transformations can, in principle, be carried out using a Cartesian notation, such rotation transformations are, in general, more easily carried out in a spherical representation. This is of further importance, since fundamental experimental techniques, such as sample rotation (see below, Section 2.3) or application of radiofrequency pulses, are rotations in real or spin space, respectively. In this spherical representation, the spatial and spin parts, $\mathcal{A}$ and $\mathcal{T}$, split into three irreducible parts of the form

$$\mathcal{A} = \mathcal{A}_0 + \mathcal{A}_1 + \mathcal{A}_2, \qquad [15]$$

where $\mathcal{A}_0$ is a scalar, and $\mathcal{A}_1$ and $\mathcal{A}_2$ are antisymmetric and symmetric (this applies to $\mathcal{T}$ identically). The $\mathcal{A}_L$ terms consist of $2L + 1$ components $A_{L,M}$, which exhibit the same transformation properties as the spherical harmonics $Y_{L,M}$ (*90*). The Hamiltonian of any interaction can thus be written as (*51, 104*)

$$\hat{\boldsymbol{H}} = \sum_L \sum_{M=-L}^{L} (-1)^M \hat{\boldsymbol{A}}_{L,M} \cdot \hat{\boldsymbol{T}}_{L,-M}. \qquad [16]$$

These spherical operators are useful in that, under a rotation specified by the three Euler angles (χ, θ, ϕ), these components $A_{L,M}$ transform into linear combinations of themselves (below written as $\widetilde{A_{L,M}}$), with the rank L being conserved and the order M ranging from $-L$ to L (*90*):

$$\widetilde{A_{L,M}} = \sum_{m=-L}^{L} A_{L,m} D^{(L)}_{m,M}(\chi, \theta, \phi) = \sum_{m=-L}^{L} A_{L,m} \exp(-im\chi) d^{(L)}_{m,M}(\theta) \exp(-iM\phi). \qquad [17]$$

$D^{(L)}_{m,M}(\chi, \theta, \phi)$ denotes the component (m, M) of a Wigner rotation matrix, and the reduced form $d^{(L)}_{m,M}(\theta)$ is a combination of basic trigonometric functions (*73, 95*).

Following Eq. [16] and considering Eqs. [10] and [12], both the dipolar and the quadrupolar Hamiltonian can be easily written as a simple product of just one component of each tensor operator, i.e., $\hat{\boldsymbol{A}}_{2,0}$ and $\hat{\boldsymbol{T}}_{2,0}$, because of two limiting conditions: First, the absence of isotropic and antisymmetric parts restricts the rank to $L = 2$ and, second, the truncation by the first-order secular approach reduces the order to $M = 0$ due to $[\hat{\boldsymbol{I}}_z, \hat{\boldsymbol{A}}_{2,m}] = m\hat{\boldsymbol{A}}_{2,m}$. Taking additional normalization factors from the tensor algebra into account, the LAB-frame Hamiltonians are obtained in the form

$$\hat{\boldsymbol{H}}^{(ij)}_D = \sqrt{\frac{2}{3}} \cdot \hat{\boldsymbol{A}}^{(ij)}_{2,0} \cdot \hat{\boldsymbol{T}}^{(ij)}_{2,0} \qquad [18]$$

and

$$\hat{\boldsymbol{H}}_Q = \frac{1}{\sqrt{6}} \cdot \hat{\boldsymbol{A}}_{2,0} \cdot \hat{\boldsymbol{T}}_{2,0}. \qquad [19]$$

The spatial parts can be viewed as the product of a dipolar and quadrupolar "frequency," $\omega^{(ij)}_D$ and ω_Q, respectively, with a factor representing the orientational dependence of the symmetric interaction tensor with respect to the magnetic field $\boldsymbol{B}_0$ (i.e., in the LAB frame),

$$A^{(ij)}_{2,0} = \omega^{(ij)}_D \cdot \frac{1}{2}(1 - 3\cos^2\theta), \qquad [20]$$

where

$$\omega^{(ij)}_D = 3D^{(ij)} = -3\frac{\mu_0\hbar\gamma_i\gamma_j}{4\pi r^3_{ij}}, \qquad [21]$$

and

$$A_{2,0} = \omega_Q \cdot \frac{1}{2}(1 - 3\cos^2\theta), \qquad [22]$$

where

$$\omega_Q = 3 \cdot \frac{e^2 q Q}{4I(2I-1)\cdot\hbar} = \frac{3\pi C_Q}{2I(2I-1)\cdot\hbar}. \qquad [23]$$

In Eq. [23], the quadrupolar coupling constant, $C_Q = e^2 q Q/2\pi$, has been introduced, which reflects, in analogy to the dipolar case (see Eq. [3]), the strength of the interaction. The spin part of the Hamiltonians is represented by the tensor operator

$$\hat{\boldsymbol{T}}_{2,0}^{(ij)} = \frac{1}{\sqrt{6}}\left(3\hat{\boldsymbol{I}}_z^{(i)} \cdot \hat{\boldsymbol{I}}_z^{(j)} - \hat{\boldsymbol{I}}^{(i)} \cdot \hat{\boldsymbol{I}}^{(j)}\right) \qquad [24]$$

in the dipolar case and by

$$\hat{\boldsymbol{T}}_{2,0} = \frac{1}{\sqrt{6}}(3\hat{\boldsymbol{I}}_z \cdot \hat{\boldsymbol{I}}_z - \hat{\boldsymbol{I}} \cdot \hat{\boldsymbol{I}}) \qquad [25]$$

in the quadrupolar case. Summation of the dipolar pair tensors $\hat{\boldsymbol{T}}_{2,0}^{(ij)}$ over indistinguishable pairs of spins (ij)_results in a virtual quadrupolar system with an effective operator $\hat{\boldsymbol{T}}_{2,0}$, scaled by a factor of 2 (see Eqs. [103] to [105] in Section 3.3.2):

$$\hat{\boldsymbol{T}}_{2,0} = 2 \cdot \sum_{i<j} \hat{\boldsymbol{T}}_{2,0}^{(ij)}. \qquad [26]$$

In this way, a quadrupolar spin-$\frac{3}{2}$ nucleus becomes formally equivalent to the dipolar-coupled system of three methyl protons, because, in the latter case, the three dipolar pair couplings are indistinguishable due to the rapid rotation of the methyl group around its threefold symmetry axis. In Section 3.3.2 we will discuss how this analogy has been used for understanding the origin of MAS sidebands in dipolar MQ MAS experiments (*37*).

With respect to the Hamiltonians, the spherical representation of the interaction tensors is particularly useful for describing the effect of sample rotation, as will be shown in the following section.

2.3. Sample Rotation at the Magic Angle

In solid-state NMR, the spatial orientation of the interaction tensors relative to the external magnetic field is of central importance. In experiments on static samples, a wealth of information about structure and, even more importantly, dynamics of systems can be obtained from a whole range of multidimensional NMR experiments (*95*). Basically, all of these correlate different resonance frequencies corresponding to different tensor orientations on various time scales, and thus allow the determination of, e.g., molecular jump angles and rates. In rigid polycrystalline ^{1}H systems, however, the homonuclear dipolar interaction is stronger than the chemical shift by about one order of magnitude, such that, in static experiments, any chemical shift information is usually obscured due to the isotropic distribution over all dipolar tensor orientations. Since spectral resolution is essential for almost all ^{1}H NMR applications, one of the main experimental goals is the reduction of the homonuclear dipolar couplings.

It is the anisotropy of the dipolar interaction which causes the unwanted line broadening. The spatial part of the Hamiltonian is represented by a second-rank tensor component $A_{2,0}$, with an orientational dependence $\propto(1-3\cos^2\theta)$, where θ, as noted above, denotes the angle of the interaction vector with respect to the external magnetic field $\boldsymbol{B}_0$. This transformation property, which results from the coordinate transformation from the PAS to the LAB frame, hints at the possibility of removing the interaction by introducing a further reference frame (ROT), whose z-axis is tilted by the so-called magic angle $\theta_m = 54.7^\circ$ with respect to $\boldsymbol{B}_0$. While, by this definition, the components along $z^{(ROT)}$ become equal to zero, the perpendicular components in the $(xy)^{(ROT)}$-plane can, in principle, also be averaged to zero by a sufficiently fast rotation of the frame (therefore called rotor-fixed frame, ROT) about its z-axis, such that the interaction would vanish completely. This approach is experimentally realized by spinning the sample mechanically about an axis which is oriented at the angle θ_m relative to $\boldsymbol{B}_0$. The technique is well known as magic-angle spinning, and is widely applied in solid-state NMR, in particular for line-narrowing purposes. Its effect on a spatial part of the form $A_{2,0}$ can be evaluated, following Eq. [16], by a successive coordinate transformation from the PAS into the ROT frame and, finally, into the LAB frame:

$$\begin{aligned} A_{2,0}^{(LAB)}(t) &= \sum_{m=-2}^{2} A_{2,0}^{(PAS)} \underbrace{D_{0,m}^{(2)}(\alpha,\beta,\gamma)}_{(PAS)\rightarrow(ROT)} \underbrace{D_{m,0}^{(2)}(\omega_R t,\theta_m,0)}_{(ROT)\rightarrow(LAB)} \\ &= \sum_{m=-2}^{2} \underbrace{A_{2,0}^{(PAS)} d_{0,m}^{(2)}(\beta) e^{-im\gamma}}_{A_{2,m}^{(ROT)}} e^{-im\omega_R t} d_{m,0}^{(2)}(\theta_m) \end{aligned} \qquad [27]$$

The Euler angles (α,β,γ) denote the relative orientation of the PAS frame to the ROT frame. The angle $\omega_R t$ is the rotor phase, corresponding to a rotation of the sample about the $z^{(ROT)}$-axis with the angular frequency $\omega_R = 2\pi\nu_R = 2\pi/\tau_R$. The Hamiltonians of rotor-modulated interactions are often written in a Fourier series of the form

$$\hat{\boldsymbol{H}}(t) = \sum_{m=-2}^{2} \underbrace{A_{2,0}^{(PAS)} d_{0,m}^{(2)}(\beta) e^{-im\gamma} d_{m,0}^{(2)}(\theta_m) \cdot \hat{\boldsymbol{T}}_{2,0}}_{\hat{\boldsymbol{H}}_m} \cdot e^{-im\omega_R t}, \qquad [28]$$

where the Hamiltonian is a product of time-independent Fourier components $\hat{\boldsymbol{H}}_m$ and rotor modulation terms $e^{-im\omega_R t}$. Carrying out the summation in Eq. [28] and using the explicit forms of the reduced rotation matrices, the rotor-modulated and, hence,

time-dependent spatial part $\boldsymbol{A}_{2,0}(t)$ of the Hamiltonian $\hat{\boldsymbol{H}}(t)$ becomes, in the LAB frame,

$$\boldsymbol{A}_{2,0}^{(LAB)}(t) = \boldsymbol{A}_{2,0}^{(PAS)} \cdot \left[\frac{1}{2}\sin^2\beta\cos(2\omega_R t + 2\gamma) - \frac{1}{\sqrt{2}}\sin 2\beta\cos(\omega_R t + \gamma)\right]. \quad [29]$$

In the case of dipolar and first-order quadrupolar interactions, it should be noted that, in the PAS frame, the tensor component $\boldsymbol{A}_{2,0}^{(PAS)}$ is identical to the dipolar and quadrupolar frequency, $\omega_D^{(ij)}$ and ω_Q, respectively (see Eqs. [21] and [23]). Consequently, the introduction of the ROT frame can formally be expressed by changing the orientational dependence from $\frac{1}{2}(1 - 3\cos^2\beta)$, as given by Eq. [20] for the static case, to $[\frac{1}{2}\sin^2\beta\cos(2\omega_R t + 2\gamma) - \frac{1}{\sqrt{2}}\sin 2\beta\cos(\omega_R t + \gamma)]$ under MAS conditions. In the simplest case, when $\hat{\boldsymbol{H}}(t)$ commutes with itself for different time arguments t, i.e., $[\hat{\boldsymbol{H}}(t), \hat{\boldsymbol{H}}(t')] = 0$ with $t \neq t'$, the net Hamiltonian acting on the spin system during a period $[t_0, t_1]$ simply corresponds to the integration of the time-dependent spatial part:

$$\Omega(t_0, t_1) = \int_{t_0}^{t_1} A_{2,0}^{(LAB)}(t)\,dt = \frac{A_{2,0}^{(PAS)}}{2\omega_R} \cdot \left[\frac{1}{2}\sin^2\beta(\sin(2\omega_R t_1 - 2\gamma) - \sin(2\omega_R t_0 - 2\gamma)) - \sqrt{2}\sin 2\beta(\sin(\omega_R t_1 - \gamma) - \sin(\omega_R t_0 - \gamma))\right]. \quad [30]$$

With respect to NMR spectra, this expression for the rotor-modulated spatial part is of fundamental importance for the evaluation of MAS-induced sideband patterns originating from dipolar or first-order quadrupolar couplings. In a first approximation, the analysis of such sideband patterns is based on a dipolar *spin-pair* Hamiltonian or, by analogy, on a first-order quadrupolar Hamiltonian, both of which fulfill the above commutation relation $[\hat{\boldsymbol{H}}(t), \hat{\boldsymbol{H}}(t')] = 0$. The fulfillment of this commutation relation is central to Maricq and Waugh's definition of an "inhomogeneous" interaction (*72*), which was introduced above. For a general consideration of MAS beyond a dipolar-coupled spin pair, an average Hamiltonian approach, corresponding to a Magnus expansion (see, e.g., (*73*, p. 12), can be used to calculate the effective Hamiltonian $\tilde{\boldsymbol{H}}$ acting on the multispin system during a rotor period τ_R,

$$\tilde{\hat{\boldsymbol{H}}} = \tilde{\hat{\boldsymbol{H}}}^{(0)} + \tilde{\hat{\boldsymbol{H}}}^{(1)} + \tilde{\hat{\boldsymbol{H}}}^{(2)} + \cdots, \quad [31]$$

with the terms $\tilde{\hat{\boldsymbol{H}}}^{(p)}$ of order p representing nested integrals over commutators of the time-dependent Hamiltonian $\hat{\boldsymbol{H}}(t)$

$$\tilde{\hat{\boldsymbol{H}}}^{(0)} = \frac{1}{\tau_R}\int_0^{\tau_R} dt'\,\hat{\boldsymbol{H}}(t'),$$

$$\tilde{\hat{\boldsymbol{H}}}^{(1)} = -\frac{i}{2\tau_R}\int_0^{\tau_R} dt' \int_0^{t'} dt''\,[\hat{\boldsymbol{H}}(t'), \hat{\boldsymbol{H}}(t'')],$$

$$\tilde{\hat{\boldsymbol{H}}}^{(2)} = -\frac{1}{6\tau_R}\int_0^{\tau_R} dt' \int_0^{t'} dt'' \int_0^{t''} dt'''[[\hat{\boldsymbol{H}}(t'), \hat{\boldsymbol{H}}(t'')], \hat{\boldsymbol{H}}(t''')] + [[\hat{\boldsymbol{H}}(t'''), \hat{\boldsymbol{H}}(t'')], \hat{\boldsymbol{H}}(t')]. \quad [32]$$

For an inhomogeneous system, the expansion obviously reduces to its zeroth-order term, as was the case in Eq. [30]. In the terminology of Maricq and Waugh, the presence of any higher-order term originating from nonvanishing commutators $[\hat{\boldsymbol{H}}(t), \hat{\boldsymbol{H}}(t')] \neq 0$ makes the system homogeneous. To understand the averaging effect of MAS, it is important to note that the zeroth- and even the first-order terms vanish for an integration over a full rotor period, as can be seen from Eqs. [29] and [30] for the zeroth-order terms. Thus, when subject to an inhomogeneous interaction, the state of the spin system is fully refocused after each rotor period and the observed time signal does not decay, resulting in infinitely narrow spinning sidebands in the spectra.

In Eq. [31], the higher-order terms of the average Hamiltonian are defined in a recursive fashion by nesting the integrals and the commutators. A closer inspection reveals that a time factor of the order τ_R is associated with each integral, whereas the normalization factor remains proportional to τ_R^{-1}. Consequently, a term $\tilde{\hat{\boldsymbol{H}}}^{(p)}$ of order p contains an effective time factor of the order $\tau_R^{(p-1)}$, such that the higher-order terms, which are responsible for the homogeneous character, converge in the following recursive form (*35*)

$$\tilde{\hat{\boldsymbol{H}}}^{(p+1)} \propto \frac{|\hat{\boldsymbol{H}}|}{\omega_R} \cdot \tilde{\hat{\boldsymbol{H}}}^{(p)}, \quad [33]$$

with the ratio of the norm $|\hat{\boldsymbol{H}}|$ and the MAS frequency ω_R determining the weight of higher-order contributions. In other words, a term of order $(p + n)$ is discriminated with respect to a term of order p by a factor $(|\hat{\boldsymbol{H}}|/\omega_R)^n$.

Purely first-order quadrupolar systems are always inhomogeneous, while in dipolar multispin systems couplings between different pairs have to be considered. If the pairs are either identical or completely different, the commutators $[\hat{\boldsymbol{H}}_D^{(ij)}(t'), \hat{\boldsymbol{H}}_D^{(ij)}(t'')]$ or $[\hat{\boldsymbol{H}}_D^{(ij)}(t'), \hat{\boldsymbol{H}}_D^{(kl)}(t'')]$, respectively, vanish. The interference of two dipolar pair couplings involving one common spin, i.e., two pairs (ij) and (ik), leads to commutators of the form

$$\left[\hat{\boldsymbol{H}}_D^{(ij)}(t'), \hat{\boldsymbol{H}}_D^{(ik)}(t'')\right] = \hat{\boldsymbol{A}}_{2,0}^{(ij)}(t')\hat{\boldsymbol{A}}_{2,0}^{(ik)}(t'') \cdot \left[\hat{\boldsymbol{T}}_{2,0}^{(ij)}, \hat{\boldsymbol{T}}_{2,0}^{(ik)}\right], \quad [34]$$

which, in general, do not vanish, except for the special case of both spatial parts $\hat{\boldsymbol{A}}_{2,0}^{(ij)}(t)$ and $\hat{\boldsymbol{A}}_{2,0}^{(ik)}(t)$ having an identical

orientation and time dependence, which means $\hat{\boldsymbol{A}}_{2,0}^{(ij)}(t')/\hat{\boldsymbol{A}}_{2,0}^{(ik)}(t') = const$ for all t'. It is thus the commutator given in Eq. [34] which causes a dipolar-coupled multispin system to behave homogeneously under MAS, unless the dipolar interaction tensors $\boldsymbol{D}^{(ij)}$ and $\boldsymbol{D}^{(ik)}$ differ only in their absolute values, but not in their orientation dependence. In other words, to conserve an inhomogeneous character, $\boldsymbol{D}^{(ij)}$ and $\boldsymbol{D}^{(ik)}$ need to be transformable into each other by a simple scaling or translation procedure, as, e.g., for a linear arrangement of the three spins i, j, and k.

To conclude the consideration of the effect of MAS on the spatial parts of NMR interactions, we now turn briefly to the observed spectra. Static spectra exhibit characteristic lineshapes which result from the integration over the distribution of orientation-dependent resonance frequencies. When rotating the sample at the magic angle, the spatial parts of all anisotropic interactions are modulated and, consequently, spinning-sideband patterns are generated in the spectra. In the case of inhomogeneous systems, the resonance lines are, in theory, infinitesimally narrow, since the state of the spin system fully recovers after each rotor period and, hence, the time signal is continuously periodic. The inhomogeneous character of a system disappears as soon as a homogeneous interaction comes into play, since then the higher-order terms $\hat{\tilde{\boldsymbol{H}}}^{(n)}$ with $n > 1$ in Eq. [31] do contribute, making the spin system evolve in the form $\hat{\rho}(0) \rightarrow \hat{\rho}(\tau_R) \neq \hat{\rho}(0)$. The spin system does then not come back to its initial state and, due to destructive interference, the remaining contribution of $\hat{\rho}(0)$ to the states $\hat{\rho}\,(t = N\tau_R)$ at the so-called rotor echoes $t = N\tau_R$ decreases with increasing N. If $\hat{\rho}(0)$ is a completely detectable state with signal intensity $S(0)$, the signal $S(t)$ will then, in general, decay with time t. This behavior is well known as the free induction decay (FID) and a fundamental phenomenon in Fourier transform NMR. From this point of view, it is intuitive that homogeneous interactions broaden resonance lines, with the linewidth being determined by the time constant of the signal decay. In reverse, this argument means that reducing the contributions of higher-order terms $\hat{\tilde{\boldsymbol{H}}}^{(n)}$ in Eq. [31] by MAS narrows the resonance lines observed in the spectrum.

2.4. Moment Analysis of Static Dipolar Lineshapes

The presence of dipolar couplings $\hat{\boldsymbol{H}}_D^{(ij)}$, in addition to the Zeeman interaction $\hat{\boldsymbol{H}}_Z$, spreads the energy levels and, hence, the nuclear resonance frequencies symmetrically around the Larmor frequency, because every spin is subject to the dipolar fields of its neighboring spins. These fields, which depend on their relative "orientation" ($\propto \pm\hat{\boldsymbol{I}}_z$, cf. discussion in Section 2.1) with respect to the quantization axis, either raise or lower the energy level of the spin state. Applying perturbation theory, which can be restricted to first order since $|\hat{\boldsymbol{H}}_D| \ll |\hat{\boldsymbol{H}}_Z|$, the correction $E_D^{(1)}$ for the unperturbed energy level $E_Z^{(0)}$ of the Zeeman state is simply given by $|\hat{\boldsymbol{H}}_D|$. In general, the exact calculation of the eigenstates of $\hat{\boldsymbol{H}} = \hat{\boldsymbol{H}}_Z + \hat{\boldsymbol{H}}_D$ is not possible, because for homonuclear dipolar couplings $\hat{\boldsymbol{H}}_D$ the terms $\propto \hat{\boldsymbol{I}}_z^{(i)}\hat{\boldsymbol{I}}_z^{(j)}$ and $\propto \hat{\boldsymbol{I}}^{(i)}\hat{\boldsymbol{I}}^{(j)}$ do not commute and cannot be separated. In practice, the distribution of energy levels, corresponding to the static spectral lineshape, is therefore described by a phenomenological moment analysis following Van Vleck's approach (*111, 1*).

For a resonance line with a spectral distribution $f(\omega)$ around a central frequency ω_0, the nth moment is given by

$$M_n = \int (\omega - \omega_0)^n f(\omega)\, d\omega. \qquad [35]$$

The spectral distribution function $f(\omega)$ and the time signal $S(t)$ are interconvertable by Fourier transformation, which, for symmetric distributions, can be restricted to its cosine part:

$$S(t) \propto \int f(\omega) e^{i\omega t} d\omega \overset{symm.}{=} \int f(\omega)\cos(\omega t)\, d\omega. \qquad [36]$$

It is obvious that the even-numbered $2n$th moments M_{2n} are related to the $2n$th derivatives of the time signal with respect to time by

$$M_{2n} = \frac{(-1)^n}{S(0)} \left(\frac{\partial^{2n} S(t)}{\partial t^{2n}} \right)_{t=0}, \qquad [37]$$

while the odd-numbered moments vanish. Technically, the moment analysis corresponds to a series expansion of the signal $S(t)$, and can thus be written in the form

$$S(t) \propto 1 - \frac{t^2}{2!} M_2 + \frac{t^4}{4!} M_4 \mp \cdots. \qquad [38]$$

Denoting the dipolar coupling strength by $D^{(ij)}$ and its orientation-dependent form $D^{(ij)} \cdot \frac{1}{2}(3\cos^2\theta_{ij} - 1)$ by $\mathcal{D}_{ij}$, the second and fourth moments are given by (for derivation see (*1*))

$$M_2 = \frac{9}{4} \sum_{i<j}^{N} \mathcal{D}_{ij}^2 \overset{powder}{=} -\frac{9}{20} \sum_{i<j}^{N} \left(D^{(ij)}\right)^2 \qquad [39]$$

and

$$M_4 = \left(\frac{3}{2}\right)^4 \left[3\left(\sum_{i<j}^{N} \mathcal{D}_{ij}^2 \right)^2 - 2 \sum_{i<j}^{N} \mathcal{D}_{ij}^4 - \frac{1}{3N} \sum_{i\neq j\neq k}^{N} \left(\mathcal{D}_{ij}^2 (\mathcal{D}_{ik} - \mathcal{D}_{jk})^2 \right) \right]. \qquad [40]$$

The second moment consists of a sum over spin-pair terms (ij) only, while in the fourth moment the presence of a third spin k gives rise to terms consisting of products of spin-pair couplings (ij), (ik), and (jk), which thus correlate three spins. Proceeding to higher moments, it is clear that the maximum number of correlated spins increases with the order of the moments. Since the contribution of higher moments to the observed signal $S(t)$ increases with time (cf. Eq. [38]), the evolution of a multispin system under dipolar interactions has the effect of incorporating more and more spins into a common state: the dipolar-coupled

spin cluster grows (*78, 75*). In a more descriptive view, the moments given in Eq. [35] reflect the lineshape in the resonance spectrum. For example, a Gaussian lineshape

$$f(\omega) = \frac{1}{\Delta\sqrt{2\pi}} \exp\left(-\frac{(\omega-\omega_0)^2}{2\Delta^2}\right) \qquad [41]$$

requires the moments to fulfill the relation $M_{2n} = (2n-1)\Delta^{2n}$ and, consequently, $M_4/(M_2)^2 = 3$. A characteristic parameter, which is obvious from the experimental spectrum, is the full width at half-maximum height Δ' of the resonance line. A Gaussian line is characterized by $\Delta' = 2\sqrt{22}\Delta$. Comparing Eq. [39] with Eq. [40], it is clear that, in a multispin system, dipolar interactions do not result in a purely Gaussian lineshape, and M_4 can be written as $M_4 = 3(M_2)^2 + \xi$, with ξ denoting the deviation from a purely Gaussian behavior.

The practical significance of the moment analysis approach is that it provides an approximate but analytically manageable formalism which allows the description of spectral lineshapes without requiring a knowledge of the eigenfunctions or eigenvalues of the Hamiltonian of the entire system. The approach is limited to the interaction and the initial state of the spin system at the start of the evolution, with the interaction containing the structural information about the system. In this way, the second moment can be identified with an effective dipolar coupling strength $D_{\text{eff}} = \sqrt{\sum_{i<j}^{N} (D^{(ij)})^2}$, or an effective internuclear distance.

The static ^{1}H NMR spectrum of adamantane, shown in Fig. 1, exhibits a static linewidth of $\Delta' = 2\pi \cdot 12$ kHz. Approximating the lineshape by a purely Gaussian line, this results in an effective dipolar coupling strength of $D_{\text{eff}} \approx \Delta'/1.58 \approx 2\pi \cdot 7.6$ kHz.

2.5. Factorization of the Time Signal under MAS

The theoretical consideration of NMR spectra is generally based on the Liouville–von Neumann equation

$$\frac{\partial\hat{\rho}}{\partial t} = -i[\hat{\boldsymbol{H}}, \hat{\rho}(t)] = -i\hat{\mathcal{H}}\hat{\rho}(t), \qquad [42]$$

which is obtained through the extension of the time-dependent Schrödinger equation from a single wavefunction Ψ to a statistical quantum-mechanical ensemble, whose properties are reflected by a density matrix $\hat{\rho}$. The Hamiltonians represent all interactions acting on the system $\hat{\rho}$. Formally, this action can equivalently be written as a commutator $[\hat{\boldsymbol{H}}, \hat{\rho}(t)]$ or a superoperator $\hat{\mathcal{H}}\hat{\rho}(t)$. The formal solution to the differential Liouville–von Neuman equation is given by

$$\hat{\rho}(t) = \hat{\boldsymbol{L}}(t)\hat{\rho}(0)\hat{\boldsymbol{L}}^{+}(t) \qquad [43]$$

with the propagator

$$\hat{\boldsymbol{L}}(t) = \hat{\boldsymbol{T}} \exp\left(-i\int_0^t \hat{\boldsymbol{H}}(t')\,dt'\right), \qquad [44]$$

which "propagates" the density matrix of the system from $t' = 0$ to $t' = t$ by subjecting it to the interactions. The time-ordering operator $\hat{\boldsymbol{T}}$ formally ensures the correct order of the Hamiltonians $\hat{\boldsymbol{H}}(t')$ with respect to the time interval dt' of the integration. This time-ordering operation is required because, in general, Hamiltonians at different points of time do not commute; i.e., $[\hat{\boldsymbol{H}}(t'), \hat{\boldsymbol{H}}(t'')] \neq 0$ for $t' \neq t''$.

An alternative approach separates the rotor modulation from the Hamiltonian (see Eq. [28])

$$\hat{\boldsymbol{H}}(t) = \sum_{m=-2}^{2} \hat{\boldsymbol{H}}_m \cdot \exp(im\omega_R t) \qquad [45]$$

by applying the so-called Floquet formalism. Changing the reference system from Hilbert space to the infinite dimensional Floquet–Hilbert space means taking the MAS-induced time dependence out of the Hamiltonian and putting it into the wavefunction. This transformation corresponds to changing from the Heisenberg to the Schrödinger representation of quantum mechanics (*93*). In this way, there is no longer the need to apply time-ordering operators to the propagators, and the problem can be solved under MAS conditions in an analogous fashion to the static case. Furthermore, each wavefunction is directly related to a MAS sideband of corresponding order, and sidebands of different order can thus be described independently (*94, 81, 70, 82*). These simplifications are accomplished at the expense of having to deal with an infinite number of dimensions in the Floquet–Hilbert space; the reduction to a manageable number of dimensions then requires an approximate approach.

As described in great detail by Filip *et al.* (*35*), the transformation of Hamiltonians and density operators into Floquet space can be carried out in such a way that, on returning back into Hilbert space and incorporating the advances of Floquet formalism, the Liouville–von Neumann equation is obtained in the form

$$\frac{\partial}{\partial t}\hat{\rho}_{n,q}(t) = \underbrace{\left(i\omega_R\frac{\partial}{\partial\phi} + \sum_m \exp(im\phi)\hat{\mathcal{H}}_m\right)}_{\hat{\mathcal{H}}'}\hat{\rho}_{n,q}(t), \qquad [46]$$

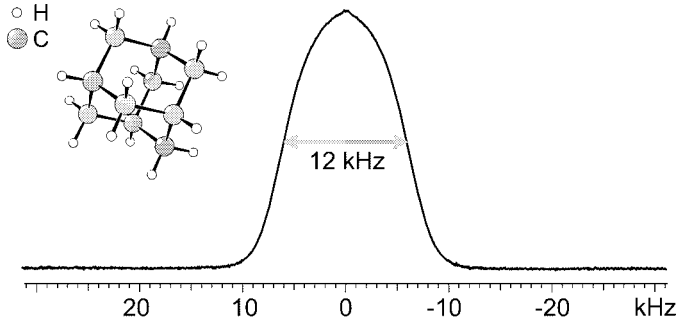

FIG. 1. Adamantane molecule $C_{10}H_{16}$ and static ^{1}H NMR spectrum of adamantane with experimental linewidth $\Delta' = 2\pi \cdot 12$ kHz.

where the operators $\hat{\mathcal{H}}_m$, $\frac{\partial}{\partial\phi}$, and $\hat{\mathcal{H}}'$ are written as superoperators $\hat{\mathcal{H}}\hat{\rho} = [\hat{\boldsymbol{H}}\hat{\rho} - \hat{\rho}\hat{\boldsymbol{H}}]$ in Liouville space. The density operator $\hat{\rho}_{n,q}$ is a matrix element of the Floquet density operator, which includes the initial state $\hat{\rho}(0)$, a MAS-related phase factor $\exp(iq\phi)$, and Fourier states $|n\rangle = \sum_{i=1}^{N} |\exp(in\omega_R t)|\Psi_i\rangle$:

$$\hat{\rho}_{n,q} = |n\rangle\langle n|\hat{\rho}(0)|n+q\rangle\langle n+q|\exp(iq\phi). \qquad [47]$$

The Hamiltonian $\hat{\mathcal{H}}'$ in Eq. [46] consists of two parts,

$$\begin{aligned}\hat{\mathcal{H}}^{(0)} &= i\omega_R\frac{\partial}{\partial\phi},\\ \hat{\mathcal{H}}^{(1)} &= \sum_m \exp(im\phi)\hat{\mathcal{H}}_m,\end{aligned} \qquad [48]$$

which, in terms of a perturbation approach, can be regarded as a dominant interaction $\hat{\mathcal{H}}^{(0)}$ perturbed by $\hat{\mathcal{H}}^{(1)}$, provided that the MAS frequency exceeds the rotor-modulated interaction to a sufficient extent, i.e., $\omega_R > |\sum_m \hat{\mathcal{H}}_m|$. Note that scaling the dominant interaction by ω_R corresponds to scaling the perturbation by ω_R^{-1}. Such a convergence with an inverse dependence on ω_R with respect to the unperturbed, i.e., dipolar-decoupled, case was encountered above in the discussion of the series expansion of an interaction under MAS (see Eq. [33]). Comparing the dipolar interaction in the rotor-modulated case with that in the static case, it is important to note that, under MAS, the zeroth Fourier component $\hat{\boldsymbol{H}}_0$ vanishes due to the magic-angle condition $\hat{\boldsymbol{H}}_0 \propto d^{(2)}_{0,0}(\theta_m) = \frac{1}{2}(3\cos^2\theta_m - 1) \stackrel{!}{=} 0$.

Proceeding with perturbation theory, the Hamiltonian $\hat{\mathcal{H}}'$ in Eq. [46] can be reexpressed in terms of the Fourier components of the rotor-modulated Hamiltonian (see Eq. [45]) (*35*):

$$\begin{aligned}\hat{\boldsymbol{H}}_{\text{eff}} = \hat{\boldsymbol{H}}_0 &+ \sum_{\substack{m=-2\\ m\neq 0}}^{2}\frac{[\hat{\boldsymbol{H}}_{-m},\hat{\boldsymbol{H}}_m]}{2m\omega_R}\\ &+ \sum_{\substack{m,p=-2\\ m,p\neq 0}}^{2}\frac{[[\hat{\boldsymbol{H}}_{-m},\hat{\boldsymbol{H}}_m],\hat{\boldsymbol{H}}_p]}{3mp\omega_R^2} + \cdots.\end{aligned} \qquad [49]$$

As a consequence of the Fourier approach, the initial state $\hat{\rho}(0)$ is formally distributed over the centerband $\hat{\rho}_0(0)$ and nth-order sidebands $\hat{\rho}_n(0)$, although at $t = 0$ obviously no rotor modulation has occurred yet,

$$\begin{aligned}\hat{\rho}_0(0) = \Bigg[1 &+ \sum_m \frac{\hat{\boldsymbol{H}}_m}{m\omega_R} + \sum_{m_1,m_2}\frac{[\hat{\boldsymbol{H}}_{m_2},\hat{\boldsymbol{H}}_{m_1}]}{2(m_1+m_2)m_2\omega_R^2}\\ &- \sum_m\frac{[\hat{\boldsymbol{H}}_{-m},\hat{\boldsymbol{H}}_m]}{2m^2\omega_R^2} - \sum_m\frac{[\hat{\boldsymbol{H}}_0,\hat{\boldsymbol{H}}_m]}{2m^2\omega_R^2}\Bigg]\hat{\rho}(0)\end{aligned} \qquad [50]$$

and

$$\hat{\rho}_n(0) = \left[-\frac{\hat{\boldsymbol{H}}_n}{n\omega_R} + \sum_m\frac{\hat{\boldsymbol{H}}_m\hat{\boldsymbol{H}}_{n-m}}{2n(n-m)\omega_R^2} - \frac{[\hat{\boldsymbol{H}}_n,\hat{\boldsymbol{H}}_0]}{2n^2\omega_R^2}\right]\hat{\rho}(0), \qquad [51]$$

where the summations are to be carried out over the range of Fourier components, i.e., $m, m_1, m_2 = 0, \pm1, \pm2$, excluding those values for which the denominator would be equal to zero. Note that the initial density operators of the MAS sidebands vanish, if there is no perturbation (i.e., $\hat{\rho}_n(0) = 0$ for $n > 0$, if $\hat{\boldsymbol{H}}_m = 0$ for all $m \neq 0$).

Considering these initial density operators, the following conclusions can directly be drawn: First, MAS sidebands originate from the rotor-modulated components $\hat{\boldsymbol{H}}_m$ with $m \neq 0$ of the Hamiltonian (see Eq. [28]); second, these components are scaled by ω_R^{-k}, where the exponent k corresponds to the degree of commutator nesting; and third, this approximation, using a first-order perturbation approach, includes only sidebands up to the second order, because the dipolar Hamiltonian, being a second-rank tensor operator, splits into Fourier components of up to second order only: $\hat{\boldsymbol{H}}_m$ with $-2 \leq m \leq 2$.

In general, the NMR time signal $S(t)$ can be expressed as $S(t) \propto \text{Tr}[\hat{\boldsymbol{I}}_x \cdot \hat{\rho}(t)]$, where $\hat{\boldsymbol{I}}_x$ represents the observation operator. Thus, starting from the initial states $\hat{\rho}_n(0)$ of all sideband orders n, the NMR time signal of a spin system, which is subject to an effective Hamiltonian $\hat{\boldsymbol{H}}_{\text{eff}}$, can be calculated using (*36*)

$$S(t) \propto \sum_{n=0}^{\infty}\text{Tr}\left[\hat{\boldsymbol{I}}_x\cdot\left(1 + \frac{(-it)}{1!}\hat{\mathcal{H}}_{\text{eff}} + \frac{(-it)^2}{2!}\hat{\mathcal{H}}_{\text{eff}}^2 + \cdots\right)\hat{\rho}_n(0)\right], \qquad [52]$$

where the exponential propagator has been approximated by a series expansion of the superoperator $\hat{\mathcal{H}}_{\text{eff}}$. This expansion can be written in a completely factorized form

$$S(t) = \sum_{n=0}^{\infty} I_n W_n(t)\exp(in\omega_R t), \qquad [53]$$

where the intensity I_n, the decay function $W_n(t)$, and the rotor modulation $\exp(in\omega_R t)$ are given by factors, each of which refers to a specific sideband order n. In analogy to the moment approach applied in the static case, the decay function $W_n(t)$, which determines the spectral lineshape, can be expanded into a series of moments $M_{k,n}$,

$$W_n(t) = \sum_{k=0}^{\infty}\frac{(-it)^k}{k!}M_{k,n}, \qquad [54]$$

with the kth moment of the nth-order spinning sideband being

given by

$$M_{k,n} = \frac{\mathrm{Tr}\left[\hat{\boldsymbol{I}}_x \cdot \hat{\boldsymbol{\mathcal{H}}}_{\mathrm{eff}}^{k} \hat{\rho}_n(0)\right]}{\mathrm{Tr}[\hat{\boldsymbol{I}}_x \cdot \hat{\rho}_n(0)]} = \frac{1}{I_n} \mathrm{Tr}\left[\hat{\boldsymbol{I}}_x \cdot \hat{\boldsymbol{\mathcal{H}}}_{\mathrm{eff}}^{k} \hat{\rho}_n(0)\right]. \quad [55]$$

Since it can be shown that $\sum_m \frac{1}{m} \hat{\boldsymbol{\mathcal{H}}}_m^{(ij)} \hat{\boldsymbol{\mathcal{H}}}_{-m}^{(ij)} = 0$, all odd-order moments vanish, so that the second moments $M_{2,n}$ are the leading terms in the series expansion of the decay functions (Eq. [54]). For the centerband ($n = 0$) and the nth-order sidebands, the intensities I_n and the second moments $M_{2,n}$ can themselves be expanded into series of the form

$$I_0 = \mathrm{Tr}\left[\hat{\boldsymbol{I}}_x \cdot \left(1 + \sum_m \frac{\hat{\boldsymbol{\mathcal{H}}}_m}{m\omega_R} + \sum_{m_1,m_2} \frac{\hat{\boldsymbol{\mathcal{H}}}_{m_2}\hat{\boldsymbol{\mathcal{H}}}_{m_1}}{(m_2+m_1)m_2\omega_R^2} - \sum_m \frac{\hat{\boldsymbol{\mathcal{H}}}_m\hat{\boldsymbol{\mathcal{H}}}_{-m}}{m^2\omega_R^2} + \cdots\right)\hat{\boldsymbol{I}}_x\right],$$

$$I_n = \mathrm{Tr}\left[\hat{\boldsymbol{I}}_x \cdot \left(-\frac{\hat{\boldsymbol{\mathcal{H}}}_n}{n\omega_R} + \sum_m \frac{\hat{\boldsymbol{\mathcal{H}}}_m\hat{\boldsymbol{\mathcal{H}}}_{n-m}}{n(n-m)\omega_R^2} - \sum_m \frac{\hat{\boldsymbol{\mathcal{H}}}_n\hat{\boldsymbol{\mathcal{H}}}_m}{nm\omega_R^2} - \frac{\hat{\boldsymbol{\mathcal{H}}}_n\hat{\boldsymbol{\mathcal{H}}}_0}{n^2\omega_R^2} + \cdots\right)\hat{\boldsymbol{I}}_x\right], \quad [56]$$

and

$$M_{2,0} = \frac{1}{I_0}\sum_{m,p} \frac{\mathrm{Tr}[\hat{\boldsymbol{I}}_x \cdot \hat{\boldsymbol{\mathcal{H}}}_m\hat{\boldsymbol{\mathcal{H}}}_{-m}\hat{\boldsymbol{\mathcal{H}}}_p\hat{\boldsymbol{\mathcal{H}}}_{-p}\hat{\boldsymbol{I}}_x]}{mp\omega_R^2} + \cdots,$$

$$M_{2,n} = \frac{1}{I_n}\sum_{m,p} \frac{\mathrm{Tr}[\hat{\boldsymbol{I}}_x \cdot \hat{\boldsymbol{\mathcal{H}}}_m\hat{\boldsymbol{\mathcal{H}}}_{-m}\hat{\boldsymbol{\mathcal{H}}}_p\hat{\boldsymbol{\mathcal{H}}}_{-p}\hat{\boldsymbol{\mathcal{H}}}_n\hat{\boldsymbol{I}}_x]}{mpn\omega_R^3} + \cdots. \quad [57]$$

Comparing $M_{2,0}$ and $M_{2,n}$, it is clear that the linewidths of the sidebands ($n \geq 1$) are determined by spin correlations, which are of higher order than those determining the width of the centerband, because the leading terms of $M_{2,0}$ and $M_{2,n}$ consist of products of four and five superoperators $\hat{\boldsymbol{\mathcal{H}}}_m$, respectively. Being written in such an elaborate way, the equations are rather complex and do not straightforwardly allow an efficient calculation of MAS spectra. The analytical expressions, however, provide valuable insight into the principal features of such spectra. With increasing time, the dipolar interaction correlates more and more spins, generating a growing dipolar-coupled cluster, which is well known from the static case. The decoupling effect of MAS counteracts this growth process through scaling the spin-correlation terms by increasing inverse powers ω_R^{-k} of the MAS frequency, with the exponent k corresponding to the order of the spin correlation, i.e., the number of coupled spins. This behavior is obvious from the intensities I_n of the centerband and the sidebands, when the terms in Eq. [55] are written in the following merged form, where the terms are ordered with respect to the inverse power of the MAS frequency, by which they are scaled (*36*):

$$I_n = I(0)\left(\delta_{n,0} + \frac{1}{\omega_R^2}\sum_{i,j}^{N} I_n^{(ij)} + \frac{1}{\omega_R^4}\sum_{i,j,k}^{N} I_n^{(ijk)} + \cdots\right). \quad [58]$$

The summations include all N spins of the system, $I(0)$ denotes the overall integral signal intensity, and the terms $I_n^{(ij)}$ and $I_n^{(ijk)}$ combine the contributions of two- and three-spin correlations (ij) and (ijk), respectively, to the intensity of the nth sideband. In the limit $\omega_R \to \infty$, all terms vanish except $\delta_{0,0} = 1$ which represents the remaining sharp central resonance line. The decay functions $W_n(t)$ from Eq. [54], which are responsible for the linewidths, can be written in an analogous form, as is shown here for the leading terms, i.e., the second moments, in the series expansion of Eq. [54]:

$$M_{2,n} = \frac{1}{I_n}\left(\frac{1}{\omega_R^2}\sum_{i,j,k}^{N} M_{2,n}^{(ijk)} + \frac{1}{\omega_R^4}\sum_{i,j,k,l}^{N} M_{2,n}^{(ijkl)} + \cdots\right). \quad [59]$$

Comparing this series to that of the intensities in Eq. [58], it is clear that two-spin correlations, in spite of being the leading terms for the intensities, do not contribute to the moments and, hence, not to the linewidth either. Instead, the latter is primarily determined by three-spin correlations and, with decreasing weight, by higher spin correlations. The intensities, on the contrary, are dominated by two-spin correlations, reflecting the inhomogeneous character of a dipolar spin-pair system. In more general terms, Eqs. [58] and [59] show that with increasing MAS frequency, ω_R, the multispin dipolar network is simplified, because low-spin correlations dominate both the intensity distribution and the linewidths of the sidebands.

2.6. Narrowing of Dipolar-Broadened Lines by MAS

In the above section, it has been shown that combining the Floquet formalism with perturbation theory allows the factorization of the NMR time signal $S(t)$ under MAS in terms of a Fourier series (see Eq. [53]). Concerning spectral resolution and, hence, the access to chemical shift information, the linewidth, determined by the decay function $W_n(t)$, is the critical parameter. From the above equations, the degree of line narrowing achievable by MAS can be estimated by comparison to the case of a static dipolar-coupled system. For the latter, assuming a Gaussian lineshape, the linewidth is proportional to the square root of the second moment. Therefore, if it is assumed that a given resonance line, in particular the centerband, under MAS can also be approximated by a Gaussian shape, the ratio of the second moments of the static line and the MAS centerband directly reflects the relative line-narrowing

effect:

$$\frac{(M_2)_{\mathrm{MAS}}}{(M_2)_{\mathrm{stat}}} = \frac{\frac{1}{\omega_R^2}\sum_{m,p}\frac{1}{mp}\,\mathrm{Tr}[\hat{\boldsymbol{I}}_x\cdot\hat{\boldsymbol{\mathcal{H}}}_m\hat{\boldsymbol{\mathcal{H}}}_{-m}\hat{\boldsymbol{\mathcal{H}}}_p\hat{\boldsymbol{\mathcal{H}}}_{-p}\hat{\boldsymbol{I}}_x]+\cdots}{\mathrm{Tr}\big[\hat{\boldsymbol{I}}_x\cdot\hat{\boldsymbol{\mathcal{H}}}_D^2\hat{\boldsymbol{I}}_x\big]}. \qquad [60]$$

Apart from the obvious ω_R^{-2}-scaling ensuring a reduction of $(M_2)_{\mathrm{MAS}}$ for high MAS frequencies, it is interesting to inspect the products of the dipolar superoperators. The leading term of the series expansion in the numerator is a sum over products of the form $\frac{1}{mp}\hat{\boldsymbol{\mathcal{H}}}_m\hat{\boldsymbol{\mathcal{H}}}_{-m}\hat{\boldsymbol{\mathcal{H}}}_p\hat{\boldsymbol{\mathcal{H}}}_{-p}$, which consist of Fourier components of the dipolar Hamiltonian with $m, p \neq 0$, with the superoperators $\hat{\boldsymbol{\mathcal{H}}}_{m,p}$ denoting the respective sums $\sum_{i<j}\hat{\boldsymbol{\mathcal{H}}}_{m,p}^{(ij)}$ over all dipolar-coupled pairs (ij). The possible combinations of indices m and p in the product are restricted by two conditions: First, one spin has to be identical in all four pair superoperators of the product, because otherwise the commutators—which are inherent to the above superoperator notation—would vanish. Second, the product is also equal to zero, if all four operators concern the same spin pair (ij), because $\sum_m \frac{1}{m}\hat{\boldsymbol{\mathcal{H}}}_m^{(ij)}\hat{\boldsymbol{\mathcal{H}}}_{-m}^{(ij)} = 0$. As a consequence of these two conditions, the product $\frac{1}{mp}\hat{\boldsymbol{\mathcal{H}}}_m\hat{\boldsymbol{\mathcal{H}}}_{-m}\hat{\boldsymbol{\mathcal{H}}}_p\hat{\boldsymbol{\mathcal{H}}}_{-p}$ gives rise to three-spin correlations only and can hence be written as

$$\sum_{m,p}\frac{1}{mp}\hat{\boldsymbol{\mathcal{H}}}_m\hat{\boldsymbol{\mathcal{H}}}_{-m}\hat{\boldsymbol{\mathcal{H}}}_p\hat{\boldsymbol{\mathcal{H}}}_{-p} = \sum_{\substack{i<j,k\\ k\neq j}}\sum_{m,p}\frac{1}{mp}\hat{\boldsymbol{\mathcal{H}}}_m^{(ij)}\hat{\boldsymbol{\mathcal{H}}}_{-m}^{(ij)}\hat{\boldsymbol{\mathcal{H}}}_p^{(ik)}\hat{\boldsymbol{\mathcal{H}}}_{-p}^{(ik)}. \qquad [61]$$

In contrast, the static term in the numerator, which contains $\hat{\boldsymbol{\mathcal{H}}}_D^2 = \sum_{i<j,k}\hat{\boldsymbol{\mathcal{H}}}_D^{(ij)}\hat{\boldsymbol{\mathcal{H}}}_D^{(ik)}$, leads to the generation of three-spin (for $j \neq k$) as well as two-spin correlations (for $j = k$). Therefore, the denominator exceeds the numerator by these two-spin correlations. Moreover, a more detailed analysis including the orientation dependencies of the dipolar couplings reveals that the contribution of spin correlations decreases with increasing number of involved spins. Though this behavior depends on the geometry of the considered system, it turns out to be a general feature when taking the following aspect into account: A two-spin correlation contributes to a large extent to the state of the spin system, if the orientation of the dipolar interaction tensor with respect to the magnetic field is favorable. In order to allow a three-spin correlation to contribute to the same extent, at least two interaction tensors have to be oriented in a comparably favorable way. The latter scenario, however, is less probable. With an increasing number of spins, the statistical probability of the system being favorably oriented decreases and, therefore, in Eq. [60] the denominator always exceeds the numerator by a considerable amount.

The line-narrowing effect of MAS is hence twofold: First, two-spin correlations no longer contribute to the linewidth, but instead give rise to the generation of sidebands; second, the second moment is, under MAS, scaled by ω_R^{-2}, which means an ω_R^{-1}-scaling of the linewidth. At first sight, the former effect appears to be independent of the MAS frequency, but in fact MAS comes into play gradually with increasing ω_R, because the approximations improve, on which the analytical considerations in the previous section are based. For the series expansions, the ratio of the dipolar coupling strength versus the MAS frequency is crucial, and the restriction to the leading terms, as in Eq. [60], represents the maximum simplification which is only justified for MAS frequencies exceeding the Fourier components $\hat{\boldsymbol{\mathcal{H}}}_m^{(ij)}$ of the dipolar interaction.

Hence, starting from the static case and increasing the spinning frequency gradually, MAS reduces the width of homogeneously broadened resonance lines at first as a result of the coaction of, first, the ω_R^{-1}-scaling and, second, the increasingly efficient suppression of the line-broadening effects of higher spin correlations. This suppression means, in other words, that the system, though homogeneous under static conditions, develops an inhomogeneous character under MAS. Once this quasi-inhomogeneous limit is reached, the linewidth shows a pure ω_R^{-1} dependence, as is depicted in Fig. 2b.

To conclude this section, we point out that the fundamental mechanism underlying the line-narrowing effect of MAS in homogeneous dipolar systems is that MAS suppresses the contributions of higher spin correlations to the observed signal, and the suppression efficiency increases with the number of spins involved in the correlation. While, in the static case, two-spin correlations are primarily responsible for ^{1}H linewidths, they no longer contribute to the broadening of a resonance line under sufficiently fast MAS, since they are of inhomogeneous character and, hence, primarily responsible for the intensity distribution over the spinning-sideband pattern. Therefore, maximum line narrowing is already achieved when the MAS frequency suffices to suppress three-spin correlations efficiently. It is hence *not* true that there is no hope to narrow a homogeneously broadened line as long as the MAS frequency is less than the observed static linewidth. Instead of the effective overall coupling, the MAS frequency needs to exceed only those dipolar pair interactions, from which three-spin correlations arise (*36*). This means that, theoretically speaking, MAS may even be less than the strongest pair interactions, because no line broadening occurs as long as only two-spin correlations are generated. In real systems, it is usually rather difficult to make this distinction, and the complexity of the equations discussed in this context indicates that it is, for a particular sample, also very difficult to predict the dependence between linewidth and MAS frequency in a fully quantitative manner. However, state-of-the-art MAS equipment allows spinning frequencies considerably above the strongest dipolar pair couplings in rigid ^{1}H systems, which are only up to about $D^{(ij)} = 2\pi \cdot 20$ kHz. In this way, quasi-inhomogeneous conditions can be achieved in most cases to a satisfactory extent.

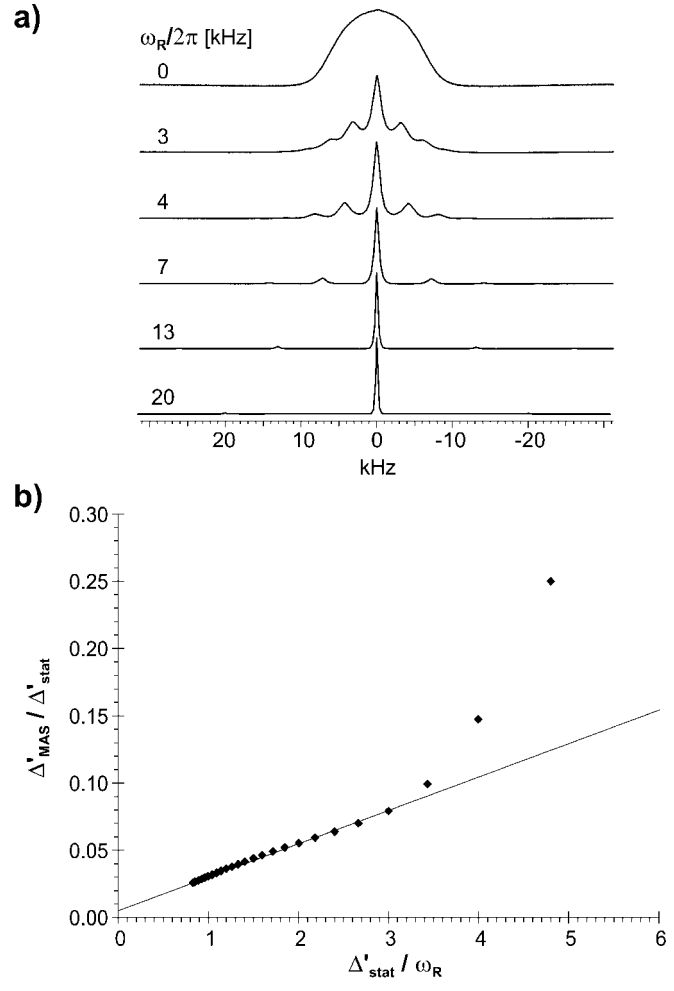

FIG. 2. (a) ^{1}H one-pulse spectra of adamantane, recorded at different MAS frequencies. (b) ^{1}H linewidth of adamantane under MAS plotted against the spinning frequency. The experimental linewidth is scaled relative to its static value of $\Delta'_{\text{stat}} = 2\pi \cdot 12$ kHz.

2.7. MAS Sideband Patterns and Model Spin Systems

The previous sections revealed that, considering the ^{1}H time domain signal under MAS, the dominating terms of the dipolar interactions, i.e., the two-spin correlations, do not broaden the resonance lines, but are instead primarily responsible for the intensity distribution over the spinning-sideband pattern. On the one hand, this points out that resolution enhancement is possible by applying MAS frequencies even below the static linewidth. On the other hand, the experimental spinning-sideband pattern itself contains information about the underlying dipolar interaction, because the pattern maps out the anisotropy of the interaction and allows the determination of the tensor and its orientation. Indeed, the inspection of MAS sideband patterns has become a well-established approach for characterizing the chemical shift anisotropy (CSA) (*72, 56*). Analogously, an analysis of the sideband pattern originating from dipolar two-spin correlations would be expected to yield the strength of the underlying dipolar pair coupling.

The NMR time signal $S(t)$ of a single dipolar-coupled spin pair can easily be calculated by integrating the rotor-modulated spatial part of the dipolar interaction $\boldsymbol{D}^{(ij)}$ over the time interval $[0, t]$ (see Eq. [30]). For powdered samples, the polar angles $(\beta_{ij}, \gamma_{ij})$ of the symmetric interaction tensor have to be averaged over all orientations with respect to $\boldsymbol{B}_0$:

$$S(t) \propto \left\langle \cos\left(\int_0^t A_{2,0}^{(LAB),(ij)}(t)\, dt \right) \right\rangle$$
$$= \left\langle \cos\left(\frac{3D^{(ij)}}{2\omega_R} \cdot \left[\frac{1}{2} \sin^2\beta(\sin(2\omega_R t - 2\gamma) + \sin(2\gamma)) \right.\right.\right.$$
$$\left.\left.\left. - \sqrt{2} \sin 2\beta(\sin(\omega_R t - \gamma) + \sin(\gamma)) \right] \right) \right\rangle. \qquad [62]$$

In Fig. 3, the characteristic behavior of an inhomogeneous dipolar spin-pair system under MAS is displayed: As soon as the sample rotation sets in, the static Pake pattern (*88*) splits immediately into a bunch of infinitesimally sharp rotational sidebands. With increasing MAS frequencies, the signal gradually concentrates in the centerband. In the static case, the strength

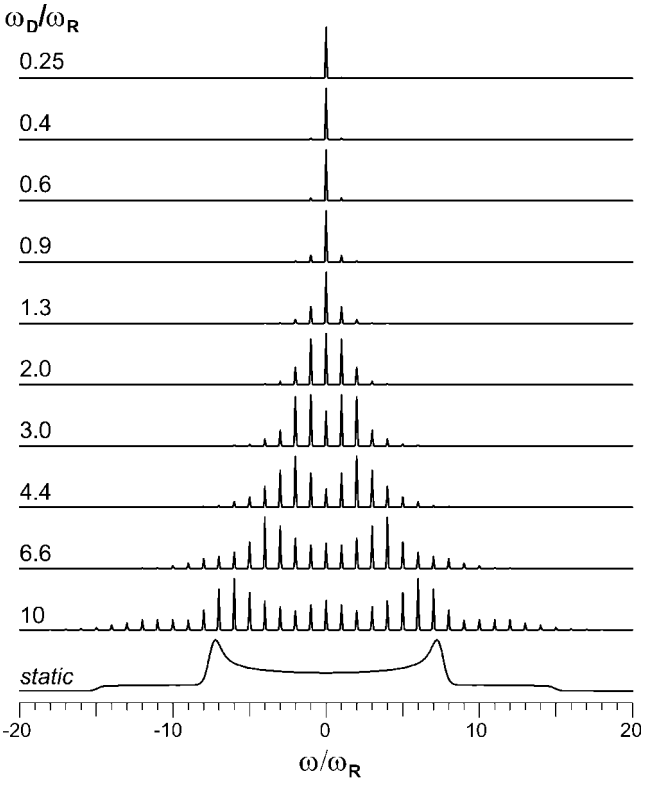

FIG. 3. ^{1}H spin-pair spectra calculated using Eq. [61] for static conditions and under MAS of different frequencies ω_R. The spinning-sideband patterns, as well as the static Pake pattern, allow the determination of the dipolar coupling strength. The spectra are scaled to equal height.

of the dipolar interaction can be directly determined from the frequency difference between the two singularities of the Pake pattern, while, under MAS, the coupling strength is reflected in the sideband pattern (*46*). From an experimental point of view, it is important to note that the signal-to-noise ratio dramatically improves under MAS, because the signal is concentrated in sharp sidebands instead of being distributed over a large spectral range.

In order to ensure simplicity, the above equation considers only a single spin pair, while real ^{1}H systems are usually characterized by many dipolar proton–proton couplings. In such ^{1}H multispin systems, three-spin and higher spin correlations give rise to the familiar homogeneous line-broadening effects and also to distortions of the intensity distribution over the MAS sideband pattern (see Section 2.5). In order to get an idea about the changes occurring in the MAS spectrum when an inhomogeneous ^{1}H system gradually becomes homogeneous, we now consider the perturbing effect of a third spin on a spin pair, with the third spin embodying all additional dipolar couplings acting on the spin pair. To provide a self-consistent scale for the perturbations as well as for the decoupling effect of MAS, both the perturbing coupling and the MAS frequency are given relative to the considered pair coupling:

$$\xi_1 = \frac{D^{\text{pert}}}{D^{\text{pair}}} \quad \text{and} \quad \xi_2 = \frac{2\pi D^{\text{pair}}}{\omega_R}. \qquad [63]$$

Consequently, with respect to the MAS frequency, ω_R, the perturbation can be represented by a dimensionless parameter ξ,

$$\xi = \xi_1 \cdot \xi_2 = \frac{2\pi D^{\text{pert}}}{\omega_R}. \qquad [64]$$

When more than one spin perturbs the pair coupling, the effective perturbing coupling strength D^{pert} can be approximated by the sum $D_{\text{eff}}^{\text{pert}} = \sqrt{\sum (D_i^{\text{pert}})^2}$ over all perturbing couplings D_i^{pert}. Thus, the perturbation decreases either when D^{pair} increases relative to D^{pert} or when the MAS frequency, i.e., the decoupling efficiency, increases.

In addition the effective strength of the perturbation, represented by ξ, also the mutual arrangement of the three spins influences the transition from an inhomogeneous to a homogeneous system. In the discussion of Eq. [34], it has already been noted that the inhomogeneous character is preserved when the three or more spins are arranged in a linear fashion. In this special and somewhat artificial case, no line broadening occurs, and the effect of the perturbing spin on the intensity distribution over the sideband pattern can be investigated selectively. Thus, to resemble the homogeneous properties of real ^{1}H systems, the three spins have to adopt a nonlinear arrangement. As a simple representative geometry, we place three spins at the vertices of an isosceles triangle, which will henceforth be referred to as the Δ-arrangement.

In the following, we consider ^{1}H spin pairs with an internuclear distance of 0.18 nm, corresponding to the protons of a CH_2 group, with a dipolar coupling of $D^{\text{pair}} = 2\pi \cdot 20.6$ kHz. A third spin interacts with this pair through perturbing couplings within the range of $D^{\text{pert}} = 0 \ldots \frac{1}{2} D^{\text{pair}}$. Both the inhomogeneous case of a linear arrangement and the homogeneous case of a Δ-geometry were numerically simulated by means of an explicit density matrix calculation. The MAS frequency is set to $\omega_R = 2\pi \cdot 10$ kHz, which is less than the dominating pair coupling, but $\omega_R \geq D^{\text{pert}}$ is ensured.

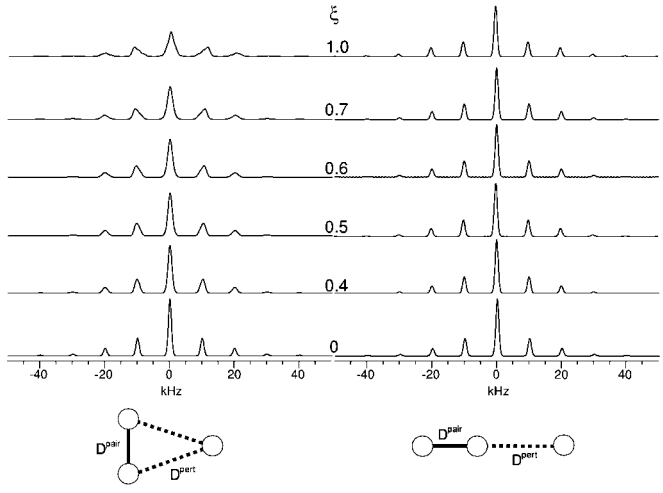

FIG. 4. MAS spectra of two ^{1}H three-spin systems of different geometry. A dominating pair interaction $D^{\text{pair}} = 2\pi \cdot 20.6$ kHz is perturbed by a coupling to a third spin of $D^{\text{pert}} = 2\pi \cdot (1 \ldots 10)$ kHz. The MAS frequency is $\omega_R = 2\pi \cdot 10$ kHz, and hence $\xi \approx 0.1 \ldots 1$.

Figure 4 shows the simulated ^{1}H MAS spectra for both considered spin arrangements. The residual linewidth for $\xi \to 0$ is purely artificial and corresponds to the number of calculated time increments for the signal and the subsequently applied weighting function. With increasing perturbation, the resonance lines decrease in height and, in the homogeneous case, undergo a severe broadening which increases with the order of the sideband. In the inhomogeneous case, as is expected, no line broadening is observed, but even the pattern seems to be only marginally distorted by the perturbation; the extent of the perturbing effect is displayed in Fig. 5a. With respect to the intensity distribution over the sideband pattern, both arrangements show effects of comparable extent, but in the Δ-arrangement the intensity of the centerband is reduced most, while in the linear arrangement the first-order sidebands are also strongly affected.

Another feature arising from the geometry is the fact that the spins in the Δ-geometry are much more likely to form three-spin correlations than in a linear arrangement. Therefore, it is interesting to investigate the actual contribution of three-spin correlations to the MAS spectrum of the Δ-system. In order to unravel these, the three-spin MAS spectrum based on two-spin correlations only is calculated for comparison. Recalling Eq. [58], it is clear that each spin contributes a normalized signal intensity of, say, one, which remains in the centerband as long as there is no dipolar interaction present: $\delta_{0,0} = 1$ and $I_n^{(\cdots)} = 0$. Any pair

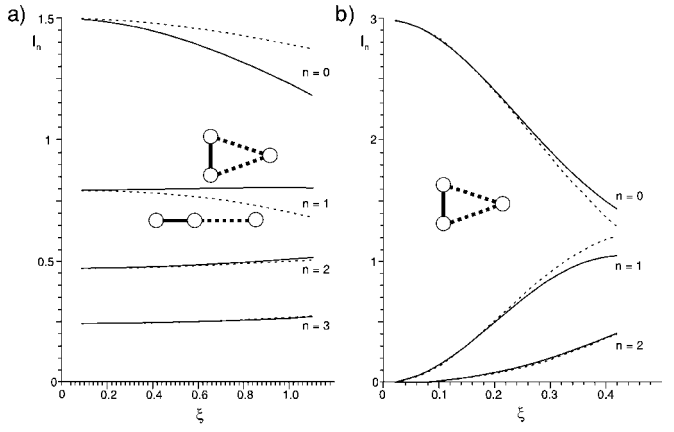

FIG. 5. (a) Centerband ($n = 0$) and sideband intensities in MAS spectra of the ^{1}H three-spin systems depicted Fig. 4: solid lines, Δ-geometry; dotted lines, linear geometry. (b) Contribution of spin correlations of different order to the intensity distribution over the sideband pattern for the Δ-geometry; solid lines, two- and three-spin correlations; dotted lines, only two-spin correlations.

coupling transfers signal intensity from the centerband into spinning sidebands. Considering again the Δ-geometry, each of the spin pairs is coupled to two spins at distances of 0.18 and 0.30 nm, corresponding to dipolar coupling strengths of $D^{(ij)}/2\pi = 20.6$ and 4.5 kHz, respectively, with the perturbing spin being symmetrically coupled to each of the spins in the pair by $D^{(ij)}/2\pi = 4.5$ kHz. Consequently, the sideband intensities are given by the sum of three spin-pair spectra with the respective coupling strengths 20.6, 4.5, and 4.5 kHz, while the centerband is reduced from its initial normalized value of 3 to the residual signal intensity which has not been transferred to the sidebands. In Fig. 5b, the sideband intensities originating from two-spin correlations only and from the entire three-spin system are compared. It is then apparent that up to a perturbation of about $\xi = 0.3 \cdots 0.4$ the three-spin correlations can safely be neglected.

Another example demonstrating the decoupling efficiency of MAS is displayed in Fig. 6, namely a planar four-spin system consisting of two spin pairs, each coupled by D^{pair} and interacting with each other by $D^{\text{pert},1} = 0.3 \cdot D^{\text{pair}}$ and $D^{\text{pert},2} = 0.17 \cdot D^{\text{pair}}$, respectively. The MAS frequency is only $\frac{2}{3}$ of the dominant pair interaction, but it provides efficient decoupling of both pairs, since it exceeds all interpair couplings. Comparing the spectrum of two superimposed spin pairs with that of the full four-spin system, it is obvious that, though the lines are clearly dipolar broadened in the latter, the intensity distribution over the sideband pattern agrees within an error of only 10%. This result confirms that perturbations are negligible, unless they become stronger than $\xi \approx 0.5$, because in the considered four-spin system the pairs perturb each other by $\xi = 0.45$ and $\xi = 0.25$, respectively. Although the perturbing effect is small, it changes, in addition to the line-broadening effect, the intensity distribution over the sideband pattern exactly as expected: While in the spin-pair spectrum the intensity ratio between the two first-order sidebands and the centerband is 0.40/0.48, the additional interpair couplings transfer intensity into the sidebands, resulting in a ratio of 0.45/0.44. As a first approximation, this effect can be taken into account by adding the first-order sideband intensities of the spin-pair spectra with the coupling strengths $D^{\text{pert},1}$ and $D^{\text{pert},2}$, respectively. These values are 0.06 and 0.02, respectively, and, after renormalizing the overall intensity to one, the ratio between first-order sideband and centerband is then 0.45/0.45, which is in good agreement with the spectrum of the whole four-spin system.

2.8. ^{1}H MAS Spectrum of Adamantane

The most stringent test for the validity and the limitation of the spin-pair approach is provided by the inspection of cubic systems of coupled spins. Therefore, in this section, we will demonstrate that the MAS spectrum of the protons in adamantane, which form a dense and cubic multispin system, can be understood in terms of a spin-pair approach. An adamantane molecule consists of six CH_2 and four CH units, whose ^{1}H chemical shift difference is too small to be detected in solid-state NMR. In this context, adamantane can be considered a spherical molecule with its 16 protons sitting on the surface of a spherical framework of 10 carbon atoms. At room temperature, each molecule rotates sufficiently fast and isotropically on its site in the crystal, so that all intramolecular dipolar couplings are effectively averaged to zero. Within a molecule, the protons are thus fully decoupled from each other, and they are all placed, on average, at the center of gravity of the molecule. The only dipolar interactions observed are hence intermolecular ones between the atoms located at these centers. In this plastic phase, the adamantane unit cell is face-centered cubic with $a = 0.945$ nm (3), so that each molecule has 12 nearest neighbors at a distance,

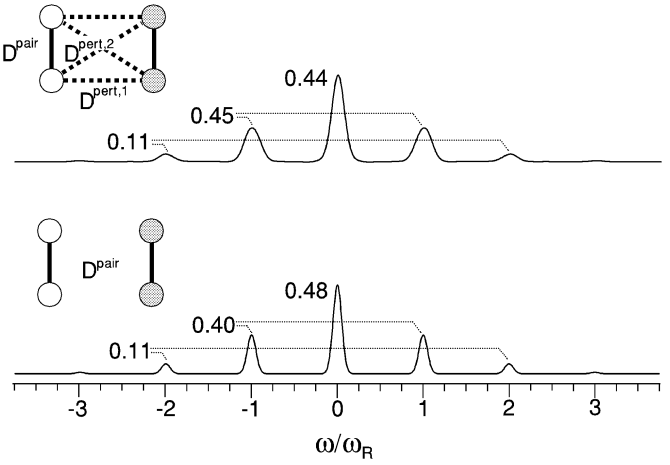

FIG. 6. MAS spectra of a four-spin system, consisting of two pairs coupled by D^{pair}, which interfere with each other by couplings of $D^{\text{pert},1} = 0.3 \cdot D^{\text{pair}}$ and $D^{\text{pert},2} = 0.17 \cdot D^{\text{pair}}$. The MAS frequency exceeds the interpair, but not the intrapair couplings ($\omega_R = \frac{2}{3} D^{\text{pair}}$), and therefore the bottom spectrum corresponding to the superposition of two pure pair spectra agrees well with the full four-spin spectrum (top) except for line-broadening effects.

measured between the centers of the molecules, of $d \approx 0.67$ nm. Therefore, each proton in adamantane is coupled to 16 protons in each of the 12 nearest-neighbor molecules, which amounts to a total of 192 nearest-neighbor protons.

Considering the adamantane molecule as a rapidly and isotropically rotating sphere with a radius of $r = 0.225$ nm, two protons of next-neighbor molecules are coupled by an averaged dipolar interaction of $\bar{D} \approx 2\pi \cdot 410$ Hz. In addition to this closest sphere of neighboring protons, there are of course couplings to all the protons in the more remote spheres, but due to the weak coupling strengths they only negligibly affect the MAS sideband pattern.

Thus, the structure of the ^{1}H multispin system in adamantane does not at all imply well-defined spin-pair interactions, but nevertheless its MAS spectrum can be explained quantitatively from two-spin correlations. For the spectrum at $\omega_R = 2\pi \cdot 4$ kHz (see Fig. 7), the two-spin approach is valid, i.e., only the leading term is required for the convergence of the relevant series expansion, because the sidebands are well resolved (see Fig. 2) and the width of the centerband belongs to the range where the linewidth decreases proportional to ω_R^{-1}. Note that such a behavior is observed, although ω_R is only $\frac{2}{3}$ of the static ^{1}H linewidth.

From the spectrum in Fig. 7 and, in particular, from the schematic representation, it is clear that the sidebands are almost twice as broad as the centerband. This observation means that higher spin correlations do affect the spectrum by line broadening, but their influence is still too weak to distort the intensity distribution—the latter statement being demonstrated by the fact that the pattern can be completely described by a spin-pair calculation. After equalizing the experimental linewidths schematically (Fig. 7), the intensity distribution agrees perfectly with a spin-pair spectrum corresponding to a dipolar coupling of $D^{\text{pair}} = 2\pi \cdot 5.6$ kHz.

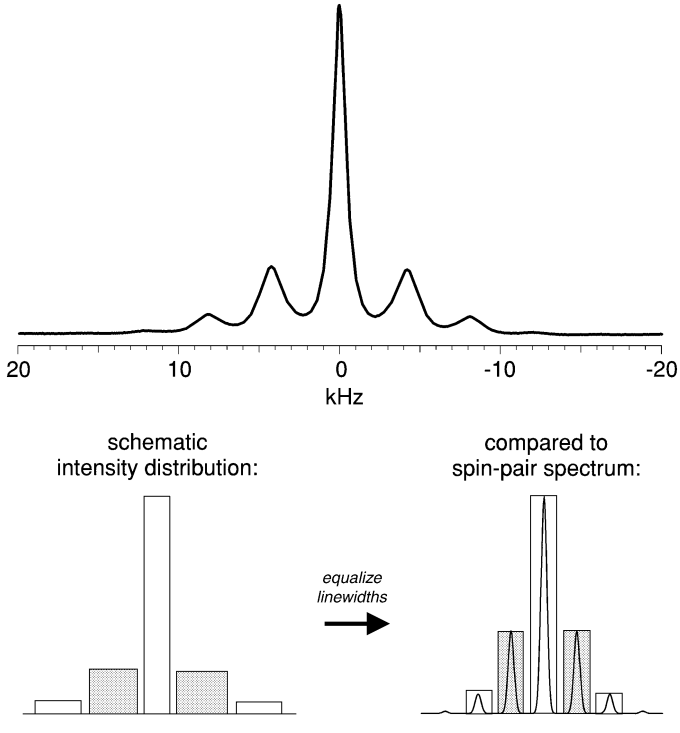

FIG. 7. ^{1}H one-pulse spectrum of adamantane under MAS at $\omega_R = 2\pi \cdot 4$ kHz. The sideband intensity distribution is schematically depicted below. In order to compare the experimental spectrum with a calculated two-spin pattern (in this case for a coupling of $D^{(ij)} = 2\pi \cdot 5.6$ kHz), the linewidths have to be equalized.

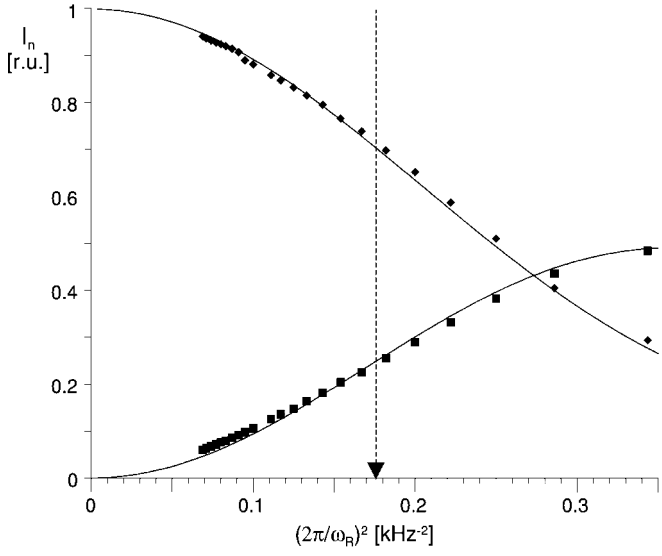

FIG. 8. Signal intensities I_n of the centerband ($n = 0$, diamonds) and of both first-order sidebands ($n = 1$, squares) in experimental ^{1}H MAS spectra of adamantane, plotted versus the inverse squared spinning frequency. The lines represent the calculated intensities of a spin-pair spectrum with a coupling of $D^{\text{pair}} = 2\pi \cdot 5.6$ kHz. The arrow indicates the position where $D^{\text{pair}} = \omega_R$.

Furthermore, the spin-pair model with the same D^{pair} describes the adamantane sideband pattern over the whole range of MAS frequencies above $\omega_R = 2\pi \cdot 3$ kHz (see Fig. 8). The coupling strength $D^{\text{pair}} = 2\pi \cdot 5.6$ kHz represents an effective coupling, given by the sum over all contributing "real" interactions in adamantane: $D_{\text{eff}} = \sqrt{\sum_{i<j}^{N} (D^{(ij)})^2}$. As discussed above, each adamantane proton i is coupled to 192 nearest-neighbor protons j with an individual coupling strength of $\bar{D} \approx 2\pi \cdot 410$ Hz each. The effective coupling is hence

$$D_{\text{eff}} \approx \sqrt{192} \cdot \bar{D} \approx 2\pi \cdot 5.7\,\text{kHz}, \qquad [65]$$

which perfectly agrees with the representative spin-pair coupling. Thus, under fast MAS, where "fast" means exceeding the perturbing interactions, the behavior of the ^{1}H multispin system in adamantane can be explained on the basis of a simple two-spin approach. More generally, the adamantane example shows that MAS is indeed capable of simplifying the network of dipolar couplings in extended multispin systems such that the spectrum is dominated by low-spin correlations.

2.9. Interference with Chemical Shift

The fundamental reason for applying MAS is to gain spectral resolution or—in other words—to uncover the chemical shift information. In the previous sections, the effect of MAS on dipolar-coupled multispin systems has been discussed and, with respect to line narrowing, the result that MAS can simplify the dense network of dipolar interactions to a superposition of spin-pair couplings is promising. However, the success of the technique critically depends on the question of if and to what extent ^{1}H chemical shift information is experimentally accessible and, as is even more desirable, if the chemical shifts can be combined with information about dipolar coupling strengths. Therefore, we now have to turn to the investigation of interference effects between the dipolar interaction and the chemical shift under MAS conditions. Since we are concerned with ^{1}H systems and relatively fast MAS frequencies, our considerations concentrate on the isotropic chemical shift, neglecting any chemical shielding anisotropy (CSA). However, in some cases, in particular those involving hydrogen bonds, we have observed characteristic, but still mostly marginal, features in ^{1}H MAS spectra, which are ascribed to CSA effects.

The isotropic chemical shift or, equivalently, the presence of a frequency offset $\Delta\omega = \omega - \omega_0$ from the Larmor frequency ω_0 can be classified as an inhomogeneous interaction, since the respective isotropic Hamiltonian $\hat{\boldsymbol{H}}_{CS}$ remains time-independent under MAS and hence commutes throughout the whole evolution period. However, the fact that the isotropic spatial part of $\hat{\boldsymbol{H}}_{CS}$ is not modulated by MAS means that it cannot be refocused by MAS. Therefore, in the NMR time signal, the periodicities of MAS and isotropic chemical shifts superimpose, and the so-called rotor echoes $S(n\tau_R)$ are not identical to the initial state $S(t = 0)$. Exceptions from this "normal" interference are expected for the special case of $\Delta\omega = n\omega_R$, known as rotational resonance (*84*).

Due to this interference, the homonuclear dipolar interaction, which is inhomogeneous for a single spin pair (ij), adopts a homogeneous character in the presence of a chemical shift $\hat{\boldsymbol{H}}_{CS} = \omega_{CS}^{(i)}\hat{\boldsymbol{I}}_z^{(i)} + \omega_{CS}^{(j)}\hat{\boldsymbol{I}}_z^{(j)}$ with different frequencies $\omega_{CS}^{(i)} \neq \omega_{CS}^{(j)}$. Then, the commutator

$$[\hat{\boldsymbol{H}}_{CS} + \hat{\boldsymbol{H}}_D(t), \hat{\boldsymbol{H}}_{CS} + \hat{\boldsymbol{H}}_D(t')] \propto \left[\hat{\boldsymbol{I}}_+^{(i)}\hat{\boldsymbol{I}}_-^{(j)} + \hat{\boldsymbol{I}}_-^{(i)}\hat{\boldsymbol{I}}_+^{(j)}, \omega_{CS}^{(i)}\hat{\boldsymbol{I}}_z^{(i)} + \omega_{CS}^{(j)}\hat{\boldsymbol{I}}_z^{(j)}\right] \quad [66]$$

does not vanish anymore, and the exchange term of the dipolar interaction acts on states which differ not only with respect to their polarization but also with respect to their precession frequencies. Since the frequency difference corresponds to an energy level difference, it has to be sufficiently small in order to allow the "flip-flop" process to conserve the total energy of the system at least approximately. Otherwise, for increasing energy level differences the exchange process is gradually suppressed, and the system approaches the so-called weak-coupling limit which is, in general, fulfilled for heteronuclear dipolar interactions.

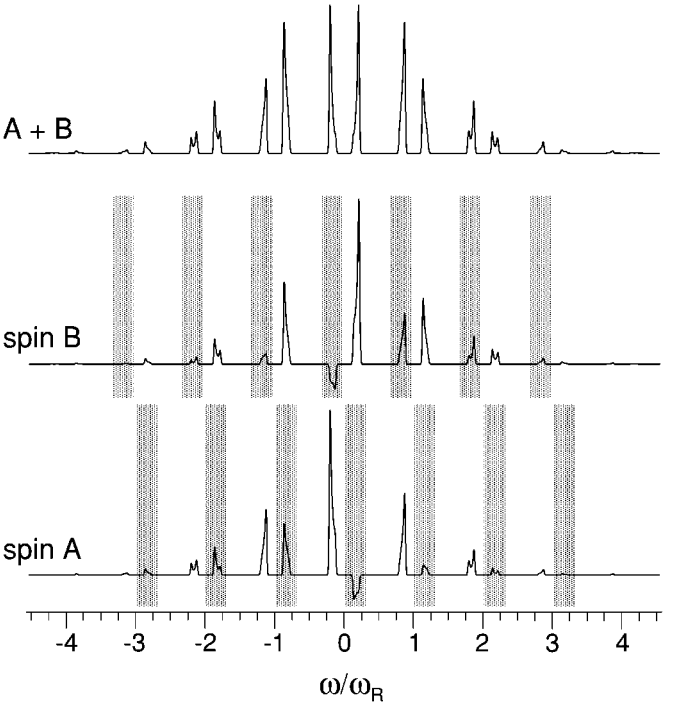

FIG. 9. Simulated MAS spectrum of a dipolar-coupled spin pair A–B, whose spins A and B have different chemical shifts ($D^{\text{pair}} = 2\pi \cdot 20$ kHz, $\Delta\omega_{CS} = 2\pi \cdot 5$ kHz, $\omega_R = 2\pi \cdot 11$ kHz, resulting in $\xi_{CS} = 0.45$). Detecting the signal either at spin A or spin B results in spectra which consist not only of the expected MAS sideband pattern centred at ω_{CS}^A or ω_{CS}^B, respectively, but also of contributions to the pattern of the other spin. The sum of the spin A and the spin B spectra results in the "$A + B$" spectrum.

Therefore, a pair of dipolar-coupled spins with different chemical shifts represents the simplest example for the interference between the chemical shift and a homonuclear dipolar interaction. For a chemical shift difference of $\Delta\omega_{CS} = 2\pi \cdot 5$ kHz, a simulated spin-pair spectrum is shown in Fig. 9. Obviously, the splitting into two resonance lines is accompanied by marked distortions of both the individual lineshapes and the sideband pattern, the former being split into small multiplet-like sets of lines and the latter showing a "roof effect" toward the centerbands. This "roof effect" arises from the fact that each of the spins A and B not only contributes to its "own" pattern centered at ω_{CS}^A and ω_{CS}^B, respectively, but also affects the pattern of the other spin by exchange processes, driven by the term $(\hat{\boldsymbol{I}}_+^A\hat{\boldsymbol{I}}_-^B + \hat{\boldsymbol{I}}_-^A\hat{\boldsymbol{I}}_+^B)$. This effect can be seen from the spin A and spin B spectra in Fig. 9, which have been simulated detecting the signal only at spin A or B, respectively. At the shaded positions, spectral intensity is transferred to the other spin, causing a distortion in its sideband pattern.

The effect on the lineshape is a kind of multiplet splitting, which becomes stronger with increasing sideband order. Although these splittings are mostly covered by the residual dipolar linewidth and are hence invisible, they contribute as an additional

mechanism to the line broadening in the spectra of real multispin systems. Consequently, the spectral resolution achievable by MAS reduces for sidebands with increasing order, because both the chemical shift-induced splitting and, as discussed in Section 2.5, the higher orders of dipolar spin correlations contributing to the decay function $W_n(t)$ broaden the resonance lines increasingly with increasing sideband order n. In spite of these clear effects on the lineshape and the sideband pattern, the intensity distribution over the sidebands, after being integrated for each order, is only negligibly affected by chemical shift differences between the spins, as long as the perturbation caused by the chemical shift does not exceed a value of $\xi_{CS} \approx 0.4$ (to obtain this parameter, the perturbing dipolar coupling D^{pert} in Eq. [64] has to be replaced by $\Delta\omega_{CS}$). Note that this limiting value, up to which the perturbing effect on the MAS spectrum may be neglected, is very close to the one which was found in Section 2.7 for the perturbations due to additional dipolar couplings.

In real samples, a spatial proximity of protons and, thus, strong dipolar couplings are often concomitant with similar chemical shifts of the involved nuclei, whereas remote and more weakly coupled spins are more likely to exhibit larger chemical shift differences. In this context, the question arises to what extent the relatively small chemical shift differences among protons help to suppress perturbing interactions. As an example, we return to the four-spin system in Fig. 6, with the two spinpairs A–A and B–B now differing in chemical shift by $\Delta\omega_{CS}^{AB} = 2\pi \cdot 3.3$ kHz. In Fig. 10, the simulated MAS spectra of such an A_2B_2 system are compared to those of an analogous A_2A_2 system without any chemical shift difference. In both cases the resonance lines broaden with increasing dipolar perturbation ξ, and the broadening effect increases with the sideband order.

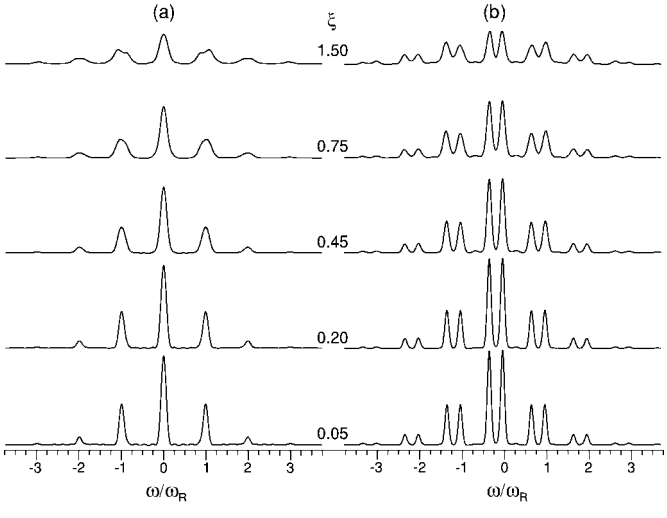

FIG. 10. Simulated MAS spectra of four-spin ^{1}H systems (a) without and (b) with a chemical shift difference of $\Delta\omega_{CS}^{AB} = 2\pi \cdot 3.3$ kHz between the pairs, which form a planar system as displayed in Fig. 6. The pair coupling is $D^{\text{pair}} = 2\pi \cdot 15$ kHz, and both pairs interfere with each other by $D^{\text{pert}} = 0 \ldots D^{\text{pair}}$, while the MAS frequency is $\omega_R = 2\pi \cdot 10$ kHz, resulting in a dipolar perturbation of $\xi = 0 \cdots 1.5$.

Considering the integral intensities, the differences between the A_2A_2 and the A_2B_2 system are minimal, although it is obvious that in the A_2B_2 system the peaks are less distorted; in the A_2A_2 system the broadening is more pronounced and a strong perturbation even gives rise to splittings of the sidebands. However, the chemical shift differences among protons are still too weak to significantly help with decoupling and, hence, to notably affect the intensity distribution over the sideband pattern.

2.10. Structural Information from One-Pulse MAS Spectra

From the considerations of this section, the following conclusions may be drawn for the information content of ^{1}H one-pulse MAS spectra with respect to the structure of solid samples: While static ^{1}H spectra allow only little information to be obtained from the linewidth about the effective dipolar interaction present in the sample, state-of-the-art MAS equipment opens up the possibility to enhance spectral resolution significantly and, in this way, to uncover the ^{1}H chemical shift information in the solid state. It has, therefore, become relevant to discuss the effect of sample spinning on dense and strongly dipolar-coupled ^{1}H systems in detail, using the analytical approach presented by Filip *et al.* (*35, 36*).

Although, in a multispin system, the homonuclear dipolar interaction is commonly classified as homogeneous, it turns out, under fast MAS conditions, that the system can be approximated by a superposition of inhomogeneous two-spin correlations, reflecting the fundamental spin-pair character of the dipolar coupling. This behavior can be rationalized by noting that, starting with a single spin i, the dipolar interaction always forms a correlation first with the most strongly coupled spin j, since the product of the coupling strength and the time of action is responsible for the weight of a correlation. At this stage, the system behaves inhomogeneously under MAS, which means that, for each correlation, the broad static resonance line splits into a pattern of, theoretically, infinitely narrow lines, which is characteristic for the strength of the underlying dipolar interaction.

However, the two-spin correlations (ij) are subject to dipolar interactions with neighboring spins, from which the one, k, with the strongest coupling to the (ij) pair will be incorporated first into a common three-spin state. With the appearance of such three-spin correlations, the system develops its homogeneous multispin character with the familiar line-broadening effects. At this point, a loss of information is encountered, because the two-spin correlations already combine the information about the dipolar pair interactions between close neighbors with maximum spectral resolution. Higher spin correlations broaden the resonance lines and impair the access to structural information. It is, thus, desirable to suppress them by MAS.

Therefore, resolution enhancement requires the suppression of unwanted higher spin correlations, which arise from an initial pair correlation plus an additional interaction to a third spin. To accomplish this, the time scale imposed on the system by the MAS averaging process, i.e., τ_R, needs to be short enough to

prevent the formation of three-spin correlations. From this scenario, it is clear that the static ^{1}H linewidth is an improper criterion to estimate the minimum spinning speed required for line narrowing. However, the distinction between dipolar pair and higher-order correlations implies the existence of a minimum coupling strength or, equivalently, of a maximum pair distance accessible by the dipolar correlation approach under MAS, depending on the spinning frequency applied, i.e., the time scale of the averaging process. In real systems, MAS usually has to deal with a whole range of dipolar couplings where the compromise between efficient decoupling of strongly coupled moieties (requiring fast spinning) and the observation of weak couplings (requiring rather moderate spinning) might be hard to find.

Another critical point is the combination of dipolar couplings with chemical shifts. The detection of the latter is the fundamental reason for applying MAS, though. In ^{1}H systems, the strongest dipolar interaction exceeds the maximum chemical shift difference, even at the highest magnetic fields currently available, to such an extent that the intensity distribution over the MAS sideband pattern is basically of dipolar origin, but, when considering spectrally resolved spins, the assignment of sideband intensities to dipolar pair correlations might turn out to be ambiguous due to the exchange term in the dipolar Hamiltonian. No problem arises as long as the dominant two-spin correlations involve only AA-type spin pairs consisting of spins with identical chemical shifts. However, for an A_2B-type system with coupling strengths D^{AB} and D^{AA} of similar size, the sideband pattern does not provide unambiguous access to the coupling strengths. Furthermore, the spectral resolution achievable in the MAS sidebands suffers from two effects as compared to the centerband: First, spin correlations of higher order contribute to the residual dipolar linewidth increasingly with the sideband order and, second, the interference of chemical shift and dipolar interaction gives rise to more pronounced line splitting.

Although, from an experimental point of view, the sideband patterns of one-pulse MAS spectra may appear to be the most direct way to combine information about dipolar interactions with chemical shifts, they bear, in fact, a major disadvantage, because the signal observed in a one-pulse experiment is spin-specific and hence fails to embody the pair character of the dipolar interaction. Thus, the experimental approach should be modified by introducing a means to detect a pair-specific NMR signal.

3. ^{1}H MULTIPLE-QUANTUM SPECTROSCOPY

In the previous section, the promising potential of fast MAS as a method for narrowing resonance lines and, thus, uncovering chemical shift information in ^{1}H solid-state spectra was demonstrated. However, the simple one-pulse experiment is not particularly well suited to obtaining information on both chemical shifts and dipolar interactions, because the detected signal is spin-specific and does not reflect the pair character inherent to the dominating dipolar two-spin correlations. In order to improve the spectroscopic approach under MAS, the experiment should take into account the major role of such two-spin correlations by detecting resonances of dipolar-coupled spin pairs. Therefore, in this section, the spectroscopy of spin pairs, i.e., double-quantum (DQ) spectroscopy, is introduced. In the following, we will discuss the theoretical background and the experimental realization as well as the information content of DQ MAS spectra, in particular the signal intensity, the excitation behavior, and the characteristic DQ MAS sideband patterns.

Furthermore, this section includes experimental approaches to higher quantum orders of dipolar-coupled spins, in particular to triple-quantum (TQ) spectroscopy of methyl groups (*38*), because in the TQ state the three methyl protons act as a single entity. The quantum order observed in TQ spectra, however, no longer reflects the pair character of the dipolar interaction. Instead, it is based on three-spin correlations which, in general, broaden resonance lines by introducing a homogeneous character to the system. However, in the special case of methyl groups, which usually rotate rapidly about their threefold symmetry axis, the three interproton pair couplings are equivalent and the inhomogeneous character is preserved even for a three-spin system.

3.1. Two-Spin Correlations and Double-Quantum Coherences

The application of a hard radiofrequency (RF) pulse, which rotates the spin part of the nuclear wavefunction by 90° (henceforth written as 90°_q, with $q = \pm x, \pm y$ denoting the direction of irradiation or, equivalently, the pulse phase), transfers a spin system from its thermal equilibrium state $\hat{\boldsymbol{\rho}}(0)$, i.e., longitudinal magnetization $\propto \hat{\boldsymbol{I}}_z$ in the presence of an external magnetic field $\mathbf{B}_0 || z$, into a nonequilibrium state of detectable transverse magnetization:

$$\hat{\boldsymbol{\rho}}(0) = \sum_i \hat{\boldsymbol{I}}_z^{(i)} = \hat{\boldsymbol{T}}_{1,0} \overset{90^\circ_y}{\rightarrow} \sum_i \hat{\boldsymbol{I}}_x^{(i)} = \frac{1}{\sqrt{2}} \sum_i \left(\hat{\boldsymbol{I}}_+^{(i)} + \hat{\boldsymbol{I}}_-^{(i)}\right)$$
$$= \frac{1}{\sqrt{2}}(-\hat{\boldsymbol{T}}_{1,1} + \hat{\boldsymbol{T}}_{1,-1}). \qquad [67]$$

Representing $\hat{\boldsymbol{\rho}}$ by the Cartesian components $\hat{\boldsymbol{I}}_q$ of the nuclear spin operator is instructive as long as the orientation of the macroscopic magnetization in the sample can be identified with the orientation q of the component $\hat{\boldsymbol{I}}_q$. In a more general context, particularly when correlated spin states are considered, rotations of the spin part are easier to handle using the components $\hat{\boldsymbol{T}}_{l,m}$ of spherical tensor operators (see Section 2.2). For systems with coupled spins $I = \frac{1}{2}$, note that the rank l and the order m reflect the number of correlated spins and the coherence order, respectively.

After a 90°_y pulse, considered an infinitely short δ pulse, a system of two dipolar-coupled spins i and j oscillates between

a state of transverse magnetization ($\hat{\boldsymbol{I}}_x^{(i)} + \hat{\boldsymbol{I}}_x^{(j)}$) and that of a two-spin correlation ($\hat{\boldsymbol{T}}_{2,1}^{(ij)} + \hat{\boldsymbol{T}}_{2,-1}^{(ij)}$):

$$\hat{\boldsymbol{\rho}}^{(ij)}(t) \propto \left(\hat{\boldsymbol{I}}_x^{(i)} + \hat{\boldsymbol{I}}_x^{(j)}\right)\cos\left(\omega_D^{(ij)}t\right) + i\left(\hat{\boldsymbol{T}}_{2,1}^{(ij)} + \hat{\boldsymbol{T}}_{2,-1}^{(ij)}\right)\sin\left(\omega_D^{(ij)}t\right). \quad [68]$$

The latter is also termed antiphase magnetization, since it consists of mixed products $\hat{\boldsymbol{I}}_y\hat{\boldsymbol{I}}_z$, i.e., a product of a transverse and a longitudinal $\hat{\boldsymbol{I}}$-component (see below, Eq. [69]). In Eq. [67] the phase of the oscillation is shifted between the transverse and the antiphase state by $\frac{\pi}{2}$, while the oscillation frequency is determined by the dipolar coupling strength: $\omega_D^{(ij)} = 3D^{(ij)}$ (see also Eq. [21]). In ^{1}H multispin systems, however, the dipolar interaction leads further to the generation of higher spin correlations, and the evolution of the system can therefore not be described by a simple oscillation, but in an approximate way through a series expansion:

$$\begin{aligned}
\hat{\boldsymbol{\rho}}(t) - \hat{\boldsymbol{\rho}}(0) \propto & -\frac{it}{1!}\left[\sum_{i<j}^{N}\hat{\boldsymbol{H}}_D^{(ij)}, \sum_{i=1}^{N}\hat{\boldsymbol{I}}_x^{(i)}\right] \\
& + \frac{(it)^2}{2!}\left[\sum_{i<j}^{N}\hat{\boldsymbol{H}}_D^{(ij)}, \left[\sum_{i<j}^{N}\hat{\boldsymbol{H}}_D^{(ij)}, \sum_{i=1}^{N}\hat{\boldsymbol{I}}_x^{(i)}\right]\right] \\
& \pm \cdots \propto -\frac{it}{1!}\cdot\sum_{i<j}^{N} a^{(ij)}\left(\hat{\boldsymbol{T}}_{2,1}^{(ij)} + \hat{\boldsymbol{T}}_{2,-1}^{(ij)}\right) + \frac{(it)^2}{2!} \\
& \cdot\left(\sum_{i=1}^{N} b^{(i)}\hat{\boldsymbol{I}}_x^{(i)} + i\sum_{\substack{i<j \\ k\neq i,j}}^{N} c^{(ijk)}\left(\hat{\boldsymbol{T}}_{2,1}^{(ik)} - \hat{\boldsymbol{T}}_{2,-1}^{(ik)}\right)\cdot\hat{\boldsymbol{I}}_z^{(j)}\right. \\
& \left. + i\sum_{\substack{i<j \\ k\neq i,j}}^{N} d^{(ijk)}\left(\hat{\boldsymbol{I}}_x^{(i)}\hat{\boldsymbol{I}}_z^{(j)}\hat{\boldsymbol{I}}_z^{(k)} + \left(\hat{\boldsymbol{I}}_+^{(i)}\hat{\boldsymbol{I}}_-^{(k)} - \hat{\boldsymbol{I}}_-^{(i)}\hat{\boldsymbol{I}}_+^{(k)}\right)\cdot\hat{\boldsymbol{I}}_y^{(j)}\right)\right) \\
& \pm \cdots.
\end{aligned} \quad [69]$$

The leading term, which is linear with respect to time,

$$i\cdot a^{(ij)}t\left(\hat{\boldsymbol{T}}_{2,1}^{(ij)} + \hat{\boldsymbol{T}}_{2,-1}^{(ij)}\right) = -\frac{1}{\sqrt{2}}a^{(ij)}t\left(\hat{\boldsymbol{I}}_z^{(i)}\hat{\boldsymbol{I}}_y^{(j)} + \hat{\boldsymbol{I}}_y^{(i)}\hat{\boldsymbol{I}}_z^{(j)}\right), \quad [70]$$

again correlates two spins i and j in terms of an antiphase magnetization. The scaling factor $a^{(ij)}$ is identical to the spatial part $\omega_D^{(ij)}$. Therefore, the coupling strength $D^{(ij)}$ determines the contribution of the respective two-spin correlation after the evolution time t through the product $D^{(ij)}\cdot t$.

A single spin $I = \frac{1}{2}$ can occupy a nonequilibrium state by forming a coherent superposition of two states with the magnetic spin-quantum numbers $M = +\frac{1}{2}$ and $M = -\frac{1}{2}$, respectively. Due to the difference $\Delta M = 1$, this coherence is termed single-quantum coherence (SQC). The term $(\hat{\boldsymbol{T}}_{2,1}^{(ij)} + \hat{\boldsymbol{T}}_{2,-1}^{(ij)})$ correlates two spins, but the spins do not yet behave as a single entity. This is clear from both the quantum order $m = \pm 1$ of the tensor components and from the notation in the form of the spin operators $(\hat{\boldsymbol{I}}_z^{(i)}\hat{\boldsymbol{I}}_y^{(j)} + \hat{\boldsymbol{I}}_y^{(i)}\hat{\boldsymbol{I}}_z^{(j)})$—the latter showing the presence of products of different components $\hat{\boldsymbol{I}}_y$ and $\hat{\boldsymbol{I}}_z$ for both spins i and j, with the spins occupying states of transverse and longitudinal magnetization, respectively. Therefore, only one spin in the products is subject to the evolution under the chemical shift Hamiltonian, $\hat{\boldsymbol{H}}_{CS} = \omega_{CS}^{(i)}\hat{\boldsymbol{I}}_z^{(i)} + \omega_{CS}^{(j)}\hat{\boldsymbol{I}}_z^{(j)}$, i.e.,

$$\begin{aligned}
&\left[\left(\hat{\boldsymbol{I}}_z^{(i)}\hat{\boldsymbol{I}}_y^{(j)} + \hat{\boldsymbol{I}}_y^{(i)}\hat{\boldsymbol{I}}_z^{(j)}\right), \left(\omega_{CS}^{(i)}\hat{\boldsymbol{I}}_z^{(i)} + \omega_{CS}^{(j)}\hat{\boldsymbol{I}}_z^{(j)}\right)\right] \\
&\quad = \omega_{CS}^{(i)}\hat{\boldsymbol{I}}_x^{(i)}\hat{\boldsymbol{I}}_z^{(j)} + \omega_{CS}^{(j)}\hat{\boldsymbol{I}}_z^{(i)}\hat{\boldsymbol{I}}_x^{(j)},
\end{aligned} \quad [71]$$

and the two spins evolve differently, which means that the state dephases. In order to observe a dipolar-coupled spin pair as a single entity, it has to have a common resonance frequency which differs from those of the single spins. Therefore, in the products $\hat{\boldsymbol{I}}_q^{(i)}\hat{\boldsymbol{I}}_{q'}^{(j)}$ which represent two-spin correlations, no components with $q, q' = \pm z$ may be involved. The products $\hat{\boldsymbol{I}}_q^{(i)}\hat{\boldsymbol{I}}_{q'}^{(j)}$ with $q, q' = x, y$ can be expressed as linear combinations of products of shift operators $\hat{\boldsymbol{I}}_\pm^{(i)}$:

$$\begin{aligned}
\hat{\boldsymbol{I}}_x^{(i)}\hat{\boldsymbol{I}}_x^{(j)} &\propto \left(\hat{\boldsymbol{I}}_+^{(i)}\hat{\boldsymbol{I}}_+^{(j)} + \hat{\boldsymbol{I}}_-^{(i)}\hat{\boldsymbol{I}}_-^{(j)}\right) + \left(\hat{\boldsymbol{I}}_+^{(i)}\hat{\boldsymbol{I}}_-^{(j)} + \hat{\boldsymbol{I}}_-^{(i)}\hat{\boldsymbol{I}}_+^{(j)}\right) \\
\hat{\boldsymbol{I}}_y^{(i)}\hat{\boldsymbol{I}}_y^{(j)} &\propto -\left(\hat{\boldsymbol{I}}_+^{(i)}\hat{\boldsymbol{I}}_+^{(j)} + \hat{\boldsymbol{I}}_-^{(i)}\hat{\boldsymbol{I}}_-^{(j)}\right) + \left(\hat{\boldsymbol{I}}_+^{(i)}\hat{\boldsymbol{I}}_-^{(j)} + \hat{\boldsymbol{I}}_-^{(i)}\hat{\boldsymbol{I}}_+^{(j)}\right) \\
i\hat{\boldsymbol{I}}_x^{(i)}\hat{\boldsymbol{I}}_y^{(j)} &\propto \left(\hat{\boldsymbol{I}}_+^{(i)}\hat{\boldsymbol{I}}_+^{(j)} - \hat{\boldsymbol{I}}_-^{(i)}\hat{\boldsymbol{I}}_-^{(j)}\right) + \left(\hat{\boldsymbol{I}}_+^{(i)}\hat{\boldsymbol{I}}_-^{(j)} - \hat{\boldsymbol{I}}_-^{(i)}\hat{\boldsymbol{I}}_+^{(j)}\right) \\
i\hat{\boldsymbol{I}}_y^{(i)}\hat{\boldsymbol{I}}_x^{(j)} &\propto \left(\hat{\boldsymbol{I}}_+^{(i)}\hat{\boldsymbol{I}}_+^{(j)} - \hat{\boldsymbol{I}}_-^{(i)}\hat{\boldsymbol{I}}_-^{(j)}\right) - \left(\hat{\boldsymbol{I}}_+^{(i)}\hat{\boldsymbol{I}}_-^{(j)} - \hat{\boldsymbol{I}}_-^{(i)}\hat{\boldsymbol{I}}_+^{(j)}\right).
\end{aligned} \quad [72]$$

In this notation, the involved coherence orders become obvious. $\hat{\boldsymbol{I}}_+^{(i)}\hat{\boldsymbol{I}}_+^{(j)}$ and $\hat{\boldsymbol{I}}_-^{(i)}\hat{\boldsymbol{I}}_-^{(j)}$ denote transitions between the states $|{\downarrow\downarrow}\rangle \rightarrow |{\uparrow\uparrow}\rangle$ and $|{\uparrow\uparrow}\rangle \rightarrow |{\downarrow\downarrow}\rangle$, corresponding to $M = -1 \rightarrow M = 1$ and $M = 1 \rightarrow M = -1$, respectively. A state represented by these operators is then characterized by a coherent superposition of the two non-equilibrium states $|{\downarrow\downarrow}\rangle$ and $|{\uparrow\uparrow}\rangle$. Since $|{\downarrow\downarrow}\rangle$ and $|{\uparrow\uparrow}\rangle$ differ by $\Delta M = \pm 2$, the state is called a double-quantum coherence (DQC). Using spherical tensor operators,

$$\hat{\boldsymbol{I}}_\pm^{(i)}\hat{\boldsymbol{I}}_\pm^{(j)} = \hat{\boldsymbol{T}}_{2,\pm 2}^{(ij)}, \quad [73]$$

the change of the magnetic spin-quantum number ΔM, i.e., the coherence order, is directly reflected by the order $m = \pm 2$ of the components $\hat{\boldsymbol{T}}_{l,m}$. Besides the DQC terms, terms consisting of products of shift operators with different signs, $\hat{\boldsymbol{I}}_+^{(i)}\hat{\boldsymbol{I}}_-^{(j)}$ and $\hat{\boldsymbol{I}}_-^{(i)}\hat{\boldsymbol{I}}_+^{(j)}$, are also present in Eq. [72]; these are known from the exchange term of the homonuclear dipolar interaction (see Eq. [10]), and represent coherences involving the states $|{\downarrow\uparrow}\rangle$ and $|{\uparrow\downarrow}\rangle$. Since $\Delta M = 0$, these are termed zero-quantum coherences (ZQCs).

The consideration of the products $\hat{\boldsymbol{I}}_q^{(i)}\hat{\boldsymbol{I}}_{q'}^{(j)}$ with $q, q' = x, y$ aims at the creation of a state which combines two dipolar-coupled spins with a single resonance frequency. ZQCs,

however, evolve under the chemical shift as follows:

$$\left[\left(\hat{I}_+^{(i)}\hat{I}_-^{(j)} \pm \hat{I}_-^{(i)}\hat{I}_+^{(j)}\right), \left(\omega_{CS}^{(i)}\hat{I}_z^{(i)} + \omega_{CS}^{(j)}\hat{I}_z^{(j)}\right)\right] = \left(\omega_{CS}^{(i)} - \omega_{CS}^{(j)}\right)\left(\hat{I}_+^{(i)}\hat{I}_-^{(j)} \mp \hat{I}_-^{(i)}\hat{I}_+^{(j)}\right). \quad [74]$$

Hence, the commutator vanishes for pairs of spins with identical chemical shift $\omega_{CS}^{(i)} = \omega_{CS}^{(j)}$, and ZQCs are not suitable for distinguishing signals of pairs of like spins in the spectrum. For DQCs, on the contrary, the corresponding commutator does not vanish in any case, because the resonance frequency of a DQC results from the sum $\omega_{CS}^{(i)}+\omega_{CS}^{(j)}$ of the frequencies of the involved spins i and j (*63*):

$$\left[\left(\hat{I}_+^{(i)}\hat{I}_+^{(j)} \pm \hat{I}_-^{(i)}\hat{I}_-^{(j)}\right), \left(\omega_{CS}^{(i)}\hat{I}_z^{(i)} + \omega_{CS}^{(j)}\hat{I}_z^{(j)}\right)\right] = \left(\omega_{CS}^{(i)} + \omega_{CS}^{(j)}\right)\left(\hat{I}_+^{(i)}\hat{I}_+^{(j)} \mp \hat{I}_-^{(i)}\hat{I}_-^{(j)}\right). \quad [75]$$

Therefore, DQCs offer themselves as a tool for observing two-spin correlations in NMR spectra. It should be noted that a state of pure DQC without any ZQC contributions can be easily obtained from linear combinations of the terms in Eq. [72].

3.2. Excitation of DQ Coherences

3.2.1. Two-Pulse Excitation under Static Conditions

In order to transform dipolar two-spin correlations represented by the term $(\hat{\boldsymbol{T}}_{2,1}^{(ij)} + \hat{\boldsymbol{T}}_{2,-1}^{(ij)})$ into DQCs, the order m of the tensor components $\hat{\boldsymbol{T}}_{l,m}$ has to be increased from $m = \pm 1$ to $m = \pm 2$. Since, under rotation operations, the components $\hat{\boldsymbol{T}}_{l,m}$ of spherical tensor operators transform into linear combinations of components of the same rank l, but different orders $m' = -l, \ldots, l$, the wanted transition $\hat{\boldsymbol{T}}_{2,\pm 1}^{(ij)} \rightarrow \hat{\boldsymbol{T}}_{2,\pm 2}^{(ij)}$ can be accomplished through the application of a RF pulse which makes the spin part of the wavefunction rotate (*31*, *95*). Such a RF pulse acts in the form of a propagator $\hat{\boldsymbol{L}}_{Pulse} = \exp(\mp i\beta\hat{\boldsymbol{I}}_q)$ on the system, where q denotes the orientation of the applied RF field or, equivalently, the pulse phase. The flip angle β is given by the product of the magnetogyric ratio γ_I, the transverse magnetic field B_1, and the pulse duration t_p: $\beta = \omega_1 t_p = \gamma_I B_1 t_p$. Hence, RF pulses transform a two-spin correlation as follows (*105*, *15*),

$$\begin{aligned}\hat{\rho}(0) &\overset{90_y^\circ}{\rightarrow} \hat{I}_x^{(i)} + \hat{I}_x^{(j)}\\ &\overset{\hat{H}_D^{(ij)}}{\longrightarrow} \cdots + \left(\hat{\boldsymbol{T}}_{2,1}^{(ij)} + \hat{\boldsymbol{T}}_{2,-1}^{(ij)}\right) + \cdots\\ &\overset{\beta_x}{\rightarrow} -i\sqrt{\frac{3}{8}}\hat{\boldsymbol{T}}_{-2,0}\sin(2\beta) + \left(\hat{\boldsymbol{T}}_{2,1}^{(ij)} + \hat{\boldsymbol{T}}_{2,-1}^{(ij)}\right)\cos(2\beta)\\ &\quad - \frac{i}{2}\left(\hat{\boldsymbol{T}}_{2,2}^{(ij)} - \hat{\boldsymbol{T}}_{2,-2}^{(ij)}\right)\sin(2\beta)\end{aligned}$$

or

$$\overset{\beta_y}{\rightarrow} \left(\hat{\boldsymbol{T}}_{2,1}^{(ij)} + \hat{\boldsymbol{T}}_{2,-1}^{(ij)}\right)\cos\beta - \left(\hat{\boldsymbol{T}}_{2,2}^{(ij)} - \hat{\boldsymbol{T}}_{2,-2}^{(ij)}\right)\sin\beta \quad [76]$$

and

$$\begin{aligned}\hat{\rho}(0) &\overset{90_x^\circ}{\rightarrow} -\left(\hat{I}_y^{(i)} + \hat{I}_y^{(j)}\right)\\ &\overset{\hat{H}_D^{(ij)}}{\longrightarrow} \cdots + \left(\hat{\boldsymbol{T}}_{2,1}^{(ij)} - \hat{\boldsymbol{T}}_{2,-1}^{(ij)}\right) + \cdots\\ &\overset{\beta_x}{\rightarrow} \left(\hat{\boldsymbol{T}}_{2,1}^{(ij)} - \hat{\boldsymbol{T}}_{2,-1}^{(ij)}\right)\cos\beta - i\left(\hat{\boldsymbol{T}}_{2,2}^{(ij)} + \hat{\boldsymbol{T}}_{2,-2}^{(ij)}\right)\sin\beta\end{aligned}$$

or

$$\begin{aligned}&\overset{\beta_y}{\rightarrow} -\sqrt{\frac{3}{8}}\hat{\boldsymbol{T}}_{2,0}\sin(2\beta) + \left(\hat{\boldsymbol{T}}_{2,1}^{(ij)} - \hat{\boldsymbol{T}}_{2,-1}^{(ij)}\right)\cos(2\beta)\\ &\quad - \frac{1}{2}\left(\hat{\boldsymbol{T}}_{2,2}^{(ij)} + \hat{\boldsymbol{T}}_{2,-2}^{(ij)}\right)\sin(2\beta), \quad [77]\end{aligned}$$

for the first RF pulse applied with y-phase or x-phase, respectively. For $\beta = 90^\circ$ and two pulses with identical phases (or with phases of different sign), the two-spin correlation $(\hat{\boldsymbol{T}}_{2,1}^{(ij)} \pm \hat{\boldsymbol{T}}_{2,-1}^{(ij)})$ is completely transformed into a DQC $(\hat{\boldsymbol{T}}_{2,2}^{(ij)} \pm \hat{\boldsymbol{T}}_{2,-2}^{(ij)})$. In the limit of $\omega_D^{(ij)}\tau \ll 1$, the weight of the DQC is determined by the coefficient $a^{(ij)}\tau = \omega_D^{(ij)}\tau$ (see Eq. [69]) and, hence, by the product of the dipolar coupling strength $D^{(ij)} = \frac{1}{3}\omega_D^{(ij)}$ and the delay τ between the two pulses.

3.2.2. Time Reversal and Detection

In NMR spectroscopy, the phase-sensitive signal detection can formally be considered as $S(t) = \mathrm{Tr}[\hat{\boldsymbol{I}}_- \cdot \hat{\boldsymbol{\rho}}(t)]$. DQCs, however, cannot be observed in this direct manner, because

$$\mathrm{Tr}\left[\left(\hat{I}_-^{(i)} + \hat{I}_-^{(j)}\right) \cdot \left(\hat{\boldsymbol{T}}_{2,2}^{(ij)} \pm \hat{\boldsymbol{T}}_{2,-2}^{(ij)}\right)\right] = 0. \quad [78]$$

Whenever direct detection is not possible or unfavorable, so-called indirect detection techniques and multidimensional methods come into play (*31*). For multiple-quantum coherences (MQCs), the technique of time reversal combined with coherence selection procedures, i.e., pulse phase cycling or magnetic field gradients, is well established (*114*, *79*, *85*).

Formally, the excitation of MQCs can be represented by a propagation $\hat{\boldsymbol{\rho}}(\tau) = \hat{\boldsymbol{L}}_{exc}^{+}(\tau)\hat{\boldsymbol{\rho}}(0)\hat{\boldsymbol{L}}_{exc}(\tau)$ with the excitation propagator $\hat{\boldsymbol{L}}_{exc}(\tau) = \exp(i\hat{\boldsymbol{H}}_{exc}\tau)$, where $\hat{\boldsymbol{H}}_{exc}$ is the excitation Hamiltonian. A further propagation with an argument of opposite sign, i.e., $-i\hat{\boldsymbol{H}}_{exc}\tau$, completely restores the initial state. The sign change can be attributed to the time τ and hence can be considered a time reversal. Obviously, the same result is obtained by changing the sign of the Hamiltonian, so that $-\hat{\boldsymbol{H}}_{exc}$ can be viewed as a reconversion operator $\hat{\boldsymbol{H}}_{rec}$. For the two-pulse excitation scheme 90_x°–τ–90_{-x}°, the excitation Hamiltonian is given

by

$$\begin{aligned}\hat{\rho}(\tau) &= \hat{\boldsymbol{L}}_{-x}\hat{\boldsymbol{L}}_D(\tau)\hat{\boldsymbol{L}}_x\hat{\rho}(0)\hat{\boldsymbol{L}}_x^+\hat{\boldsymbol{L}}_D^+(\tau)\hat{\boldsymbol{L}}_{-x}^+ \\ &= \exp\left(i\frac{\pi}{2}\hat{\boldsymbol{I}}_x\right)\exp(-i\hat{\boldsymbol{H}}_D\tau)\exp\left(-i\frac{\pi}{2}\hat{\boldsymbol{I}}_x\right) \\ &\quad\times\hat{\rho}(0)\exp\left(i\frac{\pi}{2}\hat{\boldsymbol{I}}_x\right)\exp(i\hat{\boldsymbol{H}}_D\tau)\exp\left(-i\frac{\pi}{2}\hat{\boldsymbol{I}}_x\right) \\ &= \exp\left(-i\left[\exp\left(i\frac{\pi}{2}\hat{\boldsymbol{I}}_x\right)\hat{\boldsymbol{H}}_D\exp\left(-i\frac{\pi}{2}\hat{\boldsymbol{I}}_x\right)\right]\tau\right)\hat{\rho}(0) \\ &\quad\times\exp\left(i\left[\exp\left(i\frac{\pi}{2}\hat{\boldsymbol{I}}_x\right)\hat{\boldsymbol{H}}_D\exp\left(-i\frac{\pi}{2}\hat{\boldsymbol{I}}_x\right)\right]\tau\right) \\ &= \exp\left(-i\left[\underbrace{\frac{1}{2}\hat{\boldsymbol{T}}_{2,0}+\sqrt{\frac{3}{8}}(\hat{\boldsymbol{T}}_{2,2}+\hat{\boldsymbol{T}}_{2,-2})}_{\hat{\boldsymbol{H}}_{exc}}\right]\tau\right)\hat{\rho}(0) \\ &\quad\times\exp\left(i\left[\underbrace{\frac{1}{2}\hat{\boldsymbol{T}}_{2,0}+\sqrt{\frac{3}{8}}(\hat{\boldsymbol{L}}_{2,2}+\hat{\boldsymbol{T}}_{2,-2})}_{\hat{\boldsymbol{H}}_{exc}^+}\right]\tau\right). \qquad [79]\end{aligned}$$

Assuming that the RF power exceeds all internal interactions and infinitely short δ pulses are applied, the propagation by such RF pulses can be understood as a transformation of the reference frame of the internal (in our case dipolar) interactions, as is expressed by the identity $\exp(\exp(iB)iA\exp(-iB)) = \exp(iB)\exp(iA)\exp(-iB)$. The interaction is then given in the so-called toggling frame, the orientation of which results from the action of the RF pulses applied on the rotating frame. Effectively, this means that the spin parts of the interaction Hamiltonians are switched by RF pulses (*51*).

In order to accomplish time reversal, the sign or, alternatively, the phase of $\hat{\boldsymbol{H}}_{exc}$ has to be manipulated. Formally, the phase behavior of the components $\hat{\boldsymbol{T}}_{l,m}$ of spherical tensor operators is based on the relation (*104*)

$$\exp(i\phi\hat{\boldsymbol{I}}_z)\hat{\boldsymbol{T}}_{l,m}\exp(-i\phi\hat{\boldsymbol{I}}_z) = \hat{\boldsymbol{T}}_{l,m}\exp(im\phi). \qquad [80]$$

The m-fold phase sensitivity of the components $\hat{\boldsymbol{T}}_{l,m}$ is also reflected in the commutator $[\hat{\boldsymbol{T}}_{l,m}, \hat{\boldsymbol{I}}_z] = -m\hat{\boldsymbol{T}}_{l,m}$. Hence, a phase shift of the two-pulse excitation scheme $(90^\circ_x\text{–}\tau\text{–}90^\circ_{-x}) \rightarrow (90^\circ_{x+\phi}\text{–}\tau\text{–}90^\circ_{-x+\phi})$ gives rise to the following modification of the excitation Hamiltonian $\hat{\boldsymbol{H}}_{exc}$:

$$\begin{aligned}&\hat{\boldsymbol{L}}_{-x+\phi}\hat{\boldsymbol{L}}_D(\tau)\hat{\boldsymbol{L}}_{x+\phi} \\ &\quad= \exp\left(-i\left[\frac{1}{2}\hat{\boldsymbol{T}}_{2,0}+\sqrt{\frac{3}{8}}(\hat{\boldsymbol{T}}_{2,2}+\hat{\boldsymbol{T}}_{2,-2})\exp(2i\phi)\right]\tau\right). \qquad [81]\end{aligned}$$

A basic feature of the dipolar interaction, also entering into the above algebra, is that it is insensitive to phase shifts,

$$\exp(-i\phi\hat{\boldsymbol{I}}_z)\exp(-i\hat{\boldsymbol{H}}_D\tau)\exp(i\phi\hat{\boldsymbol{I}}_z) = \exp(-i\hat{\boldsymbol{H}}_D\tau), \qquad [82]$$

because $[\hat{\boldsymbol{T}}_{2,0}, \hat{\boldsymbol{I}}_z] = 0$. Corresponding to the coherence orders, it is clear from Eq. [80] that the term representing the ZQC, $\hat{\boldsymbol{T}}_{2,0}$, is not affected by phase shifts, while the term representing the DQC, $(\hat{\boldsymbol{T}}_{2,2}+\hat{\boldsymbol{T}}_{2,-2})$, is doubly sensitive. Shifting the phases of both pulses by $\frac{\pi}{2}$ thus results in a phase factor $\exp(2i\cdot\frac{\pi}{2}) = -1$ for the DQCs, providing time reversal for the DQ part of the excitation Hamiltonian.

3.2.3. Selection of Coherence Orders

Combining two-pulse excitation and reconversion under time reversal, the DQ experiment adopts the form $(90^\circ_x\text{–}\tau\text{–}90^\circ_{-x})_{exc}(90^\circ_y\text{–}\tau\text{–}90^\circ_{-y})_{rec}$. The reconversion leads to a state of longitudinal magnetization, whose amplitude reflects the DQ signal; this can be read out by applying a further 90° pulse. It is necessary to ensure that all contributions from unwanted coherence pathways to the signal are suppressed; i.e., the following pathway is to be selected: $0 \overset{exc}{\rightarrow} \pm2 \overset{rec}{\rightarrow} 0 \overset{read}{\rightarrow} -1$. Since coherences are sensitive to pulse-phase shifts according to their order (see Eq. [80]), the use of phase cycles of the RF pulses to select the desired coherence pathway is well established. A suitable phase cycle can be easily derived by obeying the following two fundamental rules (*14*):

- If the phase of a pulse or group of pulses is shifted by ϕ, then a coherence undergoing a change in coherence order of $\Delta p = p' - p$ experiences a phase shift of $-\phi\Delta p$, as detected by the receiver.
- If a phase cycle uses steps of $360^\circ/N$, along with the desired pathway Δp, the pathways $\Delta p \pm n\cdot N$, where $n = 1, 2, 3, \ldots$, will also be selected, while all other pathways will be suppressed.

Hence, the selection of a pathway $0 \overset{exc}{\rightarrow} \pm2 \overset{rec}{\rightarrow} 0 \overset{read}{\rightarrow} -1$ requires two nested 4-step phase cycles, each in steps of $\frac{\pi}{2}$, resulting in an overall 16-step phase cycle. They select $\Delta p = \pm2, \pm6, \pm10, \ldots$ and $\Delta p = \pm1, \pm5, \pm9, \ldots$ during the reconversion and the final detection period, respectively.

3.2.4. Short-Time Excitation under MAS

An essential part of ^{1}H DQ spectroscopy is the application of MAS, which can straightforwardly be incorporated into our consideration of the excitation of DQCs by replacing the time-independent spatial part by the respective rotor-modulated term in the dipolar Hamiltonian $\hat{\boldsymbol{H}}_D^{(ij)}(t) = \hat{\boldsymbol{A}}^{(ij)}(t)\cdot\hat{\boldsymbol{T}}_{2,0}^{(ij)}$, with $\hat{\boldsymbol{A}}^{(ij)}(t)$ being defined in Eq. [29] (*46*). Considering again the two-pulse excitation scheme, the weight of a two-spin correlation immediately before the second pulse or, equivalently, the weight of a DQC immediately after the second pulse is,

in the limit of short excitation times, given by the integrated spatial part $\Omega_D^{(ij)}(0,\tau)$ of the dipolar interaction, according to Eq. [30]. Note that $\Omega_D^{(ij)}(0,\tau)$ is not normalized with respect to the time interval $[0,\tau]$ and hence represents a phase rather than a frequency.

$$\Omega_D^{(ij)}(0,\tau) = \int_0^\tau \omega_D^{(ij)}(t)\,dt = \frac{\omega_D^{(ij)}}{2\omega_R} \cdot \left[\frac{1}{2}\sin^2\beta_{ij}(\sin(2\omega_R\tau + 2\gamma_{ij}) - \sin(2\gamma_{ij})) - \sqrt{2}\sin 2\beta_{ij}(\sin(\omega_R\tau + \gamma_{ij}) - \sin\gamma_{ij})\right]. \quad [83]$$

The angles β_{ij} and γ_{ij} denote the azimuthal and polar angle of the internuclear vector $\boldsymbol{r}_{ij}$ in the ROT frame. In the case of powder samples, an isotropic average over both these angles has to be performed. Being a second-rank tensor, the dipolar interaction is subject to a twofold rotor modulation, one by the MAS frequency ω_R and the other by twice the frequency $2\omega_R$. The overall weight of a DQC is thus determined by the product of an integral rotor-phase factor and the ratio $\omega_D^{(ij)}/\omega_R$, where $\omega_D^{(ij)} = 3D^{(ij)}$ (see Eq. [21]).

Since the experimental detection of DQCs requires a reconversion period, during which the dipolar interaction acts in the same, but effectively reversed, way as during the excitation, the integral $\Omega_D^{(ij)}$ enters twice in the weighting factor of the resulting DQC signal: $\Omega_{D,exc}^{(ij)} = \Omega_D^{(ij)}(0,\tau)$ and $\Omega_{D,rec}^{(ij)} = \Omega_D^{(ij)}(\tau,2\tau)$, for the excitation during $[0,\tau]$ and the reconversion during $[\tau,2\tau]$, respectively. In the case of a single spin pair, the integrated spatial parts $\Omega_{D,exc}^{(ij)}$ and $\Omega_{D,rec}^{(ij)}$ become the arguments of sine functions, as can be seen from Eq. [67].

Expanding this sine dependence into a series, as is necessary for the consideration of multispin systems and as has been performed in Eq. [68], the leading term determining the weight of a DQC is simply given by the product $\Omega_{D,exc}^{(ij)} \cdot \Omega_{D,rec}^{(ij)}$. Therefore, in the limit $\Omega_{D,exc}^{(ij)}, \Omega_{D,rec}^{(ij)} \ll 1$, i.e., for short excitation times τ or weak couplings $D^{(ij)}$, the signal intensity $I_{DQ}^{(ij)}$ of a DQC involving spins i and j depends on the strength $D^{(ij)}$ of the underlying dipolar coupling and the applied excitation time τ in the following simple form:

$$\begin{aligned} I_{DQ}^{(ij)} &\propto \sin\left(\Omega_D^{(ij)}(0,\tau)\right)\cdot\sin\left(\Omega_D^{(ij)}(\tau,2\tau)\right) \\ &\approx \Omega_D^{(ij)}(0,\tau)\cdot\Omega_D^{(ij)}(\tau,2\tau) + \cdots \\ &\propto \left(D^{(ij)}\right)^2\tau^2 + \cdots \\ &\propto \frac{\tau^2}{r_{ij}^6} + \cdots. \end{aligned} \quad [84]$$

In Fig. 11, the DQ intensity I_{DQ} is plotted in two dimensions versus the dipolar coupling strength $D^{(ij)}$ and the excitation time τ for a single spin-pair (ij). Both axes are normalized with respect to MAS, i.e., $D^{(ij)}$ to the MAS frequency ω_R and τ to the rotor period τ_R. It is clear that the excitation profile is symmetric about $\tau = \frac{1}{2}\tau_R$, reflecting the refocusing procedure. Moreover, three regions of efficient DQ excitation can be identified: the first and most efficient at $\tau = \frac{1}{2}\tau_R$ and two others at about $\tau = 0.06\tau_R$ and $\tau = 0.94\tau_R$. From the two-dimensional contour level diagram, two DQ excitation curves, one with respect to the excitation time and the other with respect to the coupling strength, are extracted and displayed on the right of Fig. 11. It is apparent that I_{DQ} decreases continuously, when the MAS frequency exceeds the dipolar coupling strength, i.e., for $D^{(ij)}\tau_R/2\pi < 1$. For $D^{(ij)}\tau_R/2\pi > 1$, the system shows an oscillating DQ excitation behavior.

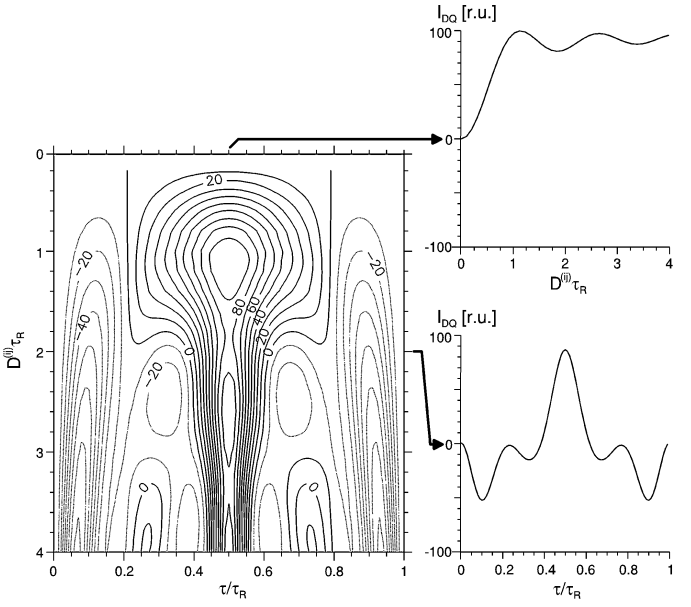

FIG. 11. Calculated DQ excitation profile for a dipolar-coupled spin pair, to which the pulse sequence $(90^\circ_x{-}\tau{-}90^\circ_{-x})_{exc}(90^\circ_y{-}\tau{-}90^\circ_{-y})_{rec}(90^\circ_x)_{read}$ is applied under MAS. The contour level diagram shows the DQ signal intensity I_{DQ} versus the dipolar coupling strength $D^{(ij)}$ and the excitation time τ, both normalized with respect to MAS. The two curves on the right show vertical and horizontal slices taken from the two-dimensional plot: A vertical slice (above) at $\tau = \tau_R/2$ along the coupling axis displays $I_{DQ}(2\pi \cdot D^{(ij)}/\omega_R)$, and a horizontal slice (below) at $2\pi \cdot D^{(ij)} = 2\omega_R$ along the time axis displays $I_{DQ}(\tau/\tau_R)$.

Using model samples providing largely isolated spin pairs, such excitation curves can be demonstrated experimentally, as is shown in Fig. 12. Crystalline tribromoacetic acid, CBr_3COOH, forms hydrogen-bonded dimers and, in this way, contains pairs of acidic protons with an interproton distance of 0.265 nm, corresponding to a dipolar coupling of $D^{(ij)} = 2\pi \cdot 6.5$ kHz. (The interproton distance was obtained from ^{1}H MAS sideband patterns, which were evaluated on the basis of neutron scattering results and previous NMR data for trichloroacetic acid (*62*, *29*).) These proton pairs are separated from each other by bulky CBr_3 groups, ensuring an interpair distance of >0.5 nm. For this model compound, the pulse sequence

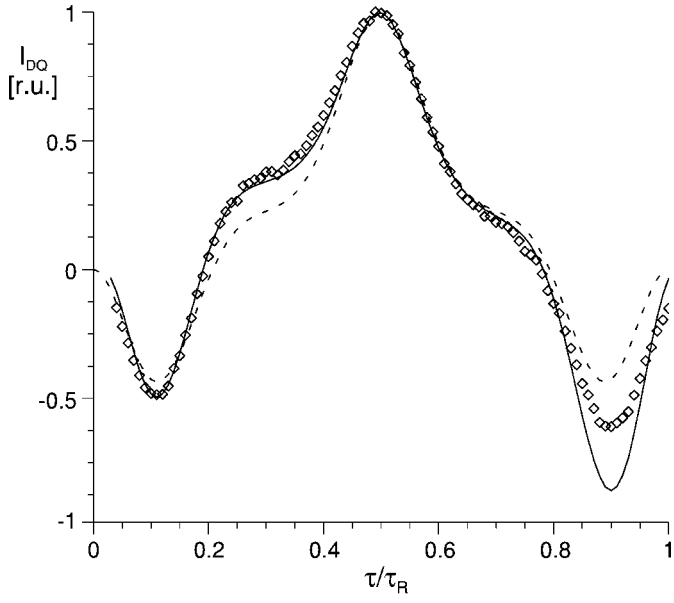

FIG. 12. Comparison of calculated DQ excitation curves with experimental data, obtained for the proton pairs in tribromoacetic acid. The pulse sequence used is $(90^\circ_x\text{–}\tau\text{–}90^\circ_{-x})_{exc}(90^\circ_y\text{–}\tau\text{–}90^\circ_{-y})_{rec}(90^\circ_x)_{read}$ and the MAS frequency is 5 kHz. The dotted line represents a direct calculation based on Eqs. [82] and [83], while the solid line results from a numerical simulation including finite pulse-length effects (3 μs in the experiments).

$(90^\circ_x\text{–}\tau\text{–}90^\circ_{-x})_{exc}(90^\circ_y\text{–}\tau\text{–}90^\circ_{-y})_{rec}(90^\circ_x)_{read}$ was applied at a MAS frequency of 5 kHz, corresponding to $\tau_R = 200\,\mu$s, and τ was varied between 0 and τ_R. In Fig. 12, the experimental DQ intensities are compared to calculated curves. On account of the inclusion of finite pulse-length effects (3 μs in the experiments), the numerical simulation (solid line) resembles the slight asymmetry of the experimental data points, while the pure spin-pair calculation (dotted line) is perfectly symmetric.

3.2.5. MAS and Time Reversal

The marked efficiency at $\tau = \frac{1}{2}\tau_R$ in the DQ excitation profile can be explained recalling Eq. [82]. In the special case of $\tau = \frac{1}{2}\tau_R$, the angular dependence of the integrated spatial part of the dipolar interaction simplifies to (*37*)

$$\Omega_D^{(ij)}\left(0, \frac{\tau_R}{2}\right) = -\Omega_D^{(ij)}\left(\frac{\tau_R}{2}, \tau_R\right) = \frac{\omega_D^{(ij)}}{\omega_R} \cdot \sqrt{2} \sin 2\beta_{ij} \sin \gamma_{ij}, \quad [85]$$

and the resulting phase factors of excitation and reconversion differ only in their signs. With respect to the aspects of MQ MAS spectroscopy considered later in this review, it is important to note that it is the above simplification (Eq. [84]) which allows the signals in MQ spectra and, in particular, the MAS sideband patterns to be recorded with pure absorptive phase.

Moreover, the sign change encountered in Eq. [84] between excitation and reconversion means that for $\tau = \frac{1}{2}\tau_R$ MAS itself provides the sign change which is vital to achieve time reversal and which is, in the static case, accomplished by a RF pulse phase shift of $\frac{\pi}{2}$. Therefore, the combination of pulse-phase-induced and MAS-induced sign changes makes them cancel each other (in the following section, this feature will form the basis for long-time excitation under dipolar recoupling). However, even-order quantum coherences are reconverted irrespective of this cancelling phenomenon. Both for formally correctly "time-reversed" Hamiltonians $\hat{\boldsymbol{H}}_{rec} = -\hat{\boldsymbol{H}}_{exc}$ and for $\hat{\boldsymbol{H}}_{rec} = \hat{\boldsymbol{H}}_{exc}$, reconversion is accomplished, because for $2m$-quantum coherences, represented by $(\hat{\boldsymbol{T}}_{l,2m} - \hat{\boldsymbol{T}}_{l,-2m})$, the sign change of the Hamiltonian can be transformed into a phase factor or, equivalently, into a sign change of the state resulting after the reconversion:

- "Time-reversed" Hamiltonians $\hat{\boldsymbol{H}}_{rec} = -\hat{\boldsymbol{H}}_{exc}$:

$$\exp(-i\hat{\boldsymbol{H}}_{rec}\tau)\exp(-i\hat{\boldsymbol{H}}_{exc}\tau)\hat{\boldsymbol{I}}_z\exp(i\hat{\boldsymbol{H}}_{exc}\tau)\exp(i\hat{\boldsymbol{H}}_{rec}\tau) = \hat{\boldsymbol{I}}_z. \quad [86]$$

- Equal Hamiltonians $\hat{\boldsymbol{H}}_{rec} = \hat{\boldsymbol{H}}_{exc}$:

$$\begin{aligned}
&\exp(-i\hat{\boldsymbol{H}}_{rec}\tau)\underbrace{\exp(-i\hat{\boldsymbol{H}}_{exc}\tau)\hat{\boldsymbol{I}}_z\exp(i\hat{\boldsymbol{H}}_{exc}\tau)}_{\propto(\hat{\boldsymbol{T}}_{l,2m}-\hat{\boldsymbol{T}}_{l,-2m})}\exp(i\hat{\boldsymbol{H}}_{rec}\tau)\\
&\quad\propto \exp\left(i\frac{\pi}{2}\hat{\boldsymbol{I}}_z\right)\exp(i\hat{\boldsymbol{H}}_{exc}\tau)\exp\left(-i\frac{\pi}{2}\hat{\boldsymbol{I}}_z\right)(\hat{\boldsymbol{T}}_{l,2m}-\hat{\boldsymbol{T}}_{l,-2m})\\
&\quad\times\exp\left(i\frac{\pi}{2}\hat{\boldsymbol{I}}_z\right)\exp(-i\hat{\boldsymbol{H}}_{exc}\tau)\exp\left(-i\frac{\pi}{2}\hat{\boldsymbol{I}}_z\right)\\
&= \exp(im\pi)\exp\left(i\frac{\pi}{2}\hat{\boldsymbol{I}}_z\right)\exp(i\hat{\boldsymbol{H}}_{exc}\tau)(\hat{\boldsymbol{T}}_{l,2m}+\hat{\boldsymbol{T}}_{l,-2m})\\
&\quad\times\exp(-i\hat{\boldsymbol{H}}_{exc}\tau)\exp\left(-i\frac{\pi}{2}\hat{\boldsymbol{I}}_z\right)\\
&= \exp(im\pi)\exp\left(i\frac{\pi}{2}\hat{\boldsymbol{I}}_z\right)\hat{\boldsymbol{I}}_z\exp\left(-i\frac{\pi}{2}\hat{\boldsymbol{I}}_z\right)\\
&= (-1)^m\hat{\boldsymbol{I}}_z. \qquad [87]
\end{aligned}$$

As a consequence of this, even-order quantum coherences can be successfully reconverted through time reversal irrespective of the pulse phases. For odd-order quantum coherences, represented by $(\hat{\boldsymbol{T}}_{l,2m+1} - \hat{\boldsymbol{T}}_{l,-(2m+1)})$, in contrast, the sign of the phase factor $\exp(\pm i(2m+1)\frac{\pi}{2}) = \pm i \cdot (-1)^m$ does depend on the sign of the order $\pm(2m+1)$ of the operator $\hat{\boldsymbol{T}}_{l,\pm(2m+1)}$. Hence, upon a pulse-phase shift of $\frac{\pi}{2}$, the linear combination $(\hat{\boldsymbol{T}}_{l,2m+1} - \hat{\boldsymbol{T}}_{l,-(2m+1)})$ changes its symmetry to $(\hat{\boldsymbol{T}}_{l,2m+1} + \hat{\boldsymbol{T}}_{l,-(2m+1)})$, and the pulse phases in the sequence have to be adapted accordingly.

3.2.6. Long-Time Excitation and Dipolar Recoupling

According to the results of the previous section, the two-pulse excitation scheme $90^\circ_x\text{–}\tau\text{–}90^\circ_{-x}$ for DQCs is limited, under

MAS conditions, to excitation times $0 < \tau \leq \tau_R/2$, because for $\tau_R/2 < \tau \leq \tau_R$ the sign of the spatial part $\Omega_D^{(ij)}$ is inverted by the rotor modulation, reflecting the refocusing action of MAS. This limitation means that, for a given MAS frequency, only DQCs based on dipolar couplings stronger than a minimum coupling can be efficiently excited, since the DQ intensity depends on the product $(D^{(ij)}\tau)^2$ of the coupling strength and the excitation time. At that point, the marked sensitivity of DQCs to internuclear distances, $I_{DQ}^{(ij)} \propto r_{ij}^{-6}$, which is in terms of selectivity an advantage of the method, would result in the considerable disadvantage that longer-range distances are only accessible for relatively low MAS frequencies, which, on the other hand, will not provide sufficient spectral resolution, if stronger dipolar couplings are also present in the sample. Therefore, the choices of spinning frequency ω_R and excitation time τ_{exc} available in an experiment need to be more flexible and independent of each other, which basically requires excitation times in the range $\tau > \tau_R/2$.

In order to gain this flexibility, the refocusing effect or, equivalently, the dipolar decoupling provided by MAS has to be canceled or, at least, reduced during the periods of excitation and reconversion. Since interrupting the sample spinning on time scales far below milliseconds is technically not possible, the averaging process in the spatial part has to be compensated by a counterrotation of the spin part, which, in this way, recouples the dipolar interaction (*12, 28*). In the past decade, numerous pulse sequences providing dipolar recoupling have been developed (e.g., (*74, 106, 83*)), some of which include compensations for experimental imperfections or other interfering interactions (e.g., the C_7 sequence (*67, 57*)). In this review, we want to focus on a rather simple, but quite flexible, approach, based on the two-pulse scheme discussed above, which was termed "back-to-back" (BABA) (*32*) and has already been applied successfully to several systems (*32, 65, 98, 47, 97, 18, 20*).

Under MAS, the application of two 90° pulses spaced by a time interval τ yields maximum excitation efficiency together with a simple phase behavior, when $\tau = \tau_R/2$. If such a pulse sequence 90°_q–$\tau_R/2$–90°_{-q} (henceforth referred to as q–$\bar{q}$) is repeated, only the sign of the spatial part of the excitation Hamiltonian $\hat{\boldsymbol{H}}_{exc}$ is inverted within a rotor period, namely between the first and the second half of the period, i.e., $\Omega_D^{(ij)}(0, \tau_R/2) = -\Omega_D^{(ij)}(\tau_R/2, \tau_R)$ (see Eqs. [82] and [84]. However, such a sign inversion can also be achieved by shifting the phases of both pulses by $\frac{\pi}{2}$, as was discussed in Section 3.2.2. Hence, a simple alternation of segments x–$\bar{x}$ and y–$\bar{y}$ provides dipolar recoupling and opens up the possibility to "pump" DQCs for excitation times $\tau_{exc} = N \cdot (\tau_R/2)$, consisting of integer multiples of half rotor periods. In Fig. 13c, such a recoupling pulse sequence is displayed, together with a schematic representation of the MQ experiment (Fig. 13a) and the two-pulse excitation scheme (Fig. 13b).

The recoupling effect of a pulse sequence consisting of alternating segments x–$\bar{x}$ and y–$\bar{y}$ becomes very clear when using the propagator formalism (the propagators on the right-hand side

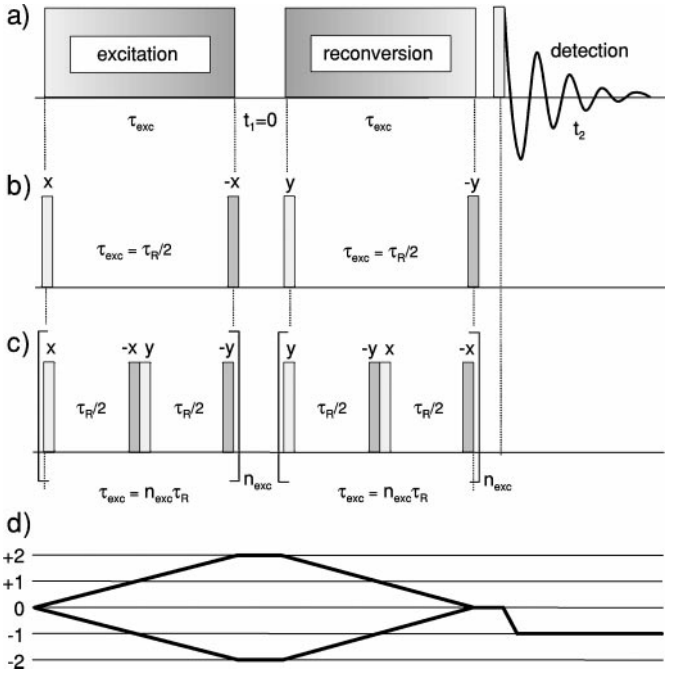

FIG. 13. (a) Schematic representation of a MQ experiment with its characteristic periods: excitation of MQCs, reconversion to longitudinal magnetization, and detection as SQCs. (The evolution during the MQ dimension t_1 is skipped here and will be discussed in Sections 3.4 and 3.5.) (b) Two-pulse segment with $\tau = \tau_R/2$. (c) Basic recoupling pulse sequence of the form x–$\bar{x}y$–$\bar{y}$, where $\tau_{exc} = n_{exc} \cdot \tau_R$. (d) Coherence transfer pathway diagram.

of $\hat{\boldsymbol{\rho}}(0)$ are skipped):

$$\begin{aligned}
&\hat{\boldsymbol{L}}_{-y}\hat{\boldsymbol{L}}_D\left(\frac{\tau_R}{2}, \tau_R\right)\hat{\boldsymbol{L}}_y\hat{\boldsymbol{L}}_{-x}\hat{\boldsymbol{L}}_D\left(0, \frac{\tau_R}{2}\right)\hat{\boldsymbol{L}}_x\hat{\boldsymbol{\rho}}(0)\cdots \\
&= \hat{\boldsymbol{L}}_y^+\hat{\boldsymbol{L}}_D^+\left(0, \frac{\tau_R}{2}\right)\hat{\boldsymbol{L}}_y\hat{\boldsymbol{L}}_x^+\hat{\boldsymbol{L}}_D\left(0, \frac{\tau_R}{2}\right)\hat{\boldsymbol{L}}_x\hat{\boldsymbol{\rho}}(0)\cdots \\
&= \hat{\boldsymbol{L}}_x^+\hat{\boldsymbol{L}}_D\left(0, \frac{\tau_R}{2}\right)\hat{\boldsymbol{L}}_x\hat{\boldsymbol{L}}_x^+\hat{\boldsymbol{L}}_D\left(0, \frac{\tau_R}{2}\right)\hat{\boldsymbol{L}}_x\hat{\boldsymbol{\rho}}(0)\cdots \\
&= \hat{\boldsymbol{L}}_x^+\hat{\boldsymbol{L}}_D\left(0, \frac{\tau_R}{2}\right)\hat{\boldsymbol{L}}_D\left(0, \frac{\tau_R}{2}\right)\hat{\boldsymbol{L}}_x\hat{\boldsymbol{\rho}}(0)\cdots. \qquad [88]
\end{aligned}$$

These transformations are based on the following identities: $\hat{\boldsymbol{L}}_{\pm q} = \hat{\boldsymbol{L}}_{\mp q}^+$ for pulses of phase $q = x, y$; $\hat{\boldsymbol{L}}_D(\tau_R/2, \tau_R) = \hat{\boldsymbol{L}}_D^+(0, \tau_R/2)$ due to the MAS-induced sign inversion, i.e., time reversal, between $[0, \tau_R/2]$ and $[\tau_R/2, \tau_R]$; $\hat{\boldsymbol{L}}_y^+\hat{\boldsymbol{L}}_D^+\hat{\boldsymbol{L}}_y = \hat{\boldsymbol{L}}_x^+\hat{\boldsymbol{L}}_D\hat{\boldsymbol{L}}_x$ due to the sign inversion of the excitation Hamiltonian arising from a pulse-phase shift by $\frac{\pi}{2}$. It is then apparent that the system is propagated twice under the dipolar interaction; i.e., the excitation time is doubled.

The distinction as to whether the pulse sequence $(x$–$\bar{x})(y$–$\bar{y})$ is to be regarded as a pure excitation scheme $[(\ldots)(\ldots)]_{exc}$ or as a combination of excitation and reconversion $(\ldots)_{exc}(\ldots)_{rec}$ depends on whether a particular coherence order is selected

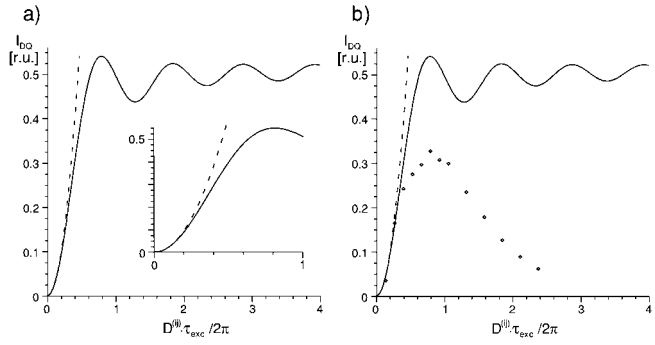

FIG. 14. (a) Calculated DQ intensities for a single spin pair (solid line) and for the leading two-spin term in the series expansion for multispin systems (dotted line). The DQCs are excited during periods $\tau_{exc} = N \cdot \tau_R/2$ by an alternating sequence of two-pulse segments (90°_x–$\tau_R/2$–90°_{-x}) and (90°_y–$\tau_R/2$–90°_{-y}). The initial slope where two-spin behavior predominates is magnified in the inset. (b) Comparison of calculated and experimentally observed DQ signal intensities. The experiments (data points) were performed on tribromoacetic acid, which is a H-H spin-pair model compound with a dipolar pair coupling of $D^{(ij)} = 2\pi \cdot 6.5$ kHz. In both diagrams, I_{DQ} is normalized with respect to the signal of a one-pulse experiment.

between the two segments, e.g., by a phase cycle, or not. This means that the above pulse sequence, if applied only once, always acts as a combined excitation and excitation/reconversion scheme and that the sequence has to undergo a phase cycling procedure (or alternatively a gradient dephasing/rephasing procedure) to select the desired coherence pathway.

In Fig. 14a, the signal intensity of two-spin DQCs is plotted versus $D^{(ij)}\tau_{exc}$ in a so-called DQ buildup curve. The solid line represents the behavior of a single spin pair, while the dotted line reflects the leading two-spin term in the series expansion for a multispin system. Due to the underlying series expansion, the simple squared dependence $I_{DQ}^{(ij)} \propto (D^{(ij)})^2\tau_{exc}^2$ is a valid approximation only for $D^{(ij)}\tau_{exc}/2\pi < 0.2$, i.e., for weak dipolar couplings or short excitation times. Subsequent to this short-time behavior the DQ intensity enters an oscillatory regime, where the amplitude of the oscillation decreases with time, approaching, for a single spin pair, the long-time limit of $\lim_{\tau_{exc}\to\infty} I_{DQ} = \frac{1}{2}$.

Experimentally, such oscillating curves are rarely observed in strongly coupled ^{1}H systems. Instead, in most cases the experimental results are rather similar to the DQ buildup curve obtained for tribromoacetic acid (data points in Fig. 14b). Although tribromoacetic acid, considering its crystal structure, is quite a reasonable model compound with largely isolated proton pairs, the DQ intensity decays before reaching the oscillatory regime. This marked loss of DQ signal is due to the interplay of a residual nonpair character of the sample and experimental imperfections.

Focusing first on the experimental side, the pulse sequence has to recouple the dipolar interaction under fast MAS conditions, while compensating for RF imperfections and additional interactions present in the sample, like a considerable CSA in the case of tribromoacetic acid. However, the recoupling and the compensating performance of the pulse sequence as well as its long-time stability is limited by experimental misadjustments and other imperfections which obviously become more important for increasing excitation times. Concerning fast MAS applications to strongly dipolar-coupled systems, it is quite challenging to design pulse sequences combining dipolar recoupling and error compensation in spite of experimental and technical limitations. In this way, though still not for rigid ^{1}H systems, oscillating DQ and TQ buildup curves have been recorded for ^{13}C model systems (*67*, *30*). In the special case of partially mobile ^{1}H systems with well-defined dynamics, like liquid crystalline phases, the oscillating regime has also been observed in ^{1}H DQ buildup curves.

In "real" rigid ^{1}H samples, the dense network of dipolar couplings is obviously a further and important reason for the observed deviations from a pure spin-pair buildup behavior. It is clear that with increasing excitation times, i.e., with increasing evolution time under dipolar recoupling conditions, the system develops its multispin character, and the buildup oscillations are damped out. As can already be shown by simulations of small model spin systems (see Fig. 15), the interference of several couplings of different strengths leads to the cancellation of oscillations, because different frequencies are then destructively superimposed. In addition to this cancellation, in multispin systems, higher spin correlations and higher-order coherences are excited, thereby reducing the DQ signal intensity. This excitation behavior, focusing on the buildup of higher-order MQCs, has been studied by Geen *et al.* (*40*) for the case of the protons in adamantane under MAS conditions. On the one hand, for long excitation times, the existence of 16-quantum coherences demonstrates the dipolar recoupling efficiency achievable by RF pulse sequences like C_7 (*67*) under fast MAS. On the other hand, the results, which are obtained using a dense and

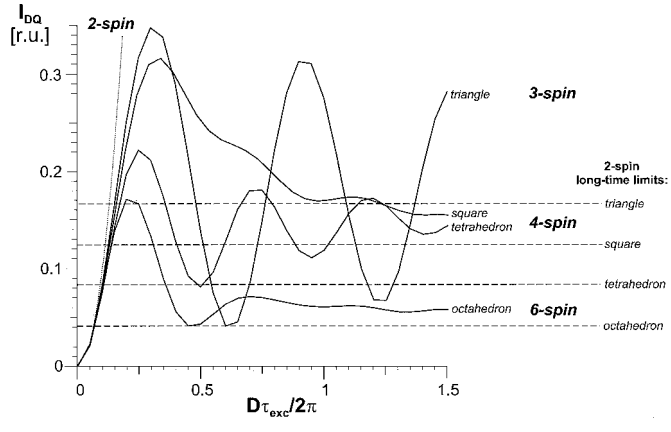

FIG. 15. Simulated DQ buildup curves for different spin systems (solid lines) and the leading two-spin term from the series expansion in Eq. [68] (dotted line). The three, four, and six spins are localized at the vertices of an equilateral triangle, a square, a tetrahedron, and an octahedron, respectively. The DQ signal intensity is normalized to the number of coupled pairs in the respective system, and the dashed lines indicate the long-time limit for DQ intensities, provided that only two-spin DQCs are excited.

cubic spin system, provide clear evidence that, for short excitation times, the MQ signal-intensity distribution is dominated by DQCs and that, for $D^{(ij)}\tau_{exc}/2\pi < 0.1$, to a good approximation *only* DQCs are generated.

In Fig. 15, simulated DQ buildup curves for different multispin model systems are displayed, which shall be discussed briefly in the following. For short excitation times, all buildup curves coincide with a simple squared dependence $I_{DQ} \propto D^2$, determined by the strongest dipolar coupling D in the system, as is characteristic for two spins (indicated by the dotted curve). It is observed that the excitation time, at which a deviation from the two-spin limit sets in, becomes shorter when the effective coupling D_{eff} becomes stronger: $D_{\text{eff}} = D$ in the two-spin system; $D_{\text{eff}} = 3\sqrt{2}D \approx 4.2D$ in the equilateral-triangular three-spin system; $D_{\text{eff}} \approx 5.8D$ and $D_{\text{eff}} = 4\sqrt{3}D \approx 6.9D$ in the squared and tetrahedral four-spin systems, respectively; and finally $D_{\text{eff}} \approx 12.2D$ in the octahedral six-spin system.

In the triangular three-spin and the tetrahedral four-spin system, all dipolar couplings $D^{(ij)}$ for all pairs (ij) are of identical strength D, because all spins are equidistant (and an isotropic distribution of orientations is assumed). Consequently, the same oscillation of the buildup curves is observed in both cases, with the frequency being determined by the effective coupling strength, which is $D_{\text{eff}} = 4.2D$ and $D_{\text{eff}} = 5.8D$ in the three- and four-spin cases, respectively. However, the presence of couplings of different strengths causes the oscillations to be damped by destructive interference as the excitation time increases. In the squared four-spin system or in the octahedral system, for example, there are couplings of two different strengths: four times D and twice $(\frac{1}{\sqrt{2}})^3 D$, or 24 times D and six times $(\frac{1}{\sqrt{2}})^3 D$, respectively.

To a first approximation, the DQ buildup curves converge, for long excitation times, to intensity values of $\frac{1}{2}$, $\frac{1}{6}$, $\frac{1}{8}$, $\frac{1}{12}$, and $\frac{1}{24}$ for a two-spin, an equilateral-triangular three-spin, a square and a tetrahedral four-spin, and an octahedral six-spin system, respectively, because two-spin systems converge to $\frac{1}{2}$ and the ratio of strongly coupled pairs in the systems is given by $1:3:4:6:12$. Taking also the weaker pair couplings of $(\frac{1}{\sqrt{2}})^3 D \approx 0.35D$ in the squared four-spin and the octahedral six-spin system into account results in a negligible deviation of $1:3:4.2:6:12.4$. In Fig. 15, these final values are indicated by the dashed horizontal lines.

While a two-spin DQ buildup curve would oscillate precisely about its final value $\frac{1}{2}$, it is obvious that all curves of multispin systems converge to higher values. In particular, for the tetrahedral four-spin system, a significantly higher DQ signal intensity is observed. This characteristic deviation is due to the fact that the final intensity values indicated by the horizontal lines in the diagram are based on a spin-pair approximation, neglecting that multispin systems can generate so-called multi-spin DQCs with a coherence order of 2, but involving more than two coupled spins. Using operator notation, a four-spin DQC of the spins i, j, k and l takes the form $(\hat{\boldsymbol{I}}_+^{(i)}\hat{\boldsymbol{I}}_+^{(j)}\hat{\boldsymbol{I}}_+^{(k)}\hat{\boldsymbol{I}}_-^{(l)} + \hat{\boldsymbol{I}}_-^{(i)}\hat{\boldsymbol{I}}_-^{(j)}\hat{\boldsymbol{I}}_-^{(k)}\hat{\boldsymbol{I}}_+^{(l)})$. The contribution of such higher spin correlations increases with the density of the dipolar coupling network between the spins. In this respect, the tetrahedral system represents the closest packing of four spins, giving rise to a significant intensity of four-spin DQCs and hence to a marked deviation from the two-spin limit, whereas in the squared arrangement the two-spin character persists to a larger extent.

Concluding these considerations, it is clear that, in "real" ^{1}H systems, DQ buildup curves are expected to be damped for long excitation times because of the destructive interference of pair couplings of different strengths and the generation of higher-order coherences. While for short excitation times the two-spin approximation is valid for multispin systems of arbitrary geometry, the onset of the breakdown of this approximation for longer excitation times depends on the overall dipolar coupling density in the system.

3.2.7. Chemical Shifts and Offsets

As was discussed in Section 3.1, DQCs are better suited to spectroscopically detecting two-spin correlations than ZQCs, because the chemical shift of DQCs allows the involved spin pairs to be unambiguously resolved in the spectrum. On the other hand, the sensitivity of DQCs to chemical shifts or, equivalently, to frequency offsets between the RF field of the pulses and the nuclear resonance frequencies requires these effects to be taken into account when the excitation of DQCs is considered. For ^{1}H systems, the chemical shielding interactions can, in most cases, be reduced to their isotropic part, so that the Hamiltonian combining the dipolar interaction with the chemical shift is simply given by

$$\hat{\boldsymbol{H}}(t) = \sum_i^N \omega_{CS}^{(i)}\hat{\boldsymbol{I}}_z^{(i)} + \sum_{i<j}^N \omega_D^{(ij)}(t)\hat{\boldsymbol{T}}_{2,0}^{(ij)}, \qquad [89]$$

where the sums include all spins i and spin pairs (ij), respectively, of the N-spin system. In the following, we will consider the special case of a two-spin system with both spins having the same chemical shift $\omega_{CS}^{(ij)}$ or, equivalently, the same resonance offset, since the formulae are then easier to handle, but still reflect the general features of the DQC excitation behavior. The Hamiltonian is then

$$\hat{\boldsymbol{H}}^{(ij)}(t) = \omega_{CS}^{(ij)}\underbrace{(\hat{\boldsymbol{I}}_z^{(i)} + \hat{\boldsymbol{I}}_z^{(j)})}_{\hat{\boldsymbol{I}}_z^{(ij)}} + \omega_D^{(ij)}(t)\hat{\boldsymbol{T}}_{2,0}^{(ij)}, \qquad [90]$$

and integration over the time interval $[0, \tau]$ yields the respective propagator,

$$\exp\left(i\int_0^\tau \hat{\boldsymbol{H}}^{(ij)}(t)\,dt\right) = \exp\left(i\omega_{CS}^{(ij)}\hat{\boldsymbol{I}}_z^{(ij)}\tau + i\Omega_D^{(ij)}(0,\tau)\hat{\boldsymbol{T}}_{2,0}^{(ij)}\right). \qquad [91]$$

Subjecting a state of transverse magnetization, $\hat{\rho} \propto \hat{I}_x^{(i)} + \hat{I}_x^{(j)}$, to such a propagation results in a two-spin correlation of the form

$$\begin{aligned}\hat{\rho}(\tau) &= \exp\bigl(i\omega_{CS}^{(ij)}\hat{I}_z^{(ij)}\tau\bigr)\bigl[\hat{T}_{2,1}^{(ij)} + \hat{T}_{2,-1}^{(ij)}\bigr]\sin\bigl(\Omega_D^{(ij)}(0,\tau)\bigr) \\ &\quad\times \exp\bigl(-i\omega_{CS}^{(ij)}\hat{I}_z^{(ij)}\tau\bigr) \\ &= \bigl[\hat{T}_{2,1}^{(ij)}\exp\bigl(i\omega_{CS}^{(ij)}\tau\bigr) + \hat{T}_{2,-1}^{(ij)}\exp\bigl(-i\omega_{CS}^{(ij)}\tau\bigr)\bigr] \\ &\quad\times \sin\bigl(\Omega_D^{(ij)}(0,\tau)\bigr) \\ &= \bigl[\bigl(\hat{T}_{2,1}^{(ij)} + \hat{T}_{2,-1}^{(ij)}\bigr)\cos\bigl(\omega_{CS}^{(ij)}\tau\bigr) + i\bigl(\hat{T}_{2,1}^{(ij)} - \hat{T}_{2,-1}^{(ij)}\bigr) \\ &\quad\times \sin\bigl(\omega_{CS}^{(ij)}\tau\bigr)\bigr]\sin\bigl(\Omega_D^{(ij)}(0,\tau)\bigr). \end{aligned} \quad [92]$$

The chemical shift evolution can be written as a phase factor $\exp(\pm i\omega_{CS}^{(ij)}\tau)$, with the sign of the exponent depending on the sign of the order ± 1 of the tensor operator $\hat{T}_{2,\pm 1}$. As a consequence of this, an antiphase term $(\hat{T}_{2,1}^{(ij)} - \hat{T}_{2,-1}^{(ij)})$ emerges from the original two-spin correlation $(\hat{T}_{2,1}^{(ij)} + \hat{T}_{2,-1}^{(ij)})$. The application of a second pulse, whose phase is identical to that of the first pulse, only converts the original term $(\hat{T}_{2,1}^{(ij)} + \hat{T}_{2,-1}^{(ij)})$, modulated by $\cos(\omega_{CS}^{(ij)}\tau)$, into a DQC of the form $(\hat{T}_{2,2}^{(ij)} - \hat{T}_{2,-2}^{(ij)})$. To convert the antiphase term $(\hat{T}_{2,1}^{(ij)} - \hat{T}_{2,-1}^{(ij)})$, modulated by $\sin(\omega_{CS}^{(ij)}\tau)$, the phase of the second pulse has to be shifted by $\frac{\pi}{2}$ with respect to the first.

During reconversion, the signal due to the DQC is modulated again by the same phase factors as during excitation. Finally, for a spin pair with a frequency offset $\omega_{CS}^{(ij)}$, the DQ signal intensity arising from the pulse sequence $(x - \bar{x})_{exc}(y - \bar{y})_{rec}$ is given by

$$I_{DQ}^{(ij)} \propto \cos^2\bigl(\omega_{CS}^{(ij)}\tau\bigr)\cdot\sin\bigl(\Omega_D^{(ij)}(0,\tau)\bigr)\cdot\sin\bigl(\Omega_D^{(ij)}(\tau,2\tau)\bigr). \quad [93]$$

In Fig. 16a, the DQ intensity is plotted versus the frequency offset for the case calculated above (Eq. [93]) and for a spin pair with symmetrical offset $\omega_{CS}^{(i)} = -\omega_{CS}^{(j)}$. In the latter case, the simple $\cos^2(\omega_{CS}^{(ij)}\tau)$ dependence is still approximately valid for small offsets of the order $\omega_{CS}^{(ij)}\tau_{exc}/2\pi < 0.1$. For an offset range of $\omega_{CS}^{(ij)}\tau_{exc}/2\pi < 0.2$, the experimental results obtained using the proton pairs of tribromoacetic acid agree with the simple theoretical approach (see Fig. 16c). (The experiments were performed under MAS at 20 kHz, applying an uncompensated back-to-back pulse sequence of the form $(x\text{–}\bar{x}y\text{–}\bar{y})_2$ for the duration of two rotor periods.)

Although in typical proton systems the chemical shift effects are relatively small compared to the dipolar interaction, an excitation bandwidth of $\Delta\omega_{CS}\tau_{exc}/2\pi \ll 1$ does not suffice in practice. Hence, a scheme providing at least partial offset compensation during DQ excitation is required. In order to derive such a scheme, first consider the effect of the pulse-sequence segments

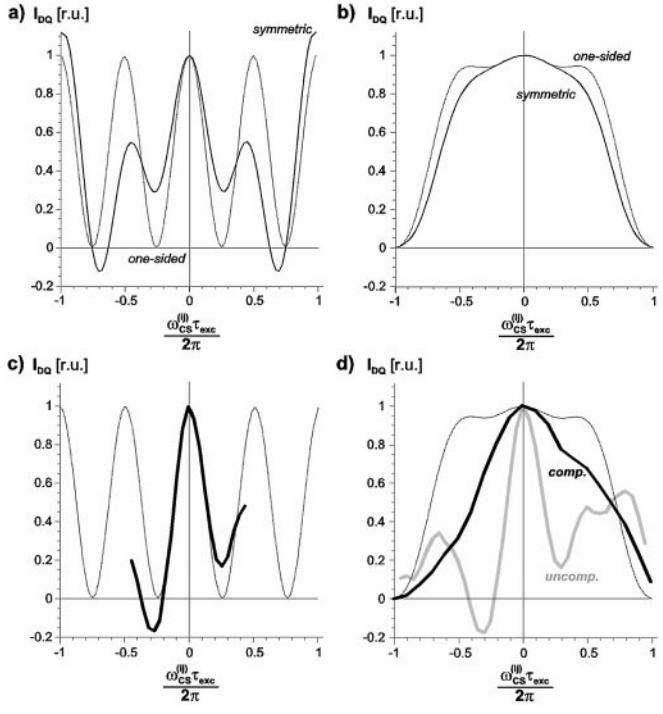

FIG. 16. Calculated (thin lines) and experimental (thick lines) DQ excitation efficiencies for a spin pair with frequency offset $\omega_{CS}^{(ij)}$. "One-sided" means that both spins have the same offset, while "symmetrical" denotes $\omega_{CS}^{(ij)} = -\omega_{CS}^{(ij)}$. Calculations (thin lines): (a) uncompensated excitation, and (b) offset-compensated excitation. For comparison, experiments on tribromoacetic acid (thick lines): (c) uncompensated excitation applying $(x\text{–}\bar{x}y\text{–}\bar{y})_2$, and (d) offset-compensated excitation applying $(x\text{–}\bar{x}y\text{–}\bar{y}\bar{x}\text{–}x\bar{y}\text{–}y)$, in both cases under MAS at 20 kHz, which corresponds to $\tau_{exc} = 100\,\mu$s.

$(90^\circ_x\text{–}\tau\text{–}90^\circ_{\pm x})$ and $(90^\circ_y\text{–}\tau\text{–}90^\circ_{\pm y})$. The effective Hamiltonian of such a segment is calculated by transforming the Hamiltonian of Eq. [90] into the toggling frame (see also Eq. [78]). In the following notation, the propagator $\hat{\boldsymbol{L}}_\phi$ reflects the action of a 90° pulse of phase ϕ, where $\phi = n\cdot\frac{\pi}{2}$, with $n = 0, 1, 2, 3$ corresponding to the orientations of the RF field along x, y, $-x$, $-y$, respectively, in the rotating frame:

$$\hat{\rho}(\tau) = \hat{\boldsymbol{L}}_{exc}\hat{\rho}(0)\hat{\boldsymbol{L}}_{exc}^{+} = \hat{\boldsymbol{L}}_{\phi'}\hat{\boldsymbol{L}}_{D+CS}\hat{\boldsymbol{L}}_{\phi}\hat{\rho}(0)\hat{\boldsymbol{L}}_{\phi}^{+}\hat{\boldsymbol{L}}_{D+CS}^{+}\hat{\boldsymbol{L}}_{\phi'}^{+}. \quad [94]$$

At this point, two cases have to be distinguished: First, a segment consisting of two pulses with opposite phases ϕ and $\phi' = \phi + \pi$, such that $\hat{\boldsymbol{L}}_{\phi'} = \hat{\boldsymbol{L}}_{\phi}^{+}$, and hence

$$\hat{\rho}(\tau) = \hat{\boldsymbol{L}}_{\phi}^{+}\hat{\boldsymbol{L}}_{D+CS}\hat{\boldsymbol{L}}_{\phi}\hat{\rho}(0)\hat{\boldsymbol{L}}_{\phi}^{+}\hat{\boldsymbol{L}}_{D+CS}^{+}\hat{\boldsymbol{L}}_{\phi}. \quad [95]$$

The excitation Hamiltonian of the propagator $\hat{\boldsymbol{L}}_{exc} = \exp(-i\hat{\boldsymbol{H}}_{exc}\tau)$ is then simply obtained from a coordinate transformation $\hat{\boldsymbol{L}}_{\phi}^{+}\cdots\hat{\boldsymbol{L}}_{\phi}$ of the original excitation Hamiltonian

$\hat{\boldsymbol{H}}^{(ij)}(t)$ (Eq. [90], see also Eq. [78]):

$$\begin{aligned}\hat{\boldsymbol{H}}_{exc} &= \exp\left(-i\frac{\pi}{2}\hat{\boldsymbol{I}}_{\phi}\right)\cdot\frac{1}{\tau}\int_0^{\tau}\hat{\boldsymbol{H}}^{(ij)}(t)\,dt\cdot\exp\left(i\frac{\pi}{2}\hat{\boldsymbol{I}}_{\phi}\right)\\ &= \omega_{CS}^{(ij)}\hat{\boldsymbol{I}}_{\phi-\frac{\pi}{2}}+\frac{\Omega_D(0,\tau)}{\tau}\\ &\quad\cdot\left(-\frac{1}{2}\hat{\boldsymbol{T}}_{2,0}-\sqrt{\frac{3}{8}}(\hat{\boldsymbol{T}}_{2,2}+\hat{\boldsymbol{T}}_{2,-2})\exp(2i\phi)\right).\end{aligned}\quad[96]$$

Second, in the case of a two-pulse segment consisting of two pulses of identical phase $\phi'=\phi$, the calculation requires the propagation in Eq. [93] to be extended several times by $\hat{L}_{\phi}\hat{L}_{\phi}^{+}=\hat{\mathbb{1}}$:

$$\begin{aligned}\hat{\boldsymbol{\rho}}(\tau) = &\overbrace{\hat{\boldsymbol{L}}_{\phi}\hat{\boldsymbol{L}}_{\phi}\hat{\boldsymbol{L}}_{\phi}^{+}\hat{\boldsymbol{L}}_{D+CS}\hat{\boldsymbol{L}}_{\phi}\hat{\boldsymbol{L}}_{\phi}^{+}\hat{\boldsymbol{L}}_{\phi}^{+}}^{\hat{\boldsymbol{L}}_{exc}}\\ &\cdot\hat{\boldsymbol{L}}_{\phi}\hat{\boldsymbol{L}}_{\phi}\hat{\boldsymbol{\rho}}(0)\hat{\boldsymbol{L}}_{\phi}^{+}\hat{\boldsymbol{L}}_{\phi}^{+}\\ &\cdot\underbrace{\hat{\boldsymbol{L}}_{\phi}\hat{\boldsymbol{L}}_{\phi}\hat{\boldsymbol{L}}_{\phi}^{+}\hat{\boldsymbol{L}}_{D+CS}^{+}\hat{\boldsymbol{L}}_{\phi}\hat{\boldsymbol{L}}_{\phi}^{+}\hat{\boldsymbol{L}}_{\phi}^{+}}_{\hat{\boldsymbol{L}}_{exc}^{+}}.\end{aligned}\quad[97]$$

In comparison to Eq. [95], both the excitation propagator $\hat{\boldsymbol{L}}_{exc}$ and the initial state $\hat{\boldsymbol{\rho}}(0)$ are now subject to an additional propagation $\hat{\boldsymbol{L}}_{\phi}\hat{\boldsymbol{L}}_{\phi}\cdots\hat{\boldsymbol{L}}_{\phi}^{+}\hat{\boldsymbol{L}}_{\phi}^{+}=\exp(-i\pi\hat{\boldsymbol{I}}_{\phi})\cdots\exp(i\pi\hat{\boldsymbol{I}}_{\phi})$. With respect to $\hat{\boldsymbol{\rho}}(0)$ and to the chemical shift term in the excitation Hamiltonian, this gives rise to a sign inversion, while the terms $\hat{\boldsymbol{T}}_{2,0}$ and $(\hat{\boldsymbol{T}}_{2,2}+\hat{\boldsymbol{T}}_{2,-2})$ remain unaffected. The excitation Hamiltonians of two-pulse segments of the form $(90^{\circ}_{x}$–τ–$90^{\circ}_{x})$ or $(90^{\circ}_{y}$–τ–$90^{\circ}_{y})$ are finally given by

$$\begin{aligned}\hat{\boldsymbol{H}}_{exc} &= -\omega_{CS}^{(ij)}\hat{\boldsymbol{I}}_{\phi-\frac{\pi}{2}}+\frac{\Omega_D(0,\tau)}{\tau}\\ &\quad\cdot\left(-\frac{1}{2}\hat{\boldsymbol{T}}_{2,0}-\sqrt{\frac{3}{8}}(\hat{\boldsymbol{T}}_{2,2}+\hat{\boldsymbol{T}}_{2,-2})\exp(2i\phi)\right).\end{aligned}\quad[98]$$

Comparing the excitation Hamiltonians in Eqs. [95] and [97], it is clear that inverting the phase of the second pulse in two-pulse segments of the form $(90^{\circ}_{q}$–τ–$90^{\circ}_{\pm q})$ results in a sign inversion of the chemical shift term. By combining two such segments, it is possible to compensate for chemical shift or resonance offset effects, although the above discussion only applies to static conditions.

Under MAS conditions, as pointed out above, a synchronization obeying $\tau=\tau_R/2$ simplifies the algebra considerably, and a pulse-phase shift of $\frac{\pi}{2}$ between two consecutive segments conserves the term $(\hat{\boldsymbol{T}}_{2,2}+\hat{\boldsymbol{T}}_{2,-2})$ and hence provides dipolar recoupling for DQ excitation, while the dipolar term $\hat{\boldsymbol{T}}_{2,0}$ vanishes. Repeating this recoupling sequence $(x$–$\bar{x}y$–$\bar{y})$ with *inverted* pulse phases, i.e., $(x$–$\bar{x}y$–$\bar{y}\bar{x}$–$x\bar{y}$–$y)$, provides offset compensation on a time scale of $2\tau_R$, which is, in fact, the minimum time required for the combination of dipolar recoupling and zeroth-order offset compensation.

Being an averaging process, the compensation does not refocus offset-induced magnetization dephasing which occurs on a time scale $t<\tau_R$. In Fig. 16b, although an offset-compensated pulse sequence $(x$–$\bar{x}y$–$\bar{y}\bar{x}$–$x\bar{y}$–$y)$ is applied for $\tau_{exc}=2\tau_R$, the loss of DQ signal intensity with increasing offset is still obvious. However, in comparison to Fig. 16a, the bandwidth of approximately uniform excitation efficiency provided by the offset-compensated pulse sequence is about a factor of 8 larger than that achievable by an uncompensated sequence. Additionally, it should be noted that increasing the MAS frequency reduces the time scale $t=2\tau_R$ required for compensation. Therefore, the excitation bandwidth of the pulse sequence can be improved by spinning faster, while the dipolar recoupling performance, at least under ideal conditions, remains unaffected.

Instead of varying the pulse phases, offset compensation can also be accomplished by inserting 180° pulses in the middle of the $(90^{\circ}_{q}$–$\tau_R/2$–$90^{\circ}_{-q})$ segments (see also (*107*)), i.e., by the application of pulse-sequence segments of the form $(90^{\circ}_{q}$–$\tau_R/4$–$180^{\circ}_{q''}$–$\tau_R/4$–$90^{\circ}_{q'})$. In this way, the time scale required for offset compensation is reduced from $2\tau_R$ to $\frac{1}{2}\tau_R$, and hence the excitation bandwidth improves. However, this improvement is gained at the expense of an additional 180° pulse. In particular on the time scale of fast MAS, the overall duration of RF irradiation becomes significant and pulses cannot be considered negligibly short as compared to the rotor period. Therefore, the reduction in the performance of a pulse sequence, which has initially been designed assuming hard pulses, due to such interference effects is discussed in the following section.

The experiments confirm, in principle, the increased excitation bandwidth for offset-compensated pulse sequences (Fig. 16d, experiment with $(x$–$\bar{x}y$–$\bar{y}\bar{x}$–$x\bar{y}$–$y)$ under MAS at 20 kHz), although the experimental offset dependence is still considerably stronger and less symmetric than theoretically predicted. These deviations are mainly due to the CSA of the protons in the tribromoacetic acid sample. Performing the same experiment, but with additional 180° pulses instead of pulse-phase variations, the excitation bandwidth can indeed be increased, but the overall excitation efficiency becomes less.

3.2.8. Finite Pulse-Length Effects

In addition to features inherent to the sample, e.g., chemical shifts, the DQ excitation scheme must also take into account experimental and technical imperfections. Concerning ^{1}H spectroscopy under fast MAS, an important technical limitation is the available RF field strength. Although the δ-pulse approach is an essential and still very reasonable starting point for analytical considerations, there are noteworthy effects due to experimental pulse lengths. However, in the context of ^{1}H NMR experiments, we are not concerned with problems arising from internal

interactions exceeding the RF field strength, but rather with problems arising from RF pulse durations interfering with the short time scale of fast MAS. In typical ^{1}H MAS experiments, the 90° pulse length is between 1.5 and 3 μs. Considering, for example, a (q–q') segment of a DQ excitation pulse sequence under MAS at 35 kHz, this means that, with both pulses covering about 20 to 40% of the excitation time, the duration of RF application can no longer be simply neglected. In addition to this, in particular for fast MAS systems using coils of 2.5 mm inner diameter, the RF field applied to the whole sample is not perfectly homogeneous and, hence, the effective flip angle of the pulses is distributed over a certain range.

A pulse of phase ϕ applied during a time t_p acts on a state of longitudinal magnetization as

$$\begin{aligned}\hat{\boldsymbol{\rho}}(t_p) &= \exp(-i\omega_1 t_p \hat{\boldsymbol{I}}_\phi)\hat{\boldsymbol{I}}_z \exp(i\omega_1 t_p \hat{\boldsymbol{I}}_\phi) \\ &= \hat{\boldsymbol{I}}_{\phi-\frac{\pi}{2}} \sin(\omega_1 t_p) + \hat{\boldsymbol{I}}_z \cos(\omega_1 t_p), \qquad [99]\end{aligned}$$

where, as stated above, the product of the RF field strength, $\omega_1 = \gamma_I B_1$, and the pulse length, t_p, determines the flip angle, β, of the pulse. As a first approximation, the weight of the initial state $\hat{\boldsymbol{I}}_z$ and the final state $\hat{\boldsymbol{I}}_{\phi-\pi/2}$ during the pulse can be calculated by integrating the phase factors $\sin(\omega_1 t_p)$ and $\cos(\omega_1 t_p)$ over the interval $[0, t_p]$. For a flip angle of $\beta = \omega_1 t_p = \frac{\pi}{2}$, the average state of the system during RF application is therefore a superposition of $\hat{\boldsymbol{I}}_z$ and $\hat{\boldsymbol{I}}_{\phi-\pi/2}$ with equal weight. This superposition $\hat{\boldsymbol{I}}_{\phi-\pi/2} + \hat{\boldsymbol{I}}_z$ affects, in principle, both the chemical shift and the dipolar term of the excitation Hamiltonian (see Eqs. [95] and [97]). From an experimental point of view, however, the effect on the latter is more important, because the dipolar term is responsible for the generation of DQCs. Since this term does not act on longitudinal magnetization, the excitation efficiency decreases when the pulse lengths increase. In contrast to this loss in efficiency, the pulse-length effect on the chemical shift term turns out to be rather advantageous, because any contribution of longitudinal magnetization reduces the evolution due to frequency offsets. If, for example, 30% of the excitation time is covered by RF pulses, a reduction of about 15% of the offset-induced dephasing can be estimated using this simple approach.

In addition, finite pulse-lengths effects not only cause a decrease in the DQ signal intensity, but also affect the phases of the signals observed in the spectrum. The origin of such phase distortions is obvious from the discussion of the phase $\Omega_D^{(ij)}(0, \tau)$ (see Section 3.2.4), which arises from the integration of the rotor-modulated spatial part over the excitation interval $[0, \tau]$ (see Eq. [82]). If the condition $\tau = \tau_R/2$ which ensures the simplification of the orientational dependence to a mere sign change (see Section 3.2.5 and Eq. [84]) is not fulfilled, the phase behavior of the signals in the spectrum is complicated such that the observation of purely absorptive resonance lines is no longer possible. Since finite pulse lengths give rise to such timing problems in the pulse sequence, it is clear that they finally lead to phase distortions.

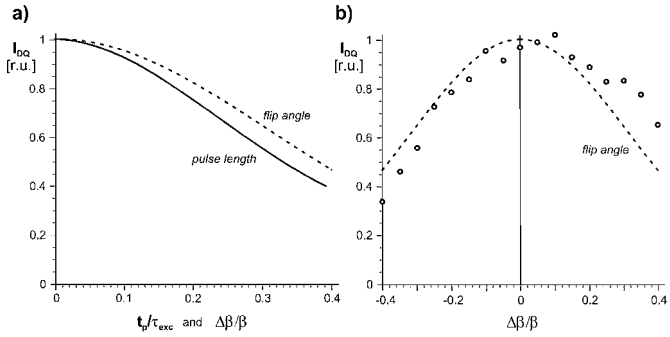

FIG. 17. (a) Calculated spin-pair DQ excitation efficiencies for two experimental imperfections: pulse lengths $t_p > 0$ (solid line) and pulse flip-angle deviations $\Delta\beta$ from the ideal value of $\beta = 90°$ (dotted line). (b) Comparison of calculated and experimental data, obtained using tribromoacetic acid, for flip-angle misadjustments.

Moreover, the DQ excitation efficiency also decreases with increasing deviations from the ideal flip angle of 90°. The latter imperfection typically arises from experimental misadjustments and B_1 inhomogeneities. Its effect on the DQ excitation efficiency, i.e., unwanted creation of SQCs, is obvious from Eqs. [75] and [76]. Figure 17 shows the loss of DQ signal which is caused either by the pulses being of finite length t_p during the excitation time τ_{exc} or by the flip angle deviating from its ideal value $\beta = 90°$ by $\frac{\Delta\beta}{\beta}$. It should be noted that the effects of pulse lengths of $t_p < 0.1\tau_{exc}$ and flip-angle deviations of $|\Delta\beta| < 10°$ on the DQ signal intensity can usually be safely neglected.

3.3. Excitation of Higher-Order Coherences

Double-quantum coherences play the major role in the investigation of dipolar-coupled multispin systems, because they embody the fundamental pair character of the dipolar interaction. They are the spectroscopically accessible equivalent of two-spin correlations, which predominate under fast MAS conditions in the network of dipolar couplings. Although, in the context of ^{1}H spectra under fast MAS, dipolar correlations of more than two spins are usually unwanted, since they give rise to line broadening and, hence, to a loss of spectral resolution, we will discuss the excitation schemes and the spectra observed for such higher-order coherences in this section for reasons of completeness and because there are special situations and certain problems where such coherences provide unique and valuable information.

3.3.1. Higher Spin Correlations

Considering the spin correlations emerging from a state of transverse magnetization through the action of dipolar couplings, as is shown in Eq. [68], correlations of more than two spins are encountered in the second term of the series expansion which describes the evolution of a multispin system. The terms correlating three spins are weighted by the squared product of time t and dipolar coupling strength, with the coupling strength $D^{(ij)}$ being hidden as a scaling part in the coefficients.

The t^2-term in Eq. [68] takes the form

$$\sum_{i=1}^{N} b^{(i)}\hat{\boldsymbol{I}}_x^{(i)} + i\sum_{\substack{i<j\\k\neq i,j}}^{N} c^{(ijk)}\big(\hat{\boldsymbol{T}}_{2,1}^{(ik)} - \hat{\boldsymbol{T}}_{2,-1}^{(ik)}\big)\cdot\hat{\boldsymbol{I}}_z^{(j)} + i\sum_{\substack{i<j\\k\neq i,j}}^{N} d^{(ijk)}\hat{\boldsymbol{I}}_x^{(i)}\hat{\boldsymbol{I}}_z^{(j)}\hat{\boldsymbol{I}}_z^{(k)} + i\sum_{\substack{i<j\\k\neq i,j}}^{N} d^{(ijk)}\big(\hat{\boldsymbol{I}}_+^{(i)}\hat{\boldsymbol{I}}_-^{(k)} - \hat{\boldsymbol{I}}_-^{(i)}\hat{\boldsymbol{I}}_+^{(k)}\big)\cdot\hat{\boldsymbol{I}}_y^{(j)}, \qquad [100]$$

which can be understood as follows: The first term $\propto\hat{\boldsymbol{I}}_x^{(i)}$ arises from the oscillation of a coupled spinpair (ij) between the states $(\hat{\boldsymbol{I}}_x^{(i)} + \hat{\boldsymbol{I}}_x^{(j)})$ and $(\hat{\boldsymbol{T}}_{2,1}^{(ij)} - \hat{\boldsymbol{T}}_{2,-1}^{(ij)})$, as is described by Eq. [67]. Hence, this term results from the partial evolution of a two-spin correlation back to a single-spin state. In contrast to this, all the other terms in Eq. [100] correlate three spins (ijk) in three-spin single-quantum coherences, where the products of the three spin operators $\hat{\boldsymbol{I}}_q^{(i,j,k)}$ differ with respect to their resulting magnetic quantum number by $\Delta M = \pm 1$. Such three-spin terms can be written in the form of two different combinations of ladder operators $\hat{\boldsymbol{I}}_\pm^{(i,j,k)}$ and longitudinal components $\hat{\boldsymbol{I}}_z^{(i,j,k)}$:

$$\hat{\boldsymbol{I}}_+^{(i)}\hat{\boldsymbol{I}}_z^{(j)}\hat{\boldsymbol{I}}_z^{(k)} \leftrightarrow \hat{\boldsymbol{I}}_-^{(i)}\hat{\boldsymbol{I}}_z^{(j)}\hat{\boldsymbol{I}}_z^{(k)} \qquad [101]$$

and

$$\hat{\boldsymbol{I}}_+^{(i)}\hat{\boldsymbol{I}}_+^{(j)}\hat{\boldsymbol{I}}_-^{(k)} \leftrightarrow \hat{\boldsymbol{I}}_-^{(i)}\hat{\boldsymbol{I}}_-^{(j)}\hat{\boldsymbol{I}}_+^{(k)}. \qquad [102]$$

In Eq. [100], the terms $(\hat{\boldsymbol{T}}_{2,1}^{(ik)} - \hat{\boldsymbol{T}}_{2,-1}^{(ik)})\cdot\hat{\boldsymbol{I}}_z^{(j)}$ and $\hat{\boldsymbol{I}}_x^{(i)}\hat{\boldsymbol{I}}_z^{(j)}\hat{\boldsymbol{I}}_z^{(k)}$ correspond to the former case, where only one of the three spins inverts its polarization within the coherence. The term $(\hat{\boldsymbol{I}}_+^{(i)}\hat{\boldsymbol{I}}_-^{(k)} - \hat{\boldsymbol{I}}_-^{(i)}\hat{\boldsymbol{I}}_+^{(k)})\cdot\hat{\boldsymbol{I}}_y^{(j)}$ corresponds to the latter case, where the inversion of polarization of one spin is combined with a flip-flop behavior of the other two spins. The indices i, j, and k are chosen such that a third spin k interacts with the two-spin correlation between the spins i and j, which has been generated before. The presence of the term $\hat{\boldsymbol{I}}_x^{(i)}\hat{\boldsymbol{I}}_z^{(j)}\hat{\boldsymbol{I}}_z^{(k)}$ is due to this special symmetric assignment.

A RF pulse can convert these three-spin correlations into triple-quantum coherences (TQCs) (*31*). Usually, this problem cannot be handled easily using analytical formulae, because the three pair couplings $\hat{\boldsymbol{H}}_D^{(ij)}$, $\hat{\boldsymbol{H}}_D^{(ik)}$, and $\hat{\boldsymbol{H}}_D^{(jk)}$, acting between the three involved spins, are of different strength due to different internuclear distances or different orientations of the internuclear vectors relative to the static magnetic field. The spin parts $\hat{\boldsymbol{T}}_{2,0}^{(ij)}$, $\hat{\boldsymbol{T}}_{2,0}^{(ik)}$, and $\hat{\boldsymbol{T}}_{2,0}^{(jk)}$ of the Hamiltonians are hence scaled by different spatial parts $\Omega_D^{(ij)}$, $\Omega_D^{(ik)}$, and $\Omega_D^{(jk)}$. Consequently, the spatial and spin parts, except for one special case discussed below, cannot be completely separated, and the three pair-related tensor operators cannot be merged to an effective operator of a "resulting" spin $I = \frac{3}{2}$. Generally speaking, an arbitrary three-spin system cannot be represented by tensor operators $\hat{\boldsymbol{T}}_{3,m}$ of rank 3. The same problem, i.e., the inequivalence of the spatial parts, occurs also for all higher spin correlations in dipolar-coupled multispin systems.

3.3.2. Methyl–Spin-$\frac{3}{2}$ Analogy

A methyl group, rotating fast about its threefold symmetry axis, represents the only frequently encountered ^{1}H spin system, whose particular symmetry properties make all internal proton–proton couplings equivalent, such that the three distinct spins $\hat{\boldsymbol{I}}^{(i)} = \frac{1}{2}$ can formally be replaced by an effective spin $\hat{\boldsymbol{I}} = \sum_i \hat{\boldsymbol{I}}^{(i)}$ (see Eq. [103]) (*37, 38*). The fast uniaxial rotation reduces the three dipolar coupling tensors to a single axially symmetric tensor, whose effective dipolar coupling strength is reduced by a factor of $\frac{1}{2}$, because for fast rotations the original coupling strength is scaled by a factor of $\frac{1}{2}(3\cos^2\theta - 1)$, with θ denoting the angle between the rotation axis and the internuclear vector, i.e., $\theta = 90^\circ$ for a methyl group (*1, 100)*. Therefore, the intramethyl dipolar couplings can be simplified as follows (*37*),

$$\hat{\boldsymbol{H}}_D = \sum_{i<j}^{3}\hat{\boldsymbol{H}}_D^{(ij)} = \sum_{i<j}^{3}\Omega_D^{(ij)}\hat{\boldsymbol{T}}_{2,0}^{(ij)} = \Omega_D\sum_{i<j}^{3}\hat{\boldsymbol{T}}_{2,0}^{(ij)},$$

since the spatial parts are equivalent, i.e., $\Omega_D^{(ij)} = \Omega_D$ for all i, j. From Eq. [24], it follows that

$$\begin{aligned}\hat{\boldsymbol{H}}_D &= \frac{\Omega_D}{\sqrt{6}}\sum_{i<j}^{3}\big(2\hat{\boldsymbol{I}}_z^{(i)}\hat{\boldsymbol{I}}_z^{(j)} - \hat{\boldsymbol{I}}_x^{(i)}\hat{\boldsymbol{I}}_x^{(j)} - \hat{\boldsymbol{I}}_y^{(i)}\hat{\boldsymbol{I}}_y^{(j)}\big)\\ &= \frac{\Omega_D}{\sqrt{6}}\cdot\frac{1}{2}\Bigg(2\sum_{i=1}^{3}\hat{\boldsymbol{I}}_z^{(i)}\cdot\sum_{i=1}^{3}\hat{\boldsymbol{I}}_z^{(i)} - \sum_{i=1}^{3}\hat{\boldsymbol{I}}_x^{(i)}\cdot\sum_{i=1}^{3}\hat{\boldsymbol{I}}_x^{(i)} - \sum_{i=1}^{3}\hat{\boldsymbol{I}}_y^{(i)}\cdot\sum_{i=1}^{3}\hat{\boldsymbol{I}}_y^{(i)}\Bigg),\end{aligned} \qquad [103]$$

since $\hat{\boldsymbol{I}}_q^{(i)}\hat{\boldsymbol{I}}_q^{(i)} = \frac{1}{4}$ due to the normalization of spin-$\frac{1}{2}$ operators, which means that

$$\sum_{i<j}^{3}\hat{\boldsymbol{I}}_q^{(i)}\hat{\boldsymbol{I}}_q^{(j)} = \frac{1}{2}\sum_{i=1}^{3}\hat{\boldsymbol{I}}_q^{(i)}\cdot\sum_{i=1}^{3}\hat{\boldsymbol{I}}_q^{(i)} - \frac{3}{4}, \qquad [104]$$

where $q = x, y, z$. In the N-spin system, the effective spin operator $\hat{\boldsymbol{I}}$ is defined by the sum $\hat{\boldsymbol{I}} = \sum_{i=1}^{N}\hat{\boldsymbol{I}}^{(i)}$ and, hence, the sum of the components $\hat{\boldsymbol{I}}_q^{(i)}$ in Eq. [103] can be considered effective

spin operators as well. Consequently, the tensor operators $\hat{\boldsymbol{T}}_{2,0}^{(ij)}$, $\hat{\boldsymbol{T}}_{2,0}^{(ik)}$, and $\hat{\boldsymbol{T}}_{2,0}^{(jk)}$ of the three spin pairs can be replaced by a single spin-$\frac{3}{2}$ operator $\hat{\boldsymbol{T}}_{2,0}$:

$$\hat{\boldsymbol{H}}_D = \frac{\Omega_D}{\sqrt{6}} \cdot \frac{1}{2}(2\hat{I}_z\hat{I}_z - \hat{I}_x\hat{I}_x - \hat{I}_y\hat{I}_y) = \frac{1}{2} \cdot \Omega_D \hat{\boldsymbol{T}}_{2,0}. \quad [105]$$

It is important to note that replacing the sum of single-spin operators by an effective-spin operator introduces an additional factor of $\frac{1}{2}$, which takes into account the double weight of the mixed products $\hat{\boldsymbol{I}}_q^{(i)}\hat{\boldsymbol{I}}_q^{(j)}$ with $i \neq j$ in the product of the sums $\sum_{i=1}^{N} \hat{\boldsymbol{I}}_q^{(i)} \cdot \sum_{i=1}^{N} \hat{\boldsymbol{I}}_q^{(i)}$. The dipolar Hamiltonian in Eq. [105] is formally analogous to that of a first-order quadrupolar interaction of a spin $I > \frac{1}{2}$ nucleus (see discussion following Eq. [18]). This means that the dipolar ^{1}H system of a methyl group is formally identical to a quadrupolar nucleus with spin $I = \frac{3}{2}$. This analogy strongly suggests the use of quadrupolar systems as models for such a small and highly symmetric ^{1}H system. It should be noted, however, that similarly symmetric systems with more than three spins and equivalent couplings do not exist. The only spin system with more than three spins, which fulfills the symmetry requirements, is represented by four spins being placed at the vertices of a tetrahedron, e.g., the protons in methane, CH_4. In this nonplanar case, however, the symmetrization of the coupling tensors with respect to their orientations relative to the static magnetic field requires a fast *isotropic* motion, which inevitably removes all dipolar interactions.

3.3.3. Double- and Triple-Quantum Coherences in Methyl Groups

The application of a pulse sequence 90°_y–τ–$90^\circ_{-y,-x}$ to the three dipolar-coupled protons of a fast rotating methyl group creates the following states (*16*):

$$\hat{\boldsymbol{\rho}}(0) \propto \hat{\boldsymbol{I}}_z = \sum_{i=1}^{3} \hat{\boldsymbol{I}}_z^{(i)} = \hat{\boldsymbol{T}}_{1,0}$$

$$\xrightarrow{90^\circ_y} \hat{\boldsymbol{I}}_x = \sum_{i=1}^{3} \hat{\boldsymbol{I}}_x^{(i)} = \frac{1}{\sqrt{2}}(\hat{\boldsymbol{T}}_{1,-1} - \hat{\boldsymbol{T}}_{1,1})$$

$$\int_0^\tau \hat{\boldsymbol{H}}_D(t)\,dt \longrightarrow \begin{pmatrix} -\frac{1}{5\sqrt{2}}(\hat{\boldsymbol{T}}_{1,1} - \hat{\boldsymbol{T}}_{1,-1})[3\cos(\Omega_D(0,\tau)) + 2] \\ +\frac{i}{2}(\hat{\boldsymbol{T}}_{2,1} + \hat{\boldsymbol{T}}_{2,-1})\sin(\Omega_D(0,\tau)) \\ -\frac{2}{\sqrt{30}}(\hat{\boldsymbol{T}}_{3,1} - \hat{\boldsymbol{T}}_{3,-1})[\cos(\Omega_D(0,\tau)) - 1] \end{pmatrix}$$

either

$$\xrightarrow{90^\circ_{-y}} \begin{pmatrix} -\frac{1}{5\sqrt{2}}\hat{\boldsymbol{T}}_{1,0}[3\cos(\Omega_D(0,\tau)) + 2] + \frac{i}{2}(\hat{\boldsymbol{T}}_{2,2} \\ -\hat{\boldsymbol{T}}_{2,-2})\sin(\Omega_D(0,\tau)) - \frac{1}{2\sqrt{15}}[\sqrt{3}\hat{\boldsymbol{T}}_{3,0} \\ +\sqrt{5}(\hat{\boldsymbol{T}}_{3,2} + \hat{\boldsymbol{T}}_{3,-2})][\cos(\Omega_D(0,\tau)) - 1] \end{pmatrix}$$

or

$$\xrightarrow{90^\circ_{-x}} \begin{pmatrix} -\frac{1}{5\sqrt{2}}(\hat{\boldsymbol{T}}_{1,1} - \hat{\boldsymbol{T}}_{1,-1})[3\cos(\Omega_D(0,\tau)) + 2] \\ -\frac{i}{2}(\hat{\boldsymbol{T}}_{2,1} + \hat{\boldsymbol{T}}_{2,-1})\sin(\Omega_D(0,\tau)) \\ +\frac{1}{2\sqrt{2}}\left[\frac{1}{\sqrt{15}}(\hat{\boldsymbol{T}}_{3,1} - \hat{\boldsymbol{T}}_{3,-1}) + (\hat{\boldsymbol{T}}_{3,3} - \hat{\boldsymbol{T}}_{3,-3})\right] \\ \times [\cos(\Omega_D(0,\tau)) - 1] \end{pmatrix}. \quad [106]$$

After the first pulse, the dipolar interaction $\hat{\boldsymbol{H}}_D$ correlates one, two, and three spins generating one-, two-, and three-spin SQCs, as can be seen from the ranks $l = 1, 2, 3$ and the orders $m = \pm 1$ of the tensor operators $\hat{\boldsymbol{T}}_{l,m}$. The contributions of the single-spin states and two- and three-spin correlations are weighted by $[3\cos(\Omega_D(0,\tau)) + 2]$, $\sin(\Omega_D(0,\tau))$, and $[\cos(\Omega_D(0,\tau)) - 1]$, respectively. In the limit of short excitation times τ, the leading terms of the series expansions are given by $[5 - 3\Omega_D^2(0,\tau) \pm \cdots]$, $[\Omega_D(0,\tau) \pm \cdots]$, and $[-\Omega_D^2(0,\tau) \pm \cdots]$, respectively. Hence, the contribution of the single-spin states decreases with $\Omega_D^2(0,\tau)$, while the contributions of the two- and three-spin correlations increase linearly and quadratically with respect to $\Omega_D(0,\tau)$, respectively. Since this approximation assumes $\Omega_D(0,\tau) \ll 1$, correlations of three spins, being proportional to $\Omega_D^2(0,\tau)$, are created to a much smaller extent than those of two spins, which depend only linearly on $\Omega_D(0,\tau)$.

A further pulse with the same or inverted phase, 90°_y–τ–$90^\circ_{\pm y}$ in Eq. [106], creates even-order coherences only, i.e., longitudinal single-spin states ($\hat{\boldsymbol{T}}_{1,0}$) and three-spin ZQCs ($\hat{\boldsymbol{T}}_{3,0}$) as well as two- and three-spin DQCs ($\hat{\boldsymbol{T}}_{2,\pm 2}$ and $\hat{\boldsymbol{T}}_{3,\pm 2}$). Therefore, the DQCs of a methyl group consist of two- and three-spin contributions with different weights, corresponding to the different phase factors $\frac{i}{2}\sin(\Omega_D(0,\tau))$ and $-\frac{1}{2\sqrt{3}}[\cos(\Omega_D(0,\tau)) - 1]$, respectively. Recall that the experimental selection of coherences by pulse phases is sensitive only to the coherence order, not to the number of correlated spins. In this context, however, it should be noted that, by application of 54.7° pulses instead of 90° pulses to a state consisting of $\hat{\boldsymbol{T}}_{2,\pm 1}$ and $\hat{\boldsymbol{T}}_{3,\pm 1}$ contributions, the latter, i.e., the rank 3 terms, are suppressed, while the rank 2 terms are preserved, though reduced by a factor of 0.8 (*64*). The DQ signal intensity of two- and three-spin contributions, excited and reconverted by a pulse sequence $(x\text{–}\bar{x})_{exc}(y\text{–}\bar{y})_{rec}$, is finally given by

$$I_{DQ}^{CH_3} \propto \overbrace{\left[\sin\left(\Omega_D\left(0, \frac{\tau_R}{2}\right)\right)\right]^2}^{\text{two-spin}} - \overbrace{\frac{1}{4}\left[\cos\left(\Omega_D\left(0, \frac{\tau_R}{2}\right)\right) - 1\right]^2}^{\text{three-spin}}$$

$$\approx \Omega_D^2\left(0, \frac{\tau_R}{2}\right) + \cdots - \frac{1}{4}\Omega_D^4\left(0, \frac{\tau_R}{2}\right) - \cdots. \quad [107]$$

Note that two- and three-spin terms have different signs. In the short-excitation-time limit, the DQ signal of a methyl group is dominated by two-spin DQCs, since the three-spin DQCs are

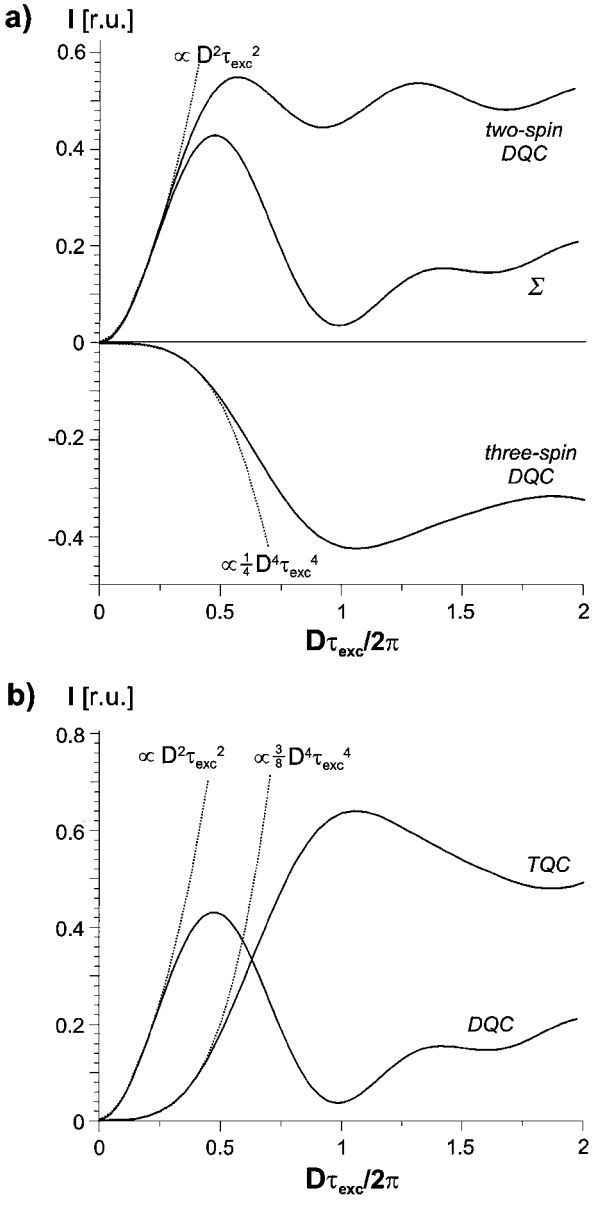

FIG. 18. Calculated DQ and TQ buildup curves for the protons of a methyl group: (a) Two- and three-spin contributions to the DQ signal (b) comparison of DQ and TQ signal. From two- and three-spin correlations, coherences are created following an initial intensity increase of the form $I \propto \Omega_D^2\tau^2$ (two-spin DQC) and $I \propto \Omega_D^4\tau^4$ (three-spin DQC and TQC), respectively. The intensities of three-spin DQC and TQC differ by a factor of $\frac{1}{4} : \frac{3}{8} = \frac{2}{3}$ (see Eqs. [107] and [108].

discriminated in a twofold manner: first by the coefficient $\frac{1}{4}$ resulting from the tensor algebra, and second, recalling the assumption $\Omega_D(0, \tau) \ll 1$ for the series expansion, by the fact that their leading term is $\Omega_D^4\tau^4$ compared to $\Omega_D^2\tau^2$ for the two-spin terms. In Fig. 18a, the DQ buildup curves are displayed separately for the two- and three-spin DQCs. As is expected, the two-spin curve is identical to that of a spin pair (see Fig. 14). During the initial increase, the three-spin contributions are so weak that they do not noticeably perturb the dominating spin-pair character of the methyl DQ signal. For $D\tau_{exc}/2\pi > 0.5$, however, the three-spin coherences form, reducing the resulting DQ signal intensity considerably (note the opposite sign in Eq. [107]).

In contrast to the DQC case, the excitation of TQCs requires a phase shift of $\pm\frac{\pi}{2}$ between the two pulses, as is shown for the sequence 90°_y–τ–90°_{-x} in Eq. [106]. In this case, only odd-order coherences are created. The TQC, i.e., the term $(\hat{\boldsymbol{T}}_{3,3} - \hat{\boldsymbol{T}}_{3,-3})$, is weighted by $[\cos(\Omega_D(0, \tau)) - 1]$ and, after the reconversion, the TQ signal intensity is given by

$$\begin{aligned} I_{TQ}^{CH_3} &\propto \frac{3}{8}[\cos(\Omega_D(0, \tau)) - 1]^2 \\ &\approx \frac{3}{8} \cdot \Omega_D^4(0, \tau) \pm \cdots \\ &\propto \frac{3}{8} \cdot D^4\tau^4. \end{aligned} \qquad [108]$$

In comparison to the DQ signal intensity $I_{DQ}^{CH_3}$ (displayed in Fig. 18b), the TQ buildup is "delayed," and the maximum intensity of $I_{TQ}^{CH_3}$ is reached at about twice the excitation time. This is due to the fact that the TQ signal intensity depends on the fourth-power $D^4\tau^4$, as is also the case for three-spin DQCs, with both three-spin DQCs and TQCs being created via three-spin correlations.

3.3.4. Pulse Phases and Dipolar Recoupling for TQ Excitation

In order to design a pulse sequence for reconverting TQCs, more attention has to be paid to the choice of pulse phases than in the DQC case. The phase sensitivity of the spin part of a DQC, represented by tensor components $\hat{\boldsymbol{T}}_{l,\pm2}$, to a phase shift ϕ can be described by a factor of $\exp(2i\phi)$, and usual pulse-phase shifts of $\phi = n \cdot \frac{\pi}{2}$, where $n = 0, 1, 2, \ldots$, merely give rise to a multiplication by a factor of $(-1)^n$, i.e., a sign inversion of the state or the excitation Hamiltonian. In the same way, the sign of the integrated spatial part $\Omega_D(t_1, t_2)$ of the dipolar interaction is inverted when shifting the rotor phase from the interval $(t_1 = 0, t_2 = \tau_R/2)$ to $(t_1 = \tau_R/2, t_2 = \tau_R)$, as can be seen from Eq. [85]. In the case of DQCs, therefore, both the spatial and the spin part phase sensitivity only affect the sign of the state of longitudinal magnetization created after the reconversion, but the actual reconversion procedure is not impaired at all. This indifference to sign inversion can be demonstrated by considering, as an analogous case, the effect of pulses on states of transverse magnetization: A $\pm y$ pulse always transforms a state $\hat{\boldsymbol{\rho}} \propto \pm\hat{\boldsymbol{I}}_x$ into longitudinal magnetization $\pm\hat{\boldsymbol{I}}_z$, with the signs of the pulse phase and the state $\hat{\boldsymbol{\rho}}$ merely determining the sign of the resulting state, but not whether transverse magnetization is transformed to longitudinal magnetization or not. In contrast to this, a phase shift of the pulse or of the initial state $\hat{\boldsymbol{\rho}}$ by $\pm\frac{\pi}{2}$ foils the effect of the pulse, because a pulse with phase $\pm q$ does not act on transverse magnetization of the same phase, i.e., on $\hat{\boldsymbol{\rho}} \propto \pm\hat{\boldsymbol{I}}_q$.

In the case of TQCs, we have to deal with such a $\frac{\pi}{2}$ phase shift, since the usual pulse-phase shifts by $\phi = n \cdot \frac{\pi}{2}$, where $n = 0, 1, 2, \ldots$, give rise to phase factors of the form $\exp(3i\phi)$, corresponding to a multiplication by a factor of $(-i)^n$. Upon shifting the phase by $\phi = n \cdot \frac{\pi}{2}$ with odd-numbered n, the pulse no longer has an effect on the TQCs. Consequently, a TQC, after being generated out of a three-spin correlation by a pulse of phase $\pm q$, can be converted back to a three-spin correlation only by a pulse of the same or sign-inverted phase.

Therefore, in order to excite and reconvert TQCs, the two-pulse scheme needs to be of the form $(90^\circ_x\text{–}\tau\text{–}90^\circ_y)$ or $(90^\circ_y\text{–}\tau\text{–}90^\circ_x)$, and it has to be combined to $(90^\circ_x\text{–}\tau\text{–}90^\circ_y)_{exc}(90^\circ_y\text{–}\tau\text{–}90^\circ_x)_{rec}$ and $(90^\circ_y\text{–}\tau\text{–}90^\circ_x)_{exc}(90^\circ_x\text{–}\tau\text{–}90^\circ_y)_{rec}$, respectively, with the signs of the pulse phases still being optional. This two-pulse excitation scheme is limited to short excitation times, i.e., under MAS to $\tau \leq \tau_R/2$, as has already been discussed in Section 3.2.4. The signal intensity of TQCs, however, grows more slowly with time than that of DQCs in the same system (see Eq. [107]) and, hence, the extension of the excitation scheme to excitation times $\tau_{exc} > \tau_R/2$ by means of dipolar recoupling is essential for TQ spectroscopy.

To achieve dipolar recoupling, the time reversal induced by MAS has to be compensated by a counterrotation in spin space, as is provided by proper coordinate transformations $\hat{\boldsymbol{L}}_\phi \cdots \hat{\boldsymbol{L}}_\phi^+$ of the dipolar Hamiltonian $\hat{\boldsymbol{H}}_D$ (see Eq. [88]). However, the two-pulse segments of the TQ excitation scheme cannot be straightforwardly considered a simple coordinate transformation for $\hat{\boldsymbol{H}}_D$, because they take the form $\hat{\boldsymbol{L}}_{\phi+\frac{\pi}{2}} \hat{\boldsymbol{H}}_D \hat{\boldsymbol{L}}_\phi$. Furthermore, the effective TQ excitation Hamiltonian needs to contain tensor operators $\hat{\boldsymbol{T}}_{3,\pm3}$ of third rank and third order, which cannot be obtained from a simple coordinate transformation of a second-rank tensor $\hat{\boldsymbol{H}}_D \propto \hat{\boldsymbol{T}}_{2,0}$.

In fact, a pulse sequence applicable for long-time TQ excitation makes use of the same dipolar recoupling scheme used for DQ excitation, but transforms the initial state from longitudinal into transverse magnetization beforehand (*98, 30*). Using propagator notation, this TQ excitation scheme can be derived, starting from the two-pulse segment (y–x), as follows:

$$\begin{aligned}\hat{\boldsymbol{\rho}}_{TQ}\left(\frac{\tau_R}{2}\right) &\propto \hat{\boldsymbol{L}}_x \hat{\boldsymbol{L}}_D\left(0, \frac{\tau_R}{2}\right) \hat{\boldsymbol{L}}_y \hat{\boldsymbol{\rho}}(0) \cdots \\ &= \underbrace{\hat{\boldsymbol{L}}_x \hat{\boldsymbol{L}}_D\left(0, \frac{\tau_R}{2}\right) \hat{\boldsymbol{L}}_x^+}_{\text{two-pulse segment } x\text{–}\bar{x}} \hat{\boldsymbol{L}}_x \hat{\boldsymbol{L}}_y \hat{\boldsymbol{\rho}}(0) \cdots \end{aligned} \qquad [109]$$

The first propagator $\hat{\boldsymbol{L}}_y$ acting on the equilibrium magnetization $\hat{\boldsymbol{\rho}}(0)$ produces transverse magnetization of the form $\hat{\boldsymbol{\rho}}(0) \propto \hat{\boldsymbol{I}}_z \rightarrow \hat{\boldsymbol{I}}_x$, on which the following 90°_x pulse $\hat{\boldsymbol{L}}_x$ has no effect. Hence, it can be dropped in the experiment. The product $\hat{\boldsymbol{L}}_x^+ \hat{\boldsymbol{L}}_x = \hat{\mathbb{I}}$ has only formally been inserted to create a two-pulse segment x–$\bar{x}$ which can be interpreted as the familiar coordinate transformation for the dipolar Hamiltonian $\hat{\boldsymbol{H}}_D$, i.e., $\hat{\boldsymbol{L}}_x \hat{\boldsymbol{L}}_D(0, \tau_R/2) \hat{\boldsymbol{L}}_x^+ = \exp(-i \hat{\boldsymbol{L}}_x \hat{\boldsymbol{H}}_D \hat{\boldsymbol{L}}_x^+ \cdot (\tau_R/2)$. In this way, longer TQ excitation times are accomplished by the same dipolar recoupling procedure as is used for DQ excitation, i.e., an alternating sequence of two-pulse segments x–$\bar{x}$ and y–$\bar{y}$. Recoupling pulse sequences for TQ excitation are hence of the form $y[x\text{–}\bar{x}y\text{–}\bar{y}]_n$, where the signs of the pulse phases are again optional and usable for the compensation of frequency offsets or pulse imperfections.

3.4. Rotor-Synchronized MQ Spectra

In the previous sections, we have focused on the excitation of MQCs among dipolar-coupled spins. In this section, we now turn to the evolution of these coherences under MAS and under the internal interactions present in the spin system. It will be shown that the isotropic chemical shift combined with the line narrowing provided by fast MAS allows DQCs and TQCs of different spin pairs or triplets to be resolved in the spectra. To observe such MQ evolutions experimentally, a so-called MQ evolution period is inserted between excitation and reconversion (see Fig. 13a). In this way, the experiment correlates the evolution of the selected MQCs during the first spectral dimension (t_1) with the SQ signal detected during the final period (t_2).

In the following, we will discuss the features observed in and the information obtainable from such two-dimensional MQ spectra. In this section, however, only the line-narrowing effect of MAS will be considered, disregarding rotor modulations leading to MAS sideband patterns, which will be discussed in Section 3.5. Experimentally, such rotor modulations can be easily avoided by detecting the signal data points in both time dimensions t_1 and t_2 using increments of full rotor periods τ_R. The resulting two-dimensional spectral width is hence $\omega_R \cdot \omega_R$, and the observed spectrum, which will henceforth be referred to as a rotor-synchronized spectrum, formally corresponds to the integration over the whole MAS sideband pattern. In this context, it is noteworthy that the application of recoupling pulse sequences of the C_n type (*67, 57, 89*) for the excitation and reconversion of DQCs allows t_1 to be incremented in steps of τ_R/n and rotor-synchronized MQ spectra to be obtained with a spectral width of $n \cdot \omega_R$ in ω_1 (*58*).

3.4.1. MQCs under Internal Interactions

In a ^{1}H multispin system, the isotropic chemical shift and the dipolar interaction are the most important internal interactions experienced by MQCs. The evolution of a DQC between two spins i and j under the chemical shift results in a modulation of the form $\exp(i(\omega_{CS}^{(i)} + \omega_{CS}^{(j)})t)$ (see Eq. [74]). Higher-order coherences are modulated in an analogous manner, obeying the simple rule that the resonance frequency of a MQC is the sum of the resonance frequencies of all involved spins. This property forms the basis for the spectral identification of different MQCs in MQ spectroscopy.

The effect of the dipolar interaction on MQCs is a little more complex, because dipolar couplings can either be an internal part or an external perturbation of the MQC. Hence, considering a DQC in a three-spin system, two types of dipolar couplings have to be distinguished: first the mediating pair coupling between the spins i and j forming the coherence, and second the coupling to the third spin k. Using commutator notation, this means

$$\begin{aligned}\left[(\hat{\boldsymbol{T}}_{2,2}^{(ij)} \pm \hat{\boldsymbol{T}}_{2,-2}^{(ij)}), \hat{\boldsymbol{H}}_D^{(ik)}\right] &\propto \left[(\hat{\boldsymbol{T}}_{2,2}^{(ij)} \pm \hat{\boldsymbol{T}}_{2,-2}^{(ij)}), \hat{\boldsymbol{T}}_{2,0}^{(ik)}\right] \\ &\propto \begin{cases} 0 & \text{for } j = k \\ (\hat{\boldsymbol{T}}_{2,2}^{(ij)} \mp \hat{\boldsymbol{T}}_{2,-2}^{(ij)})\hat{\boldsymbol{I}}_z^{(k)} - \hat{\boldsymbol{I}}_z^{(i)}(\hat{\boldsymbol{T}}_{2,2}^{(jk)} \mp \hat{\boldsymbol{T}}_{2,-2}^{(jk)}) & \text{for } j \neq k \end{cases}. \end{aligned} \quad [110]$$

In the first case ($j = k$), it is clear that a DQC does not evolve under a dipolar coupling which is part of the coherence, since in a DQC the spin pair (ij) and the mediating coupling $D^{(ij)}$ behave as a single entity. However, any coupling to a spin outside the coherence gives rise to an evolution of the DQC during t_1 and, in this way, usually to a loss of signal, because the reconversion only reverses the effects of dipolar couplings, which have occurred during the excitation period τ_{exc}, but not any dipolar evolution thereafter. Coupling the spin k to the two-spin coherence (ij) produces a three-spin DQC $\propto[(\hat{\boldsymbol{T}}_{2,2}^{(ij)} \mp \hat{\boldsymbol{T}}_{2,-2}^{(ij)})\hat{\boldsymbol{I}}_z^{(k)} - \hat{\boldsymbol{I}}_z^{(i)}(\hat{\boldsymbol{T}}_{2,2}^{(jk)} \mp \hat{\boldsymbol{T}}_{2,-2}^{(jk)})]$, as can be seen from the commutator in Eq. [110]. This kind of evolution, by which higher spin correlations are generated without changing the coherence order, is characteristic for a dipolar-coupled multispin system, as is well known from the evolution of transverse magnetization (see Eqs. [68] and [100]).

Fast MAS reduces the dipolar interaction to an effective part $\hat{\boldsymbol{H}}_{D,\text{eff}}$ which, using Eq. [48], can be written as

$$\hat{\boldsymbol{H}}_{D,\text{eff}} = \sum_{\substack{m=-2 \\ m\neq 0}}^{2} \frac{[\hat{\boldsymbol{H}}_{-m}, \hat{\boldsymbol{H}}_m]}{2m\omega_R} + \sum_{\substack{m,p=-2 \\ m,p\neq 0}}^{2} \frac{[[\hat{\boldsymbol{H}}_{-m}, \hat{\boldsymbol{H}}_m], \hat{\boldsymbol{H}}_p]}{3mp\omega_R^2} + \cdots, \quad [111]$$

with the Fourier components $\hat{\boldsymbol{H}}_m$ including the sum over all pairs (ij): $\hat{\boldsymbol{H}}_m = \sum_{i<j} \hat{\boldsymbol{H}}_m^{(ij)}$. The commutator $[\hat{\boldsymbol{H}}_{-m}, \hat{\boldsymbol{H}}_m]$ in the leading term hence corresponds to a three-spin interaction (ijk), since the components $\hat{\boldsymbol{H}}_m$ commute for a single pair (ij) as well as for two pairs (ij) and (kl) consisting of four different spins: $[\hat{\boldsymbol{H}}_{-m}^{(ij)}, \hat{\boldsymbol{H}}_m^{(ij)}] = [\hat{\boldsymbol{H}}_{-m}^{(ij)}, \hat{\boldsymbol{H}}_m^{(kl)}] = 0$. Furthermore, this residual part of the interaction is scaled by a factor of ω_R^{-1}. In this way, MAS reduces the evolution of DQCs under dipolar couplings and narrows the resonance lines. This effect has already been discussed in detail in Section 2.6, the results of which, though obtained from SQC considerations, can be directly applied to DQCs, since they concern the dipolar Hamiltonian and not the state on which the Hamiltonian acts. However, in contrast to SQCs, every DQC is invariant with respect to its mediating coupling, which therefore needs to be excluded when considering the evolution of DQCs. This feature is of particular importance for the mechanisms which generate MAS sideband patterns. It is also important to note that, in a dipolar-coupled spin-$\frac{1}{2}$ system, MQCs rely on the presence of the mediating dipolar couplings for their excitation, but not at all for their conservation. Consequently, a DQC between the spins i and j persists even if the mediating coupling $\hat{\boldsymbol{H}}_D^{(ij)}$ is averaged to zero by MAS.

Although, with increasing coherence order, the number of couplings which are part of, but not acting on, the coherences increases as well, the signal decay usually does not become less and the linewidths are not reduced in the experimental spectra. On the contrary, the linewidth in general is found to increase with the coherence order. Empirically, in dense and strongly dipolar-coupled systems, the linewidths seem to be broadened almost proportionally to the coherence order. In Fig. 19, the ^{1}H SQ, DQ, and TQ spectrum of L-alanine under MAS at 35 kHz is displayed (*98*). The experimentally observed linewidths of the protonated amino group (NH_3^+) and of the methyl group (CH_3) are graphically compared with each other. The reason for this, at first sight, unexpected line broadening is that the sensitivity of MQCs to external perturbing couplings increases with the

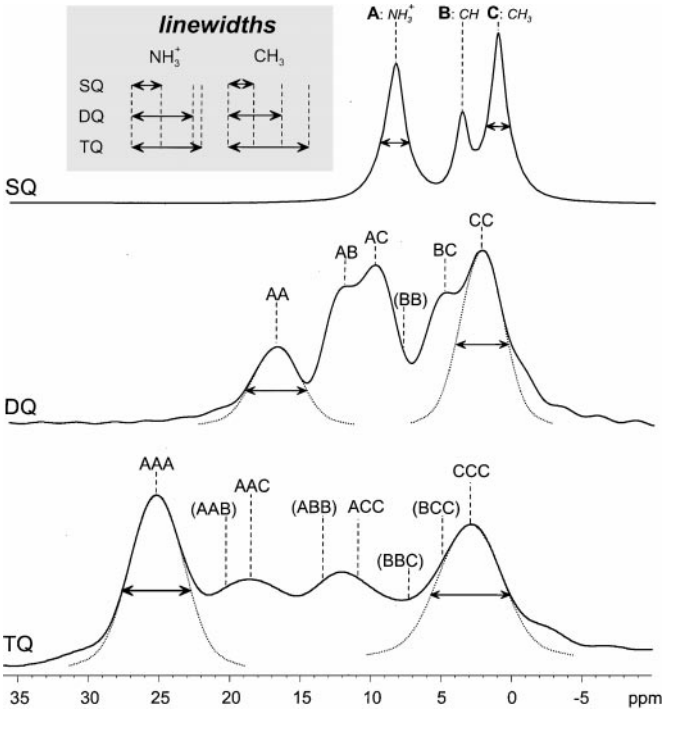

FIG. 19. Experimental ^{1}H SQ, DQ, and TQ spectra of L-alanine under MAS at $\omega_R/2\pi = 35$ kHz. The resonance lines are assigned to the spins involved in the respective coherence. The assignments in parentheses are based on the knowledge of the two-dimensional spectra, depicted in Fig. 20 . In the inset, the linewidths of the NH_3^+ and CH_3 resonances are graphically compared to each other. It can be seen that, due to the increased sensitivity of MQCs to perturbing interactions, the linewidths increase with the coherence order.

coherence order (*25, 38*): A MQC of order p evolves under a dipolar coupling to the pth power, as has been demonstrated by Friedrich *et al.* for a first-order quadrupolar MQC which is subject to heteronuclear dipolar couplings (*37*). Apart from this order effect on the propagation, the elevated sensitivity of dipolar MQCs is also due to the simple statistical fact that the higher the coherence order, the more spins are involved, providing more "points of attack" for external perturbing couplings.

In addition to the sensitivity problem, the spectral resolution achievable in MQ spectra suffers from the fact that the number of spin combinations forming a MQC and, consequently, the number of resonance lines also increases with the coherence order. For example, 2, 3, or 4 SQ resonances give rise to a maximum number of 3, 6, or 10 DQ and 4, 10, or 18 TQ signals, respectively. In the case of L-alanine, 3 ^{1}H SQ resonance lines are observed (see Fig. 19: NH_3^+ (**A**), CH (**B**), and CH_3 (**C**)). Since all interproton distances are relatively small, corresponding to a dense network of dipolar couplings, NMR signals of all 6 possible DQCs and 8 of 10 possible TQCs are detected, even though with different intensity. In the TQ spectrum, the signals **BBB** and **ABC** are missing because of the spatial separation of the involved nuclei. However, for a clear identification of all signals, the spectral resolution of the one-dimensional MQ spectra is usually not sufficient. Instead, the full assignment requires the spectra to be inspected in their full two-dimensional form.

3.4.2. The Two-Dimensional Form of MQ Spectra

In Fig. 20, rotor-synchronized DQ and TQ spectra are displayed in their typical two-dimensional form, correlating the MQ signal on the ω_1 frequency axis (t_1 dimension) with the SQ signal detected during t_2. The ω_1 axis is scaled by the order of the observed MQ coherence, yielding a diagonal which is the bisecting line of the angle between the SQ and the scaled MQ axis. The sample used for these example spectra is L-alanine, and the spectra were recorded applying MAS at 35 kHz and excitation times of $\tau_{exc} = \tau_R = 28.6\,\mu$s and $\tau_{exc} = 2\tau_R = 57.2\,\mu$s for DQCs and TQCs, respectively (*98*).

Considering first the DQ spectrum, it is clear that the two-dimensional correlation spectrum consists of two types of signal patterns (see also the schematic representation in Fig. 21): A DQC between two like spins **AA** gives rise to a single peak observed at the position $(2\omega_A, \omega_A)$ on the diagonal of the spectrum (the notation (ω_1, ω_2) refers to the ω_1 (DQ) and ω_2 (SQ) frequencies of the peak). A DQC between unlike spins **AB** also generates only one DQ signal along the ω_1 axis, but the signal is split into two resonance lines at ω_A and ω_B along the ω_2 axis. Therefore, a pair of peaks is observed in the DQ spectrum at the positions $(\omega_A + \omega_B, \omega_A)$ and $(\omega_A + \omega_B, \omega_B)$, i.e., symmetrically on either side of the diagonal. DQ signals of the former type (**AA**, **A**) are henceforth referred to as "diagonal peaks," while signal pairs (**AB**, **A**), (**AB**, **B**) of the latter type are termed "cross peaks."

At first sight, the solid-state DQ MAS experiment seems to yield spectra which are very similar to those obtained by the INADEQUATE experiment in solution- or liquid-state NMR, since both DQ MAS and INADEQUATE correlate a DQ with a SQ dimension. However, a noteworthy difference between DQ MAS and INADEQUATE spectra is the absence of diagonal peaks in the latter (*31*). This remarkable difference arises from the fact that, in the solid state, the homonuclear DQCs are generated using dipolar couplings, while the INADEQUATE approach makes use of J-couplings. *Isotropic* J-couplings, however, do not give rise to DQCs between indistinguishable nuclei, whereas in the solid-state DQ experiment the mediating dipolar interactions are inherently *anisotropic*, such that a coherence can be generated even between "indistinguishable" spins.

In the TQ spectrum, the situation is complicated by the need to distinguish three types of signal patterns (*38*), as are depicted in Fig. 21: In the simplest case, a TQC consists of three like

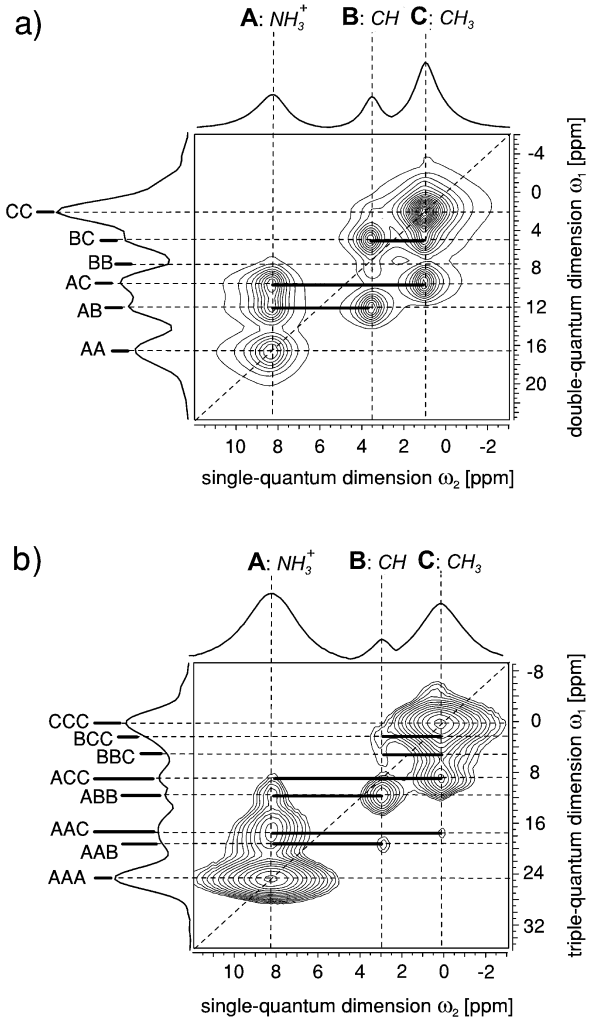

FIG. 20. Two-dimensional rotor-synchronized ^{1}H DQ spectrum (a) and TQ spectrum (b) of L-alanine at a ^{1}H Larmor frequency of 500 MHz and under MAS at $\omega_R/2\pi = 35$ kHz, correlating the MQ signals with the SQ signals. The ω_1 (MQ) axis is scaled by the coherence order such that the spectral widths in ω_1 are twice or three times as large as those in ω_2.

spins **AAA**, whose signal appears as a TQ diagonal peak at the position $(3\omega_A, \omega_A)$ in the spectrum. If two like spins are involved in a TQC (**AAB**), the TQ signal splits into a pair of cross peaks at the positions $(2\omega_A + \omega_B, \omega_A)$ and $(2\omega_A + \omega_B, \omega_B)$. In rare cases, a TQC may consist of three unlike spins **ABC**, whose TQ signal splits into three peaks at $(\omega_A+\omega_B+\omega_C, \omega_A)$, $(\omega_A+\omega_B+\omega_C, \omega_B)$, and $(\omega_A + \omega_B + \omega_C, \omega_C)$. The latter situation is not shown in Fig. 21. Note that TQ signals do not split symmetrically with respect to the diagonal.

For a MQ signal of unlike spins, the intensity distribution over the cross peaks corresponds, in the ideal case, to the number of involved spins. Thus, the two DQ cross peaks of an **AB** coherence are in principle of equal intensity, because both spins contribute to the coherence with equal weight. Therefore, DQ cross peaks are symmetric not only with respect to their positions relative to the diagonal, but also with respect to their intensity distribution. The same kind of symmetry—though only with respect to the intensity distribution, but not with respect to the positions—is also observed for a TQC of three unlike spins. TQCs of the **AAB** type, however, should show an asymmetric intensity ratio of 2 : 1 in favor of the **A** spins.

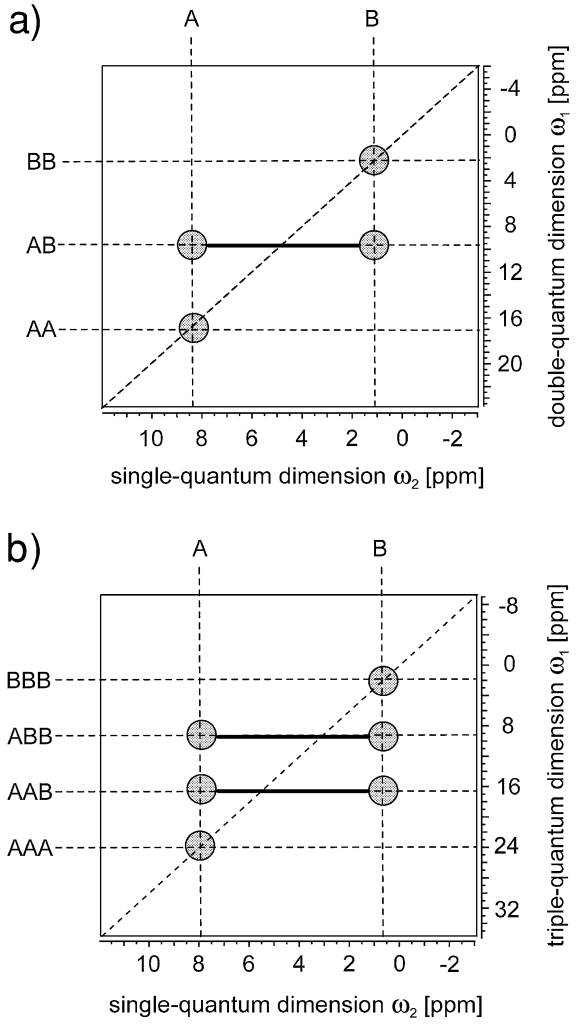

FIG. 21. Schematic representation of the typical patterns observed in two-dimensional rotor-synchronized DQ (a) and TQ (b) spectra. The DQ cross peaks are located symmetrically with respect to the diagonal, while the TQ diagonal intersects the splitting of TQ cross peaks along ω_2 at a ratio of 2 : 1 or 1 : 2, respectively.

The experimentally observed intensity distributions of DQ and TQ cross peaks may appear less symmetric than theoretically expected. For example, while in the DQ spectrum in Fig. 20a the cross-peak intensities are distributed symmetrically throughout, in the TQ spectrum in Fig. 20b the **C** peak of the **AAC** cross peak is considerably weaker than expected. Intensity distortions of this kind are in most cases due to experimental baseline problems around strong peaks, such as the **CCC** diagonal peak in Fig. 20b (*97*). These baseline problems are exacerbated by motional effects in the sample, for example, by the dynamics associated with long alkyl chains, since then, with increasing t_1, a continuous loss of coherence, i.e., relaxation, takes place, distributing the signal statistically along the ω_1 axis (so-called t_1 noise) (*65*). If an intense MQ signal suffers from such a kind of relaxation, another weaker MQ signal may even be lost in the noise.

3.4.3. Semi-quantitative Information

The information obtainable from rotor-synchronized two-dimensional MQ spectra is based on the intensities of the observed signals (*96*). For DQ spectra with short excitation times, the signal intensity, $I_{DQ}^{(ij)}$, of a DQC between the spins i and j is proportional to the squared product of the underlying dipolar coupling strength, $D^{(ij)}$, and the excitation time, τ_{exc} (see Eq. [84]). In the spectrum, the DQ signals are resolved with respect to the chemical shifts of the involved spins. Hence, all DQCs between spins i and j forming a pair of the type, say, **AB** contribute to the same pair of peaks at $(\omega_A + \omega_B, \omega_A)$ and $(\omega_A + \omega_B, \omega_B)$ in the spectrum. Therefore, as a first approximation valid for short excitation times, the detected DQ signal intensity I_{DQ}^{AB} is given by the sum over all DQ intensities $I_{DQ}^{(ij)}$ with $(ij) = \mathbf{AB}$:

$$I_{DQ}^{AB} = \sum_{\substack{i<j \\ (ij)=AB}} I_{DQ}^{(ij)} \propto \sum_{\substack{i<j \\ (ij)=AB}} \left(D^{(ij)}\tau_{exc}\right)^2$$

$$\propto \tau_{exc}^2 \cdot \sum_{\substack{i<j \\ (ij)=AB}} \frac{1}{r_{ij}^6} \propto \frac{\tau_{exc}^2}{r_{AB\,\mathrm{eff}}^6}. \qquad [112]$$

The sum over all pair distances r_{ij} suggests the definition of an effective distance $r_{AB\mathrm{eff}}$ between spin pairs of the type **AB**. The contribution of each real distance r_{ij} is weighted by the reciprocal sixth power, thereby ensuring a rapid convergence of the sum for increasing distances, as can be demonstrated as follows: Starting from a spin i, the number of potentially coupled spins j up to a maximum distance r_{ij} is limited by the spherical

volume $V \propto r_{ij}^3$. Consequently, when extending the distance range from r_{ij} to $r_{ij} + dr_{ij}$, the maximum statistical increase in the number of coupled pairs (ij) is proportional to $dV \propto r_{ij}^2 dr_{ij}$ which is, with respect to the distance, four orders of magnitude less than the DQ signal discrimination. Considering, e.g., two DQCs between spin pairs of the same type, but with different internuclear distances r and $r' = \frac{3}{2}r$, the DQ signal of the more weakly coupled pair contributes to the overall DQ signal by an amount of only 8%. In addition to the purely statistical argument, the volume around a spin is, in general, not close-packed with other spins due to the chemical structure of the molecules. Therefore, DQ signals are dominated by the nearest-neighbor pairs.

Since the excitation time τ_{exc} is fixed by the experiment, the intensity ratio $I_{DQ}^{AB} : I_{DQ}^{CD}$ of two DQ signals directly corresponds to the ratio $(r_{AB\text{eff}} : r_{CD\text{eff}})^{-6}$ of the two effective internuclear distances of pairs of the types **AB** and **CD**, respectively. The validity of this simple interpretation of the DQ signal intensities relies on the assumption that all pair couplings $D^{(ij)}$ fulfill the short-time condition $D^{(ij)}\tau_{exc}/2\pi \ll 1$, which means—in other words—that during the period τ_{exc} only two-spin correlations are created. As soon as there are higher spin correlations present to a noticeable extent, the pair-related DQ signals start to decay, and the intensities of different DQ signals can no longer be compared to each other in this simple manner.

Turning to typical experimental conditions for rigid ^{1}H systems, the strongest dipolar proton–proton coupling is at about $D^{(ij)} = 2\pi \cdot 20$ kHz (i.e., a rigid CH_2 group with an interproton distance of $r_{ij} = 0.18$ nm). The short-excitation-time limit is then given by $\tau_{exc} < 15\,\mu$s, corresponding to a two-pulse excitation scheme 90°_q–$\tau_R/2$–$90^\circ_{q'}$ for MAS frequencies of $\omega_R > 2\pi \cdot 30$ kHz. For longer excitation times, the DQ signal of the most strongly coupled protons usually decays relative to that of the more weakly coupled protons. Depending on the demand on the accuracy of the distances determined from the experiment, the simple pair-related interpretation of DQ signal intensities is still applicable for excitation times of up to $\tau_{exc} < 30\,\mu$s, since a deviation of the DQ signal intensity by 10% leads to an error of only 1.5% in the distance determination and can, in addition, easily be corrected for. Assuming that the weakest observable DQ signal should have an intensity of at least 1% of that of the strongest signal (which is often that of the CH_2 groups), the short-excitation-time approach with $\tau_{exc} < 30\,\mu$s allows DQ signals to be detected up to an effective interproton distance of about $r_{\text{eff}} < 0.4$ nm. Therefore, the mere existence of a DQ signal of the type **AB** contains the semi-quantitative information that the respective nuclei H_A and H_B have an effective distance $r_{\text{eff}} = \sum r_{ij}^{-6}$ of less than 0.4 nm.

3.4.4. Proton–Proton Distances from DQ Signal Intensities

In this section, we will proceed to a fully quantitative interpretation of the DQ signals in rotor-synchronized two-dimensional spectra and outline the experimental approaches to quantitative DQ spectroscopy. Relying on the spin-pair approximation, the relative intensities of DQ signals can be used to measure the effective distances between spectrally resolved spins in a quantitative manner, provided that one signal, arising from a dipolar coupling of known strength, can serve as a reference intensity. In the following we will distinguish between *internal* and *external reference* signals. An internal standard requires the sample to contain molecular units where, under MAS conditions, a proton pair of known distance or a methyl group is dipolar decoupled from other protons to such an extent that the observed DQ signal arises only from this spin pair or intramethyl coherence, respectively. In other words; the effective dipolar coupling underlying the DQ reference signal needs to consist of one pair coupling or one intramethyl coupling only. From an experimental point of view, this requirement is usually fulfilled to a satisfactory extent, if perturbing dipolar interactions are weaker than $\frac{1}{3}$ of the dominating coupling of interest or—in terms of distances—if the effective distance to perturbing protons is larger than about $\frac{3}{2}$ of the considered pair distance. In some cases, it may also be possible to use a signal arising from a known effective coupling instead of a pure spin pair or methyl signal. Nevertheless, for unknown samples it is often hard to estimate whether there are DQ signals which originate from molecular units fulfilling the structural requirements and which therefore are suitable as internal standards.

As an alternative approach, the sample can be measured together with a compound, e.g., tribromoacetic acid, which contains an isolated proton pair and whose DQ signal can serve as an external intensity reference. Since this approach is based on the presence of an additional peak in the spectrum, care has to be taken to avoid overlapping with the sample signals. When using tribromoacetic acid as a standard, the protons are part of hydrogen bonds and, hence, their resonance frequency is shifted to 12.3 ppm, which is well outside of the typical ^{1}H frequency range of 0 . . . 10 ppm. This marked low-field shift is achieved at the expense of a strong acidity of the compound, which usually makes it impossible to mix the standard with the sample and hence requires them to be packed in separate parts of the MAS rotor.

Apart from the problem of DQ intensity calibration, the relaxation of two-spin correlations during the excitation period needs also to be considered. Although, for short excitation times, the DQ signal is built up according to $I_{DQ}^{(ij)} \propto (D^{(ij)}\tau_{exc})^2$, decay processes are known to come into play before the DQ buildup curve reaches its oscillatory regime (see Fig. 14a). As has been discussed in Section 3.2.6, these decay processes are due to experimental imperfections and, far more importantly, due to perturbing dipolar interactions of the considered pair (ij) with surrounding spins. From the latter reason it is obvious that the excitation time, after which such decays set in, represents the time scale on which three-spin contributions start to perturb the two-spin approximation. The importance of such perturbations is demonstrated by the fact that they are clearly observed even for the spin-pair model compound tribromoacetic acid (see

Fig. 14b). Since the extent of perturbing couplings strongly depends on the local arrangement of the spins, different DQCs are subject to different perturbations and, therefore, in general no uniform DQ decay process is observed.

Experimentally, DQ buildup curves including the DQ decay are obtained from a series of two-dimensional rotor-synchronized spectra with increasing excitation time $\tau_{exc} = n \cdot (\tau_R/2)$ where $n = 1, 2, 3, \ldots$. The DQ signal intensities of all spectrally resolved peaks are evaluated by integration and then plotted as a function of τ_{exc}. Strong dipolar couplings give rise to pronounced DQ decay effects and hence require MAS to be applied at high spinning frequencies, such that, on the other hand, great demands are made on the performance of the recoupling pulse sequence. As a consequence of these complications, DQ buildup measurements have to date only been successfully carried out on systems where the dipolar couplings are considerably weaker than in dense and rigid ^{1}H systems, e.g., in mobile polymer melts (*49, 50*) or in liquid-crystalline phases (*66*) or, alternatively, in nonproton systems with weaker homonuclear dipolar couplings, e.g., ^{31}P–^{31}P in crystalline phosphates (*96*) or thiophosphates (*6*). In all these examples, the experimental DQ buildup curves $I_{DQ}^{(ij)}(\tau_{exc})$ have been fitted by a semi-empirical function, which combines the initial squared signal increase from theory with an empirical exponential decay,

$$I_{DQ}^{(ij)}(\tau_{exc}) = A \cdot \left(D^{(ij)}\tau_{exc}\right)^2 \cdot \exp\left(-\frac{\tau_{exc}}{\tau}\right), \qquad [113]$$

where A contains several constants and is fixed for a series of experiments. In this way, the relative strengths of dipolar couplings are straightforwardly accessible and, furthermore, the decay time τ, which represents the effective relaxation time of the two-spin correlations during the DQ excitation, can be determined. Combining these two parameters, DQ buildup curves provide information about both the pair interactions and the extent of perturbations acting on them.

However, in dense and rigid ^{1}H systems, the DQ buildup approach is often undesirable because there are only a few DQ intensity values experimentally accessible before the decay sets in. This experimental limitation results from the combination of the following two features: First, the presence of strong dipolar couplings restricts the initial DQ buildup to very short excitation times and, second, the basic two-pulse segment of recoupling pulse sequences allows only time increments of $\Delta\tau_{exc} = \tau_R/2$. Additionally, the pulse sequence needs to be applied on time scales of at least $\tau_{exc} = 2\tau_R \cdots 4\tau_R$ in order to compensate for experimental imperfections or unwanted additional interactions, such as frequency offsets. Therefore, the few accessible data points may even suffer from a relatively pronounced experimental inaccuracy.

In conclusion, from a practical point of view, the approach of choice for dense and rigid ^{1}H systems is the recording of a two-dimensional DQ spectrum for the shortest possible excitation time, i.e., $\tau_{exc} = \tau_R/2$, at the maximum available MAS frequency, coupled with an internal or external reference for intensity calibration. In terms of accuracy, the external reference is expected to be superior to the internal reference, but the marked discrimination of DQ signal arising from remote couplings, $I_{DQ}^{(ij)} \propto r_{ij}^{-6}$, drastically reduces the effect of all methodical and experimental imperfections on the resulting proton–proton distances. Note that a deviation of $\pm 50\%$ in the observed signal intensity gives rise to an error of only $\pm 10\%$ in the distance. Hence, drawing attention to the ease with which the experiments can be performed, ^{1}H DQ MAS spectra provide quick and remarkably detailed insight into the structure of ^{1}H spin systems and are well suited as a routine method to substance characterization in the solid state. In particular, different structural alternatives can often clearly be distinguished (*98*).

3.5. Mechanisms of Rotor Modulation

After considering rotor-synchronized experiments in the previous section, we now turn to the modulations introduced by MAS when incrementing the time dimensions t_1 and t_2 in arbitrary steps, i.e., $\Delta t_{1,2} \neq \tau_R$. Concerning the final detection period t_2, however, no further discussion of the effect of MAS is necessary, since this period is, in principle, a simple one-pulse experiment performed on a nonequilibrium state of longitudinal magnetization, whose amplitude is modulated by the previous periods of MQ excitation, evolution (during t_1), and reconversion. Hence, during t_2, the rotor modulations give rise to the familiar sideband patterns, which only provide limited access to structural information (see Section 2.10). In fact, at the high MAS frequencies required for sufficient spectral resolution in rigid ^{1}H systems, the intensities of these sidebands are in most cases negligible as compared to the centerband. Recall that these disadvantages of dipolar SQ MAS sideband patterns initiated the DQ approach. Therefore, we now focus on the rotor modulations acting on the MQCs during t_1 and on the mechanisms responsible for the generation of MQ MAS sideband patterns (*37*).

3.5.1. Reconversion Rotor Encoding (RRE)

At first, we concentrate on the reconversion, neglecting the actual evolution of the coherences under the rotor-modulated interactions during t_1. When t_1 is incremented in arbitrary steps, the rotor orientations at the beginning of the excitation and reconversion period will not be identical and, hence, the rotor will pass through different sequences of orientations in both periods (see Fig. 22). Therefore, the integrated dipolar interactions responsible for the excitation and the reconversion of MQCs differ with respect to their phases. Taking the rotor phase of the excitation as a reference, the phase of reconversion is shifted or—in other words—the *reconversion* is *rotor-encoded*. Without causing any further evolution, MAS modulates the MQCs by means of a phase encoding which arises solely as a consequence of the two-dimensional character of the experiment. Hence, all MQCs are subject to this encoding mechanism, even those which do not evolve during t_1.

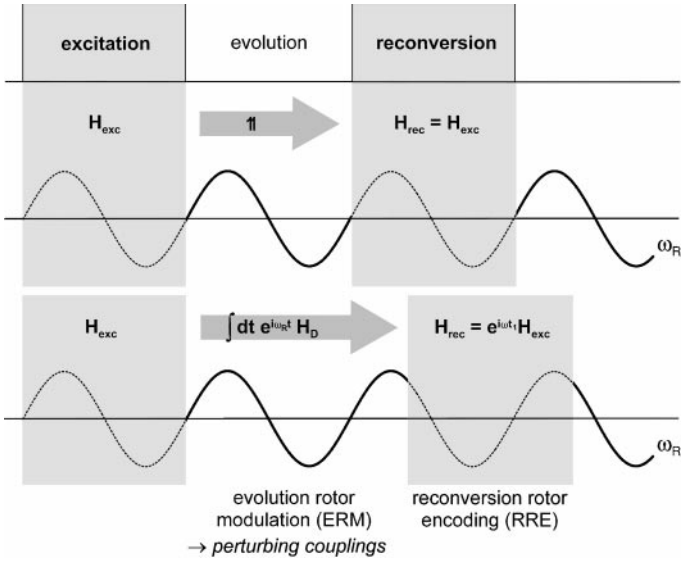

FIG. 22. Schematic representation of the mechanisms responsible for the generation of spinning sidebands in a MQ MAS experiment. (a) No sidebands are observed in rotor-synchronized experiments. (b) In a non-rotor-synchronized experiment, sidebands are generated by RRE and ERM, with the former being due to the rotor-phase shift between excitation and reconversion and the latter relying on the action of perturbing couplings on the observed MQC.

Experimentally, MQCs can be excited by a pulse sequence consisting of segments of the form 90°_q–$\tau_R/2$–$90^\circ_{q'}$, as has been discussed in Sections 3.2 and 3.3. Being concerned with ^{1}H systems, only the spatial parts ω_D of the dipolar interactions depend on the rotor orientation, with the integrals $\Omega_D(0, \tau_R/2)$ and $\Omega_D(\tau_R/2, \tau_R)$ over the intervals $[0, \tau_R/2]$ and $[\tau_R/2, \tau_R]$ differing only with respect to their signs (see Eq. [85]). Introducing a MQ evolution period t_1 by applying a pulse sequence of the form $(x–\bar{x})_{exc}$–t_1–$(y–\bar{y})_{rec}$, the integrated spatial parts of the dipolar interactions for excitation and reconversion, according to Eq. [30], are given by

$$\Omega_D^{(ij)}\left(0, \frac{\tau_R}{2}\right) = \frac{\omega_D^{(ij)}}{\omega_R} \cdot \sqrt{2} \sin 2\beta_{ij} \sin \gamma_{ij},$$

and

$$\Omega_D^{(ij)}\left(\frac{\tau_R}{2} + t_1, \tau_R + t_1\right) = -\frac{\omega_D^{(ij)}}{\omega_R} \cdot \sqrt{2} \sin 2\beta_{ij} \sin(\omega_R t_1 + \gamma_{ij}). \quad [114]$$

It is clear that the expression for the excitation is identical to that of Eq. [86], because it is independent of t_1. However, the reconversion is rotor-encoded by the term $\omega_R t_1$ in the argument of the sine function. Consequently, no rotor modulations occur if t_1 is incremented in steps of rotor periods (as has been assumed for the discussion of the rotor-synchronized MQ spectra in the previous section), but as soon as $t_1 \neq n\tau_R$, rotor echoes and MAS sidebands are induced in the MQ time signal and in the MQ spectrum, respectively. Considering, for example, spin-pair DQCs and CH_3 TQCs, the time signals can be written using Eqs. [83] and [107] as

$$S_{DQ}^{(ij)}(t_1) \propto \sin\left(\Omega_D^{(ij)}\left(0, \frac{\tau_R}{2}\right)\right) \cdot \sin\left(\Omega_D^{(ij)}\left(\frac{\tau_R}{2} + t_1, \tau_R + t_1\right)\right)$$
$$\propto \sin(C_{ij} \cdot \sin(\omega_R t_1)) \quad [115]$$

and

$$S_{TQ}^{CH_3}(t_1) \propto \left[\cos\left(\Omega_D^{(ij)}\left(0, \frac{\tau_R}{2}\right)\right) - 1\right] \cdot \left[\cos\left(\Omega_D^{(ij)}\left(\frac{\tau_R}{2} + t_1, \tau_R + t_1\right)\right) - 1\right]$$
$$\propto \cos(C_{ij} \cdot \sin(\omega_R t_1)) - 1, \quad [116]$$

respectively. The coefficient C_{ij} includes all terms which do not depend on t_1, but only on the orientation of the dipolar coupling vector $(\beta_{ij}, \gamma_{ij})$, for which, in powdered samples, an orientational averaging procedure has to be performed. The resulting expressions $\sin(C_{ij} \sin(\omega_R t_1 + \gamma_{ij}))$ and $\cos(C_{ij} \sin(\omega_R t_1 + \gamma_{ij}))$ can be written as Fourier series, whose terms contain Bessel functions $J_n(C_{ij})$ of nth order (*2, 17*):

$$S_{DQ}^{(ij)}(t_1) \propto \sin(C_{ij} \cdot \sin(\omega_R t_1))$$
$$= 2\sum_{n=1}^{\infty} J_{2n+1}(C_{ij}) \sin((2n-1)\omega_R t_1) \quad [117]$$

and

$$S_{TQ}^{CH_3}(t_1) \propto \cos(C_{ij} \cdot \sin(\omega_R t_1))$$
$$= J_0(C_{ij}) + 2\sum_{n=1}^{\infty} J_{2n}(C_{ij}) \cos(2n\omega_R t_1). \quad [118]$$

From the Fourier series it is clear that the DQ and TQ signal are modulated by odd and even multiples of the spinning frequency, respectively. Thus, after a Fourier transformation in t_1, the spin-pair DQ and the CH_3 TQ spectrum consist of solely odd- and even-order MAS sidebands, respectively. The intensity distribution over the MAS sideband pattern is determined by the Bessel functions and the coefficients C_{ij}, with the latter depending on the orientation $(\beta_{ij}, \gamma_{ij})$ and on the ratio $\omega_D^{(ij)}/\omega_R$ of the dipolar coupling strength $D^{(ij)} = \frac{1}{3}\omega_D^{(ij)}$ and the MAS frequency ω_R. After the orientational dependence has been taken into account by, e.g., a powder averaging procedure, the term $\omega_D^{(ij)}/\omega_R$, which can alternatively be written as a product of the dipolar coupling strength $D^{(ij)}$ and the excitation time τ_{exc}, represents the essential parameter which determines the envelope of the MAS sideband pattern.

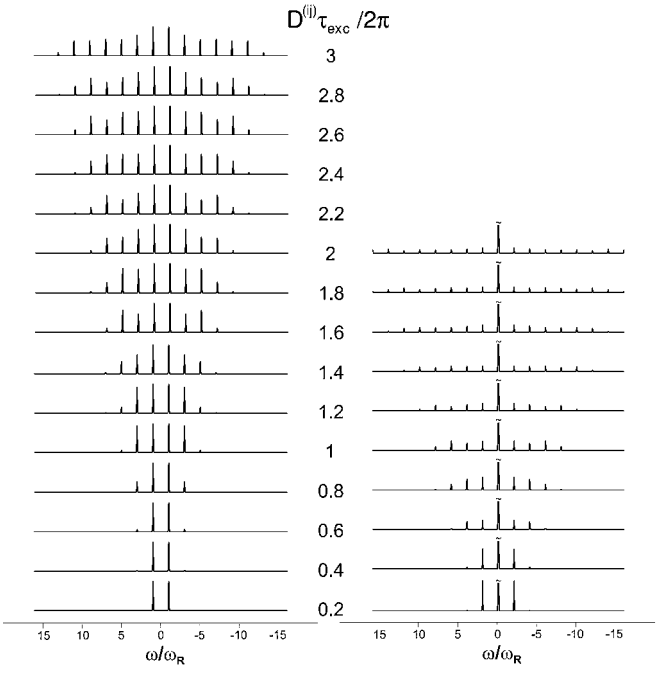

FIG. 23. Calculated MAS sideband patterns of a spin-pair DQ (left) and a CH_3 TQ spectrum (right) for a range of $D^{(ij)}\tau_{exc}$. In the TQ spectra, the centerbands are cut to $\frac{1}{4}$ of their full height.

In Fig. 23, calculated MAS sideband patterns of a spin-pair DQ and a CH_3 TQ spectrum are displayed for the range of $D^{(ij)}\tau_{exc}/2\pi = 0 \cdots 3$. Obviously, the DQ and TQ spectra consist of only odd- and even-order sidebands, respectively. The larger the product $D^{(ij)}\tau_{exc}$, the more sidebands appear. For $D^{(ij)}\tau_{exc} \to 0$, the spin-pair DQ spectrum converges toward a spectrum consisting of two resonance lines of equal intensity at $\pm\omega_R$, while the CH_3 TQ spectrum converges toward a triplet of lines at $-2\omega_R, 0, 2\omega_R$ with an intensity distribution of $1:3:1$ (clearly, for $D^{(ij)}\tau_{exc} = 0$ the signal intensity drops to zero). From a practical point of view, a sideband pattern which is spread over a wide frequency range is disadvantageous, because the spectral intensity is distributed over a lot of weak sidebands with a poor signal-to-noise ratio. Therefore, spin-pair DQ and CH_3 TQ spectra should possibly be recorded with $D^{(ij)}\tau_{exc}/2\pi < 3$ and $D^{(ij)}\tau_{exc}/2\pi < 1.5$, respectively.

In conclusion, the rotor encoding of the reconversion makes MQ spectra split into sidebands. Although, for experimental applications to ^{1}H systems, the relevant MQ orders are in most cases limited to DQCs and TQCs, it is clear from tensor algebra and from analogy considerations that, in general, the RRE mechanism produces solely *odd*-order sidebands for *even*-order MQCs and vice versa.

3.5.2. Evolution Rotor Modulation (ERM)

In the previous section, we have discussed an indirect type of mechanism leading to spinning sidebands in MQ spectra. However, besides this rotor encoding of the reconversion period, the MQCs are also, during the evolution period t_1, in a more direct way subject to rotor-modulated interactions. In fact, the latter mechanism is well known from the one-pulse experiment under MAS and from the resulting sideband patterns of SQ spectra. The essential condition for the presence of such a rotor-modulated evolution is that the considered MQCs do evolve under anisotropic interactions during t_1 at all. With respect to ^{1}H systems, this evolution is absent for two special cases: the DQC of a spin pair and the TQC of a methyl group, provided that there is no chemical shift anisotropy (as is assumed throughout in our discussion) and, more importantly, that there are no dipolar couplings to further spins. As soon as the MQC interacts with a further spin not involved in the coherence or, even more restrictively, as soon as the mediating dipolar couplings within the MQC are not all equivalent, the MQC evolves under dipolar interactions, whose spatial parts are modulated by the sample rotation. In this way, rotor modulations enter into the MQ time signal.

Usually, it is not possible to describe this evolution using a simple analytical formalism, because in dense ^{1}H systems the dipolar coupling network tends to generate higher spin correlations which can be handled only by use of series expansions (see Section 2.5). For example, from Eq. [110] it can be seen how a three-spin DQC arises from a spin-pair DQC between the spins i and j via the additional dipolar coupling $\hat{\boldsymbol{H}}_D^{(ik)}(t) = \omega_D^{(ik)}(t)\hat{\boldsymbol{T}}_{2,0}^{(ik)}$ of the spin i to the third spin k. Assuming that this process occurs during the evolution period t_1, the three-spin DQC introduces a rotor modulation into the coherence, because it includes the integrated spatial part of the additional coupling $\Omega_D^{(ik)}(\tau_{exc}, \tau_{exc} + t_1) = \int_{\tau_{exc}}^{\tau_{exc}+t_1} \omega_D^{(ik)}(t)\,dt$ as a coefficient.

To discuss the rotor-modulated evolution in a clear and instructive way, we consider the DQC of the protons of a fast rotating methyl group. As has already been pointed out in Eqs. [105] and [107], the CH_3 DQ signal consists of two- and three-spin contributions, $(\hat{\boldsymbol{T}}_{2,2} - \hat{\boldsymbol{T}}_{2,-2})$ and $(\hat{\boldsymbol{T}}_{3,2} + \hat{\boldsymbol{T}}_{3,-2})$. Since the DQ state does not include all spins and couplings present in the methyl group, as is the case for the CH_3 TQC, both DQ terms evolve after the excitation under the intramethyl dipolar couplings $\hat{\boldsymbol{H}}_D(t) = \omega_D(t)\hat{\boldsymbol{T}}_{2,0}$ (*16*):

$$(\hat{\boldsymbol{T}}_{2,2} - \hat{\boldsymbol{T}}_{2,-2}) \xrightarrow{\int_{\tau_{exc}}^{\tau_{exc}+t_1} \hat{\boldsymbol{H}}_D(t)\,dt} \cos\Omega_{ev}(\hat{\boldsymbol{T}}_{2,2} - \hat{\boldsymbol{T}}_{2,-2}) - \frac{2i}{\sqrt{3}}\sin\Omega_{ev}(\hat{\boldsymbol{T}}_{3,2} + \hat{\boldsymbol{T}}_{3,-2})$$

and

$$(\hat{\boldsymbol{T}}_{3,2} + \hat{\boldsymbol{T}}_{3,-2}) \xrightarrow{\int_{\tau_{exc}}^{\tau_{exc}+t_1} \hat{\boldsymbol{H}}_D(t)\,dt} -\frac{2i}{\sqrt{3}}\sin\Omega_{ev}(\hat{\boldsymbol{T}}_{2,2} - \hat{\boldsymbol{T}}_{2,-2}) + \cos\Omega_{ev}(\hat{\boldsymbol{T}}_{3,2} + \hat{\boldsymbol{T}}_{3,-2}). \quad [119]$$

Ω_{ev} denotes the integrated spatial part of the dipolar interaction

during t_1, i.e., $\Omega_{ev} = \Omega_D(\tau_{exc}, \tau_{exc} + t_1)$, and the t_1 dependence results in a rotor modulation. Since the system under consideration is an isolated methyl group, the evolution of the DQC during t_1 is restricted to a redistribution of the two- and three-spin contributions, with both terms being weighted by additional phase factors, $\sin\Omega_{ev}$ and $\cos\Omega_{ev}$. Denoting the integrated spatial part of the excitation period $\Omega_D(0, \tau_{exc})$ by Ω_{exc}, the initial state

$$\frac{i}{2}\sin\Omega_{exc}(\hat{\boldsymbol{T}}_{2,2} - \hat{\boldsymbol{T}}_{2,-2}) - \frac{1}{2\sqrt{3}}(\cos\Omega_{exc} - 1)(\hat{\boldsymbol{T}}_{3,2} + \hat{\boldsymbol{T}}_{3,-2}) \qquad [120]$$

evolves to

$$\left[\frac{i}{2}\sin\Omega_{exc}\cos\Omega_{ev} + \frac{i}{3}(\cos\Omega_{exc} - 1)\sin\Omega_{ev}\right] \cdot (\hat{\boldsymbol{T}}_{2,2} - \hat{\boldsymbol{T}}_{2,-2}) + \left[\frac{1}{\sqrt{3}}\sin\Omega_{exc}\sin\Omega_{ev} - \frac{1}{2\sqrt{3}}(\cos\Omega_{exc} - 1)\cos\Omega_{ev}\right] \cdot (\hat{\boldsymbol{T}}_{3,2} + \hat{\boldsymbol{T}}_{3,-2}). \qquad [121]$$

As has been described in Section 3.3.3, the reconversion of the DQCs gives rise to a further multiplication of the coefficients by terms analogous to those of the excitation. Thus, the detected CH_3 DQ signal is given by (*37*)

$$S_{DQ}^{CH_3}(t_1) \propto \sin\Omega_{exc}\cos\Omega_{ev}\sin\Omega_{rec} + \frac{1}{2}(\cos\Omega_{exc} - 1)\sin\Omega_{ev}\sin\Omega_{rec} + \frac{1}{2}\sin\Omega_{exc}\sin\Omega_{ev}(\cos\Omega_{rec} - 1) - \frac{1}{4}(\cos\Omega_{exc} - 1)\cos\Omega_{ev}(\cos\Omega_{rec} - 1), \qquad [122]$$

where $\Omega_{rec} = \Omega_D(\tau_{exc} + t_1, 2\tau_{exc} + t_1)$. The rotor modulations, reflected by the t_1 dependencies, now appear in the arguments $\Omega_{ev} = \int_{\tau_{exc}}^{\tau_{exc}+t_1}\omega_D(t)\,dt$ and $\Omega_{rec} = \int_{\tau_{exc}+t_1}^{2\tau_{exc}+t_1}\omega_D(t)\,dt$, arising from the evolution and the reconversion period, respectively. The rotor modulation introduced by the Ω_{ev}-term is responsible for the generation of MAS sidebands by means of a mechanism which will henceforth be called *evolution rotor modulation* (ERM), while the Ω_{rec}-terms lead to the generation of sidebands via the RRE mechanism described in the previous section. The complication of both the Ω_{ev}- and the Ω_{rec}-term depending on t_1 does not allow the DQ signal $S_{DQ}^{CH_3}(t_1)$ to be expanded into a simple Fourier series with Bessel functions as coefficients. Hence, $S_{DQ}^{CH_3}(t_1)$ cannot be written in the same form as the spin-pair DQ signal and the CH_3 TQ signal (see Eqs. [115] to [117]).

In Fig. 24, experimental and calculated SQ, DQ, and TQ spectra of a spin-$\frac{3}{2}$ system are displayed. The experiments were not performed on methyl groups, because real samples do not provide spatially isolated methyl units without perturbing interactions, as is desirable for demonstration purposes. Instead, taking advantage of the analogy of a methyl group and a spin-$\frac{3}{2}$ nucleus (see Section 3.3.2), the measurements were performed on the ^{23}Na nuclei of crystalline sodium nitrate, which represent a first-order quadrupolar system with a quadrupolar coupling constant of $C_Q = 337$ kHz and a symmetric electric-field gradient tensor, i.e., $\eta = 0$. Converting the quadrupolar into a dipolar coupling strength by use of Eqs. [21] and [23], the ^{23}Na nucleus in sodium nitrate corresponds to a methyl group with a hypothetical dipolar coupling of $D^{(ij)} = 2\pi \cdot 28.1$ kHz or, equivalently, with a hypothetical interproton distance of 0.129 nm.

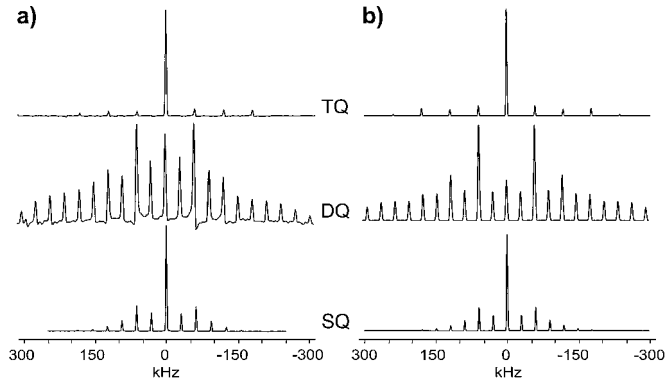

FIG. 24. (a) Experimental and (b) calculated SQ, DQ, and TQ spectra of the ^{23}Na nuclei in sodium nitrate, applying MAS at $\omega_R/2\pi = 15625$ Hz. The excitation time for the DQCs and TQCs is $\tau_{exc} = \tau_R/2 = 32\,\mu$s. The spin-$\frac{3}{2}$ nuclei with a quadrupolar coupling constant of $C_Q = 337$ kHz and negligible asymmetry, i.e., $\eta \approx 0$, serve as a model for the protons of an isolated methyl group with a hypothetical interproton distance of 0.129 nm.

In the TQ spectrum, the MAS sidebands arise solely from the rotor encoding of the reconversion (RRE mechanism), and are hence located at even multiples of the rotor frequency (*38*). The calculated spectrum was simulated using Eq. [115]. In the DQ spectrum, both mechanisms responsible for the generation of sidebands, the reconversion rotor encoding (RRE) and the evolution rotor modulation (ERM), superimpose, leading to the following consequences for the sideband pattern, which are clear from an inspection of Fig. 24: First, the sidebands now appear at all multiples of the MAS frequency, because the signal cannot be written in the simple form $\cos(C_{ij}\sin(\omega_R t_1 + \gamma_{ij}))$ and, hence, cannot be decomposed in the Fourier components of either even or odd multiples of ω_R only. Second, as compared to the TQ spectrum, the spectral range, over which the sideband pattern is spread, is widened. The additional terms $\sin\Omega_{ev}$ and $\cos\Omega_{ev}$ give rise to a product of the form $\cos\Omega_{ev}\cos\Omega_{rec} = \frac{1}{2}\cos(\Omega_{ev} + \Omega_{rec}) + \frac{1}{2}\cos(\Omega_{ev} - \Omega_{rec})$, which includes the sum $\Omega_{ev} + \Omega_{rec}$ of the arguments and hence the sum of the frequencies, so that after the Fourier transformation sidebands are expected to be spread over a wider frequency range.

For comparison, the SQ spectrum is also displayed in Fig. 24; since there is no reconversion period in the one-dimensional SQ MAS experiment, the sidebands are generated solely by the rotor-modulated evolution. The SQ time signal of a methyl group or, equivalently, of a spin-$\frac{3}{2}$ nucleus is given by

$$S_{SQ}^{CH_3}(t) \propto 3\cos\Omega_D(0,t) + 2, \qquad [123]$$

as is clear from the $(\hat{\boldsymbol{T}}_{1,1} - \hat{\boldsymbol{T}}_{1,-1})$ term in Eq. [106] after application of the first pulse. Since, as in the TQ case, again only one mechanism is responsible for the generation of sidebands, the spectral width is similar to that of the TQ spectrum and considerably smaller than that of the DQ spectrum. The pattern consists of sidebands of all orders, because—as in the DQ case—the argument $\Omega_D(0,t)$ in Eq. [123] does not include only one sine or cosine modulation and, hence, the signal cannot be written as $\cos(C_{ij}\sin(\omega_R t + \gamma_{ij}))$.

After having demonstrated, using the simple example of a methyl group, how the two mechanisms RRE and ERM generate MAS sidebands in MQ spectra, it is straightforward to derive a criterion which allows the decision to be made as to what extent an observed spin-pair DQC or a CH_3 TQC is subject to perturbing interactions to neighboring spins: As long as there is no perturbing interaction present, the MAS sideband patterns of spin-pair DQ and CH_3 TQ spectra consist of only odd- and even-order sidebands, respectively. Any further coupling gives rise to additional sidebands of the other order, whose intensities allow the degree of perturbation or, conversely, the degree of isolation of the spin pair or the methyl group to be determined. The additional sidebands are generated primarily by means of the ERM mechanism, i.e., by the evolution of the MQCs under perturbing interactions during t_1. For reasons of completeness, it should be noted that, theoretically, weak additional sidebands could also arise from the action of perturbing dipolar couplings during the excitation and reconversion period, i.e., even in the (hypothetical) absence of any evolution during t_1. However, this mechanism of sideband generation relies on the excitation of higher spin correlations which always arise out of existing two-spin correlations and which therefore represent a second step in the excitation process. Consequently, such higher-order effects are usually small, because the excitation time is adjusted such that it suffices for the generation of two-spin correlations, but not for the subsequent and unwanted formation of three- and higher-spin correlations. As a result of this, additional sidebands generated in this way are a concomitant phenomenon of minor and mostly negligible importance, because, experimentally, they are very weak and, in addition, always concealed by the dominating sidebands arising from the ERM mechanism.

In conclusion, MAS sideband patterns permit the quantification of dipolar coupling strengths in spin pairs or within methyl groups and, at the same time, provide an estimate as to what extent the underlying approximations are valid for the complex dipolar coupling network under inspection by quantifying the degree of perturbation. As to measuring dipolar coupling strengths, MAS sideband patterns are superior to DQ buildup curves, because no further calibration of the signal intensities is required. Instead, the patterns are "inherently" calibrated and allow absolute values for coupling strengths to be derived. Moreover, in DQ MAS sideband experiments, the t_1 dimension serves as a spectral DQ dimension as well as a period for introducing the rotor encoding. Hence, DQ coherences between different pairs of spins can readily be resolved in *two*-dimensional DQ MAS spectra together with the individual MAS sideband patterns, while for the DQ build up approach the distinction of DQ coherences requires a *three*-dimensional experiment where τ_{exc} and t_1 are incremented independently.

3.6. Spin Topologies and MAS Sideband Patterns

In the previous section we have demonstrated that MAS sideband patterns of ^{1}H DQ and TQ spectra can, in principle, serve as a source of information about dipolar coupling strengths, while the chemical shift resolution allows the coupled spins forming a coherence to be identified. In this section, we now discuss how much information can be obtained from the sideband patterns about the actual geometry of the coupled spins. Besides the "original" spin-pair or methyl pattern, which measures the strength of the pair or the intramethyl coupling, the additional sidebands arising via the ERM mechanism during t_1 provide particular insight into the spatial arrangement of the coupled spins in the system, including perturbing spins.

This property makes the MQ MAS sideband patterns superior to rotor-synchronized spectra, because the latter only contain the signal intensities of the resolved MQCs. From the signal intensities, an effective dipolar coupling strength can be derived, corresponding to the sum over all pair couplings between spins of the respective species, but no further details about the terms of the sum are accessible. This means, for example, that a sum of many weak couplings cannot be distinguished from a sum over a few strong couplings. Therefore, most of the information about the geometry of the dipolar-coupled spin system is concealed as long as there is only a single intensity parameter experimentally available.

In the following, we will discuss the MAS sideband patterns of DQ and TQ spectra obtained from simulations of three- and four-spin systems as well as from experiments on a $(CH_3 + H)$ model compound. In this way, the effect of an additional perturbing spin on the spectra of a spin pair or a methyl group shall be investigated. The parameter ξ, correlating the perturbing coupling D^{pert} to the MAS frequency ω_R (see definition in Eq. [64]), serves as a measure of the strength of the perturbation.

3.6.1. Spin-Pair DQ Spectra

By means of numerical simulations, we consider a proton spin pair with a dipolar coupling of $D^{\text{pair}} = 2\pi \cdot 20$ kHz, corresponding to a distance of $r_{\text{pair}} = 0.18$ nm, as is known from CH_2

groups. Resembling realistic situations, this pair is perturbed by a coupling D^{pert} varying between 5 and 75% of the dominating pair coupling, corresponding to a distance range between 0.5 and 0.2 nm from the remote spin. With respect to the perturbing couplings, the three-spin system can adopt two extreme geometries, whose SQ MAS spectra have already been investigated in Section 2.7 (see Fig. 4): first, a linear arrangement where the coupling between the remote spin and one of the pair spins is negligible and where the whole three-spin system behaves inhomogeneously due to the colinear orientation of all dipolar coupling vectors; and second, a triangular Δ-arrangement where the spins are placed on the vertices of an isosceles triangle and where the two perturbing couplings are hence of equal strength. The chosen MAS frequency, 10 kHz, is rather low, resulting in a perturbation parameter ξ ranging from 0.1 to 1.5. The excitation time for DQCs is set to $\tau_{exc} = \tau_R/2 = 50\,\mu$s, corresponding to $D^{\text{pair}}\tau_{exc}/2\pi = 1$ for the pair. In accordance with the experiments, the length of the 90° RF pulses is 3 μs throughout the following simulations.

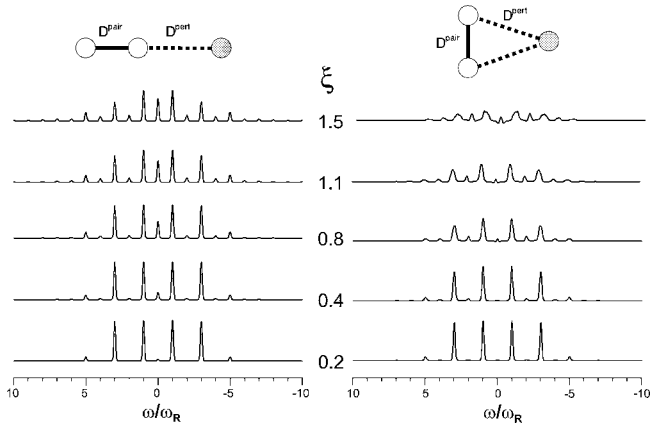

FIG. 25. Simulated DQ MAS sideband patterns for a spin pair plus a perturbing spin, with the three-spin system adopting a linear and a Δ-arrangement. The parameters are $D^{\text{pair}} = 2\pi \cdot 20\,\text{kHz}$, $\omega_R = 2\pi \cdot 10\,\text{kHz}$, and $\tau_{exc} = \tau_R/2 = 50\,\mu$s.

For vanishing perturbations $\xi \to 0$, i.e., for the isolated spin pair, we expect, under these conditions, a symmetric DQ MAS sideband pattern, consisting of only *odd-order* sidebands, with the first- and the third-order sideband being of almost equal intensity (see the DQ spectrum for $D^{(ij)}\tau_{exc}/2\pi = 1$ in Fig. 23). Irrespective of the spin geometry, this pattern is observed in the simulated spectra displayed in Fig. 25.

In the DQ spectra for both three-spin geometries depicted in Fig. 25, the main effect of the perturbation introduced by the third spin is the appearance of MAS sidebands at *even* multiples of the MAS frequency, including the center of the spectrum. Depending on the spin geometry, either the centerband or the second-order sideband are the most intense of these additional signals which clearly arise from the ERM mechanism during t_1 (see Figs. 26a and 26b). Apart from this effect, in the Δ-arrangement, the perturbation by a third spin severely broadens the lines, while in the linear arrangement the spin system behaves inhomogeneously under MAS; i.e., no line-broadening effects are observed. These features are known from the MAS sidebands in SQ spectra (see Fig. 4). Moreover, the presence of perturbing couplings also gives rise to distortions of the original spin-pair pattern at odd multiples of the MAS frequency, although this is less obvious than the appearance of additional sidebands and the line broadening.

In the diagrams in Fig. 26, the changes of the DQ MAS sideband patterns are plotted versus the perturbation ξ caused by a third spin. The three-spin systems adopt either a linear or a Δ-arrangement with inhomogeneous or homogeneous properties, respectively. Up to a perturbation of about $\xi < 0.5$, the distortions of the patterns (Figs. 26a and 26b) as well as the loss of DQ signal intensity (Fig. 26c) are small enough to allow dipolar couplings strengths to be determined with acceptable accuracy, since considering the range $0.5 < D^{(ij)}\tau_{exc}/2\pi < 1.0$ a deviation of 10% in the intensity ratio of the third- and first-order sideband leads to an error of about 5% in the dipolar coupling strength, corresponding to an error of less than 2% in the internuclear distance. Note that, in inhomogeneous spin systems, the overall DQ signal intensity is even constant, because no dephasing occurs during t_1. However, any homogeneous character gives rise

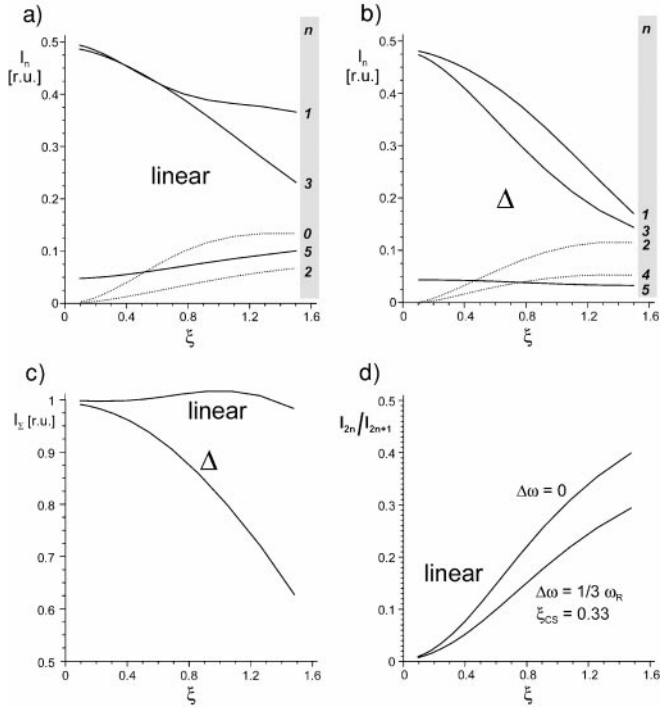

FIG. 26. Effect of a perturbation ξ caused by a third spin on the DQ MAS sideband pattern of a spin pair, with the three-spin system adopting either a linear or a Δ-arrangement: (*a, b*) Sideband intensities, with *n* denoting the sideband order. (*c*) Overall DQ signal intensity. (*d*) Ratio of the odd-order sidebands, i.e., the "original" spin-pair pattern, to even-order sidebands arising from the perturbation. $\Delta\omega$ denotes a chemical shift difference between the pair and the perturbing spin.

to coherence losses, since then MAS does not fully refocus, during the reconversion period, the effect of the dipolar interactions present in the excitation period. With respect to the perturbing effects, the situation is improved by the presence of a chemical shift difference between the perturbing spin and the pair, because the frequency difference $\Delta\omega$ assists the MAS in decoupling the dipolar-coupled network and reduces the dipolar perturbation by a factor of about $\xi_{CS} = \Delta\omega/\omega_R$. This is demonstrated in Fig. 26d, where the ratio of the odd-order sidebands, i.e., the "original" spin-pair pattern, to the even-order sidebands arising from the perturbation is plotted versus the dipolar perturbation ξ. Without a chemical shift difference, the even-order signals are below 10% for perturbations $\xi < 0.5$, while a shift difference of $\Delta\omega = \frac{1}{3}\omega_R$, which corresponds to $\xi_{CS} = 0.33$, increases this 10% signal threshold to $\xi < 0.7$.

After having considered the two extreme geometries of a three-spin system, we now briefly turn to the intermediate cases by inspecting angular geometries, as are depicted in the inset in Fig. 27a. The simulated spectra in Fig. 27a are based on the parameters given in the figure legend. On increasing the angle θ from 0° to 90°, the system undergoes a continuous change from an inhomogeneous to a homogeneous character, because the projection of the vector of the perturbing dipolar coupling onto the direction of the pair-coupling vector decreases according to $\cos\theta$. Therefore, following a $\sin\theta$ dependence, the lines become more and more broadened when increasing the angle θ. Moreover, the sideband pattern is characteristically distorted: For $\theta \to 0^\circ$ and $\theta \to 90^\circ$, the additional signals arising from the perturbing interactions via the ERM mechanism are concentrated in the centerband and the second-order sidebands, respectively. The original spin-pair pattern, located at the odd-order sidebands, also depends, though less pronounced, on the angle θ. For $\theta = 50^\circ \cdots 60^\circ$, the intensity of the first-order sidebands, measured relative to the third-order sidebands, passes through a minimum. The same behavior is observed for the overall DQ signal intensity, which is reduced to half of the maximum intensity, when the angle θ is close to the "magic" angle of 54.7°. The latter feature arises as a consequence of the complex orientational dependence of a DQC which is subject to a further dipolar coupling and, in this way, resembles to some extent the familiar $(3\cos^2\theta - 1)$ dependence.

Thus, the MAS sideband pattern of a spin-pair DQ spectrum in principle provides information about both the strength and the relative orientation of a perturbing coupling to a third spin. It should be noted, however, that in dense multispin systems each pair is likely to be subject to more than one or two perturbing couplings and, consequently, there are more unknown orientational parameters to be determined in the system under investigation. If the spins are resolved with respect to their chemical shifts, it is possible to access these parameters separately by means of DQ MAS sideband patterns.

3.6.2. *Methyl DQ Spectra*

Usually, under fast MAS conditions, the ^{1}H signal of methyl groups can be spectrally resolved from other ^{1}H resonances except where there are many other alkyl resonances. Perturbing couplings to remote spins do not only give rise to a distortion of the original methyl sideband pattern, but also to DQCs between the methyl group and the remote spin, which form their own MAS sideband pattern. The latter type of coherence will henceforth be referred to as a $(CH_3 + H)$ DQC. In addition to the advantage of being spectrally resolved, the methyl group is also particularly suitable for serving as a sensor for the strength and the orientation of dipolar couplings to neighboring spins, because, for topological reference purposes, the fast rotation of the three spins around their threefold symmetry axis provides a single and well-defined average position of the methyl protons as well as a well-defined axis.

However, it is important to note that, in contrast to spin-pair DQ spectra, the MAS sideband patterns of methyl DQ spectra consist of signals appearing at *all* multiples of the MAS frequency, because the intramethyl couplings already generate sidebands via the ERM mechanism. Hence, although the strength of the perturbation can still be determined from the distortion of the original methyl pattern and, more importantly, from the signal of the $(CH_3 + H)$ DQCs, the same information is not available in a simple and sensitive way by the presence of *additional* sidebands. In fact, this disadvantage of methyl DQ spectra is one of the main motivations for recording methyl TQ spectra, since, in analogy to spin-pair DQCs, a pure methyl-TQC is not subject to the ERM, but only to the RRE mechanism generating sidebands, such that additional sidebands indicate the presence of perturbing couplings acting on the methyl

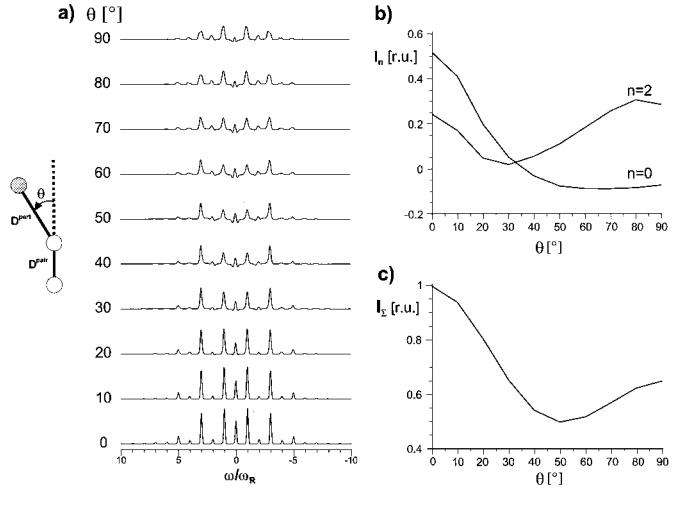

FIG. 27. (*a*) Simulated DQ MAS sideband patterns for a three-spin geometry, as depicted in the inset, with the angle θ ranging from 0° to 90°. The parameters are $D^{\text{pair}} = 2\pi \cdot 20$ kHz, $D^{\text{pert}} = 2\pi \cdot 10$ kHz (for the stronger coupling), $\omega_R = 2\pi \cdot 10$ kHz, resulting in a perturbation of $\xi = 1.0 \ldots 1.1$, and $\tau_{exc} = \tau_R/2 = 50\,\mu$s. (*b*) Intensities of the centerband ($n = 0$) and the second-order sidebands ($n = 2$). (*c*) Integrated DQ signal intensities of the spectra shown in (*a*).

groups. This TQ approach will be discussed in the following section.

We now focus on the MAS sideband patterns of CH_3 and (CH_3 + H) DQCs. The simulations are based on the four-spin system depicted in Fig. 28 with the parameters given in the figure legend. Under these conditions, the DQ sideband pattern of an isolated methyl group consists of sidebands of up to the seventh order. A fourth spin of type B approaching a methyl group AAA along its threefold symmetry axis gives rise to a distortion of the MAS sideband pattern of the pure methyl DQ signal as well as to an additional sideband pattern originating from DQCs of the type AB. The latter feature allows the spectrum to be decomposed into its CH_3 and its (CH_3 + H) signal pattern, as is demonstrated in Fig. 28. Consider first the distortions of the pure methyl pattern: It is clear from Fig. 29a that the first-order sideband is affected most, while all other signals are more or less constantly decreasing for increasing perturbations. This decrease of the methyl signal is also reflected in Fig. 29b, while the (CH_3 + H) signal is built up. However, the (CH_3 + H) signal intensity is too weak to compensate for the loss of methyl signal and, therefore, the overall DQ intensity decreases due to the formation of higher spin correlations within the four-spin system. However, up to a perturbation of $\xi < 0.4$, such higher-order correlations contribute less than 5% to the overall DQ signal and are negligible. With respect to the geometry of the spin system, the relative intensities of the CH_3 and the (CH_3 + H) signal thus allow the effective perturbation ξ acting on the methyl group to be determined.

Although the effects are less pronounced, the same information is, in principle, also obtainable from the distortion of the CH_3 pattern. More detailed insight into the spin topology is provided by the sideband pattern of the (CH_3 + H) DQ signal, which allows the angle θ to be straightforwardly derived. Figure 29c clearly shows that the relative intensities of the first-order sidebands and the centerband are particularly sensitive to the angle θ, since the pattern changes from a centerband-dominated spectrum for $\theta \to 0^\circ$ to a spectrum which is dominated by the first-order sidebands for $\theta \to 90^\circ$. Hence, combined DQ MAS sideband patterns of CH_3 and (CH_3 + H) DQCs represent a sensitive probe for spin topologies.

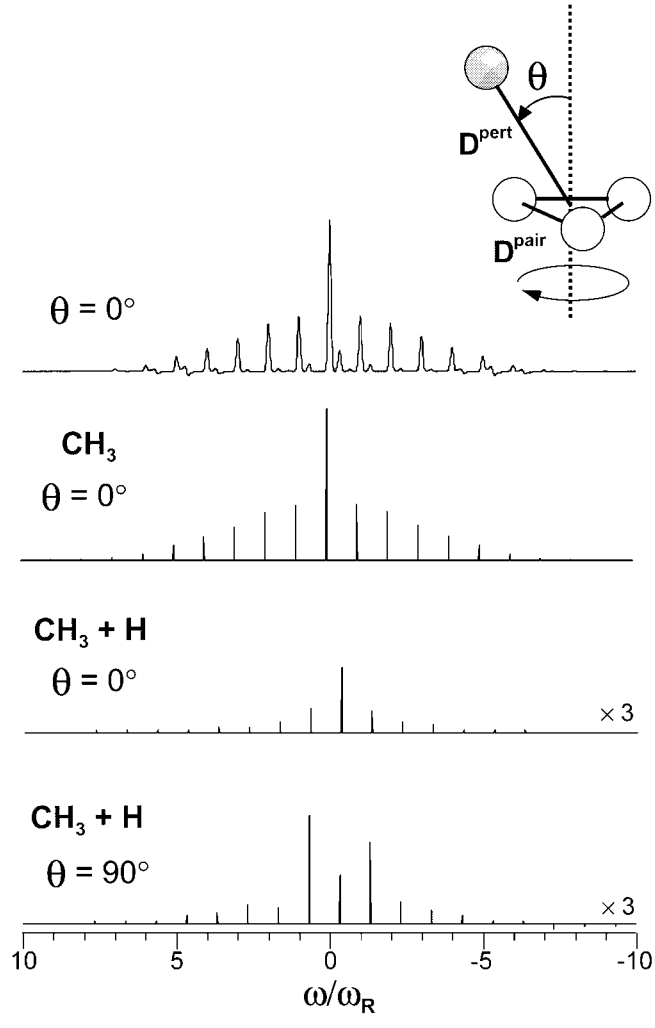

FIG. 28. Simulated DQ MAS sideband patterns for the three protons of a fast rotating methyl group plus a fourth spin, whose resonance frequency is shifted by $\Delta\omega = 2\pi \cdot 3.3$ kHz relative to the methyl signals. The parameters are $D^{\text{pair}} = 2\pi \cdot 8.8$ kHz, corresponding to an interproton distance of $r_{\text{pair}} = 0.19$ nm; $D^{\text{pert}} = 2\pi \cdot 2.6$ kHz for $\theta = 0^\circ$, corresponding to a distance of $r_{\text{pert}} = 0.32$ nm; $\omega_R = 2\pi \cdot 10$ kHz, resulting in a perturbation of $\xi = 0.26$; and $\tau_{exc} = \tau_R/2 = 50\,\mu$s. Below the spectrum ($\theta = 0^\circ$), the CH_3 and the (CH_3 + H) patterns are schematically extracted. For comparison, the (CH_3 + H) pattern obtained for $\theta = 90^\circ$ is also displayed.

3.6.3. Methyl TQ Spectra

Being combined into a TQC, the three protons of a methyl group and the intramethyl proton–proton couplings act as a single entity such that, in the TQ spectrum of an isolated methyl group, the MAS sidebands are solely generated by the RRE mechanism. Applying a proper excitation pulse sequence, the sidebands thus appear only at *even* multiples of the MAS frequency. The absence of any "internal" dipolar evolution during t_1 makes the TQC of a methyl group a very sensitive probe for additional couplings to neighboring spins, since any of these gives rise to a dipolar t_1-evolution and, hence, to the generation of odd-order sidebands via the ERM mechanism (see Section 3.5.2 and (*38*)), as can be clearly seen from the simulated spectra shown in Fig. 30a.

In Fig. 30b, the intensity of the sidebands is plotted versus the perturbation ξ. The intensity increase at the first-order sideband is apparent, while the signals of the original TQ pattern at the centerband and the second-order sidebands constantly decrease. As has already been observed for the methyl DQ coherences, the overall TQ signal decreases as well, because the buildup of the "mixed" (CH_3 + H) TQC cannot compensate for the loss of the methyl TQ signal (see Fig. 30c). Comparing the "mixed" TQC with the "mixed" DQC (see Fig. 29b), it is clear that the DQC is built up faster than the TQC; this is what we expect from

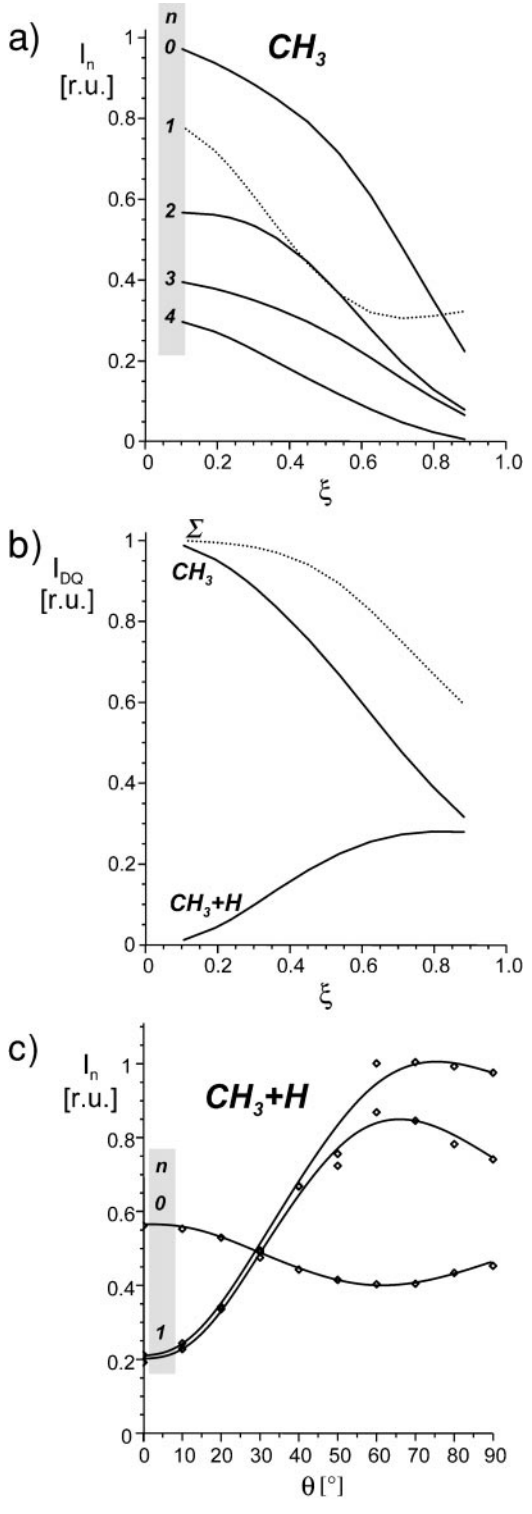

FIG. 29. Sideband intensities in the simulated DQ MAS spectra of a methyl group plus a perturbing spin (see Fig. 28). (a) Intensity distribution over the methyl pattern, with n denoting the sideband order. (b) DQ signal intensity of the CH_3 and the (CH_3 + H) coherences for a methyl group perturbed by a fourth spin which is located on the threefold symmetry axis at distances $r_{\text{pert}} = 0.5 \ldots 0.16$ nm. (c) Intensity distribution over the (CH_3 + H) pattern for the four-spin geometry depicted in Fig. 28, with θ ranging from 0° to 90°.

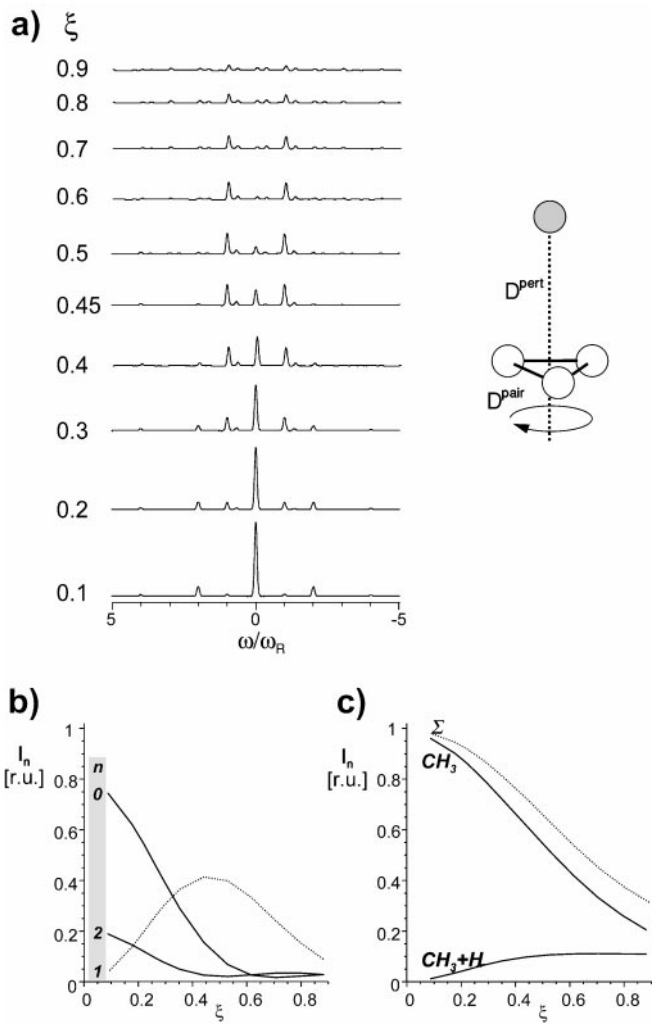

FIG. 30. (a) Simulated TQ MAS sideband patterns for a methyl group perturbed by a fourth spin, which is located on the threefold symmetry axis (see inset) and whose resonance frequency is shifted by $\Delta\omega = 2\pi \cdot 3.3$ kHz relative to the methyl signals. The further parameters are $D^{\text{pair}} = 2\pi \cdot 9$ kHz, $D^{\text{pert}} = 2\pi \cdot 0.9 \ldots 9$ kHz, $\omega_R = 2\pi \cdot 10$ kHz, resulting in a perturbation of $\xi = 0.1 \ldots 0.9$, and $\tau_{exc} = \frac{1}{2}\tau_R = 50\,\mu$s. (b) Intensity distribution over the methyl TQ sideband pattern, with n denoting the sideband order. (c) TQ signal intensity of the CH_3 and the (CH_3 + H) coherences.

the excitation behavior in the short-time limit, as has been discussed in Section 3.3.3. However, it is interesting to note that, for the same perturbation represented by the parameter ξ, the distortions occurring in TQ spectra are stronger than those in the DQ spectrum, because, already for $\xi \geq 0.1$, the additional odd-order TQ sidebands contribute more than 5% to the overall intensity, while in the DQ spectra the additional sidebands are negligible for perturbations up to $\xi < 0.2$. Obviously, the TQCs are more sensitive to dipolar couplings. This fact is well known from investigations of quadrupolar systems, since quadrupolar MQCs of nth order were shown to experience homo- or heteronuclear dipolar couplings at an amplification to the nth power (*25*, *37*).

Here, it can be seen that this n-fold sensitivity of nth-order MQCs is also observed for dipolar coherences in ^{1}H systems.

In spite of this pronounced sensitivity and the appearance of additional sidebands, the original methyl TQ pattern allows the intramethyl coupling strength to be determined to a sufficient accuracy for perturbations of up to $\xi < 0.4$. However, with respect to the spin topology, the TQ spectra provide less information than the DQ spectra, because the TQ patterns of the "mixed" TQCs are usually too weak to be exploited experimentally.

3.6.4. Decoupling Effect of MAS

In the context of the perturbations caused by additional dipolar couplings on ^{1}H MQCs, a central point worth being considered in detail is the dipolar decoupling provided by MAS. We have already stated that, in the fast spinning limit, MAS simplifies the dipolar network to a superposition of spin pairs. In MQ spectra, the perturbing effects, i.e., mainly the MAS sidebands arising from the ERM mechanism, represent the deviations from the simple spin-pair approach, which can be reduced by increasing the MAS frequency, while independent of this the excitation of MQCs and the generation of a RRE sideband pattern can be accomplished by adjusting the duration of the recoupling pulse sequence. In this way, MQ spectroscopy allows the two mechanisms responsible for the generation of MQ MAS sidebands to be straightforwardly distinguished, and the MQ experiments can be tailored to investigate either the individual pair couplings or the topology of a small spin system.

In Fig. 31, the effect of the MAS frequency on the DQ MAS sideband pattern of a linear three-spin system *AAB* is displayed. Since the two pair couplings differ by a factor of 2, the DQ signal of the *AB* coherence is much weaker (by about a factor of 4) than that of the *AA* coherence. In the sideband patterns, which are schematically extracted from the spectrum in Fig. 31, the even-order sidebands indicate residual dipolar evolution during t_1. However, from the dominating pattern located at odd multiples of the MAS frequency, the *AA* pair coupling can be determined quite reliably. This is demonstrated by the fact that the simulated *AA* DQ MAS patterns are very similar to the pattern of the respective isolated pair, with the exception of some minor deviations in the fifth-order sidebands which, as well as the even-order sidebands, indicate the presence of perturbing couplings. The agreement between the three-spin spectrum and the pair spectrum slightly improves at the higher MAS frequency. This improvement, demonstrating the decoupling efficiency of MAS, is much more pronounced for the *AB* pattern, because the *AB* DQC, being severely perturbed by a strong dipolar coupling between the *A* spins, desperately requires dipolar decoupling and thereby separation into spin pairs by MAS. At a MAS frequency of 10 kHz, which is, in the case of the *AB* coherence, of exactly the same magnitude as the perturbing coupling (corresponding to $\xi = 1$), the *AB* pattern is heavily distorted, and resembles the *AA* pattern; consequently, determining the *AB* coupling from this pattern would yield a value which is far too high. By comparison, for $\omega_R = 2\pi \cdot 20$ kHz (corresponding to $\xi = 0.5$) the interproton distance of the *AB* pair can be determined from the *AB* DQ MAS pattern to an accuracy of about +10%. Since additional couplings generally increase the intensity of the higher-order sidebands in the patterns, the principal trend of a supplementary correction is also known.

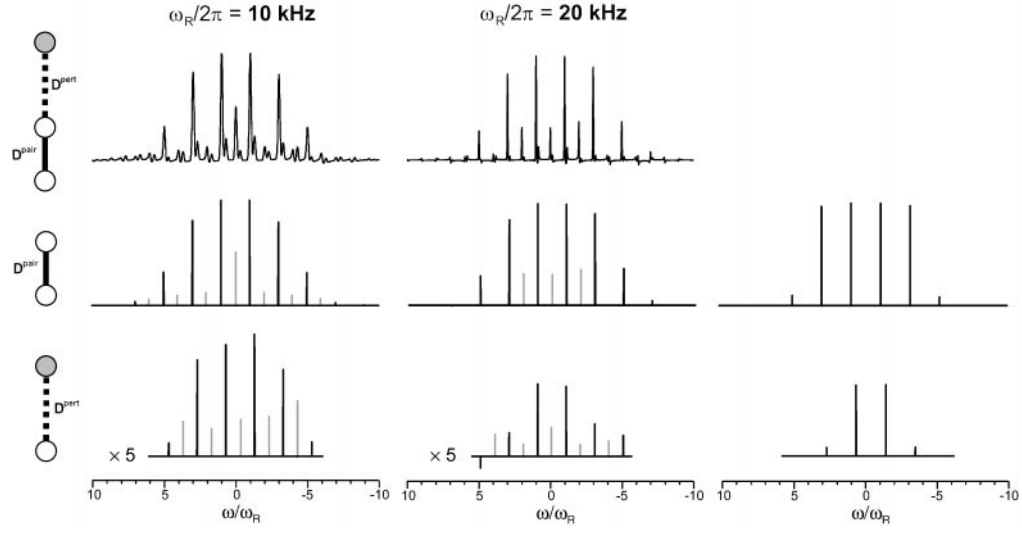

FIG. 31. Simulated DQ MAS sideband patterns for a spin pair *AA* plus a perturbing spin *B*, whose resonance frequency is shifted by $\Delta\omega = 2\pi \cdot 3.3$ kHz relative to that of the pair, in a linear arrangement: $D^{\text{pair}} = 2\pi \cdot 20$ kHz, $D^{\text{pert}} = 2\pi \cdot 10$ kHz (the other perturbing coupling is negligibly weak), $\tau_{exc} = 50\,\mu$s, with MAS being applied at 10 and 20 kHz, respectively. The two sideband patterns, *AA* and *AB*, are schematically extracted from the spectra and compared to the patterns expected for isolated pairs (on the right). For distinction, the even-order sidebands arising from the ERM mechanism are displayed in gray. Note that in the 20-kHz spectrum the lines are only seemingly narrowed due to the larger spectral width.

3.6.5. *Acetonitrile in Hydroquinone*

In this section, concluding the discussion of ^{1}H MQ MAS sideband patterns, we demonstrate how DQ and TQ sideband patterns allow the determination of a four-spin ($CH_3 + H$) topology. The model sample is acetonitrile, CH_3CN, in the cavities of crystalline and deuterated hydroquinone, DO–C_6D_4–OD, where 20% of the deuterons are replaced by protons due to back exchange processes occurring upon exposure to air, as can be directly determined from ^{1}H MAS one-pulse spectra (see Fig. 33a). Using this sample, ^{1}H MQ spectroscopy on methyl groups, including MQ MAS sideband patterns as well as the principal effect of a perturbing spin, has been introduced in previous work (*37*, *38*).

In the crystal structure (*21*), depicted in Fig. 32a, six hydroquinone molecules are located around the molecular axis of the linear acetonitrile molecule, and the deuterons of the OD groups approximately fulfill a sixfold symmetry. According to the X-ray structure analysis, the distance between the center of the methyl protons and three deuterons is $r_{\text{pert}} \approx 0.33$ nm, and the angle between the molecular N–C–C axis and the three distance vectors r_{pert} is $\theta \approx 44^\circ$. Since 20% of the OD positions are reprotonated, each methyl group has, on average, to a good approximation one neighboring OH proton, resulting in a four-spin model system which is schematically depicted in Fig. 32b.

Figure 33a shows the centerband of a ^{1}H one-pulse spectrum, recorded under MAS at 14 kHz. The most intense signals **A**, **B**, **C**, and **C**′ stem from the methyl protons of the acetonitrile (**A**) as well as from the reprotonated OD and aromatic CH positions of hydroquinone (**B** and **C**, **C**′, respectively). The signals marked by an asterisk are due to impurities. A noteworthy, though in this context minor, feature is the splitting of the aromatic ^{1}H resonance into two lines **C** and **C**′ of almost the same intensity. Provided that the spectral resolution suffices, such ^{1}H resonance shifts are frequently observed for protons which experience so-called ring-current effects of nearby aromatic systems. In the case of the acetonitrile sample, it is obvious that about half of the aromatic protons of each hydroquinone molecule are oriented differently relative to neighboring benzene rings than the others, resulting in different shielding effects. In addition to this example, similar shifts have been reported for tyrosine (*92*) and alkyl-substituted hexa-*peri*-hexabenzocoronenes (see Section 4.2 and (*18*, *19*)).

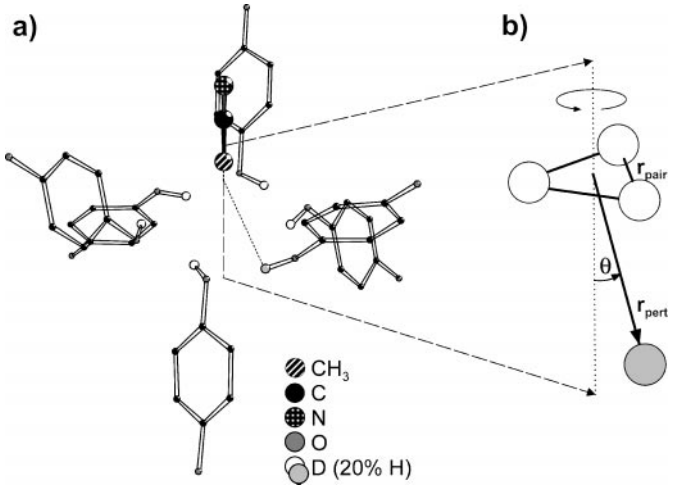

FIG. 32. (a) Crystal structure of the inclusion compound $[DO–C_6H_4–OD]_3 \cdot CH_3CN$ (acetonitrile hydroquinone d_6-clathrate). Due to partial reprotonation of the DO positions, each methyl group (with $r_{\text{pair}} \approx 0.19$ nm) has on average one neighboring HO proton at $r_{\text{pert}} \approx 0.33$ nm and $\theta \approx 44^\circ$, resulting in a ^{1}H four-spin model system whose topology is schematically represented in (b).

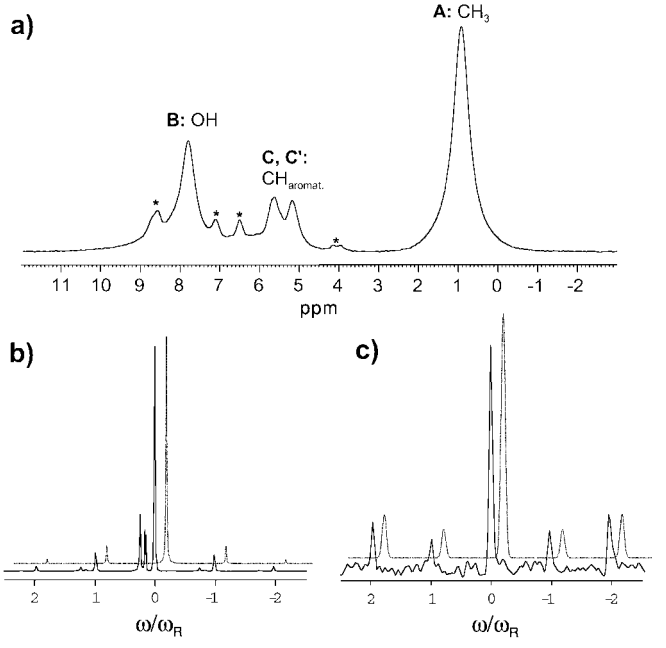

FIG. 33. ^{1}H MAS spectra of acetonitrile in hydroquinone, recorded under MAS at 14 kHz. (a) Centerband of the one-pulse spectrum and peak assignment (impurities are marked by $*$). (b) Comparison of the experimental CH_3 SQ MAS sideband pattern with a calculated pattern (dotted) for a methyl group with a proton-pair coupling of $D_{\text{pair}} = 2\pi \cdot 8.8$ kHz, corresponding to an interproton distance of $r_{\text{pair}} = 0.19$ nm. (c) Comparison of the experimental CH_3 TQ MAS sideband pattern, recorded for $\tau_{exc} = \frac{1}{2}\tau_R$, with a simulated spectrum (dotted) for a methyl group, perturbed by a fourth spin in linear arrangement by $\xi = 0.14$ (see Fig. 30a).

From the SQ MAS sideband pattern of the methyl protons (Fig. 33b), a proton-pair coupling of $D_{\text{pair}} = 2\pi \cdot 8.8$ kHz, corresponding to an interproton distance of $r_{\text{pair}} = 0.19$ nm, is determined with high accuracy. However, being dominated by the intramethyl couplings, the SQ MAS spectrum is not sensitive enough to the perturbation arising from the OH proton to allow the determination of the latter. In contrast to SQCs, methyl TQCs are extremely sensitive to extramethyl couplings in that they give rise to odd-order MAS sidebands in methyl TQ spectra via the ERM mechanism. The experimental spectrum indeed shows such first-order sidebands (Fig. 33c), from the relative intensity of which an effective perturbation of $\xi \approx 0.14$ can be determined. Note that, although the ERM sidebands are

clearly present in the methyl spectrum, there is no evidence for a "mixed" ($CH_3 + H$) TQC. This is also obvious from the full two-dimensional sideband pattern shown in Fig. 34c. Hence, the determination of the four-spin topology requires DQ MAS sideband patterns or, conversely speaking, TQ spectra allow efficient filtering of pure methyl signals.

Consider first the two-dimensional DQ subspectrum (in Fig. 34a) at the first-order DQ MAS sideband of the full pattern which is displayed in Fig. 34b. As has been described in Section 3.4 for rotor-synchronized two-dimensional DQ spectra, the DQ peaks allow the different DQCs and the involved spins to be identified, and from their signal intensities relative dipolar couplings strengths can be estimated. The subspectrum displayed in Fig. 34a, however, only provides qualitative insight into the dipolar pair couplings, since it is cut out of the full two-dimensional pattern instead of being integrated over all sidebands. For example, the **AA** peak is far too weak in Fig. 34a, because the methyl DQ pattern has an intense centerband, while in the case of a typical pair-like DQ pattern, the spectral intensity is concentrated the first-order sidebands. As is expected for the four-spin geometry depicted in Fig. 32b, the pure methyl DQ signal (**AA**) is accompanied by the two cross peaks of the methyl-OH DQC (**AB**). Moreover, there are considerably weaker DQCs between methyl and residual aromatic protons **C** and **C**′ as well as very weak DQCs involving solely residual protons **A**, **C**, and **C**′. As a side aspect, it is interesting to note that the protons **C** and **C**′ only form mixed **CC**′ DQCs, but no **CC** or **C**′**C**′ DQCs. From this feature, it can be concluded that the ^{1}H signals **C** and **C**′ arise from neighboring protons which are attached to the same benzene ring. The following discussions focus on the strongest DQ signals of the methyl coherence **AA** and its perturbation **AB**.

The DQ spectrum displayed in Fig. 35 consists of the MAS sideband patterns of two different DQCs, i.e., the pure methyl DQC and the mixed methyl-OH DQC. Although the high spectral resolution inherent to the model sample allows the spectra to be recorded at the relatively low MAS frequency of 7 kHz, intense DQ signals and MAS sideband patterns are also obtainable under high-speed MAS conditions when the DQ excitation time is extended by means of recoupling pulse sequences. Since, from the SQ and TQ MAS sideband patterns, the intramethyl coupling as well as the effective perturbation is already known, the evaluation of the DQ MAS pattern can now focus on the details of the four-spin geometry, i.e., the angle θ and the precise distance r_{pert} between the fourth spin and the center of the three methyl protons. In Fig. 36, the experimental spectrum (Fig. 35) is compared to a series of simulated spectra for different θ and r_{pert}, showing the marked sensitivity of the pattern to the geometrical parameters. Note that there are no ambiguities for the parameter pair $(\theta, r_{\text{pert}})$, because the angle and the distance affect different lines of the pattern. The best agreement is achieved for $r_{\text{pert}} = 0.30 \cdots 0.32$ nm and $\theta = 40 \cdots 50^\circ$.

The result $r_{\text{pert}} = (0.31 \pm 0.02)$ nm and $\theta = 45^\circ \pm 5^\circ$ agrees well with the values $r_{\text{pert}} \approx 0.33$ nm and $\theta \approx 44^\circ$ obtained from the X-ray structure analysis. Apart from the general difficulty

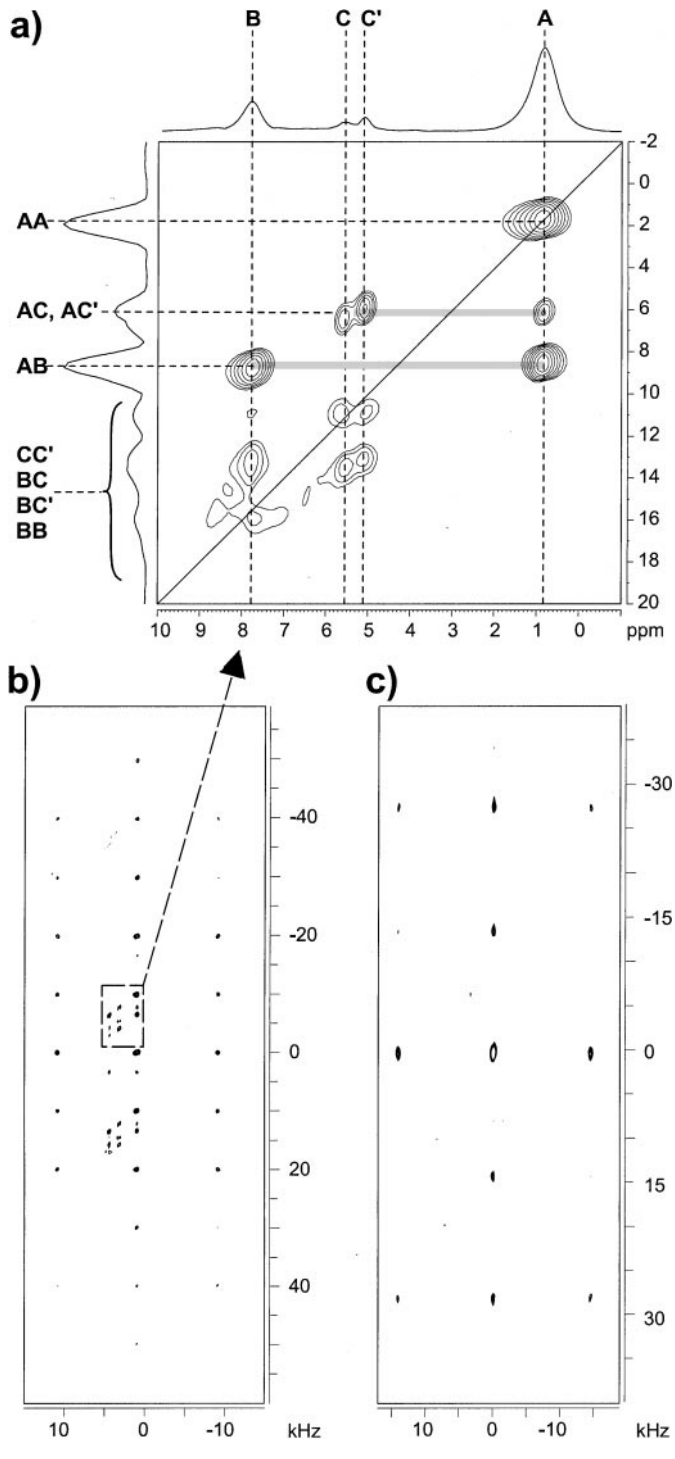

FIG. 34. (a) Two-dimensional ^{1}H DQ spectrum of acetonitrile in hydroquinone, recorded under MAS at 10 kHz with $\tau_{exc} = \frac{1}{2}\tau_R$. The subspectrum at the first-order DQ MAS sideband is shown, which allows—analogously to the rotor-synchronized two-dimensional spectra—the different DQCs to be identified. (b) Full two-dimensional MAS sideband pattern of the DQ spectrum displayed in (a). (c) Full two-dimensional MAS sideband pattern of the TQ spectrum, recorded under MAS at 14 kHz with $\tau_{exc} = \frac{1}{2}\tau_R$.

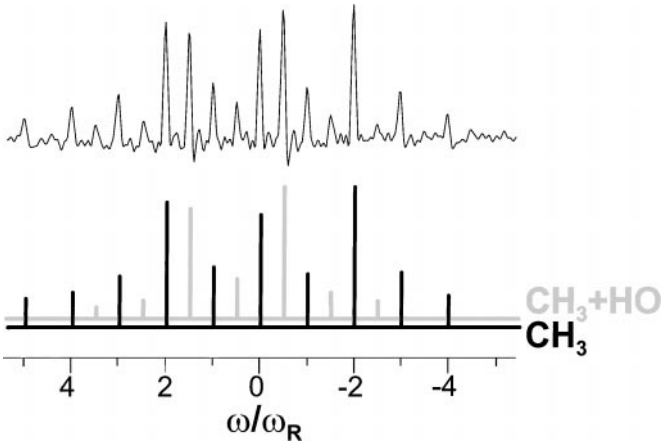

FIG. 35. ^{1}H DQ MAS sideband pattern of acetonitrile in hydroquinone, recorded under MAS at 7 kHz with $\tau_{exc} = \frac{1}{2}\tau_R$. The pattern consists of the two subpatterns of the pure methyl DQC and the mixed methyl-OH DQC. These are schematically depicted below.

of precisely locating protons using X-ray techniques, the distance determined by our NMR measurements deviates from the X-ray result according to what is expected when comparing both methods, because they operate on entirely different time scales and therefore depend on different averaging processes. While in scattering methods internuclear distances are averaged according to $\langle r^{-1}\rangle$, the dipolar coupling depends on such distances according to $\langle r^{-3}\rangle$. Consequently, with respect to vibrational processes, NMR methods detect a higher moment (*54, 61*). It is well known, for example, that NMR yields the internuclear distance of C–H bonds by about 5% longer than X-ray or neutron scattering.

To conclude our NMR investigations of the four-spin model compound, Fig. 37 gives an overview of experimental DQ and TQ MAS spectra recorded with excitation times $\tau_{exc} = \frac{1}{2}\tau_R$ at different MAS frequencies. These spectra are compared to simulated patterns which are based on the four-spin system depicted in Fig. 32 with $r_{\text{pert}} = 0.31$ nm and $\theta = 45^\circ$. The experimental and simulated patterns agree perfectly, reflecting the four-spin topology consistently, although a minor difference can be seen in Fig. 37c: The "mixed" ($CH_3 + OH$) signal is weaker in the experiment than in the simulation. At this point, the limitations of the experimental approach become clear, since an excitation time of $\tau_{exc} = \frac{1}{2}\tau_R = 35\,\mu$s is very short for the weak dipolar coupling underlying the (CH_3 + OH) DQC, resulting in a considerable experimental error. Therefore, the experimental conditions have to be carefully chosen in accordance to the dipolar coupling range of interest, and the consistency of the results needs to be checked.

3.7. Slow Dynamics and MQ Exchange Spectra

In the previous sections, we have demonstrated that MQ MAS sideband patterns can be used to measure the strengths and

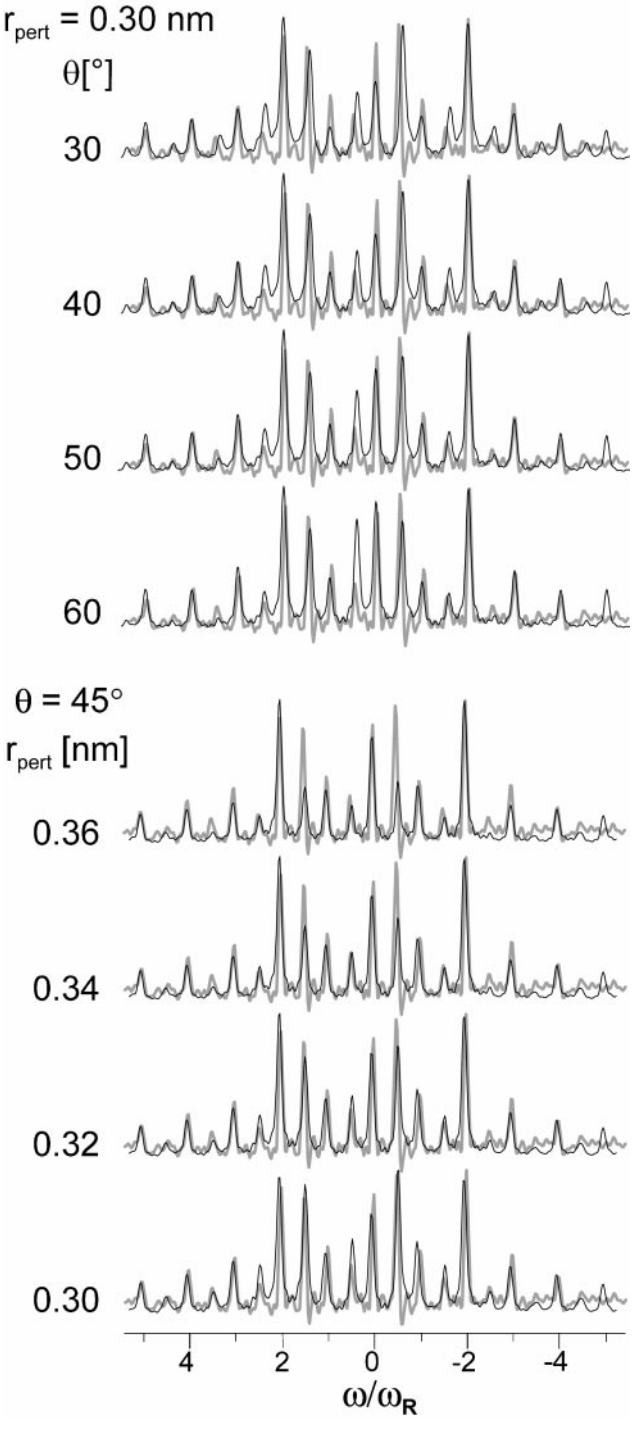

FIG. 36. Comparison of the experimental ^{1}H DQ MAS spectrum of acetonitrile in hydroquinone (shaded in the background) with simulated spectra. The experiment was performed under MAS at 7 kHz with $\tau_{exc} = \frac{1}{2}\tau_R$. The simulations are based on the four-spin geometry shown in Fig. 32, varying the distance r_{pert} about the result obtained from the SQ and TQ MAS spectra (see Figs. 33b and 33c), while the angle θ is determined solely from the DQ MAS pattern.

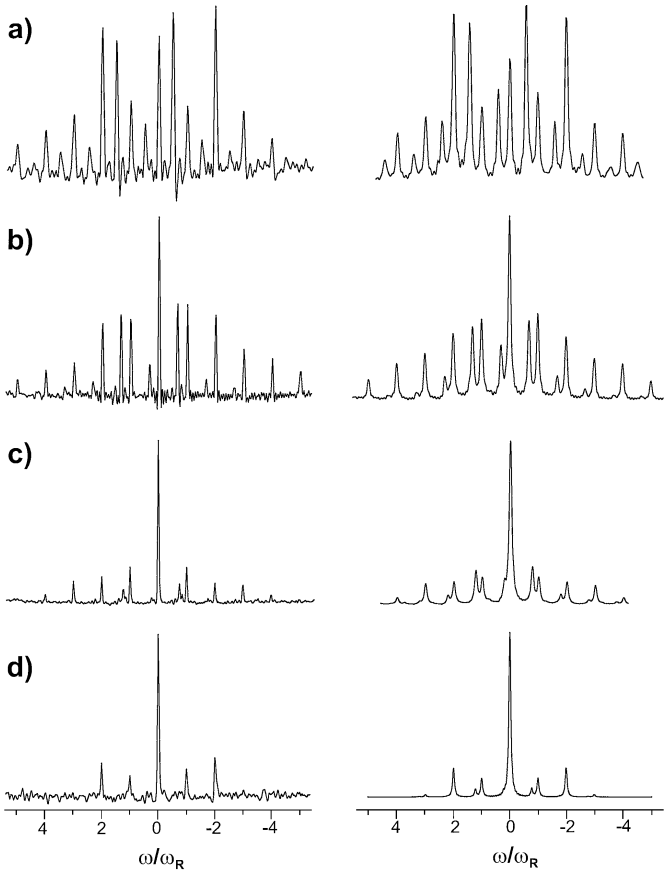

FIG. 37. Overview of experimental (left) and simulated (right) DQ and TQ MAS spectra of acetonitrile in hydroquinone, recorded with $\tau_{exc} = \frac{1}{2}\tau_R$ at different MAS frequencies: (a, b, c) DQ at 7, 10 and 14 kHz, and (d) TQ MAS at 14 kHz. The simulations are based on the four-spin model system depicted in Fig. 32 with $r_{\text{pert}} = 0.31$ nm and $\theta = 45^\circ$.

orientations of dipolar coupling tensors. This information can be exploited not only to investigate the structure and geometry of spin systems, but also to elucidate processes of slow molecular dynamics. In the following, we will briefly introduce the principal design of such experiments as well as the procedure for evaluating the resulting sideband patterns (*99*).

In the context of NMR, the distinction between fast and slow dynamics depends on the strength of the respective dipolar coupling, meaning that processes on time scales faster than $\tau \leq 10^{-5}$ s are considered fast, while motions on time scales on the order of $\tau \geq 10^{-3}$ s are slow. Motions on time scales 10^{-5} s $\leq \tau \leq 10^{-3}$ s, in general, interfere with dipolar MQ MAS experiments and can hence not be described by the simple approximations valid in the fast and slow regimes, which assume either a fast averaging process or a static system, respectively. In the previous considerations, the case of a fast motion has already been discussed for the three protons of fast rotating methyl groups. In general, such processes can simply be taken into account by replacing the static dipolar interaction tensor with the motionally averaged one.

In order to investigate slow motions by NMR, a wealth of so-called exchange experiments have been designed during the past decades (*95*), which are, in principle, all based on the same experimental scheme: During two evolution periods, a spin evolves under an anisotropic interaction, with the tensor orientation being probed by the nuclear resonance frequency each time. These two periods are separated by a "mixing period," during which the slow molecular motion of interest is allowed to occur. In this way, the orientation of the interaction tensor before and after the motional process is spectrally correlated.

For this purpose, in standard applications, the anisotropies of CSA and quadrupolar tensors are routinely used, in most cases detecting ^{13}C and ^{2}H resonances, respectively. From the formal analogy of first-order quadrupolar interactions and dipolar couplings, it is clear that the dipolar tensors of spin pairs, as well as that of fast rotating methyl groups, can serve as probes for molecular orientations in the same way, provided that additional dipolar couplings of the spins of interest to neighboring spins are sufficiently reduced. Due to the reliance on this condition, the dipolar interaction has to date not been widely exploited for investigations of slow molecular motions. However, based on the improved dipolar decoupling conditions afforded by fast MAS techniques, our theoretical considerations of dense dipolar-coupled networks have revealed the dominant role of two-spin correlations. Therefore, in the presence of fast MAS, the dipolar spin-pair approach opens up the possibility for exchange experiments which use dipolar tensors as probes for molecular reorientations.

3.7.1. Scheme of DQ–DQ MAS Exchange Experiments

In dipolar MQ MAS experiments, the MAS sideband pattern, generated by the rotor encoding of the MQ reconversion period (RRE mechanism, see Section 3.5.1), allows the determination of dipolar coupling strengths in principle without requiring any spectral evolution period. Consequently, instead of using nuclear resonance frequencies, the RRE sideband patterns can serve as a sensor for coupling strengths and, in this way, for tensor orientations. Hence, two such RRE patterns can be correlated by catenating two standard MQ MAS experiments and introducing a mixing time in between. Thus, the extension of MQ MAS experiments to MQ–MQ MAS exchange experiments is very straightforward, and the resulting experimental scheme is depicted in Fig. 38. Note that, due to the fundamental role of rotor modulations in this experimental approach, each of the two combined MQ experiments must start with the same initial phase of the rotor. Experimentally, this is accomplished by triggering the first and the second MQ excitation pulse train by the rotor signal.

By introducing a mixing period, during which the slow-motional process of interest is allowed to occur, between two "standard" MQ MAS experiments, the experiment becomes three-dimensional. To maintain reasonably short experiment times as well as manageable data-set sizes, the exchange experiment can be performed in a reduced three-dimensional version

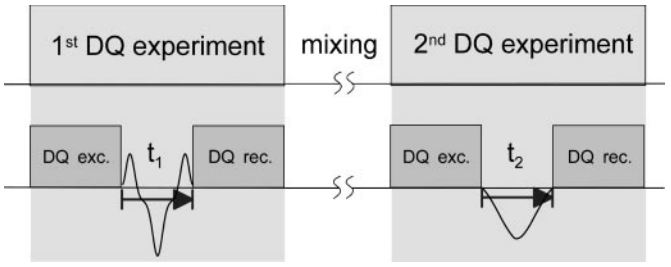

FIG. 38. Schematic representation of a dipolar MQ–MQ MAS exchange experiment.

by incrementing t_1 and t_2 synchronously. In the following, we will focus on this two-dimensional type of DQ–DQ exchange experiment.

3.7.2. MAS Sideband Patterns of DQ–DQ Exchange Experiments

In a standard two-dimensional DQ MAS spectrum of a dipolar-coupled spin pair (ij), the RRE mechanism generates sidebands by modulating the time signal according to (see Section 3.5.1)

$$S_{DQ}^{(ij)}(t) \propto \sin \Omega_{exc} \cdot \sin \Omega_{rec}, \qquad [124]$$

where $\Omega_{exc} = \Omega_D(0, \tau_{exc})$ and $\Omega_{rec} = \Omega_D(\tau_{exc} + t_1, 2\tau_{exc} + t_1)$. Since τ_{exc} is an integer number of rotor periods τ_R, the integrated spatial parts of the dipolar coupling, Ω_{exc} and Ω_{rec}, differ only by the t_1-shift of the integration limits, which corresponds to a difference of $\omega_R t_1$ between the excitation and reconversion rotor phases. Catenating two DQ MAS experiments according to the scheme of Fig. 38 results in an additional rotor modulation of the observed time signal by the same factors as in Eq. [124], which can be formally written as a simple multiplication of the form

$$S_{DQ-DQ}^{(ij)}(t) \propto \underbrace{\sin \Omega_{exc}^{(1)} \cdot \sin \Omega_{rec}^{(1)}}_{\text{first DQ exp.}} \cdot \underbrace{\sin \Omega_{exc}^{(2)} \cdot \sin \Omega_{rec}^{(2)}}_{\text{second DQ exp.}}, \qquad [125]$$

where $\Omega_{exc}^{(1,2)} = \Omega_D(0, \tau_{exc})$ and $\Omega_{rec}^{(1,2)} = \Omega_D(\tau_{exc} + t, 2\tau_{exc} + t)$ and $t = t_1 = t_2$ because of the reduced three-dimensional form of the experiment. Note the absence of any dipolar evolution, because the system under consideration is an isolated spin pair, whose DQC does not evolve under the mediating dipolar coupling. The superscripts 1 and 2 indicate that the spatial parts of the dipolar interaction before and after the mixing time might differ as a result of a molecular motion occurring during the mixing period.

In the presence of a strong static magnetic field $\boldsymbol{B}_0$, the strength $D^{(ij)}$ of a dipolar coupling depends on the orientation of the internuclear vector r_{ij} according to $D^{(ij)} \propto (3\cos^2\theta_{ij} - 1)$, where θ_{ij} denotes the angle between r_{ij} and $\boldsymbol{B}_0$. Consequently, when the orientation of the dipolar coupling tensor has changed from $\theta_{ij}^{(1)}$ to $\theta_{ij}^{(2)}$ during the mixing period, the integrated spatial parts $\Omega_{exc}^{(1)}$, $\Omega_{rec}^{(1)}$, and $\Omega_{exc}^{(2)}$, $\Omega_{rec}^{(2)}$ contain the factors $(3\cos^2\theta_{ij}^{(1)} - 1)$ and $(3\cos^2\theta_{ij}^{(2)} - 1)$, respectively. Therefore, the rotor modulation (see Eq. [125]) and the resulting sideband pattern depend on the difference $\Delta\theta = \theta_{ij}^{(2)} - \theta_{ij}^{(1)}$ between the final and the initial orientation of the internuclear vector r_{ij}. Note that, under MAS conditions, this $\Delta\theta$ dependence splits into a twofold $(\Delta\beta, \Delta\gamma)$ dependence, because then the coordinate transformation needs to be carried out first from the principal axes system into the rotor-fixed frame, and second from the rotor-fixed frame into the laboratory frame (see Eq. [27] in Section 2.3). The reorientation process, however, can still be completely characterized by a single angle $\Delta\theta$.

In order to be able to detect the difference $\Delta\theta$ by the DQ–DQ MAS sideband pattern, the RRE sideband pattern of each individual DQ experiment must allow the determination of the underlying pair-coupling strength, which means that it must consist of at least first- and third-order sidebands, corresponding to $D^{(ij)}\tau_{exc}/2\pi > 0.5$. The following discussion of DQ–DQ MAS sideband patterns and their evaluation will be based, as an example, on a dipolar pair coupling of $D^{(ij)} = 2\pi \cdot 8$ kHz, which is, for DQ excitation and reconversion, subject to a back-to-back recoupling pulse sequence of duration $\tau_{exc} = \tau_{rec} = \tau_R$, while MAS is applied at 8 kHz, providing $D^{(ij)}\tau_{exc}/2\pi = 1$.

Figure 39a shows the MAS sideband patterns obtainable in such a DQ–DQ exchange experiment. The patterns consist of

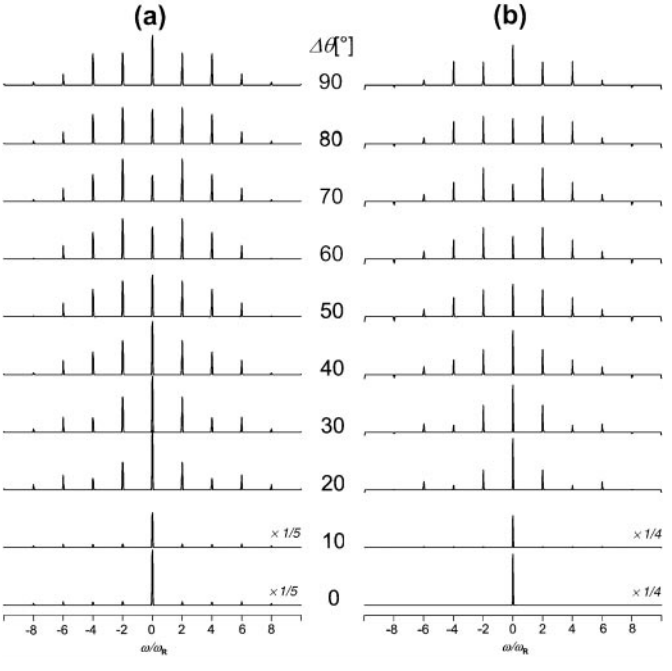

FIG. 39. (a) MAS sideband patterns of DQ–DQ exchange experiments with $D^{(ij)}\tau_{exc}/2\pi = 1$. The pattern depends characteristically on the angle of the reorientation occurring during the mixing time. (b) Pattern of the same experiments as in (a), but with the time signals being divided by the time signal for $\Delta\theta = 0$.

even-order sidebands only and clearly depend on the change of the angle θ which is due to a molecular reorientation process during the mixing time. Hence, the pattern allows the "jump angle" $\Delta\theta$ to be determined within the range from 0° to 90°. However, in practice, not only the angle of the reorientation but also the fraction of molecules which undergo this motional process needs to be determined. As a very simple approach, the observed time signal can be divided by the signal expected for $\Delta\theta = 0$. In this way, the signal of all spin pairs, which are oriented at the same angle θ before and after the mixing time, is transferred completely to the centerband, while the presence of sidebands indicates a motional process involving $\Delta\theta \neq 0$. The MAS sideband patterns resulting from this procedure are displayed in Fig. 39b.

Thus, after this analytical procedure, the whole pattern consists of two parts: first, a sideband pattern, from which the "jump angle" $\Delta\theta$ can be determined and, second, an additional contribution to the centerband, whose intensity relative to the sideband pattern reflects the ratio of spin pairs with $\Delta\theta \neq 0$ and $\Delta\theta = 0$. The latter case means either that the spin pair has remained in its initial orientation throughout the experiment or that, after a first jump, it has reversed into its initial orientation by a subsequent second jump. In this context, note that the angular dependence of Ω_{exc} and Ω_{rec} according to (effectively) $\sin 2\Delta\theta$ restricts the range of sensitivity to $\Delta\theta = 0^\circ \ldots 90^\circ$. Figure 40 shows the dependence of the centerband and sideband intensities on the jump angle $\Delta\theta$. Obviously, the intensity distribution allows the jump angle to be identified unambiguously, and the accuracy expected for experimental determinations can be estimated to be about $\pm 5^\circ$. An important feature of the DQ–DQ exchange method is that the sensitivity of the experiment can be increased by increasing the excitation time τ_{exc} and hence $D^{(ij)}\tau_{exc}$. In this way, more sidebands are observable over a wider spectral range.

The evaluation of the sideband patterns of DQ–DQ exchange spectra is illustrated in Fig. 41, using a spin-pair model sample with well-known motional properties as an example: The experimental pattern, displayed in Fig. 41c, has been recorded on ^{13}C–^{13}C spin pairs in crystalline polyethylene (PE), whose chains contain 4% of such double-labeled pairs. The homonuclear dipolar coupling between these two carbon atoms is approximately $D^{(ij)} = 2\pi \cdot 2$ kHz, so that the case of $D^{(ij)}\tau_{exc}/2\pi = 1$ discussed above can be achieved by applying MAS at 8 kHz and using $\tau_{exc} = 4\tau_R$ for the excitation and reconversion of the ^{13}C DQCs. Furthermore, the PE chains are known to undergo, at room temperature, a slow 180° jump motion, which results in a reorientation of the carbon pairs along the chain of $\Delta\theta \approx 112^\circ$ (*59*). Note that, in the DQ–DQ exchange experiment, this angle will be detected as a reorientation of $\Delta\theta \approx 68^\circ$. The ^{13}C DQ–DQ MAS experiment is carried out analogously to the ^{1}H case. In addition, ^{13}C magnetization is enhanced by a preceding Hartmann–Hahn cross-polarization (*53*) from protons to carbons, and heteronuclear dipolar decoupling is accomplished by applying a broadband RF field to the protons throughout the experiment except for the mixing time.

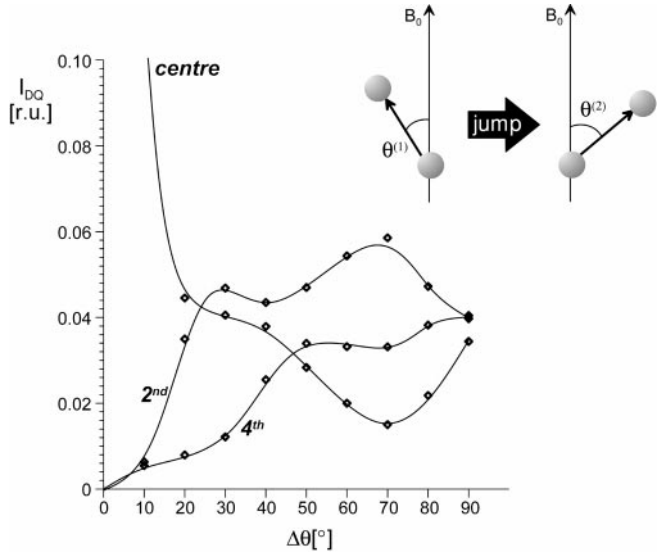

FIG. 40. Intensity of the centerband and the second- and fourth-order sidebands of the DQ–DQ MAS sideband patterns shown in Fig. 39b. In the inset, the reorientation process giving rise to $\Delta\theta = \theta_{ij}^{(2)} - \theta_{ij}^{(1)}$ is depicted schematically.

The MAS sideband pattern of the ^{13}C DQ–DQ exchange experiment (see Fig. 41c) has been obtained for a mixing time of 300 ms at room temperature and, subsequently, by dividing the experimental time signal by the theoretical time signal for $\Delta\theta = 0$. Obviously, the experimental pattern agrees well with a calculated pattern (note that the experiment yields even the weak negative sidebands of eighth order), consisting of two contributions: first, a sideband pattern for a $70^\circ \pm 5^\circ$ reorientation and, second, additional centerband intensity of the same relative weight. Hence, the experiment yields the expected jump angle. Furthermore, the 1 : 1 ratio of the two contributions means that the motional process has, at a mixing time of 300 ms, already reached its equilibrium stage, i.e., an equal distribution of forward and forward–backward jumps. This observation is again in agreement with the chain jump dynamics, as have been determined by Hu *et al.* (*59*). A full investigation of the jump dynamics by means of DQ–DQ MAS exchange spectroscopy is given in (*99*).

In conclusion, the extension of the DQ MAS method to an exchange experiment as well as the evaluation of the observed DQ–DQ MAS sideband patterns is straightforward. Such DQ–DQ exchange patterns combine information about both the angle and the rate of the slow molecular reorientations. Furthermore, the experiment allows different resonance lines and sideband patterns to be resolved in the spectrum. In this way, different spin pairs can be observed at the same time, so that the method does not rely on site-specific spin labels and is therefore applicable to multiply labeled samples or ^{1}H systems. In general, the combination of multidimensional NMR techniques (see, e.g., (*95*) or (*31*), Chap. 6) with MQ MAS methods appears to be a promising approach for future methodological developments in solid-state NMR.

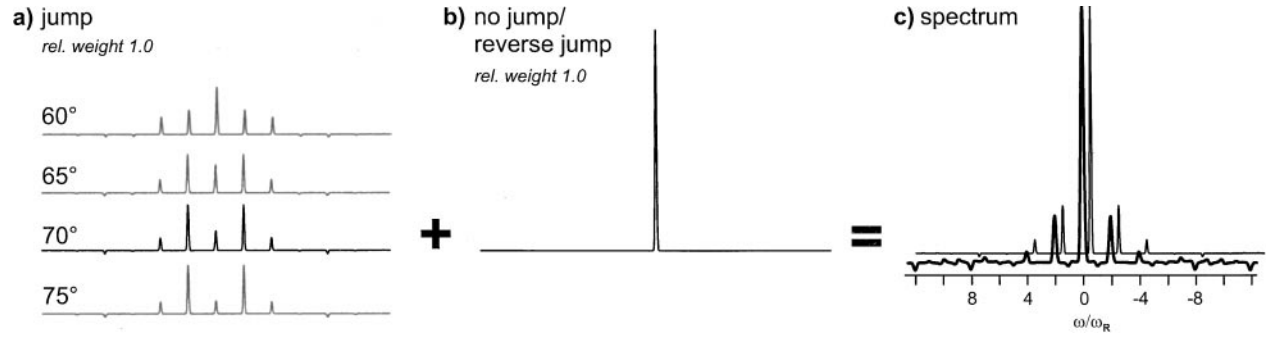

FIG. 41. Decomposition of the MAS signal pattern of a DQ–DQ exchange experiment into (a) the spinning sidebands, from which the angle of the reorientation can be determined, and (b) the additional centerband intensity, from the relative weight of which the rate of the reorientational process can be evaluated. (c) Experimental sideband pattern of a ^{13}C–^{13}C DQ–DQ exchange experiment performed on ^{13}C–^{13}C pairs in crystalline polyethylene, whose chains have been enriched with 4% of such ^{13}C–^{13}C pairs. The excitation time was $\tau_{exc} = 4\tau_R$ with MAS being applied at 8 kHz, resulting in $D^{(ij)}\tau_{exc}/2\pi = 1$. The temperature was 298 K, and the mixing time was set to 300 ms.

4. APPLICATIONS

In this Section, we will give an overview of the investigations carried out to date applying ^1H MQ MAS spectroscopy in the solid state. Following methodological work, the main focus of ^1H MQ MAS research has been on structural investigations of supramolecular structures, in particular on hydrogen bonds, since the combined information of chemical shifts and dipolar coupling strengths accessible by ^1H DQ NMR is perfectly suited to probing such noncovalent interproton interactions. In addition to this field of interest, the resolution enhancement afforded by fast MAS techniques allows ^1H nuclei to be used as probes for vicinal π-electron systems and, in this way, allows unexpectedly far reaching structural conclusions to be drawn for extended aromatic molecules. Although such "ring-current" effects on ^1H resonances are well known in NMR (*113*), the poor spectral resolution prevented them from being exploited in the solid state. Combining the applications to hydrogen bonds and π-electron systems, ^1H MQ MAS spectroscopy commends itself as a versatile tool for the elucidation of two interactions primarily responsible for the induction of supramolecular order.

Apart from such structural information obtained on basically rigid systems, ^1H MQ MAS methods, i.e., MAS sideband patterns and DQ buildup curves, provide detailed and quantitative insight into molecular dynamics, in particular for partially ordered systems. In this way, molecular motions as well as chain dynamics have been analyzed in liquid-crystalline phases and polymer melts, respectively.

4.1. Hydrogen Bonds

Multiple hydrogen bonds are particularly well suited to ^1H MQ MAS NMR investigations, since in general they combine a pronounced low-field chemical shift of the resonance frequencies with spatial proximities of protons. The ^1H chemical shifts of hydrogen-bonded protons make the resonance lines not only relatively easy to resolve under MAS conditions, but they also indicate the strength of the hydrogen bond, in which the respective proton is involved (*52*, *10*). Furthermore, based on the spectral resolution, the strengths of the dipolar couplings between distinct hydrogen-bonded protons can be measured separately by DQ MAS methods. In this way, a wealth of structural information is accessible from unaltered as-synthesized samples; in particular, there is no reliance on isotopic labeling, e.g., by ^2H nuclei. The latter are, though twice as heavy as protons, an inevitable prerequisite for neutron scattering approaches.

4.1.1. Pairs of Hydrogen-Bonded Protons

One of the first samples used for demonstrating the approach of ^1H DQ MAS spectroscopy was malonic acid (*46*), because its two ^1H resonance lines are already well resolved under moderate MAS, and each of its two proton species, i.e., aliphatic CH_2 and acidic COOH, form dipolar-coupled homonuclear spin pairs, with the aliphatic proton pair being inherent to the molecular CH_2 unit and the acidic proton pair being due to the dimeric arrangement of the carboxylic acid groups (see Fig. 42a). Hence, the pairs are part of either a covalent or a noncovalent structural motif. The crystal structure of malonic acid reveals that both proton pairs are separated from each other to such an extent that interfering effects of interpair couplings are, though not negligible, considerably smaller than the dominating intrapair couplings. Hence, under MAS, the proton pairs can be well decoupled from each other, and in this respect a spin-pair model character prevails in malonic acid.

In Fig. 42b, the static ^1H one-pulse spectrum of malonic acid is compared to the spectrum obtained under MAS at 13 kHz, demonstrating the resolution enhancement afforded by MAS. The MAS sideband patterns of both proton species are also clearly resolved and can be evaluated separately, yielding homonuclear dipolar coupling strengths of $D^{CH_2} = 2\pi \cdot 20$ kHz and $D^{COOH} = 2\pi \cdot 10$ kHz, respectively, in the spin-pair approximation. These couplings correspond to interproton distances of $r_{CH_2} = 0.18$ nm and $r_{COOH} = 0.23$ nm. From the SQ MAS

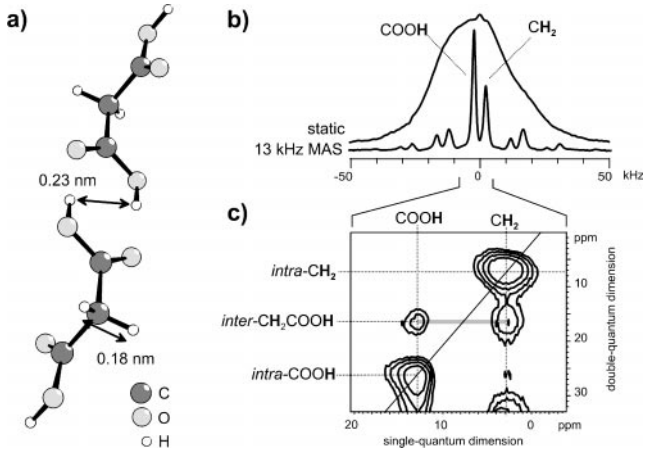

FIG. 42. (a) Dimeric arrangement of the carboxylic acid groups in the crystal structure of malonic acid. The interproton distances obtained from ^{1}H SQ and DQ MAS spectra are also shown. (b) ^{1}H one-pulse spectra of malonic acid under static conditions and under MAS at 13 kHz. (c) ^{1}H DQ MAS spectrum of malonic acid from Ref. (*46*), recorded for $\tau_{exc} \approx 35\ \mu$s under MAS at 13 kHz at a ^{1}H Larmor frequency of 500 MHz. The subspectrum at the first-order MAS sideband in the DQ dimension is displayed.

patterns, however, it can still be argued that there is, apart from the expected pair couplings, an additional contribution from "interpair" couplings, i.e., from pairs consisting of an aliphatic and an acidic proton. These interactions can be unambiguously identified in the DQ MAS spectrum, which is shown in Fig. 42c. Although the spectrum is clearly dominated by the two peaks on the diagonal, indicating pure aliphatic and acidic DQCs, respectively, there is a weak symmetric cross peak due to "mixed" DQCs. Since, in the DQ spectrum, the signals are spectrally resolved according to the spin species involved in the underlying dipolar couplings, the respective coupling strengths can be evaluated from the DQ MAS sideband pattern separately and hence to a higher accuracy than from the SQ MAS pattern (*46*).

Concerning the applicability of ^{1}H DQ MAS spectroscopy for the elucidation of hydrogen-bonding schemes, it is clear from the simple case of malonic acid that a purely acidic ^{1}H DQ signal arising from "noncovalent" acidic proton pairs allows spatial proximities of these protons to be straightforwardly identified, which means that in most cases the DQ signal can serve as a simple and reliable proof for the existence of hydrogen-bonded acid dimers.

4.1.2. Arrays of Multiple Hydrogen Bonds

After considering the double hydrogen bonds present in carboxylic acid dimers, we now turn to investigations of more extended arrays of hydrogen bonds. Such multiple hydrogen bonds play an increasingly important role in the design of supramolecular architectures (*68*) and, hence, there is increasing demand for a technique elucidating the structure of such noncovalent bonds and their thermal or dynamical properties in solid-state samples. As an example, we briefly present the basic results obtained for systems based on ureido-pyrimidinone moieties, which are capable of forming a quadruple hydrogen bond. In the group of Meijer, these units have been successfully used to synthesize supramolecular polymers (*102*). Figure 43 shows the chemical structures of the ureido-pyrimidinone moieties and the quadruple hydrogen bonds of the compounds discussed in this section, i.e., the monomers **2** and the polymers **3**. Due to the tautomerism of the structure, both compounds contain the ureido-pyrimidinone moiety either in a keto or enol form, corresponding to a 4[1H]-pyrimidinone or a pyrimidin-4-ol six ring, respectively. Using the labels **2** and **3** for the monomer and polymer, respectively, the keto and the enol tautomer are distinguished by the letters **a** and **b** following the number.

From the ^{1}H one-pulse spectra of compounds **2a** and **2b**, recorded under MAS at 30 kHz at a ^{1}H Larmor frequency of 700 MHz (Fig. 44), it is clear that the spectral resolution achievable at such high MAS and Larmor frequencies allows all resonance lines of the protons involved in hydrogen bonds to be clearly identified: H^a, H^b, and H^c, while H^d is a "free" aromatic proton. It is even possible to spot slight shifts of the lines between

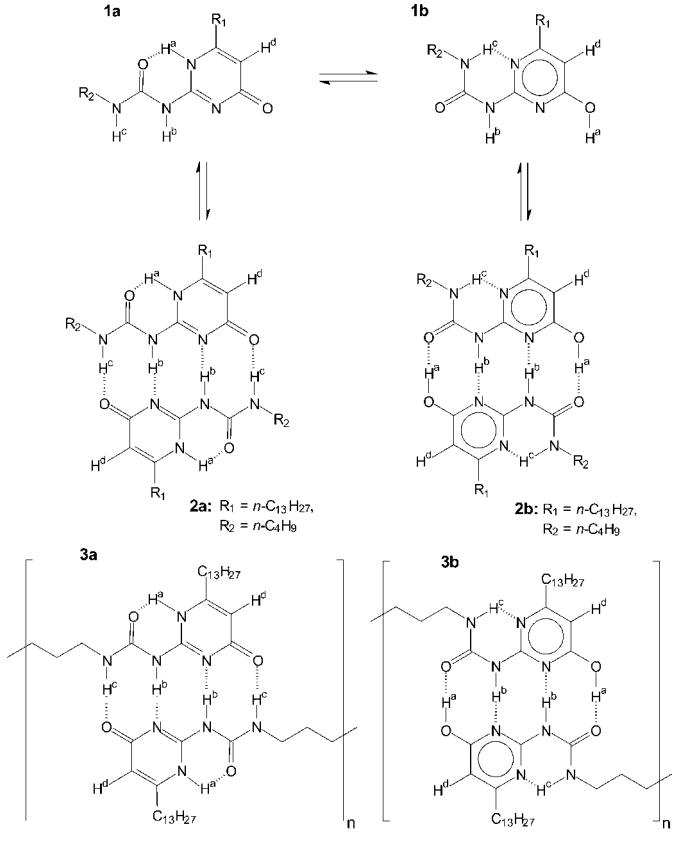

FIG. 43. Tautomeric structures of the ureido-pyrimidinone moiety, which is capable of forming arrays of four hydrogen bonds: free form **1**, hydrogen-bonded form **2** and supramolecular polymer **3** consisting of monomers with an ureido-pyrimidinone moiety on either side of a short linear aliphatic chain. The letters **a** and **b** denote the keto and the enol tautomer, respectively.

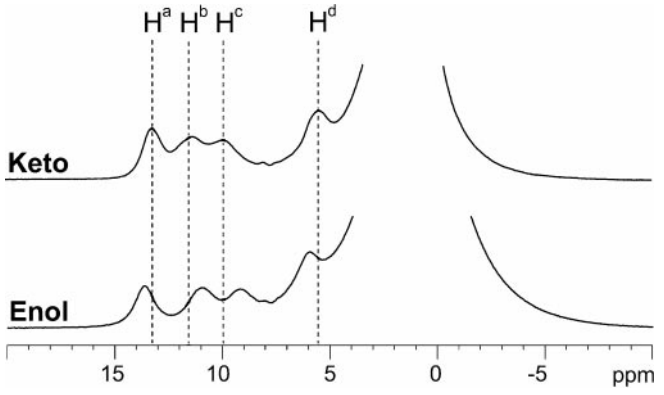

FIG. 44. ^{1}H one-pulse spectra of the compounds **2a** (keto) and **2b** (enol), recorded under MAS at 30 kHz at a ^{1}H Larmor frequency of 700 MHz.

the two tautomers, as is known from solution-state NMR spectra (*11*). However, even such detailed SQ spectra do not provide insight into the actual arrangement of the hydrogen bonds.

Information on the hydrogen bonds can be straightforwardly obtained from the signals in two-dimensional ^{1}H DQ spectra, which allow spatial proximities between proton species to be detected. Such DQ spectra, recorded in a rotor-synchronized fashion (i.e., $\Delta t_1 = \tau_R$), are shown in Fig. 45 for both tautomers of compound **2**. The arrangement of the four hydrogen bonds is unambiguously reflected in the DQ peak pattern in the NH region of the two-dimensional spectrum: The H^c–H^b–H^b–H^c sequence of the protons in the quadruple hydrogen bond of the keto form gives rise to a clear H^b–H^c cross peak and an H^b–H^b diagonal peak, which is not resolved from the adjacent cross peak. These "keto-type" DQ signals are marked by the letter *k* in Fig. 45a. For the enol form with an H^a–H^b–H^b–H^a sequence in the quadruple hydrogen bond, the peak pattern changes characteristically: The H^b–H^c cross peak is replaced by an H^a–H^b cross peak, while the H^b–H^b diagonal peak remains. These "enol-type" DQ signals are well resolved and marked by the letter *e* in Fig. 45b.

In addition to the information about the hydrogen-bonding scheme, the DQ spectra also contain information about all other spatial proton–proton proximities. A noteworthy feature is the presence and the absence of the H^d–H^d diagonal peak in the spectrum of the keto and the enol form, respectively. The presence of an intense H^d–H^d diagonal peak, marked by the letter *p* in Fig. 45a, cannot be explained in terms of an intramolecular coupling. Rather, it indicates that, in the keto form, the packing of molecules gives rise to a short intermolecular distance between two aromatic H^d protons, while in the enol form the packing is different, with the aromatic H^d protons being spatially separated from each other.

The fact that the hydrogen-bonding scheme is so clearly reflected in the DQ signals opens up the possibility of following, in the polymer sample **3**, the tautomeric rearrangement of the ureido-pyrimidinone moiety, which occurs upon heating the polymer **3a**. It turns out that the transition **3a** → **3b** (schematically represented in Fig. 46) is irreversible in the solid state, meaning that the process is of kinetic rather than thermodynamic nature. Although such solid-state investigations can alternatively be carried out by IR spectroscopy, the information

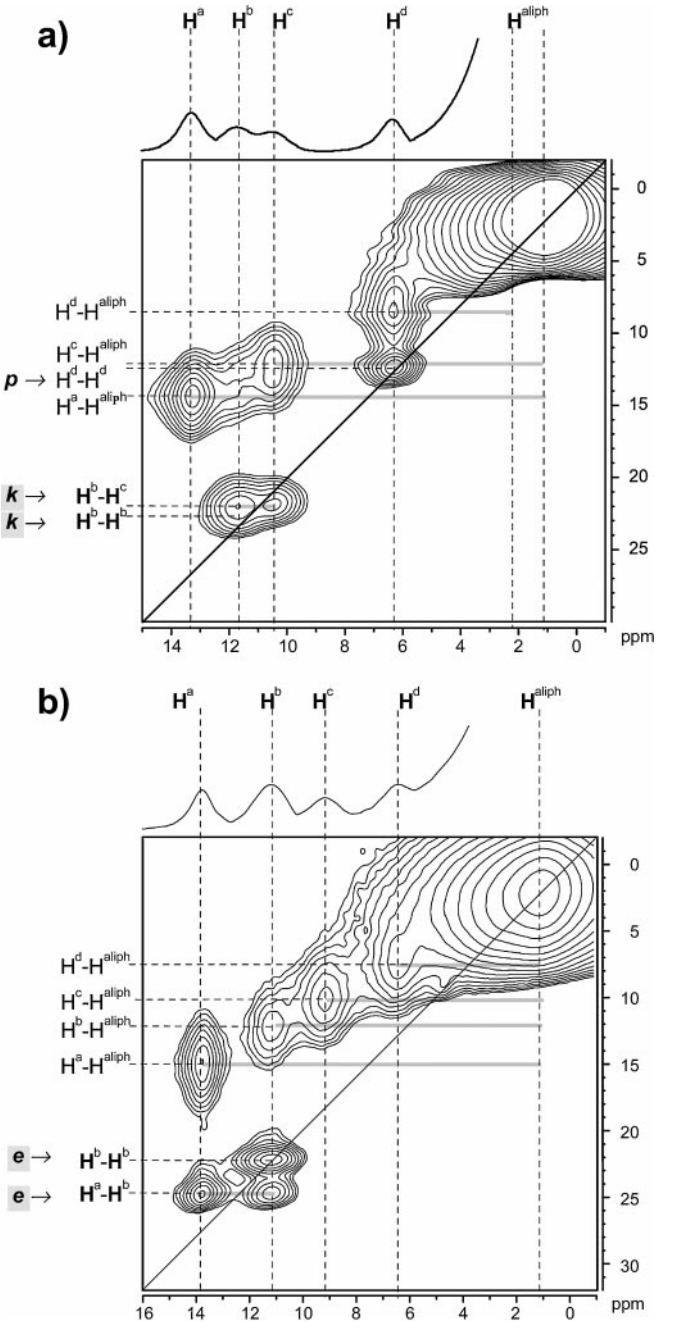

FIG. 45. ^{1}H DQ spectra of the compounds **2a** (a) and **2b** (b), recorded with a DQ excitation time of $\tau_{exc} = \tau_R$ under MAS at 30 kHz at a ^{1}H Larmor frequency of 700 MHz. The peaks of interest are assigned to the protons of the structures, with the letters *k*, *e*, and *p* denoting signals which identify the *k*eto or the *e*nol tautomer or intermolecular *p*acking effects, respectively. The cross peaks at the aliphatic SQ resonance frequency are obscured by baseline distortions due to the intense aliphatic diagonal peak.

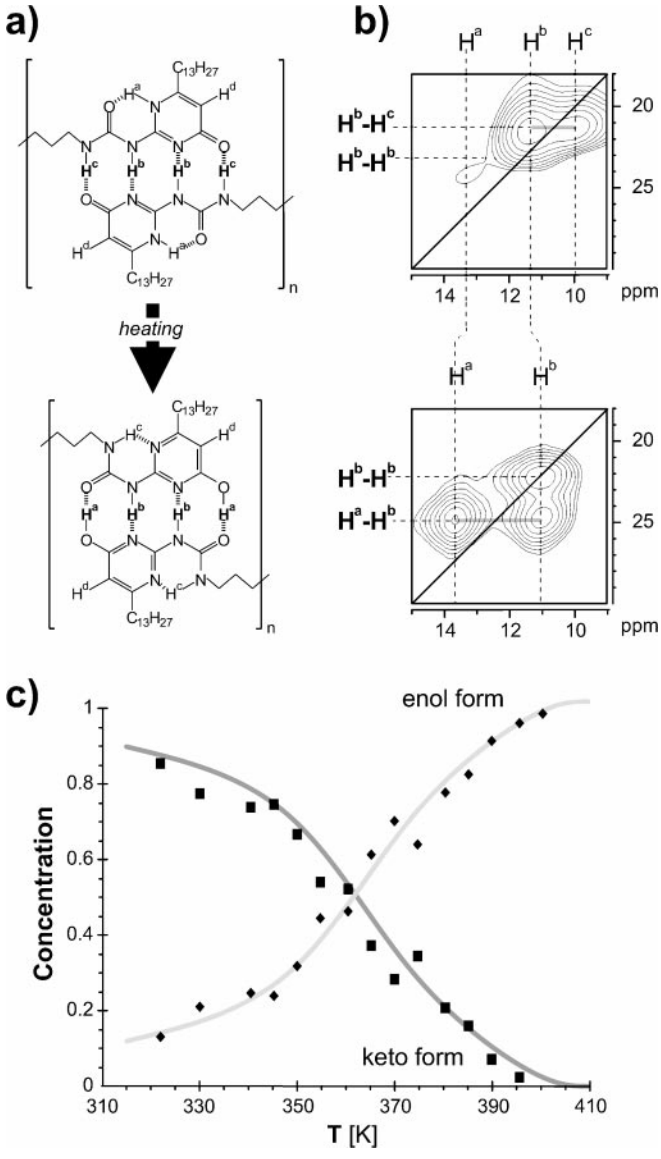

FIG. 46. Tautomeric rearrangement of the ureido-pyrimidinone moieties, observed for the supramolecular polymer, i.e., **3a** → **3b**, upon heating. (a) Molecular structures of the two tautomeric forms. (b) ^{1}H DQ MAS spectra with the characteristic signals of the pure keto and enol state at the start and the end of the transition. (c) Gradual change of the tautomer concentrations with increasing temperature, as determined from ^{1}H DQ signal intensities.

obtainable by IR is less detailed and not quantitative, whereas ^{1}H NMR measurements allow the determination of the kinetic parameters.

In addition to the identification of the type of quadruple hydrogen bond, the actual interproton distances can be determined from DQ MAS sideband patterns. In combination with analogous heteronuclear MQ MAS experiments (see Section 5), the geometry of the four hydrogen bonds can be completely elucidated for both tautomeric structures as well as for all their derivatives.

4.1.3. Identification of Geminate and Chain-like Arrangements

In the previous section, the hydrogen bonds were used for the formation of a supramolecular polymer by linking bifunctional monomers in a noncovalent manner. Besides this, they can also play an important role in determining the physical properties of "classical," i.e., chemically linked, polymers by inducing a supramolecular order to the polymer chains. As an example of such an effect, we will now briefly discuss the case of the polybenzoxazines (*60*), which represent a new type of phenolic resins showing unusual properties potentially relevant for high-performance applications. These interesting material properties are likely to be due to the formation of complex hydrogen-bonded superstructures (*115*). In this context, the investigation of dimeric model systems by ^{1}H MQ MAS techniques revealed that, in these materials, there are two distinct hydrogen-bonding schemes which strongly depend on the size of an alkyl substituent (*97*).

In the following, we will focus on two of these dimeric models: a methyl-substituted and an ethyl-substituted dimer (henceforth referred to as me-dimer and et-dimer, respectively), the chemical structures of which are depicted in Fig. 47a (*26*). Previous investigations by IR spectroscopy, X-ray scattering, and molecular modeling suggested the presence of a complex network of inter- and intramolecular hydrogen bonds between the dimers (*27*). For the me-dimer, it was possible to prepare single crystals, whose analysis provided evidence for a geminate hydrogen-bonded arrangement of the dimers (see Fig. 47b) involving two intra- and two intermolecular hydrogen bonds, but without localizing the protons precisely. From the et-dimer, no single crystals were available.

In Fig. 48a, the effect of MAS on the spectral resolution of the ^{1}H resonance lines is illustrated for the case of the et-dimer. For MAS frequencies above 20 kHz the line at 13.2 ppm can be

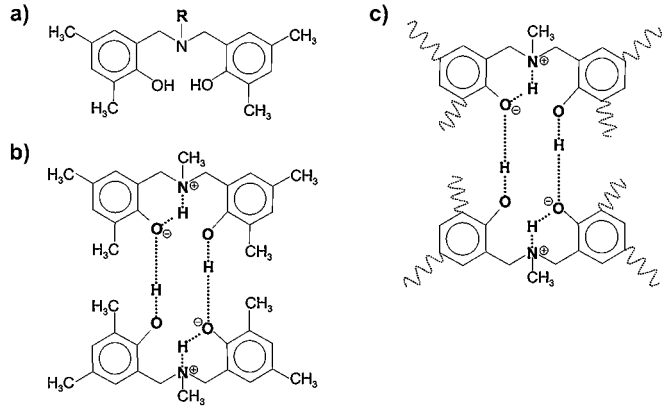

FIG. 47. (a) Dimeric model compounds for polybenzoxazines, with the *n*-alkyl substituent *R* being either $R = CH_3$ or $R = CH_2CH_3$. (b) Hydrogen-bonded pair of two methyl-substituted dimers. (c) Schematic representation of chemically cross-linked structures in the polybenzoxazines.

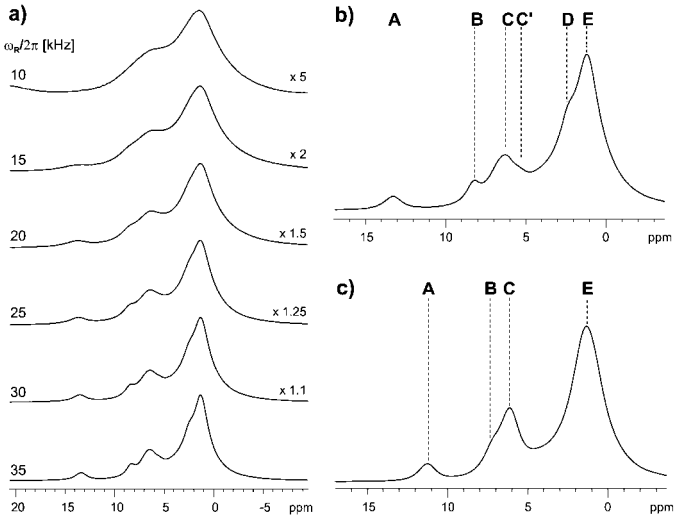

FIG. 48. (a) ^{1}H one-pulse MAS spectra of the et-dimer, recorded for a series of MAS frequencies at a Larmor frequency of 500 MHz. The spectra are magnified according to the factor given on the right. (b, c) ^{1}H one-pulse spectra, recorded under MAS at 35 kHz. The assignment of the resonance lines for the et-dimer (b) and the me-dimer (c) is as follows: NH (**A**), OH (**B**), aromatic CH (**C**, **C**′), CH_2 (**D**), and CH_3 (**E**).

evaluated, while above 25 kHz the shoulder in the aliphatic signal at 2.2 ppm appears, and at 35 kHz a weak signal at 5.4 ppm becomes visible. Note as well the sensitivity improvement related to the increase of the MAS frequency: The faster the spinning, the narrower the lines and the more the signal is concentrated in the centerband. Applying MAS at 35 kHz yields the spectra shown in Figs. 48b and 48c for the et-dimer and the me-dimer, respectively. For both samples, signals in the aliphatic (**D**, **E**) and the aromatic frequency range (**C**, **C**′) are clearly observed. When comparing both spectra, the additional signals present in the et-dimer, i.e., **D** and **C**′, can be explained by the additional CH_2 group in the et-dimer (**D**) and by packing effects (**C**′), the latter being of similar origin as the splitting observed in the acetonitrile-hydroquinone sample (see Fig. 33a). Furthermore, both spectra contain resonance lines labeled **A** and **B**, which are shifted to high field for the me-dimer in comparison to the et-dimer. This variation of the resonance frequencies suggests the assignment of these signals to hydrogen-bonded protons, whose structural arrangement differs slightly for the two dimers. Moreover, the shift difference between **A** and **B** as well as the pronounced low-field shift of **A** > 10 ppm is not straightforwardly compatible to the presence of two OH protons. The latter observation rather supports the assumption that one OH proton is involved in a N···H···O hydrogen bond, with the proton developing partial NH character. For simplicity, the signals **A** and **B** are assigned to a "NH" and a "OH" proton, respectively.

To obtain a first idea of the dipolar coupling strengths experienced by the individual proton species, the SQ MAS sideband patterns could in principle be analyzed, as has been described in Section 2.7. However, it should be kept in mind that SQ spectra consist of spin-specific rather than pair-specific signals and, hence, *all* dipolar couplings acting on a single proton contribute to its MAS sideband pattern. Moreover, the spectral resolution achievable in the sidebands is usually less than that in the centerband, because residual line broadening affects the sidebands increasingly with their order. The latter problem is illustrated in Fig. 49 by the ^{1}H one-pulse spectrum of the et-dimer, recorded under MAS at 35 kHz. The lines in the sidebands are less resolved and, even more importantly, their intensity is so poor at such high MAS frequencies that there is no hope for a quantitative evaluation. In fact, the clear asymmetry between the two first-order sidebands means that MAS has already reduced the dipolar interactions so efficiently that besides the residual dipolar interactions other mechanisms, e.g., B_1 inhomogeneities, contribute appreciably.

Therefore, two-dimensional DQ MAS spectra are again required to shed light on the hydrogen-bonding arrangement. It should be noted that rotor-synchronized ^{1}H DQ spectra can usually be recorded in less than 1 or 2 h. Hence, such spectra provide fast access to detailed information, without requiring sophisticated setup procedures or long experiment times. For the two dimers, such DQ spectra are shown in Figs. 50a and 50b. At first sight, the two spectra, being dominated by aliphatic and aromatic ^{1}H signals, are very similar. However, the DQCs involving the aliphatic and aromatic protons **C**, **C**′, **D**, and **E** are irrelevant for the determination of the hydrogen-bonding schemes and, hence, will not be further considered. The only exception is the purely aromatic diagonal peak **CC**. Together with the peaks involving NH and OH protons **A** and **B**, the relative intensities of these peaks reveal characteristic differences between the me- and the et-dimer:

- For both dimers, the NH–OH cross peak **AB** indicates the presence of a N···H···O···H···O hydrogen bond. In addition, the et-dimer exhibits an intense cross peak **AC**, evidencing a spatial proximity between NH and aromatic protons.

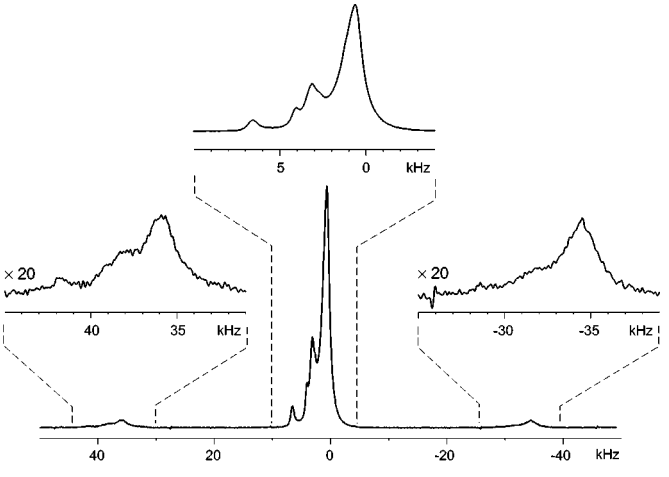

FIG. 49. ^{1}H one-pulse spectrum of the ethyl dimer, recorded under MAS at 35 kHz. On top, the centerband and the first-order MAS sidebands are magnified.

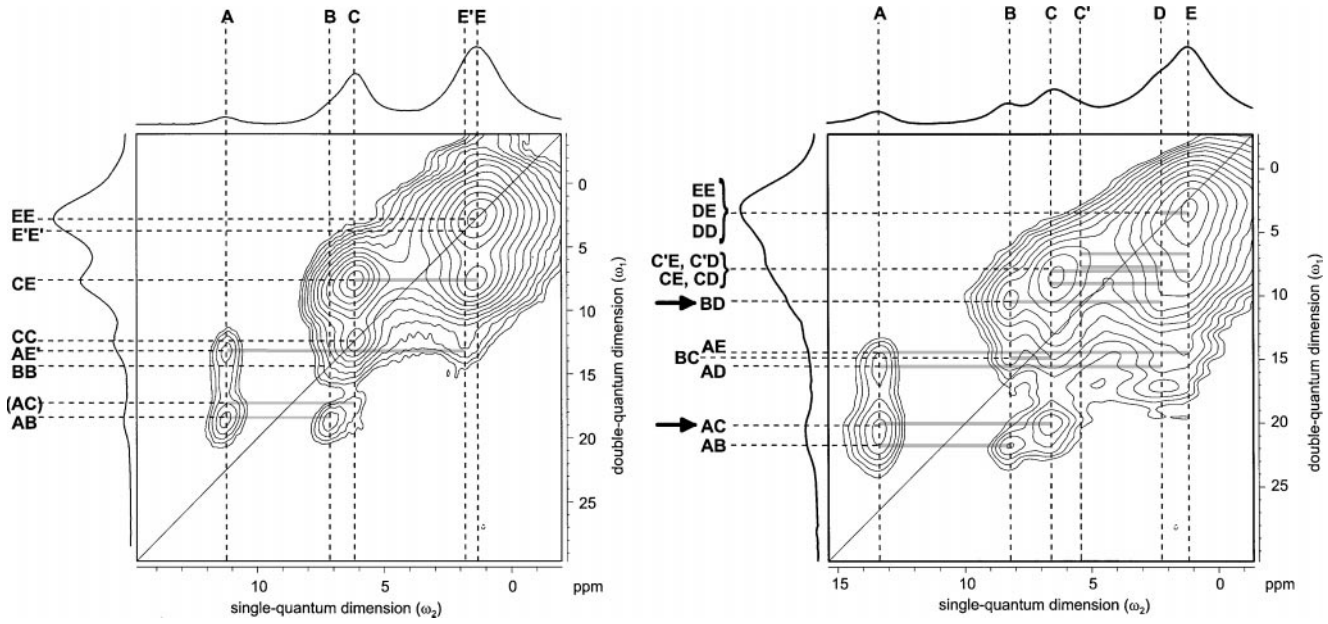

FIG. 50. Two-dimensional ^{1}H DQ spectra of the me-dimer (a) and the et-dimer (b), recorded at a Larmor frequency of 500 MHz with a DQ excitation time of $\tau_{exc} = \tau_R$ under MAS at 35 kHz. The arrows indicate the differences between both spectra, which are crucial for the distinction of the hydrogen-bonding schemes.

• For the et-dimer, the OH protons are involved in a strong DQC (**BD**) with CH_2 protons, which is absent for the me-dimer.

• The diagonal peak **CC** in the spectrum of the me-dimer, which cannot be due to a *intra*molecular proximity, but rather indicates a "back-to-back" packing arrangement of the molecules, is absent in the spectrum of the et-dimer.

• The diagonal peak **BB** of two OH protons is weak in the spectrum of the me-dimer, but is virtually absent in the spectrum of the et-dimer, even though it should be easier to resolve it there because of its low-field shift.

For both dimers, the **AB** signal provides a plausible explanation for the presence of NH-type protons: In the course of the formation of a double hydrogen bond, one of the two OH protons develops partial NH character, i.e., in a schematical representation $N+H-O+H-O \rightarrow N\cdots H\cdots O\cdots H\cdots O$. Turning to the obvious differences between both spectra, the absence and the presence of an **AC** signal for the me- and et-dimer, respectively, strongly suggest that, apart from the $N\cdots H\cdots O\cdots H\cdots O$ motif, the overall hydrogen-bonding schemes are different for the two dimers. While the structural implications from the DQ spectrum of the me-dimer agree with a geminate hydrogen bonding of the dimers, the proximity between a NH proton **A** and an aromatic proton **C** in the case of the et-dimer is not at all compatible with this arrangement. In fact, in order to make the structure of the et-dimer correspond to its DQ spectrum, the geminate hydrogen-bonding scheme needs to be modified in the following way: Starting from the conformation of the methyl dimer depicted in Fig. 47b, one of the phenyl substituents attached to the central ($–CH_2–N(C_2H_5)–CH_2–$) bridge is rotated such that an aromatic proton takes the position occupied by the OH proton before. After this conformational change, the "new" DQ signals **AC** and **BD** as well as the unaltered **AB** signal can be explained, because, by this rotation, the proximity between the aromatic and the NH protons as well as the proximity between the CH_2 and OH protons is achieved, while the $N\cdots H\cdots O\cdots H\cdots O$ bridge is kept. In Fig. 51, the proposed structure of the et-dimer is compared to that of the me-dimer.

In conclusion, replacing the methyl by an ethyl substituent gives rise to a conformational change of the dimer, which subsequently induces the change of the hydrogen-bonding scheme from a geminate to a chain-like supramolecular arrangement. In fact, it is rewarding that recently such a chain-like structure has indeed been identified also by an X-ray structure analysis of the propyl derivative, confirming the structure previously proposed solely on the basis of the ^{1}H DQ MAS results (*97*). In addition to this principal result, a closer inspection of the DQ spectrum of the me-dimer reveals the presence of a weak **AC** signal, indicating the coexistence of a majority of hydrogen-bonded pairs with a minority of hydrogen-bonded chains of dimers. With respect to the identification of such minority conformations, the DQ NMR method is superior to scattering methods, because the former is applicable to powdered as-synthesized samples, while the latter require single crystals, which are, as a result of the preparation procedure, free of structural impurities.

4.1.4. Thermodynamics of Hydrogen-Bonding Processes

In the previous sections, we demonstrated how ^{1}H DQ spectroscopy can, in a straightforward and qualitative manner, be

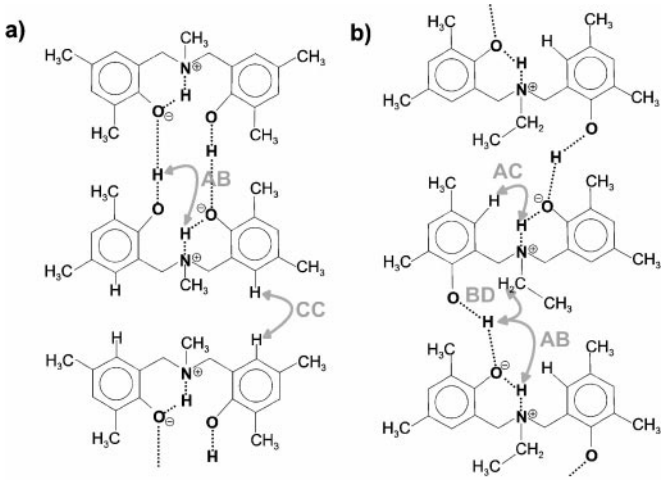

FIG. 51. Comparison of the schematic hydrogen-bonded structures of the me-dimer (a) and the et-dimer (b), i.e., geminate and chain-like, respectively, as derived from ^{1}H DQ spectra.

used to identify multiple hydrogen-bonds and the details of their bonding arrangement. We will now turn to quantitative results about the structure as well as the thermodynamics and kinetics of hydrogen bonds, obtained by ^{1}H SQ and DQ MAS techniques (*20*). The sample, which will serve as an example in the following discussion, is a hexabenzocoronene (HBC) derivative, namely 2,5,8,11,14,17-hexa[10-carboxydecyl]hexa-*peri*-hexabenzocoronene, henceforth referred to as HBC-C_{10}COOH, whose structure is depicted in Fig. 52a. Aliphatic HBC derivatives represent a relatively new family of discotic aromatic mesogen, which have a number of favorable properties as compared to the more established triphenylenes (*55, 109*). Due to the extended π-electron systems and favorable π–π interactions, these molecules are capable of forming columnar phases by stacking the disc-shaped cores. The solid-state structure as well as the dynamics of the high-temperature liquid-crystalline (LC) phases will be discussed in the following section. Here, we will consider the HBC-C_{10}COOH derivative, where each of the six linear

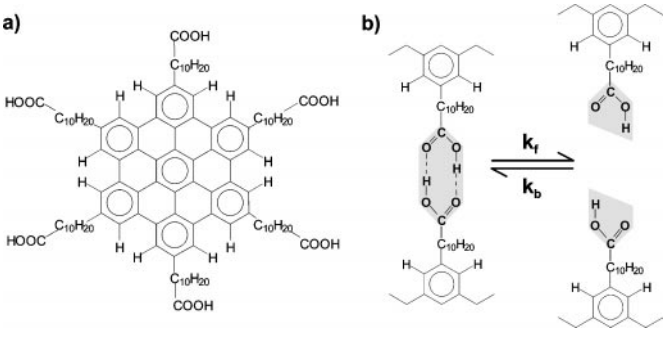

FIG. 52. (a) Chemical structure of HBC-C_{10}COOH. (b) Equilibrium between the making and breaking of hydrogen-bonded carboxylic acid dimers in HBC-C_{10}COOH.

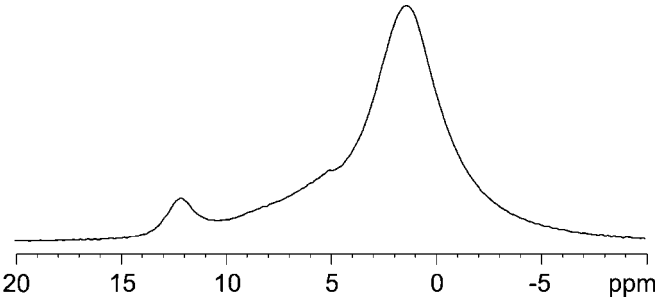

FIG. 53. ^{1}H one-pulse spectrum of HBC-C_{10}COOH, recorded under MAS at 30 kHz at a Larmor frequency of 500 MHz.

alkyl chains is capped by a carboxylic acid group, and focus on its hydrogen-bonding properties (see Fig. 52b).

In the SQ MAS spectrum shown in Fig. 53, the ^{1}H resonance line of the COOH protons is clearly resolved at 12 ppm. The aliphatic protons give rise to an intense peak centered at 1.5 ppm, while the signals of the aromatic protons are spread over a range between 5 and 10 ppm, forming a long low-field shoulder of the aliphatic signal. This broad aromatic signal as well as the underlying phenomena will be discussed in detail in the following section. Concentrating on the COOH signal, it is not clear from the SQ spectrum if and to what extent the carboxylic acid groups form hydrogen bonds. The two-dimensional rotor-synchronized ^{1}H DQ spectrum (Fig. 54a) gives the immediate answer to this question: The purely acidic diagonal peak provides evidence for the presence of hydrogen-bonded dimers of acid groups. The acidic–aliphatic cross peak is due to dipolar couplings between COOH and ($\omega - 1$)–CH_2 protons, while the aromatic and aliphatic diagonal peaks indicate aromatic–aromatic and aliphatic–aliphatic dipolar couplings, which are obvious from the structure of the molecule (see Fig. 52a).

Beyond the simple identification of a double hydrogen-bond, the MAS sideband pattern of the purely acidic DQ signal allows the determination of the interproton distance within the carboxylic acid dimer. Figure 55a shows the extracted column from a non-rotor-synchronized two-dimensional DQ spectrum at the SQ resonance frequency of the COOH protons at 12 ppm. The additional experimental peaks marked by asterisks correspond to DQCs between the COOH and aliphatic protons. Based on a spin-pair model, the purely acidic MAS sideband pattern observed in the experiment agrees with that of two protons with a homonuclear dipolar coupling of $D^{\mathrm{HH}} = 2\pi \cdot 5.5$ kHz, corresponding to an interproton distance of $r_{\mathrm{HH}} = 0.28$ nm (calculated pattern shown in Fig. 55b).

Upon heating, HBC derivatives undergo a phase transition from the solid low-temperature phase to a LC high-temperature phase. While the following section will focus on the molecular motions present in the LC phase, we briefly summarize here the information obtainable from ^{1}H spectroscopy about the kinetics and thermodynamics of the making and breaking of hydrogen

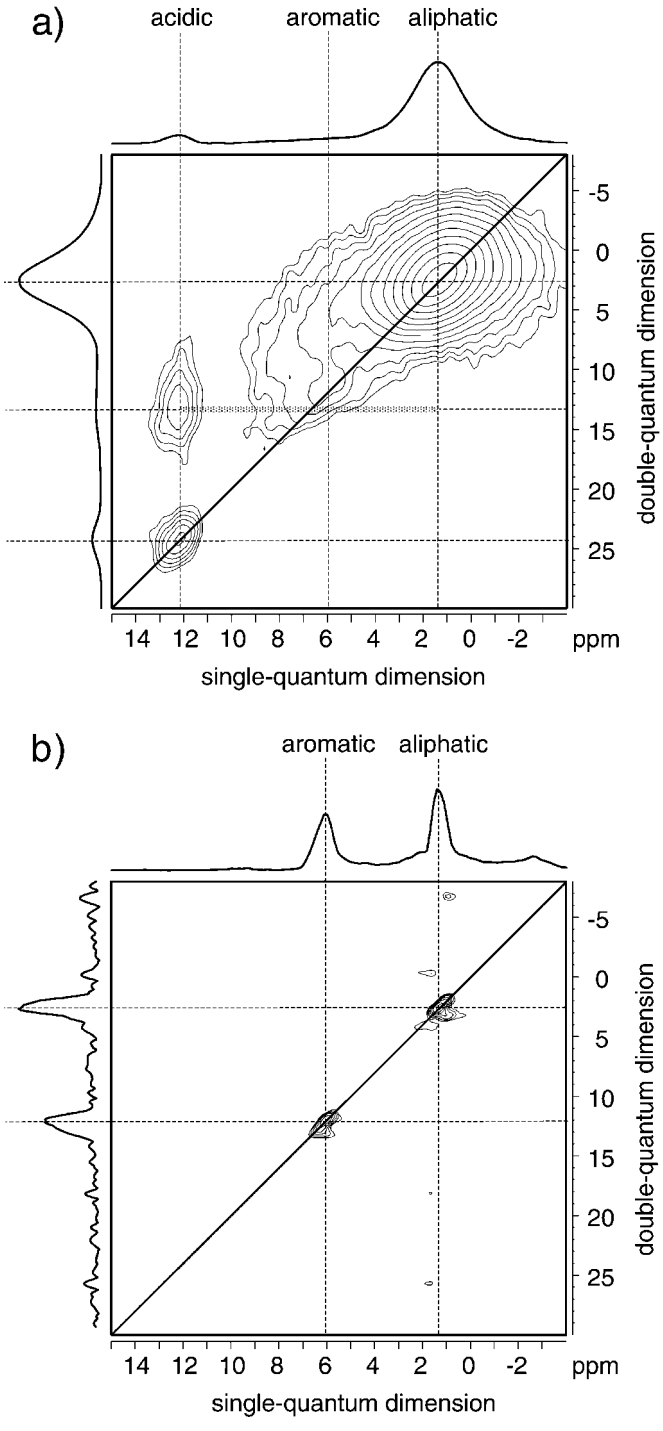

FIG. 54. Two-dimensional rotor-synchronized ^{1}H DQ spectra of HBC-C_{10}COOH, recorded with a DQ excitation time of $\tau_{exc} = \tau_R$ under MAS at 30 kHz at a Larmor frequency of 500 MHz: (a) solid phase at $T = 322$ K and (b) liquid-crystalline phase at $T = 438$ K.

bonds. From the absence of a purely acidic DQ signal in the rotor-synchronized two-dimensional DQ spectrum recorded for the LC phase of HBC-C_{10}COOH (Fig. 54b), it is clear that the hydrogen bonds are broken on a time scale faster than that of the DQ experiment at such elevated temperatures. In addition to this, the presence of fast molecular motions is obvious from the considerable narrowing of the ^{1}H resonance lines, in particular of the aromatic signal, as well as from the absence of any DQ cross peak.

The dynamic processes, which the hydrogen bonds undergo upon heating, can be analyzed by means of ^{1}H resonance frequencies and COOH signal intensities in ^{1}H one-pulse and double-quantum-filtered (DQF) MAS spectra. A series of experimental SQ and DQF spectra, recorded at different temperatures, are shown in Figs. 56a and 56b, respectively. In the SQ spectra, a clear shift of the COOH peak to high field is observed for increasing temperatures. A closer inspection reveals that two shifting processes can be distinguished: a gradual shift from 12 to 10 ppm for $T = 324 \rightarrow 419$ K (plotted in Figs. 57a) and a jump from 10 to 9 ppm for $T = 419 \rightarrow 438$ K. These observations can be interpreted in terms of a chemical exchange process. The approach is based on the assumption that, in the LC phase at $T \geq 438$ K, all hydrogen bonds are initially broken, and the COOH resonance frequency at 9 ppm is that of free carboxylic acid groups. The jump of the COOH signal occurring from $T = 419$ to $T = 438$ K hence corresponds to the difference in the ^{1}H resonance frequencies observed for fast exchange process and the free acid, respectively. The fast exchange occurs between hydrogen-bonded and free COOH groups, with the resonance frequencies of the former and the latter being equal to that of the COOH protons in the SQ spectra at $T = 324$ K and $T = 438$ K, respectively, i.e., 12 and 9 ppm. For decreasing temperatures, the exchange rate decreases and, in the SQ spectra, the transition from fast exchange to slow exchange can be followed, passing

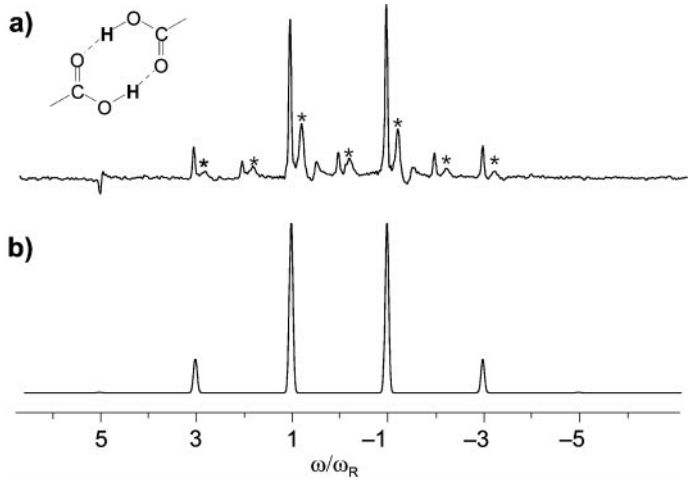

FIG. 55. (a) Extracted DQ column at the COOH resonance at 12 ppm from a two-dimensional ^{1}H DQ spectrum of HBC-C_{10}COOH, recorded with a DQ excitation time of $\tau_{exc} = 3\tau_R$ under MAS at 30 kHz at a Larmor frequency of 700 MHz. The signals marked by $*$ correspond to DQCs between the COOH and aliphatic protons. (b) Calculated DQ MAS sideband pattern of a proton pair with $D^{HH} = 2\pi \cdot 5.5$ kHz, corresponding to a distance of $r_{HH} = 0.28$ nm, for the experimental parameters in (a).

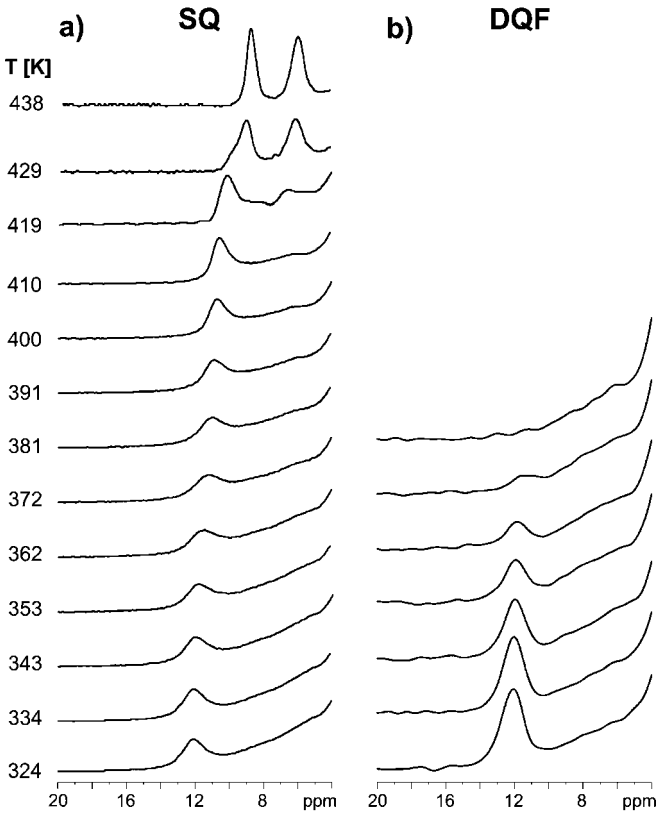

FIG. 56. Series of ^{1}H MAS spectra of HBC-C_{10}COOH for temperatures $T \approx 320 \ldots 440$ K, recorded under MAS at 30 kHz at a Larmor frequency of 500 MHz: (a) one-pulse spectra and (b) double-quantum-filtered (DQF) spectra, applying a DQ excitation time of $\tau_{exc} = 2\tau_R$.

the coalescence point at about 362 K, as is apparent from the observed linewidth change. At lower temperatures, the COOH resonance is split into a pair of resonance lines, a low-field line for the hydrogen-bonded and a high-field line for the free form, with the latter being obscured by the aromatic ^{1}H signals.

Based on this chemical exchange approach, a quantitative analysis of the COOH resonance frequencies yields the equilibrium constant K for the making and breaking processes of the hydrogen bonds in HBC-C_{10}COOH. The resulting K-values are plotted in Fig. 57b, and the thermodynamics of the equilibrium are given by a reaction enthalpy $\Delta H = 45 \pm 4$ kJ/mol and a reaction entropy $\Delta S = 113 \pm 11$ J K^{-1} mol^{-1} (*20*).

While the temperature dependence of the SQ spectra allows the thermodynamics to be determined, the temperature dependence of the DQF signal intensities provides quantitative insight into the kinetics of the hydrogen-bonding process in HBC-C_{10}COOH. From the ^{1}H DQF spectra shown in Fig. 56b, as well as from the DQ intensity values plotted in Fig. 57c, it is clear that the purely acidic DQC vanishes for increasing temperatures. In order to observe a DQ or DQF signal with maximum amplitude, the respective dipolar coupling must persist unchanged for the duration of the DQ experiment. Conversely, any dynamic process which destroys or modifies the underlying dipolar coupling during the DQ experiment cancels or reduces the DQ signal intensity accordingly. The time scale, on which a DQF experiment is sensitive to such processes, is therefore given by the sum of the excitation and reconversion periods, i.e., 133 μs for the spectra shown in Fig. 56b.

In the case of the hydrogen bonds investigated here, the situation can be described by a simple two-state model where the reaction occurs between a hydrogen-bonded and a free state. Hence, the dipolar couplings change from $D^{\mathrm{HH}} = 2\pi \cdot 5.5$ to 0 kHz. Based on this model, the DQ signal intensity observed in the spectra shown in Fig. 56b directly reflects the probability that the lifetime of the hydrogen-bonded form is longer than 133 μs. Taking the change in the equilibrium constant as well as the general loss of NMR signal inherent to temperature increase into account and assuming an exponential distribution of dimer lifetimes, we obtain the rate constants k_f for the breaking reaction, which are plotted in Fig. 57d (*20*). An Arrhenius analysis results in an activation energy of $E_A = 89 \pm 10$ kJ/mol and an Arrhenius parameter of $A = 4.2 \times 10^{16}$ s^{-1}. Due to the time scale of the DQ experiment, this approach is, in general, limited to rate constants higher than $k_f \approx 10^6$ s^{-1}.

In conclusion, ^{1}H MAS and in particular ^{1}H DQ MAS spectroscopy offer themselves as valuable and straightforwardly applicable techniques for the investigation of hydrogen bonds with respect to their structure as well as their dynamics in the solid state:

- Based on the ^{1}H chemical shift resolution provided by fast MAS, the presence of DQ signal provides evidence for the existence of hydrogen bonds.
- In the case of multiple hydrogen bonds, their arrangement can be directly derived from the peak pattern in two-dimensional DQ spectra.
- DQ MAS sideband patterns allow the accurate determination of interproton distances.
- From the changes of ^{1}H chemical shifts as well as from the variation of DQ signal intensities occurring upon temperature changes, quantitative thermodynamic or kinetic information about the making and breaking processes can be obtained.

4.2. Packing of π-Electron Systems

The hydrogen-bonding properties of the particular HBC hexaacid derivative discussed in the last section represent only a side aspect of the main features of HBC compounds, which are predominantly controlled by the π–π interactions between the extended aromatic cores of the molecules. In the following, we focus on these interactions and demonstrate how ^{1}H SQ and DQ MAS approaches can, in general, be used to explore the packing arrangement of π-electron systems in the solid state.

Using ^{1}H instead of ^{13}C resonances for mapping π-electron densities might appear a bit odd at first sight, but protons have the undeniable advantage of combining high NMR signal

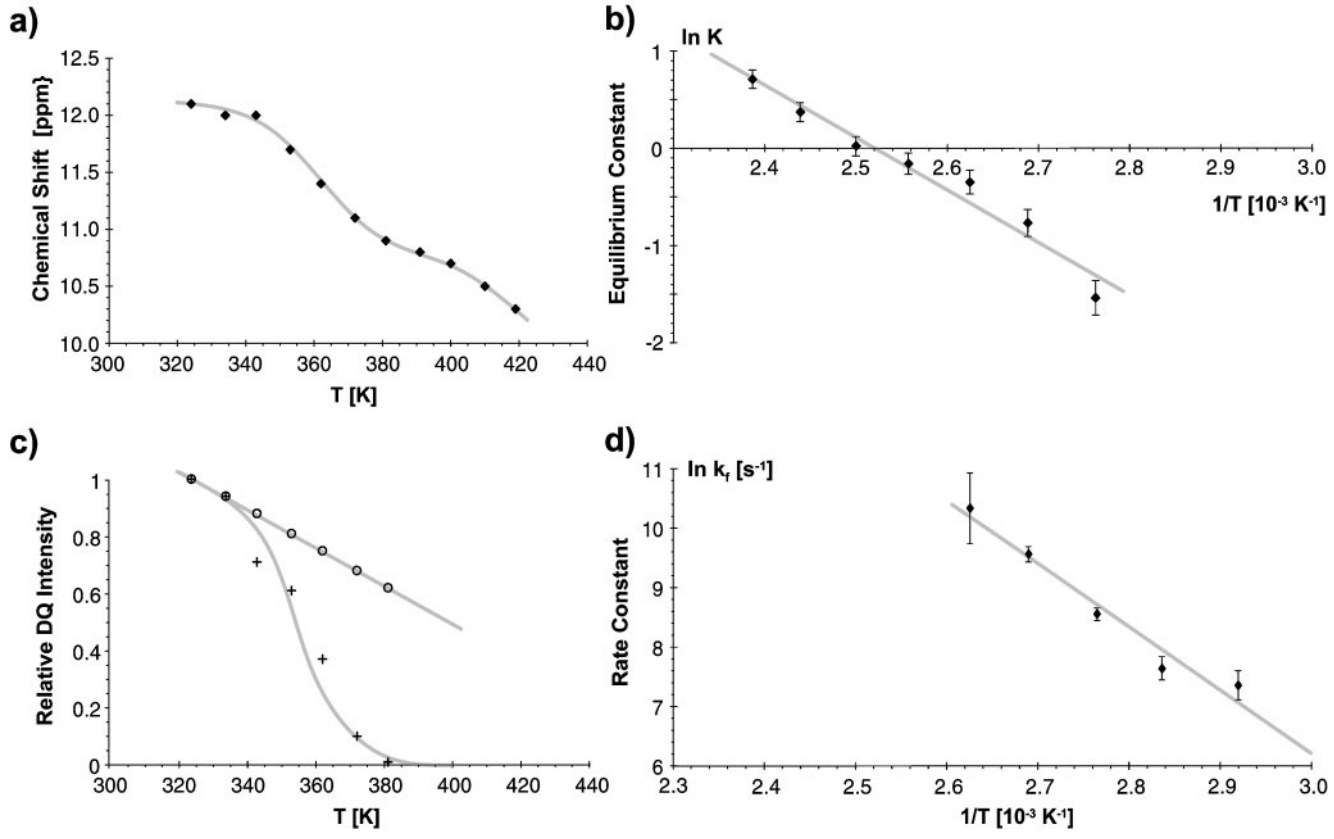

FIG. 57. (a) The change of the chemical shift of the acidic ^{1}H resonance in HBC-C_{10}COOH upon heating (spectra shown in Fig. 56a). (b) Thermodynamic constant K of the equilibrium between the making and the breaking reaction of COOH hydrogen bonds in HBC-C_{10}COOH , as schematically depicted in Fig. 52b. (c) DQ signal intensity of the COOH signal in the ^{1}H DQF spectra shown in Fig. 56b. The crosses denote the experimental DQF data, while the circles indicate the temperature dependence of the equilibrium together with the general loss in any NMR signal due to heating. (d) Kinetic rate constant k_f of the breaking reaction of the hydrogen bonds in HBC-C_{10}COOH, as evaluated from the DQF signal intensities.

sensitivity with a high chemical shift sensitivity to nearby electrons. The latter feature is due to the fact that, in NMR, the electrons surrounding the nucleus are responsible for magnetic shielding effects, thereby determining the actual nuclear resonance frequency. Since hydrogen atoms themselves are only provided with a single electron, which is moreover well localized in the chemical bond, external electrons have a major effect on ^{1}H chemical shifts. Although this phenomenon is well known in NMR (*113*) and routinely exploited in solution- or liquid-state applications, the lack of spectral resolution has prevented it from being utilized in the solid state. However, fast MAS techniques are now able to overcome this problem and to uncover the ^{1}H chemical shift information, as will be shown, in this review, for the example of the large aromatic core of alkyl-substituted HBC derivatives (see Fig. 58).

The protons of interest are those directly attached to the aromatic core. Due to the presence of the alkyl substituents, these protons in the "bays" of the core form spin pairs which are well separated from neighboring protons. This feature will be exploited in the following section for investigating the molecular dynamics in the solid and the LC phase by DQ MAS spectroscopy. Anticipating these investigations, we now consider hexa-(α-deuterododecyl)-hexa-*peri*-hexabenzocoronene (structure **2** in Fig. 58 (*18*)), which is henceforth referred to as HBC-$C_{12}^{\alpha D}$. In this sample, the α-CH_2 positions were

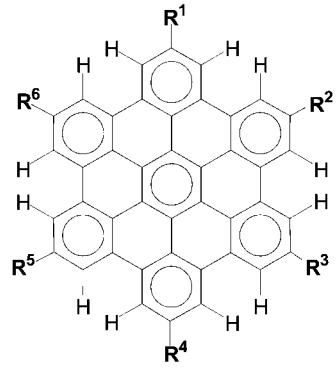

1: R^n = -$(CH_2)_{11}CH_3$
2: R^n = -$CD_2(CH_2)_{10}CH_3$
3: R^n = -$CH(CH_3)_2$
4: R^n = -$C(CH_3)_3$
5: $R^{1,2}$ = -$C(CH_3)_3$, R^{3-6} = -$(CH_2)_{11}CH_3$

FIG. 58. Chemical structure of the alkylated hexabenzocoronene (HBC) derivatives discussed in this section: hexa-*n*-dodecyl, **1**; hexa-(α-deuterododecyl), **2**; hexa-*i*-propyl, **3**; hexa-*t*-butyl, **4**; and di-*ortho*-*t*-butyl-tetra-*n*-dodecyl, **5**.

originally deuterated in order to carry out ^{2}H NMR investigations of the side chains (*55, 13*). With respect to the ^{1}H MAS experiments discussed here, the deuterons provide additional spatial separation and, in this way, dipolar decoupling for the bay proton pairs. However, ^{1}H MAS NMR is able to provide the same information for the fully protonated hexa-*n*-dodecylhexa-*peri*-hexabenzocoronene (structure **1** in Fig. 58), which is henceforth referred to as HBC-C_{12}.

The fundamental feature of the solid-state ^{1}H resonances in HBC derivatives becomes obvious from the one-pulse MAS spectrum of HBC-$C_{12}^{\alpha D}$, displayed in Fig. 59a: Instead of only one, there are three aromatic ^{1}H resonances of equal intensity. The presence of a higher magnetic field, i.e., a Larmor frequency of 700 instead of 500 MHz, as well as the deuteration of the α-CH_2 positions helps with the spectral resolution of three lines, as can be seen from comparing the insets in Fig. 59a as well as Figs. 59a and 59b, respectively. The splitting of the aromatic ^{1}H resonance cannot be due to an asymmetry of the molecule, because the six alkyl substituents are chemically identical and conserve the sixfold symmetry of the aromatic core, as is also proved by the presence of only one aromatic ^{1}H resonance in the spectrum of a solution of HBC-$C_{12}^{\alpha D}$ in $CDCl_3$ (see Fig. 59d). In the LC phase of HBC-$C_{12}^{\alpha D}$ the aromatic resonance is considerably shifted to high field relative to its solution-state position (see Fig. 59c), but no splitting is observed. Apparently, some molecular motion cancels the resonance splitting. Therefore, the presence of three lines must be due to a structural feature which is specific for the solid state, such as the packing of the disc-shaped aromatic cores. An appropriate packing could make the aromatic protons experience "ring-current" effects of nearby π-electrons to different degrees, depending on the individual electronic environment.

In order to shed more light on the origin of the resonance line splitting induced by π-electrons, the pronounced spin-pair character of the aromatic protons in HBC-$C_{12}^{\alpha D}$ strongly suggests the recording of two-dimensional DQ spectra. In this way, proton species forming bay proton pairs can be easily identified. Labeling the three aromatic lines with **A**, **B** and **C**, the rotor-synchronized DQ spectrum (see Fig. 60a) clearly shows that two types of bay proton pairs can be distinguished, one of which consists of proton species **C** only, while the other consists of **A**–**B** pairs. Note that this result is obvious from the spectra of both the deuterated HBC-$C_{12}^{\alpha D}$ and the fully protonated HBC-C_{12}. In the latter case, as is expected, the aromatic–aromatic and aliphatic–aliphatic DQ signals are accompanied by "mixed" aromatic-aliphatic signals because of the proximity between aromatic and α-CH_2 protons.

Considering the three aromatic DQ signals quantitatively, it is clear that they are of about the same integrated intensity, which means that the cross peak **AB** is twice as intense as the diagonal peak **CC**. To a first approximation, the intensity of the DQ signal is proportional to the square of the underlying dipolar coupling strength as well as to the number of contributing spins. Relying on the self-evident assumption that the dipolar coupling

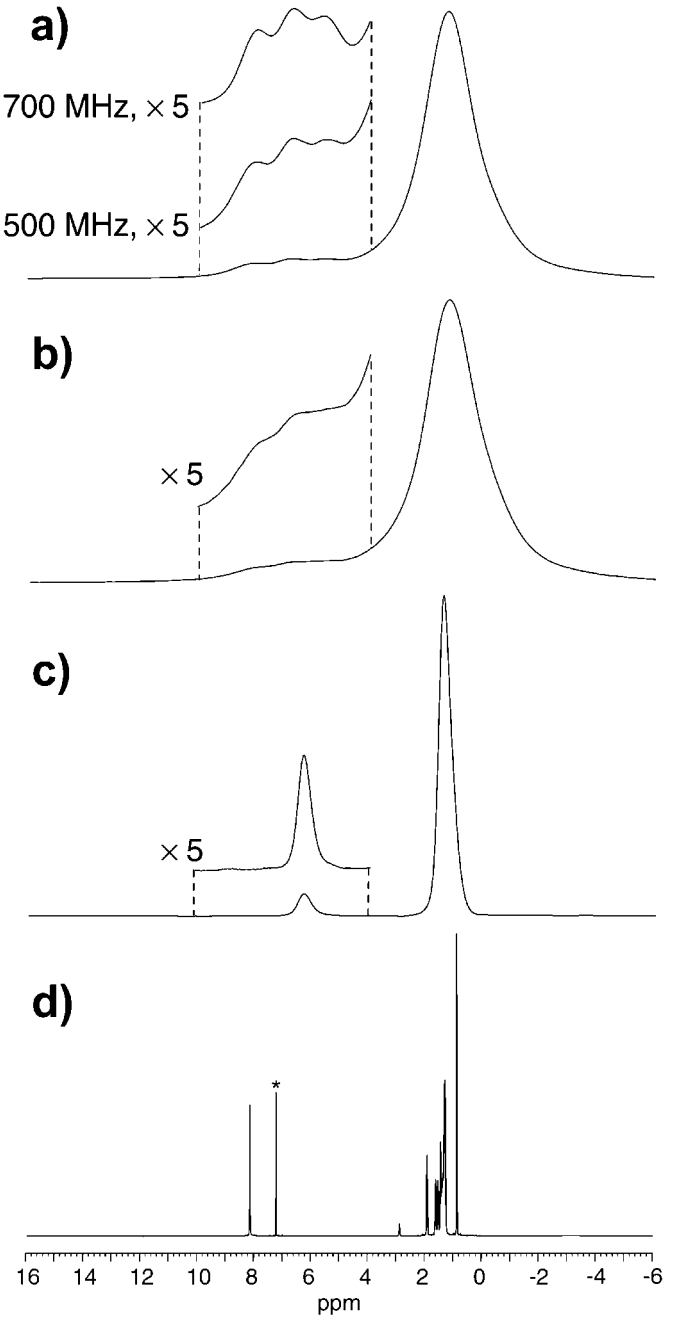

FIG. 59. ^{1}H one-pulse spectra, recorded at a Larmor frequency of 500 MHz: (a) solid phase of HBC-$C_{12}^{\alpha D}$ under MAS at 35 kHz, with the 700-MHz spectrum in the inset for comparison. (b) Solid phase of HBC-C_{12} under MAS at 35 kHz. (c) LC phase of HBC-$C_{12}^{\alpha D}$ under MAS at 35 kHz. (d) Solution of HBC-$C_{12}^{\alpha D}$ in $CDCl_3$, with the solvent signal being marked by $*$.

strengths are equal for all bay proton pairs, we can conclude that there are twice as many **AB**-type than **CC**-type pairs. This observation, together with the existence of an **AB** DQ cross peak, allows the rejection of any suspicion that the three resonances could be due to a coexistence of three different solid-state phases of the material. It rather supports the assumption that the

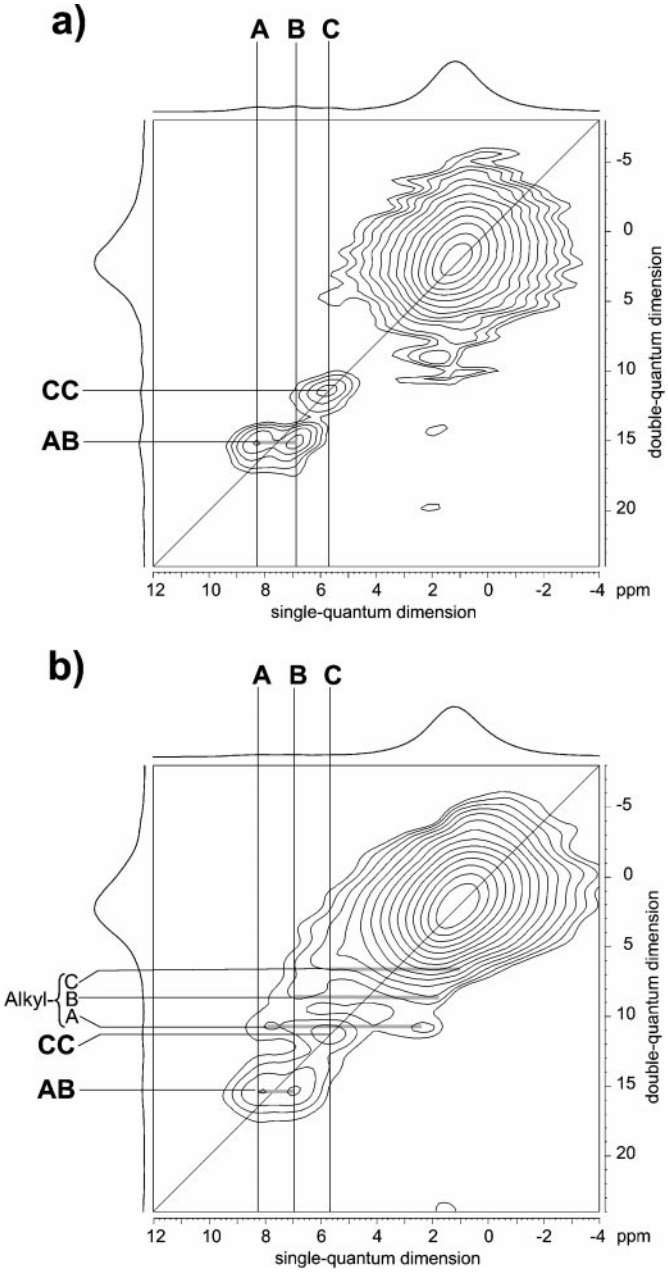

FIG. 60. Two-dimensional rotor-synchronized ^{1}H DQ spectra, recorded with a DQ excitation time of $\tau_{exc} = \tau_R$ under MAS at 35 kHz at a Larmor frequency of 500 MHz: (a) HBC-$C_{12}^{\alpha D}$ and (b) HBC-C_{12}. The sample temperature was at 330 K, such that both samples were in their solid low-temperature phases.

packing effect inducing the line splitting occurs on a molecular nearest-neighbor level throughout the whole sample.

In fact, the ^{1}H NMR observations can be rationalized quite straightforwardly by considering the packing arrangement of unsubstituted HBC, whose crystal structure is known from an X-ray analysis (*45*). The planar HBC discs pack in columns, with their molecular plane being tilted relative to the columnar axis. In this way, the molecules of two neighboring columns form a herring-bone pattern, as depicted in Fig. 61a. Picking out a single molecule, this packing arrangement results in a displacement of its two neighbor molecules such that the interaction of the π-electrons is optimized. This relative orientation of extended planar π-electron systems is well known from the carbon layers in graphite. Focusing on the aromatic protons, the displacement of the molecules means that three types of protons can be distinguished with respect to the degree of π-electron density they experience from the neighbor molecule (see Fig. 61b): **A**-type protons lie neither above nor below the π orbitals of an adjacent layer and, therefore, correspond to the least shielded resonance (highest ppm). **B**- and **C**-type protons lie over or below an inner and outer part, respectively, of an adjacent ring system and are thus expected to correspond to the medium and most shielded resonances, respectively.

Thus, proposing an analogous packing in the alkylated derivative HBC-C_{12}, the existence of three aromatic ^{1}H resonances as well as the two types of bay proton pairs, including their numerical ratio of 2 : 1, can be explained. Moreover, based on theoretical quantum-chemical approaches, ^{1}H chemical shift calculations have recently shown (*86, 87*) that the packing of the HBC cores described above is indeed the only relative orientation which gives rise to the observed ^{1}H resonances and, in particular, to the DQ peak pattern. Conversely, utilizing the sensitivity of ^{1}H resonances to nearby π-electron densities, a single ^{1}H DQ spectrum allows the unambiguous determination of the molecular packing in the solid phase of HBC-C_{12}. Furthermore, the collapse of the splitting of the aromatic ^{1}H resonances in the high-temperature LC phase of HBC-C_{12} can now be rationalized in terms of a molecular motion which averages the three different π-electron environments of the aromatic protons and results in a mean π-electron density which is then equally experienced by all six protons. We will turn to a detailed discussion of the

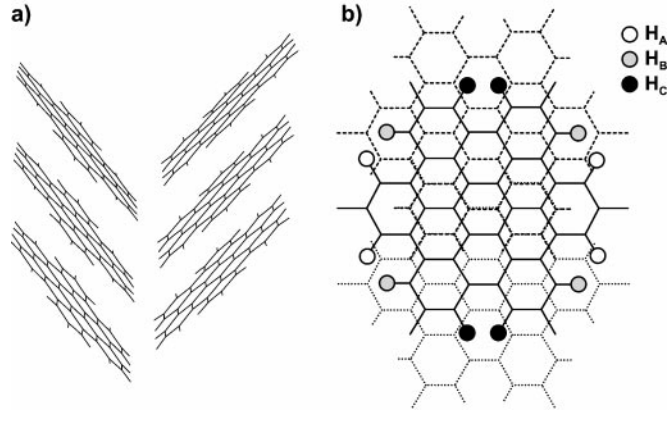

FIG. 61. (a) Columnar packing and herring-bone arrangement of the disc-shaped aromatic cores in the crystal structure of unsubstituted HBC (*45*). (b) Packing arrangement of the aromatic HBC cores in a column: the central molecule (solid lines) with its neighbor molecules above (dashed) and below (dotted). The three aromatic ^{1}H resonances are assigned according to the spectra obtained for HBC-$C_{12}^{\alpha D}$ and HBC-C_{12}.

motion present in the LC phase of HBC derivatives in the following section.

Considering the other alkylated HBC derivatives, i.e., structures **3** to **5** in Fig. 58, we will now briefly demonstrate that the molecular packing of the HBC cores depends on the alkyl substituents and that the DQ peak pattern observed in rotor-synchronized ^{1}H DQ MAS spectra again provides detailed insight into the relative orientation of the aromatic discs (*19*). Comparing Figs. 62a and 62b, it is clear that the hexa-*i*-propyl derivative exhibits the same aromatic ^{1}H DQ peak pattern and hence the same packing arrangement as HBC-$C_{12}^{\alpha D}$ or HBC-C_{12} in the solid phase. For the hexa-*t*-butyl derivative, however, a considerably different aromatic DQ signal is observed (see Fig. 62c), from which the existence of at least five distinct aromatic ^{1}H resonances can be concluded (*19*). Here, the bulky *t*-butyl substituents prevent the cores from being packed in a column and, instead, hexa-*t*-butyl HBC forms "sandwiches" consisting of only two molecules, which crystallize in a non-columnar fashion. The ^{1}H DQ spectra support the relative orientation of the cores in these sandwiches (*19*), as is proposed by a preliminary X-ray analysis. Finally, considering the di-*ortho*-*t*-butyl-tetra-*n*-dodecyl HBC, the DQ spectrum shows a DQ peak pattern which seems to be a mixture of HBC-like signals plus an additional low-field diagonal peak. Without going into details, these signals apparently indicate that the aromatic cores of di-*ortho*-*t*-butyl-tetra-*n*-dodecyl HBC pack similarly to HBC and hexa-*i*-propyl HBC, with the two bulky *ortho*-*t*-butyl groups separating one bay proton pair from adjacent π-electron systems such that no additional high-field shift is observed.

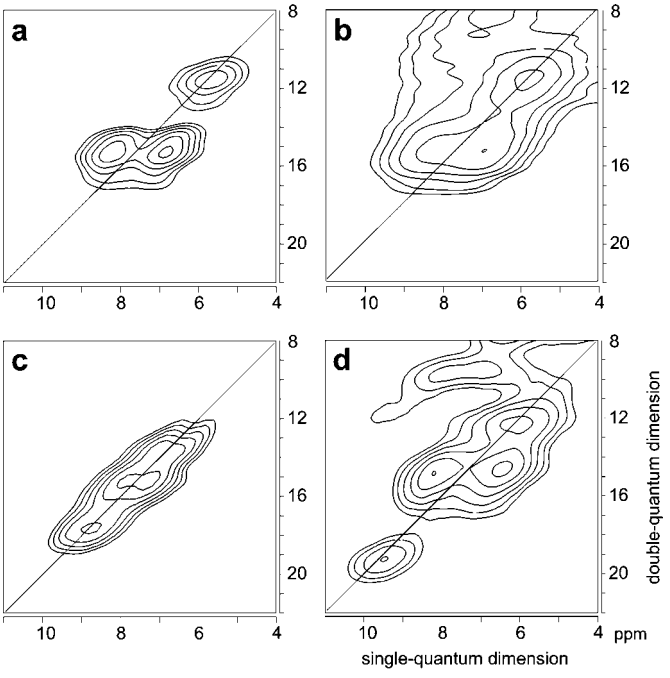

FIG. 62. Aromatic ^{1}H DQ signals observed in rotor-synchronized ^{1}H DQ MAS spectra of alkylated HBC derivatives: (a) hexa-(α-deuterododecyl), **2**; (b) hexa-*i*-propyl, **3**; (c) hexa-*t*-butyl, **4**; and (d) di-*ortho*-*t*-butyl-tetra-*n*-dodecyl, **5**. All spectra were recorded at a Larmor frequency of 500 MHz at $T \approx 330$ K, applying a DQ excitation time of $\tau_{exc} = \tau_R$ under MAS at 30 kHz.

Apart from the aromatic ^{1}H resonances, the chemical shifts of the aliphatic signals can also serve as sensitive probes for the proximity of aromatic rings. The basic effect of the π-electrons on the aliphatic chemical shifts is analogous to that on the aromatic signals, as is demonstrated in the ^{1}H DQ spectrum of HBC-C_{12} (Fig. 60b) by the three aromatic–aliphatic cross peaks: Their aliphatic and aromatic SQ resonance frequencies are shifted in parallel, meaning that the aromatic and the aliphatic protons nearby, i.e., the α-CH_2 protons, experience the same shift effect from adjacent π-electrons. Moreover, in hexa-*t*-butyl HBC, for example, at least four ^{1}H methyl resonances could be identified from the ^{1}H DQ spectrum and rationalized in terms of different degrees to which the methyl protons are subject to additional shielding. In this way, the proposed sandwich-like packing of the molecules could be confirmed (*19, 86*).

Although, in this discussion, quite extended π-electron systems served as examples for demonstrating the feasibility and the versatility of using ^{1}H resonances as probes for aromatic systems, analogous chemical shift effects are also observed for small phenyl rings. In crystalline tyrosine·HCl, for example, the two aromatic protons on either side of the phenyl ring show a shift difference of about 2 ppm because of different shielding effects, as becomes obvious in ^{1}H–^{13}C correlation experiments (*92, 110*).

4.3. Molecular Dynamics

While, in the previous section, we focused on the structural information obtainable from ^{1}H spectra, we now turn to the investigation of molecular dynamics and to a discussion of feasible ^{1}H MQ MAS approaches. In fact, when discussing the fundamentals of ^{1}H MQ MAS spectroscopy in Section 3.3.2, we have already encountered a very simple case of molecular motion, i.e., the fast rotation of methyl groups. This type of oriented, fast, and well-defined motion can be easily investigated by ^{1}H MQ MAS techniques, because it just requires the static dipolar interaction tensor to be replaced by the motionally averaged one. In the following we will consider, as an example for first applications, molecular dynamics in liquid-crystalline HBC derivatives which, though still resembling a simple kind of oriented motion, demonstrate the potential of solid-state ^{1}H MQ MAS methods. Furthermore, nonoriented statistical motions can also be explored and characterized in terms of, e.g., residual order parameters or inherent time scales, as will be shown for ^{1}H DQ MAS investigations of a polymer melt, namely polybutadiene.

4.3.1. Molecular Motions in Liquid-Crystalline Phases

In the solid phases of HBC derivatives, the presence of multiple aromatic ^{1}H resonances has been rationalized in terms of the degree to which each proton experiences the effect of

π-electrons of adjacent molecules. Hence, the occurrence of this kind of line splitting has been identified as an intermolecular effect resulting from the packing arrangement in the solid state. Moreover, it has already been observed that the splitting of the aromatic resonances collapses into a single line both upon heating into the LC phase and upon dissolving (see Figs. 59c and 59d). While, in the latter case, this observation is not at all surprising, because in a dilute solution the HBC molecules are well separated from each other, the presence of a single aromatic line in the high-temperature LC phase deserves a more detailed analysis. Although the aromatic ^{1}H resonance at 6.2 ppm (see Fig. 59c) does not reflect any well-defined packing arrangement, it is still clearly shifted to high field, indicating residual "ring-current" effects from adjacent layers. An obvious explanation for this feature would be the presence of a molecular motion in the LC phase, which averages over the different π-electron environments and results in a single average shift effect.

In order to investigate the underlying process of molecular motion by ^{1}H MQ MAS approaches, the chemical structure of the HBC derivatives suggests the exploitation of the bay proton pairs. Under fast MAS conditions, in particular for the deuterated compound HBC-$C_{12}^{\alpha D}$, these proton pairs are effectively decoupled from surrounding protons, as is experimentally proved by the absence of any even-order sidebands in the DQ MAS sideband patterns (see Fig. 63). Consequently, these patterns can safely and straightforwardly be used to measure precisely the dipolar pair-coupling strengths and, in this way, the motional reduction of the dipolar coupling occurring upon the transition into the LC phase.

In Fig. 63, DQ MAS sideband patterns at the aromatic ^{1}H SQ resonances at 7.9 and 6.2 ppm of the solid and the LC phase, respectively, of HBC-$C_{12}^{\alpha D}$ are compared to each other (*18*). (At all three aromatic ^{1}H resonances at 7.9, 6.6, and 5.4 ppm in the solid phase, the same pattern is observed.) In order to obtain a pattern corresponding to $D^{(ij)}\tau_{exc}/2\pi \approx 0.8 \ldots 1.2$, excitation times τ_{exc} of 57 and 200 μs have to be applied to the solid and the LC phase, respectively, indicating that the underlying pair-coupling strengths $D^{(ij)}$ are considerably reduced in the LC phase. By comparing the experimental patterns to spin-pair calculations, the coupling strengths of $D_{\mathrm{sol}}^{(ij)} = 2\pi \cdot 15.0$ kHz and $D_{\mathrm{LC}}^{(ij)} = 2\pi \cdot 6.0$ kHz are determined to an accuracy of better than ± 0.5 kHz. For the solid phase, where the aromatic cores of HBC molecules are assumed to be static, the coupling strength corresponds to an interproton distance of $r_{\mathrm{HH}} = (0.200 \pm 0.004)$ nm,

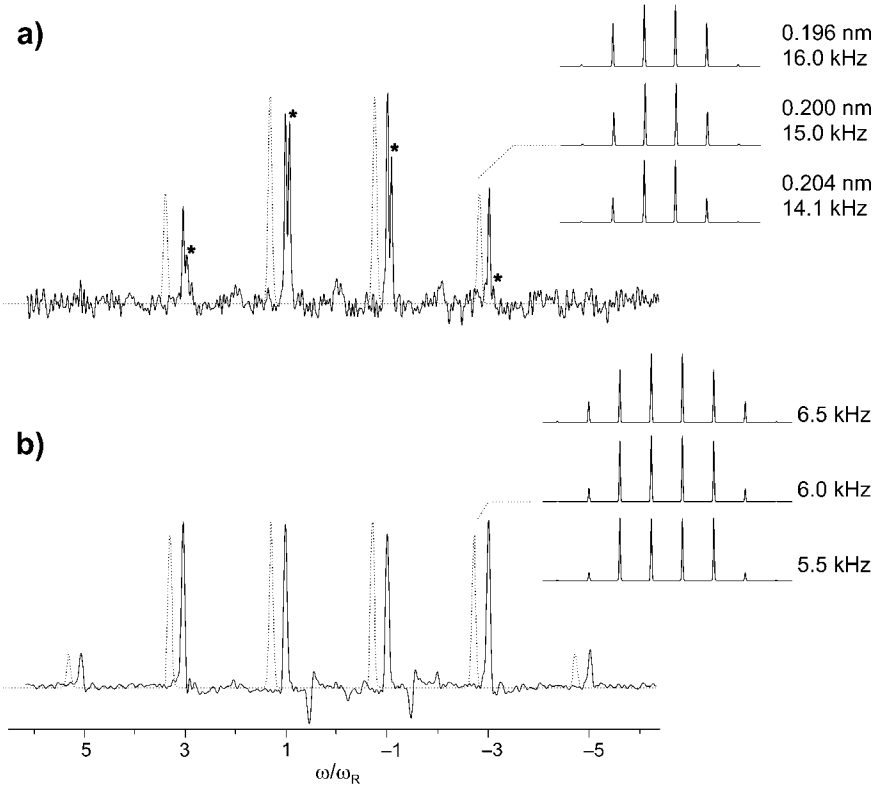

FIG. 63. ^{1}H DQ MAS sideband patterns of HBC-$C_{12}^{\alpha D}$. The ^{1}H Larmor frequency is 500 MHz. (a) Pattern at the aromatic ^{1}H SQ resonance at 7.9 ppm of the solid phase at $T = 330$ K, recorded with a DQ excitation time of $\tau_{exc} = 2\tau_R = 57$ μs under MAS at 35 kHz. The asterisks mark "mixed" aromatic–aliphatic DQ signals. (b) Pattern at the aromatic ^{1}H SQ resonance at 6.2 ppm of the LC phase at $T = 430$ K, recorded with a DQ excitation time of $\tau_{exc} = 2\tau_R = 200$ μs under MAS at 10 kHz. Note the absence of even-order sidebands or centerbands. On the right, calculated DQ MAS patterns of a spin pair are displayed for comparison. The parameters of the calculations correspond to those of the experimental spectra. The resulting pair-coupling strengths (and the corresponding interproton distances in a) are also given.

which is in perfect agreement with the value expected for an almost planar molecule as well as with the crystal structure of unsubstituted HBC (*45*).

For the high-temperature LC phase, the coupling strength is reduced by a factor of 0.4. It is self-evident that the interproton distance does not change upon heating the sample from 330 to 430 K, and hence the reduction of the coupling must be due to motional averaging effects. Considering the disc-shaped structure of the HBC molecule, it is obvious that such molecules are likely to undergo in-plane rotations. In fact, such rotations or six-site jumps are, even at room temperature, well known for aromatic molecules with a sixfold symmetry, such as benzene, coronene, and unsubstituted HBC. In the columnar packing arrangement of HBC-C_{12}, the onset of this rotation is accompanied by a tilt of the aromatic cores such that their planes become orthogonal to the columnar axis, which is, for stability reasons, identical to the rotation axis (*22*).

In general, a fast rotation about an axis which is orthogonal to the orientation of the dipolar interaction vector reduces the dipolar coupling strength by a factor of 0.5. Hence, the observed reduction of 0.4 agrees well with this type of molecular motion, if, in addition to the fast rotation, a small out-of-plane tumbling motion is assumed. Clearly, the columnar packing persists in the LC phase, as is proved by the high-field shift of the aromatic resonance at 6.2 ppm (instead of about 9 ppm for isolated molecules). It should be noted that, in the LC phase, the aromatic chemical shift is not simply the average of the three different chemical shifts in the solid phase. This implies that the relative position of the aromatic cores in the LC phase slightly differs from the solid-phase arrangement.

In this way, ^{1}H DQ MAS sideband patterns serve as a precise measure of dipolar coupling strengths, from which molecular motions can then be concluded. In the case of the HBC derivatives, ^{1}H spectra do not only provide clear evidence for the presence of a LC phase, they also allow the persistence of the columnar packing as well as the underlying processes of molecular rotations to be identified (*18, 19, 20*). In contrast to previous NMR investigations performed on this class of materials (*69, 55*), all the results presented here are directly obtainable from as-synthesized samples, requiring experimental times on the order of a few hours, so that ^{1}H MAS methods are particularly well suited to routine spectroscopic investigations in the course of the synthesis of solid-state materials.

In addition to the purely aromatic SQ and DQ signals providing insight into the packing and dynamics of the aromatic core of HBC-C_{12}, the aliphatic signals arising from the alkyl chain substituents can be used to estimate the mobility of the chains and to compare this to the motion of the core. Considering the DQ MAS sideband patterns of the aliphatic and the aromatic resonance in the solid phase of HBC-$C_{12}^{\alpha D}$ (displayed in Figs. 64 and 63a, respectively), it is clear that the width of the aliphatic pattern, i.e., the number of sidebands, is much less than that of the aromatic one. This indicates that the dipolar coupling strength of the aromatic proton pairs is significantly stronger

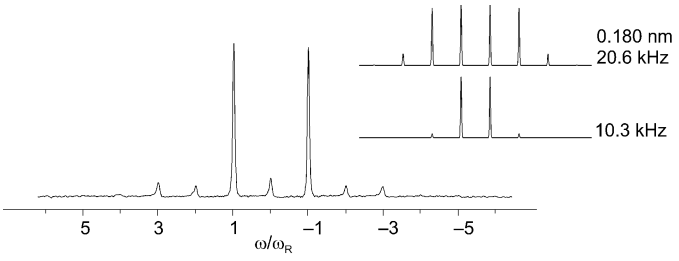

FIG. 64. ^{1}H DQ MAS sideband pattern of HBC-$C_{12}^{\alpha D}$ of the aliphatic ^{1}H SQ resonance at 1.3 ppm for the solid phase at $T = 330$ K, recorded with a DQ excitation time of $\tau_{exc} = 2\tau_R = 57\,\mu$s under MAS at 35 kHz. The ^{1}H Larmor frequency is 500 MHz. On the right, two calculated DQ MAS patterns of a spin pair are displayed for comparison, the upper resembling a rigid CH_2 group and the lower corresponding to half the CH_2 coupling strength.

than that of the CH_2 proton pairs in the alkyl chains, although the distance between the latter is only 0.18 nm compared to 0.20 nm for the bay protons. Consequently, the dipolar interactions among aliphatic chain protons must be subject to motional averaging processes, while the aromatic core is rigid. This obviously implies the existence of a mobility gradient along the alkyl substituents, as has previously been studied for triphenylene systems by use of ^{2}H NMR (*69*). The overall reduction of the dipolar coupling strengths in the CH_2 groups of the chains is of the order of 0.5, as can be seen from comparing the experimental DQ MAS pattern to spin-pair calculations (see Fig. 64). However, the fact that the centerband and the second-order sidebands have about the same intensity in the DQ MAS pattern as the expected third-order sidebands clearly indicates that the CH_2 DQCs are perturbed by couplings to neighboring protons. Since motional averaging gives rise to dipolar decoupling and hence helps to suppress interpair couplings, the presence of such perturbations in the DQ MAS pattern supports the assumption of almost rigid chain segments, presumably close to the rigid aromatic core.

In the case of HBC-C_{12}, the lack of spectral resolution among the CH_2 protons does not allow the mobility along the alkyl chain to be differentiated. In order to demonstrate the possibility of obtaining specific mobility information on distinct parts of a molecule, we briefly turn to a ring-shaped molecule whose structure is depicted in Fig. 65c and which consists of an alternating sequence **fsfs** of **f**lexible alkyl chains and stiff aromatic/aromatic-alkyne chains (*108*). Above $T \approx 395$ K, this molecule forms a LC phase, for which the ^{1}H one-pulse MAS spectrum is shown in Fig. 65a. Although the CH_2 protons of the long alkyl chain still cannot be spectrally distinguished from each other, many other proton positions are clearly resolved—in particular four different aromatic proton resonances can be assigned. Based on this ^{1}H resolution in the SQ dimension, a whole set of different ^{1}H DQ MAS sideband patterns (Fig. 65b) can be extracted from a single two-dimensional DQ spectrum, with each of the patterns providing specific and precise information about the strengths of the underlying dipolar couplings between the individual proton pairs. Relating the

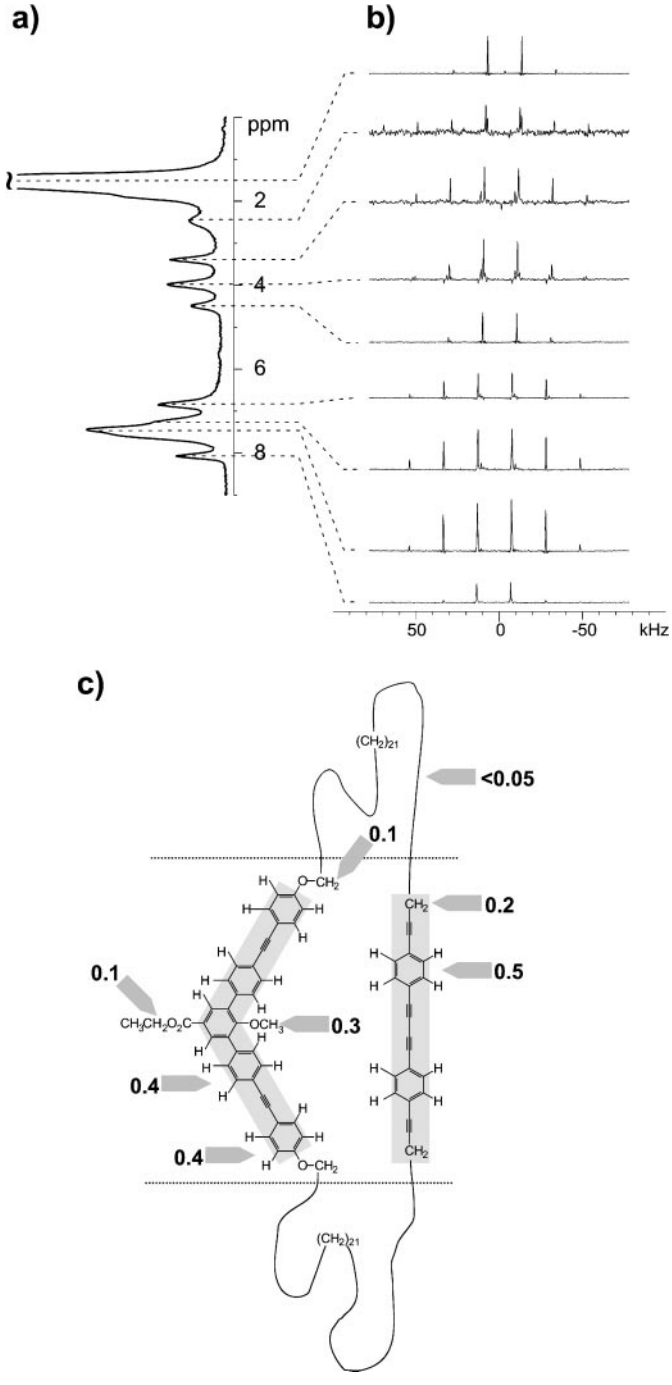

FIG. 65. LC phase of a ring-shaped molecule with alternating aliphatic and aromatic parts at $T = 415$ K. (a) ^{1}H one-pulse spectrum, recorded at a Larmor frequency of 500 MHz under MAS at 10 kHz. The peaks are assigned as follows (from top): aliphatic chain, alkyne-CH_2, OCH_3, OCH_2CH_3, OCH_2, and four aromatic lines. (b) ^{1}H DQ MAS sideband patterns of the different SQ resonances, recorded with $\tau_{exc} = 4\tau_R$ under MAS at 10 kHz. (c) Structure of the molecule, with the reduction factors of the dipolar coupling (as obtained from the patterns in b) being assigned to the corresponding positions.

coupling strengths obtained from the DQ patterns of the LC phase to the static coupling strengths of each proton pair results in a set of reduction factors or, equivalently, order parameters, each of which corresponds to a specific position in the molecule (see schematical assignment in Fig. 65c). In this way, site-specific mobility information is accessible.

4.3.2. Chain Dynamics in Polymer Melts

Turning from liquid-crystalline materials to melts of linear aliphatic polymers, we now proceed from relatively ordered to much more mobile systems. On the theoretical side, the dynamics of such flexible polymer chains is usually described by statistical approaches, starting from a free Gaussian chain and successively restricting the degrees of mobility by introducing entanglements (*23*). However, the site-specific mobility information obtained from ^{1}H DQ MAS investigations of polybutadiene melts has revealed unexpectedly high residual order parameters (*50*), as we will briefly outline in the following.

Even well above the glass transition temperature T_g, intense ^{1}H DQ signals are observed in polybutadiene melts. Figure 66 shows the two-dimensional ^{1}H DQ spectrum obtained for a polybutadiene melt with an average molecular weight of $M_W = 130\ \mathrm{kg \cdot mol^{-1}}$ at room temperature, i.e., $T \approx T_g + 120$ K. Besides the presence of the characteristic pattern of DQ diagonal and cross peaks, it is also clear that the spectral resolution of ^{1}H resonances even suffices to identify the shoulders in the DQ peaks at the olefinic ^{1}H SQ resonance arising from the *cis* and *trans* conformation of the butadiene monomer. (The sample consisted of polybutadiene chains with a statistical 1:1 *cis/trans* sequence.) The olefinic–aliphatic cross peak is more intense in the case of the *trans* conformation, because

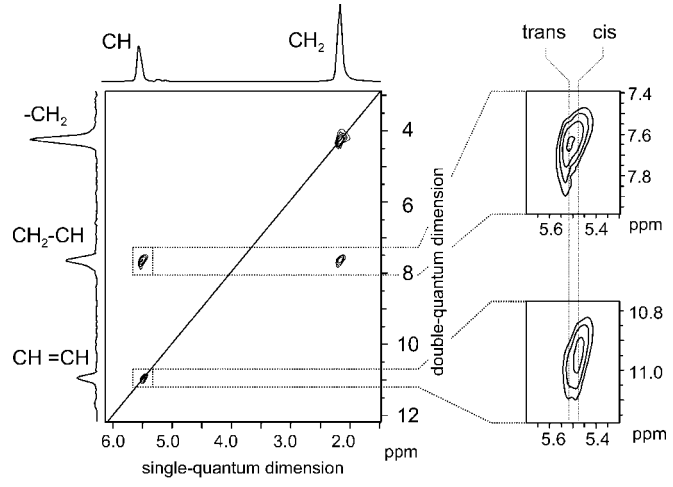

FIG. 66. ^{1}H DQ MAS spectrum of a polybutadiene melt ($M_W = 130\ \mathrm{kg \cdot mol^{-1}}$), recorded at $T = 296$ K with $\tau_{exc} = 8\tau_R$ under MAS at 8 kHz applying the C_7 pulse sequence. On the right, the DQ signals at the olefinic ^{1}H SQ resonance are magnified such that the shoulders arising from the *cis* and *trans* conformation can be identified.

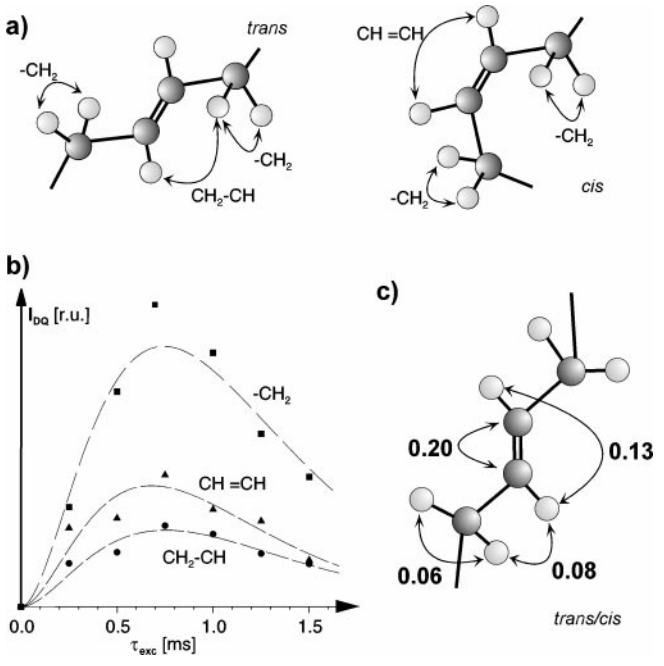

FIG. 67. (a) *Trans* and *cis* conformation of the butadiene monomer. The dominating intramolecular proton–proton couplings are indicated for both cases. (b) ^{1}H DQ buildup curves for a statistical 1:1 *cis/trans* polybutadiene. The spectra were recorded at $T = 223$ K, corresponding to $T_g + 50$ K, applying the C_7 pulse sequence for $\tau_{exc} = 2 \ldots 12\tau_R$ under MAS at 8 kHz. (c) Local order parameters in the butadiene monomer (1:1 *cis/trans* mixture), as obtained from ^{1}H buildup curves.

in *trans*-butadiene the minimum distance between the involved protons is much shorter than that in *cis*-butadiene. Conversely, in the latter conformation, the two olefinic protons are much closer and therefore the olefinic diagonal peak is stronger at the *cis* resonance. The *cis/trans* geometries of butadiene and the resulting proton–proton proximities are depicted in Fig. 67a.

To extract order parameters, the strengths of the distinct dipolar couplings need to be quantified. This can be accomplished either by DQ MAS sideband patterns, as has been demonstrated in the previous sections, or by DQ buildup curves. In the case of the polybutadiene melt discussed here, the DQ signals are, though clearly present, relatively weak, because, as is expected for a melt, the underlying dipolar interactions $\bar{D}$ are considerably reduced due to molecular motions. The observation of DQ MAS sidebands, however, requires DQCs to be excited long enough to fulfill the condition $\bar{D}\tau_{exc}/2\pi > 0.5$, which means, in particular for mobile samples, running the risk of losing signal due to relaxation. Therefore, a method using short-time excitation, i.e., the observation of DQ buildup curves, may turn out to be superior in such cases. The diagram in Fig. 67b displays the buildup curves of the three DQCs in *cis/trans* polybutadiene, not differentiating between the two conformations. Relying on the spin-pair approximation and taking the relative numbers of pairs into account, the ratio between the strengths of the three different dipolar pair couplings can be derived from fitting the three initial slopes with a function of the form given in Eq. [113] in Section 3.4.4. However, in contrast to the MAS sideband pattern analysis, this approach only yields relative values for the couplings strengths, which need to be calibrated by an absolute value in order to determine order parameters. This calibration can, for example, be performed by analyzing the SQ MAS sideband pattern. Following this procedure, the order parameters displayed in Fig. 67c have been obtained (*50*). The order parameter of the C=C double bond can be derived from the interproton parameters through geometrical relations.

On a relative scale, these experimental results were found to agree with an RIS (random isomeric states) calculation, but the absolute order parameter of 0.2 for the C=C bond is by about an order of magnitude higher than theoretically expected. For comparison, nematic liquid crystals are characterized by order parameters typically around 0.4. (Note that the reduction factor of about 0.4 determined for the HBC samples in the previous section is to be multiplied by a factor of 2 before comparing it to the order parameters discussed here.)

In addition to this information about the local mobility of chain segments in the melt, the time scale of the translational motion of polybutadiene chains has been studied by observing the decrease of the DQ signal intensity when increasing the temperature and decreasing the chain length. As soon as the characteristic time scale of the translational motion becomes shorter than the time required for the DQ experiment, the dipolar interaction tensors can reorient isotropically between the excitation and the reconversion period. As a consequence of this, the DQ signal disappears. The results obtained for the motion of polymers of different chain lengths could be explained on the basis of a reptation model (*43, 23, 50*).

In conclusion, the site-specific information about molecular dynamics, which is uniquely provided by ^{1}H DQ MAS spectroscopy, has, in the case of polymer dynamics, initiated further considerations of order phenomena in polymer melts.

5. SUMMARY AND OUTLOOK

Undoubtedly, fast sample spinning at the magic angle is the key to the wealth of information obtainable from ^{1}H NMR spectra in the solid state. Therefore, this review looked first into the question how a ^{1}H multispin system evolves under the combined action of dipolar couplings and MAS (see Section 2). Considering the time signal observed in a simple one-pulse experiment, the following conclusions can be drawn:

- The dipolar interaction is originally a spin-pair type of coupling. In the course of its action on a spin system, a dipolar-coupled network is built up by the successive formation of two-, three-, four-, and higher spin correlations. MAS counteracts this process by weighting the N-spin correlations with the inverse $(N-1)$-th power of the MAS frequency ω_R. As a consequence of this, MAS suppresses the formation of higher spin correlations, and the efficiency of this suppression increases

with the number of spins involved and with the MAS frequency applied (Section 2.5).

• Based on a perturbation approach combined with Floquet formalism (*35*), the time signal $S(t)$ of a dipolar-coupled ^{1}H multispin system in a one-pulse MAS experiment can be written in the following factorized form (see Eq. [53] and (*36*)),

$$S(t) = \sum_{n=0}^{\infty} I_n W_n(t) \exp(in\omega_R t),$$

with n denoting the sideband order. I_n and $W_n(t)$ are the intensity and the width, respectively, of the nth order sideband, and $\exp(in\omega_R t)$ is the rotor modulation. Essentially, the intensity distribution I_n over the sideband pattern is dominated by two-spin correlations, while three- and higher spin correlations determine the linewidths. Consequently, to achieve maximum resolution, MAS only needs to suppress the three-spin correlations efficiently, but the MAS frequency does *not* need to exceed the dipolar coupling strengths of the dominating two-spin correlations. In other words, in the fast spinning limit, MAS cuts a dipolar-coupled multispin system down into two-spin systems which behave inhomogeneously.

• Once the network of dipolar couplings in the ^{1}H multispin system is reduced and simplified to two-spin correlations, distinct dipolar coupling strengths and, in this way, structural information can be accessed. The MAS sideband patterns of one-pulse MAS spectra, in principle, contain this information in the intensity distribution I_n, but it is, in general, unavoidable that the patterns of different pair couplings superimpose, even if the involved spins are spectrally resolved and distinguishable. Basically, the *spin*-specific signal of the one-pulse experiment is not properly suited to obtaining *pair*-specific coupling information.

A multispin system adopting a state of superimposed two-spin correlations represents, in a sense, a map of the dipolar interactions, which merely requires us to apply a suitable technique for reading. Appreciating the fundamental role of two-spin correlations, the introduction of ^{1}H MQ MAS spectroscopy in Section 3 begins with identifying a spin state which gives rise to a spin-pair NMR signal.

• Double-quantum coherences (DQC) represent the spectroscopically accessible equivalent of two-spin correlations. Their properties, in particular their chemical shifts, are composed of the properties of the two involved spins (Section 3.1).

• The signal intensity $I_{DQ}^{(AB)}$ of a DQC between spins of the types A and B is, in the limit of short excitation times, proportional to the square of the underlying effective dipolar coupling strength D_{eff} and therefore proportional to the inverse sixth power of the effective internuclear distance r_{eff} (Section 3.2):

$$I_{DQ}^{(AB)} \propto D_{\text{eff}}^2 \propto r_{\text{eff}}^{-6}, \quad \text{where } r_{\text{eff}} = \left(\sum_{ij=AB} r_{ij}^{-6} \right)^{-1/6}.$$

Due to the efficient suppression of signal contributions from more remote nuclei, the summation may usually be restricted to internuclear distances within the range $r_{ij} \leq \frac{3}{2} r_{\min}$, starting from the shortest distance $r_{\min}$ (Section 3.4). In standard DQ experiments under fast MAS, proton–proton distances of up to $r_{ij} \leq 0.35 \cdots 0.40$ nm can, in general, be detected. A further consequence arising from this pronounced distance sensitivity is the high precision of internuclear distance determinations from DQ measurements, which is in most cases better than ± 0.005 nm.

• In MQ MAS experiments, sidebands arise in the MQ dimension from two distinct mechanisms (Section 3.5): reconversion rotor encoding (RRE) and evolution rotor modulation (ERM). The rotor encoding of the reconversion gives rise to well-defined patterns, from whose intensity distribution the underlying coupling strength can be straightforwardly determined. For a spin-pair DQC or a methyl TQC, rotor-modulated evolution occurs only if the observed coherence is subject to external interactions, in particular to dipolar couplings to surrounding spins. The ERM sideband patterns, which can moreover be clearly identified in the spectrum by means of their sideband orders, thus provide quantitative information about the degree of perturbation. It should be noted that the sensitivity of a MQC to perturbing external interactions increases with its quantum order.

• From the nested MAS sideband patterns of MQCs, in particular of DQCs, the topology of the dipolar-coupled spin system can be derived, resulting in a complete set of distances and angles for systems of up to five spins (Section 3.6).

To provide an overview of the research which has been carried out to date applying very fast MAS and ^{1}H MQ MAS methods, this review has presented several examples, all of which deal with the investigation of phenomena responsible for the induction of *supramolecular* or *local order*, e.g., hydrogen bonds, π–π interactions, or partial alignment of building blocks (Section 4). In terms of applicability, ^{1}H MQ MAS approaches exhibit major advantages in that they can be performed on as-synthesized samples without being reliant on any kind of isotopic labeling or the availability of single crystals, in contrast to most other NMR and scattering techniques. Moreover, the experiment times are on the order of a few hours and, using MAS rotors of 2.5 mm outer diameter, only about 10 mg of sample is required.

• In the case of hydrogen bonds, the resolution enhancement afforded by fast MAS permits the exploitation of ^{1}H signals and their chemical shifts in solid-state samples. The resonance positions of the ^{1}H signals in one-pulse MAS spectra already provide first evidence for the existence and strength of hydrogen bonds. Using ^{1}H DQ MAS spectroscopy, it is straightforward to identify double and multiple hydrogen bonds and to explore their arrangement, allowing the localization of protons in hydrogen-bonded systems. In addition, thermodynamic and kinetic parameters for making and breaking processes are also accessible.

• Based on the ^{1}H spectral resolution achievable by fast MAS, it could also be demonstrated that, in the solid state, the chemical

shift of protons can be used as a sensitive probe for surrounding π-electron densities. In this way, ^{1}H MAS and DQ MAS spectra yield valuable information about the packing of aromatic systems.

- By measuring ^{1}H–^{1}H dipolar coupling strengths of spin pairs or within methyl groups, ^{1}H MQ MAS provides detailed and site-specific insight into molecular order and dynamics, e.g., molecular motions in LC phases, reorientation motions of molecular segments, or residual order phenomena in polymer melts.

In the field of dipolar MQ MAS spectroscopy, on-going NMR methodological development focuses on the extension of MQ MAS techniques to heteronuclear spin systems, making use of the spectral resolution characteristic for, e.g., ^{13}C or ^{15}N, the latter however being again reliant on isotopic enrichment. The dipolar interaction tensors of heteronuclear spin pairs are, for example, well suited to serving as sensitive and site-specific probes for molecular motion. Future developments will include the combination of established multidimensional NMR methods with MQ NMR as well as the exploitation of combined homo heteronuclear MQCs.

ACKNOWLEDGMENTS

The authors thank Dr. Steven P. Brown for carefully checking and proofreading the manuscript. The following co-workers in the group have been involved in the ^{1}H MQ MAS NMR research work, and their vital scientific contributions are gratefully acknowledged: Dr. Steven P. Brown, Professor Dan E. Demco, Dr. Susan DePaul, Dr. Claudiu Filip, Dr. Ulli Friedrich, Dr. Helen Geen, Dr. Johannes Gottwald, Dr. Robert Graf, Dr. Siegfried Hafner, Benedikt Langer, Adonis Lupulescu, Dr. Kay Saalwächter, and Dr. Jeremy J. Titman. The authors also thank Manfred Hehn and Hanspeter Raich for the indispensable technical maintenance of the MAS probes and the NMR spectrometers.

Many of the experimental results presented in this review were obtained on samples generously provided by the following researchers:

- H. Zimmermann, Max-Planck-Institut für medizinische Forschung, Heidelberg, Germany (acetonitrile in hydrochinone, Section 3.6.5).
- G. Fink, Max-Planck-Institut für Kohleforschung, Mühlheim, Germany (^{13}C–^{13}C-labeled poly(ethylene) sample, Section 3.7.2).
- M. H. P. van Genderen, R. P. Sijbesma, and E. W. Meijer, Eindhoven University of Technology, Eindhoven, The Netherlands (ureido-pyrimidinone samples, Section 4.1.2).
- H. Y. Low and H. Ishida, Case Western Reserve University, Cleveland, Ohio (benzoxazine samples, Section 4.1.3).
- C. Kayser, J. D. Brand, and K. Müllen, Max-Planck-Institut für Polymerforschung, Mainz, Germany (HBC samples, Sections 4.1.4, 4.2, and 4.3.1).
- Ö. Ünsal and A. Godt, Max-Planck-Institut für Polymerforschung, Mainz, Germany (catenane samples, Section 4.3.1).
- U. Pawelzik, Max-Planck-Institut für Polymerforschung, Mainz, Germany (polybutadiene samples, Section 4.3.2).

The authors thank them for fruitful collaborations and stimulating discussions, and for sharing their experience and materials with us.

REFERENCES

1. A. Abragam, "The Principles of Nuclear Magnetism," Oxford Univ. Press, Oxford (1961).
2. M. Abramowitz and I. A. Stegun "Handbook of Mathematical Functions," Dover, New York (1989).
3. J. P. Amoureux, M. Bee, and J. C. Damien, Structure of adamantane, $C_{10}H_{16}$, in the disordered phase, *Acta Crystallogr. B* **36,** 2633 (1980).
4. E. R. Andrew, A. Bradbury, and R. G. Eades, Nuclear magnetic resonance spectra from a crystal rotated at high speed, *Nature* **182,** 1659 (1958).
5. E. R. Andrew, A. Bradbury, and R. G. Eades, Removal of dipolar broadening of nuclear magnetic resonance spectra of solids by specimen rotation, *Nature* **183,** 1802 (1959).
6. J. Schmedt auf der Günne and H. Eckert, High-resolution double-quantum ^{31}P NMR: A new approach to structural studies of thiophosphates, *Chem. Eur. J.* **4,** 1762–1767 (1998).
7. Y. Ba and W. S. Veeman, Multiple-quantum nuclear magnetic resonance spectroscopy of coupled $1/2$ spins in solids: Combination with cross polarization and magic-angle spinning, *Solid State Nucl. Magn. Reson.* **3,** 249 (1994).
8. J. Baum, M. Munowitz, A. N. Garroway, and A. Pines, Multiple-quantum dynamics in solid state NMR, *J. Chem. Phys.* **83,** 2015 (1985).
9. J. Baum and A. Pines, Multiple-quantum NMR studies of clustering in solids, *J. Am. Chem. Soc.* **108,** 7447 (1986).
10. E. D. Becker, "Hydrogen Bonding," Chap. 4, pp. 2409–2415, Wiley, Chichester (1996).
11. F. H. Beijer, R. P. Sijbesma, H. Kooijman, A. L. Spek, and E. W. Meijer, Strong dimerization of ureidopyrimidones via quadruple hydrogen bonding, *J. Am. Chem. Soc.* **120,** 6761–6769 (1998).
12. A. E. Bennett, R. G. Griffin, and S. Vega, Recoupling of homo- and heteronuclear dipolar interactions in rotating solids, *in* "NMR Basic Principles and Progress" (P. Diehl, E. Fluck, H. Günter, R. Kosfeld, and J. Seelig, Eds.), Vol. 33, pp. 1–77, Springer-Verlag, Berlin (1994).
13. M. A. Biasutti, J. Rommens, A. Vaes, S. de Feyter, F. D. de Schryver, P. Herwig, and K. Müllen, Photophysical properties of a new class of discotic liquid crystalline compounds: Hexa (dodecyl) hexa peri benzyl coronene, *Bull. Soc. Chim. Belg.* **106,** 659 (1997).
14. G. Bodenhausen, H. Kogler, and R. R. Ernst, Selection of Coherence-transfer pathways in NMR pulse experiments, *J. Magn. Reson.* **58,** 370 (1984).
15. G. J. Bowden and W. D. Hutchison, Tensor operator formalism for multiple-quantum NMR. 1. Spin-1 nuclei, *J. Magn. Reson.* **67,** 403–414 (1986).
16. G. J. Bowden, W. D. Hutchison, and J. Khachan, Tensor operator formalism for multiple-quantum NMR. 2. Spins $\frac{3}{2}$, 2, and $\frac{5}{2}$ and general I, *J. Magn. Reson.* **67,** 415–437 (1986).
17. I. N. Bronstein and K. A. Semendjajew, "Taschenbuch der Mathematik," Verlag Harri Deutsch, Thun (1987).
18. S. P. Brown, I. Schnell, J. D. Brand, K. Müllen, and H. W. Spiess, An investigation of π–π packing in a columnar hexabenzocoronene by fast magic-angle spinning and double-quantum ^{1}H solid-state NMR spectroscopy, *J. Am. Chem. Soc.* **121,** 6712–6718 (1999).
19. S. P. Brown, I. Schnell, J. D. Brand, K. Müllen, and H. W. Spiess, A ^{1}H double-quantum magic-angle spinning solid-state NMR investigation of packing and dynamics in triphenylene and hexabenzocoronene derivatives, *J. Mol. Struct.* **521,** 179–195 (2000).
20. S. P. Brown, I. Schnell, J. D. Brand, K. Müllen, and H. W. Spiess, The competing effects of π–π packing and hydrogen bonding in a hexabenzocoronene carboxylic acid derivative: A ^{1}H solid-state MAS NMR investigation, *Phys. Chem. Chem. Phys.* **2,** 1735–1745 (2000).
21. B. M. Craven, C. H. Chang, and D. Ghosh, Crystal structure of hydroquinone-acetonitrile (3 : 1) clathrate, *Acta Crystallogr. B* **35,** 2962 (1979).
22. D. Demus, J. W. Goodby, G. W. Gray, H. W. Spiess, and V. Vill (Hrsg.), "Handbook of Liquid Crystals," Wiley–VCH, Weinheim (1998).

23. M. Doi and S. F. Edwards, "The Theory of Polymer Dynamics," Clarendon Press, Oxford (1986).
24. W. A. Dollase, M. Feike, H. Förster, T. Schaller, I. Schnell, A. Sebald, and S. Steuernagel, A 2D ^{31}P MAS NMR study of polycrystalline $Cd_3(PO_4)_2$, *J. Am. Chem. Soc.* **119,** 3807–3810 (1997).
25. M. J. Duer, Determination of structural data from multiple-quantum magic-angle spinning NMR experiments, *Chem. Phys. Lett.* **277,** 167–174 (1997).
26. J. Dunkers and H. Ishida, Vibrational assignments of 3,5-dimethyl-bis(2-hydroxybenzyl)methylamine, *Spectrochim. Acta* **51,** 885 (1995).
27. J. Dunkers, E. A. Zarate, and H. Ishida, The crystal structure and hydrogen bonding characteristics of 3,5-dimethyl-bis(2-hydroxybenzyl)methylamine: A benzoxazine dimer, *J. Phys. Chem.* **100,** 13512 (1996).
28. S. Dusold and A. Sebald, Dipolar recoupling under magic-angle spinning conditions, *Annu. Rep. NMR Spectrosc.* **41,** 185–264 (2000).
29. C. R. Dybowski, B. C. Gerstein, and R. W. Vaughan, The proton chemical shift tensor in trichloroacetic acid, *J. Chem. Phys.* **67,** 3412–3415 (1977).
30. M. Edén and M. H. Levitt, Excitation of carbon-13 triple quantum coherence in magic-angle-spinning NMR, *Chem. Phys. Lett.* **293,** 173–179 (1998).
31. R. R. Ernst, G. Bodenhausen, and A. Wokaun. "Principles of Nuclear Magnetic Resonance in One and Two Dimensions," Clarendon Press, Oxford (1997).
32. M. Feike, D. E. Demco, R. Graf, J. Gottwald, S. Hafner, and H. W. Spiess, Broadband multiple-quantum NMR spectroscopy, *J. Magn. Reson. A* **122,** 214–221 (1996).
33. M. Feike, R. Graf, I. Schnell, C. Jäger, and H. W. Spiess, Structure of crystalline phosphates from ^{31}P double-quantum NMR spectroscopy, *J. Am. Chem. Soc.* **118,** 9631–9634 (1996).
34. M. Feike, C. Jäger, and H. W. Spiess, Connectivities of coordination polyhedra in phosphate glasses from ^{31}P double-quantum NMR spectroscopy, *J. Non-Cryst. Solids* **223,** 200–206 (1998).
35. C. Filip, X. Filip, D. E. Demco, and S. Hafner, Spin dynamics under magic angle spinning by Floquet formalism, *Mol. Phys.* **92,** 757–771 (1997).
36. C. Filip, S. Hafner, I. Schnell, D. E. Demco, and H. W. Spiess, Solid-state nuclear magnetic resonance spectra of dipolar-coupled multi-spin systems under fast magic angle spinning, *J. Chem. Phys.* **110,** 423–440 (1999).
37. U. Friedrich, I. Schnell, S. P. Brown, A. Lupulescu, D. E. Demco, and H. W. Spiess, Spinning-sideband patterns in multiple-quantum magic-angle spinning NMR spectroscopy, *Mol. Phys.* **95,** 1209–1227 (1998).
38. U. Friedrich, I. Schnell, D. E. Demco, and H. W. Spiess, Triple-quantum NMR spectroscopy in dipolar solids, *Chem. Phys. Lett.* **285,** 49–58 (1998).
39. H. Geen, J. Gottwald, R. Graf, I. Schnell, H. W. Spiess, and J. J. Titman, Elucidation of dipolar coupling networks under magic-angle spinning, *J. Magn. Reson.* **125,** 224–227 (1997).
40. H. Geen, R. Graf, A. S. D. Heindrichs, B. S. Hickman, I. Schnell, H. W. Spiess, and J. J. Titman, Spin counting with fast MAS, *J. Magn. Reson.* **138,** 167–172 (1999).
41. H. Geen, J. J. Titman, J. Gottwald, and H. W. Spiess, Spinning sidebands in the fast-MAS multiple-quantum spectra of protons in solids, *J. Magn. Reson. A* **114**, 264–267 (1995).
42. H. Geen, J. J. Titman, J. Gottwald, and H. W. Spiess, Solid-state proton multiple-quantum NMR spectroscopy with fast magic angle spinning, *Chem. Phys. Lett.* **227,** 79–86 (1994).
43. P.-G. De Gennes, Reptation of a polymer chain in the presence of fixed obstacles, *J. Chem. Phys.* **55,** 572 (1971).
44. K. Glock, O. Hirsch, P. Rehak, B. Thomas, and C. Jäger, Novel opportunities for studying the short and medium range order of glasses by MAS NMR, ^{29}Si double quantum NMR and IR spectroscopies, *J. Non-Cryst. Solids* **234,** 113–118 (1998).
45. R. Goddard, M. W. Haenel, W. C. Herndon, C. Krüger, and M. Zander, Crystallization of large planar polycyclic aromatic hydrocarbons: The molecular and crystal structures of hexabenzo[*bc,ef,hi,kl,no,qr*]coronene and benzo[1,2,3-*bc*:4,5,6-*b'c'*]dicoronene, *J. Am. Chem. Soc.* **117,** 30 (1995).
46. J. Gottwald, D. E. Demco, R. Graf, and H. W. Spiess, High-resolution double-quantum NMR spectroscopy of homonuclear spin pairs and proton connectivities in solids, *Chem. Phys. Lett.* **243,** 314–323 (1995).
47. R. Graf, "Hochauflösende Doppelquanten-NMR-Spektroskopie an amorphen Polymeren," Dissertation, Universität Mainz (1998).
48. R. Graf, D. E. Demco, J. Gottwald, S. Hafner, and H. W. Spiess, Dipolar couplings and internuclear distances by double-quantum nuclear magnetic resonance spectroscopy of solids, *J. Chem. Phys.* **106,** 885–895 (1996).
49. R. Graf, D. E. Demco, S. Hafner, and H. W. Spiess, Selective residual dipolar couplings in cross-linked elastomers by ^{1}H double-quantum NMR spectroscopy, *Solid State Nucl. Magn. Reson.* **12,** 139–152 (1998).
50. R. Graf, A. Heuer, and H. W. Spiess, Chain-order effects in polymer melts probed by ^{1}H double-quantum NMR spectrocopy, *Phys. Rev. Lett.* **80,** 5738–5741 (1998).
51. U. Haeberlen, High resolution NMR of solids, *in* "Advances in Magnetic Resonance," Suppl. 1, Academic Press, London (1976).
52. W. C. Hamilton and J. A. Ibers. "Hydrogen Bonding in Solids," Benjamin, New York (1968).
53. S. R. Hartmann and E. L. Hahn, Nuclear double resonance in the rotating frame, *Phys. Rev.* **128,** 2024 (1962).
54. E. R. Henry and A. Szabo, Influence of vibrational motion on solid-state line-shapes and NMR relaxation, *J. Chem. Phys.* **82,** 4753–4761 (1985).
55. P. Herwig, C. W. Kayser, K. Müllen, and H. W. Spiess, Columnar mesophases of alkylated hexa-*peri*-hexabenzocoronenes with remarkably large phase widths, *Adv. Mater.* **8,** 510 (1996).
56. J. Herzfeld and A. E. Berger, Sideband intensities in NMR spectra of samples spinning at the magic angle, *J. Chem. Phys.* **73,** 6021 (1980).
57. M. Hohwy, H. J. Jakobsen, M. Edén, M. H. Levitt, and N. C. Nielsen, Broadband dipolar recoupling in the nuclear magnetic resonance of rotating solids: A compensated C7 pulse sequence, *J. Chem. Phys.* **108,** 2686–2694 (1998).
58. M. Hong, Solid-state dipolar INADEQUATE NMR spectroscopy with a large double-quantum spectral width, *J. Magn. Reson.* **136,** 86–91 (1999).
59. W.-G. Hu, C. Boeffel, and K. Schmidt-Rohr, Chain flips in polyethylene crystallites and fibers characterized by dipolar ^{13}C NMR, *Macromolecules* **32,** 1611–1619 (1999).
60. H. Ishida and H. Y. Low, A study on the volumetric expansion of benzoxazine-based phenolic resin, *Macromolecules* **30,** 30 (1997).
61. Y. Ishii, T. Terao, and S. Hayashi, Theory and simulation of vibrational effects on structural measurements by solid-state nuclear magnetic resonance, *J. Chem. Phys.* **107,** 2760–2774 (1997).
62. P.-G. Jönsson and W. C. Hamilton, Hydrogen bond studies. LX. A single crystal neutron diffraction study of trichloroacetic acid dimer, *J. Chem. Phys.* **56,** 4433 (1972).
63. A. Keller, Spin-1 behavior of systems of dipolar coupled pairs of spin-$\frac{1}{2}$ nuclei, *Adv. Magn. Reson.* **12,** 184 (1988).
64. R. Kemp-Harper, S. P. Brown, C. E. Hughes, P. Styles, and S. Wimperis, ^{23}Na NMR methods for selective observation of sodium ions in ordered environments, *Prog. NMR Spectrosc.* **30,** 157–181 (1997).
65. B. Langer, "Hochaufgelöste ^{1}H-Festkörper-NMR-Spekrosk opie an wasserstoffbrückenbildenden Systemen," Diplomarbeit, Universität Mainz (1998).
66. B. Langer, I. Schnell, and H. W. Spiess, Investigation of structure and dynamics in supramolecular systems and liquid crystalline phases by ^{1}H MQ MAS NMR spectroscopy, *in* ENC (2000).

67. Y. K. Lee, N. D. Kurur, M. Helmle, O. G. Johannessen, N. C. Nielsen, and M. H. Levitt, Efficient dipolar recoupling in the NMR of rotating solids. A sevenfold symmetric radiofrequency pulse sequence, *Chem. Phys. Lett.* **242,** 304–309 (1995).

68. J.-M. Lehn, "Supramolecular Chemistry," VCH, New York (1995).

69. J. Leisen, M. Werth, C. Boeffel, and H. W. Spiess, Molecular dynamics at the glass transition: One dimensional and two dimensional nuclear magnetic resonance studies of a glass-forming discotic liquid crystal, *J. Chem. Phys.* **97,** 3749–3759 (1992).

70. T. O. Levante, M. Baldus, B. H. Meier, and R. R. Ernst, Formalized quantum-mechanical Floquet theory and its application to sample-spinning in nuclear magnetic resonance, *Mol. Phys.* **86,** 1195–1212 (1995).

71. I. J. Lowe, Free induction decay of rotating solids, *Phys. Rev. Lett.* **2,** 285 (1959).

72. M. M. Maricq and J. S. Waugh, NMR in rotating solids, *J. Chem. Phys.* **70,** 3300 (1979).

73. M. Mehring, "High Resolution NMR of Solids," Springer-Verlag, Berlin (1983).

74. B. H. Meier and W. L. Earl, Excitation of multiple-quantum transitions under magic-angle spinning conditions: Adamantane, *J. Chem. Phys.* **85,** 4905 (1986).

75. M. Munowitz, "Coherence and NMR," Wiley, London (1988).

76. M. Munowitz, Exact simulation of multiple-quantum dynamics in solid-state NMR: Implications for spin counting, *Mol. Phys.* **71,** 959–978 (1990).

77. M. Munowitz and M. Mehring, Liouville space revisited: Excitation and relaxation of multiple-quantum nuclear spin coherences in dipolar systems, *Solid State Commun.* **64,** 605 (1987).

78. M. Munowitz and M. Mehring, Whither the free induction: An analysis of multiple spin dynamics in strongly coupled systems, *Chem. Phys.* **116,** 79 (1987).

79. M. Munowitz and A. Pines, Principles and applications of multiple-quantum NMR, *Adv. Chem. Phys.* **66,** 1 (1987).

80. M. Munowitz, A. Pines, and M. Mehring, Multiple-quantum dynamics in NMR: A directed walk through Liouville space, *J. Chem. Phys.* **86,** 3172 (1987).

81. T. Nakai and C. A. McDowell, Application of Floquet theory to the nuclear-magnetic-resonance spectra of homonuclear 2-spin systems in rotating solids, *J. Chem. Phys.* **96,** 3452–3466 (1992).

82. T. Nakai and C. A. McDowell, Calculation of rotational resonance NMR spectra using Floquet theory combined with perturbation treatment, *Mol. Phys.* **88,** 1263–1275 (1996).

83. N. C. Nielsen, H. Bilsøe, H. J. Jakobsen, and M. H. Levitt, Double-quantum homonuclear rotary resonance: Efficient dipolar recovery in magic-angle spinning nuclear magnetic resonance, *J. Chem. Phys.* **101,** 1805–1812 (1994).

84. N. C. Nielsen, F. Creuzet, R. G. Griffin, and M. H. Levitt, Enhanced double-quantum nuclear-magnetic-resonance in spinning solids at rotational resonance, *J. Chem. Phys.* **96,** 5668–5677 (1992).

85. T. J. Norwood, Multiple quantum NMR methods, *Prog. NMR Spectrosc.* **24,** 295–375 (1992).

86. C. Ochsenfeld, An ab-initio study of the relation between NMR chemical shifts and solid state structures, *Phys. Chem. Chem. Phys.* **2,** 2153 (2000).

87. C. Ochsenfeld, S. P. Brown, I. Schnell, J. Gauss, and H. W. Spiess, Structure assignments in solid states by coupling ab-initio theory and NMR experiments: Columnar hexabenzocoronene derivatives, submitted for publication.

88. G. E. Pake, Nuclear resonance absorption in hydrated crystals, Fine structure of the proton line, *J. Chem. Phys.* **16,** 327 (1948).

89. C. M. Rienstra, M. E. Hatcher, L. J. Mueller, B. Q. Sun, S. W. Fesik, and R. G. Griffin, Efficient multispin homonuclear double-quantum recoupling for magic-angle spinning NMR: ^{13}C–^{13}C correlation spectroscopy of U-^{13}C-erythromycin A, *J. Am. Chem. Soc.* **120,** 10602–10612 (1998).

90. M. E. Rose, "Elementary Theory of Angular Momentum," Wiley, London (1959).

91. K. Saalwächter, R. Graf, D. E. Demco, and H. W. Spiess, Heteronuclear double-quantum MAS NMR spectroscopy in dipolar solids, *J. Magn. Reson.* **139,** 287 (1999).

92. K. Saalwächter, R. Graf, and H. W. Spiess, Recoupled polarization transfer heteronuclear ^{1}H-^{13}C multiple-quantum correlation in solids under ultrafast MAS, *J. Magn. Reson.* **140,** 471–476 (1999).

93. J. J. Sakurai. "Modern Quantum Mechanics," Addison–Wesley, New York (1985).

94. A. Schmidt and S. Vega, The Floquet theory of nuclear-magnetic-resonance spectroscopy of single spins and dipolar coupled spin pairs in rotating solids, *J. Chem. Phys.* **96,** 2655–2680 (1992).

95. K. Schmidt-Rohr and H. W. Spiess. "Multidimensional Solid-State NMR and Polymers," Academic Press, London (1997).

96. I. Schnell. "Doppelquanten-NMR-Spektroskopie an polykristallinen Phosphaten," Diplomarbeit, Universität Mainz (1996).

97. I. Schnell, S. P. Brown, H. Y. Low, H. Ishida, and H. W. Spiess, An investigation of hydrogen bonding in benzoxazine dimers by fast magic-angle spinning and double-quantum ^{1}H NMR spectroscopy, *J. Am. Chem. Soc.* **120,** 11784–11795 (1998).

98. I. Schnell, A. Lupulescu, S. Hafner, D. E. Demco, and H. W. Spiess, Resolution enhancement in multiple-quantum MAS NMR spectroscopy, *J. Magn. Reson.* **133,** 61–69 (1998).

99. I. Schnell, A. Watts, and H. W. Spiess, Double-quantum double-quantum MAS exchange NMR spectroscopy: Dipolar coupled spin-pairs as probes for slow molecular dynamics, *J. Magn. Reson.* **149,** 90–102 (2001).

100. S. Sekine, A. Kubo, and H. Sano, Motional narrowing of ^{1}H magic-angle-spinning nuclear magnetic resonance spectra, *Chem. Phys. Lett.* **171,** 155 (1990).

101. D. N. Shykind, J. Baum, S. B. Liu, and A. Pines, Phase-incremented multiple-quantum NMR experiments, *J. Magn. Reson.* **76,** 149–154 (1988).

102. R. P. Sijbesma, F. H. Beijer, L. Brunsveld, B. J. B. Folmer, J. H. K. K. Hirschberg, R. F. M. Lange, J. K. L. Lowe, and E. W. Meijer, Reversible polymers formed from self-complementary monomers using quadruple hydrogen bonding, *Science* **278,** 1601–1604 (1997).

103. W. Sommer, J. Gottwald, D. E. Demco, and H. W. Spiess, Dipolar heteronuclear multiple-quantum NMR spectroscopy in rotating solids, *J. Magn. Reson. A* **113,** 131–134 (1995).

104. H. W. Spiess, Rotation of molecules and nuclear spin relaxation, *in* "NMR Basic Principles and Progress" (P. Diehl, E. Fluck, and R. Kosfeld, Eds.), Vol. 15, p. 55, Springer-Verlag, Berlin (1978).

105. H. W. Spiess, Deuteron spin alignment—A probe for studying ultraslow motions in solids and solid polymers, *J. Chem. Phys.* **72,** 6755–6762 (1980).

106. R. Tycko and G. Dabbagh, Measurement of nuclear magnetic dipole–dipole couplings in magic angle spinning NMR, *Chem. Phys. Lett.* **173,** 461–465 (1990).

107. R. Tycko and S. O. Smith, Symmetry principles in the design of pulse sequences for structural measurements in magic angle spinning nuclear-magnetic-resonance, *J. Chem. Phys.* **98,** 932–943 (1993).

108. Ö. Ünsal and A. Godt, Synthesis of a [2]catenane with functionalities and 87-membered rings, *Chem. Eur. J.* **5,** 1728 (1999).

109. A. M. van de Craats, J. M. Warman, K. Müllen, Y. Geerts, and J. D. Brand, Rapid charge transport along self-assembling graphitic nanowires, *Adv. Mater.* **10,** 36 (1998).

110. B.-J. van Rossum, H. Förster, and H. J. M. de Groot, High-field and high-speed CP-MAS ^{13}C NMR heteronuclear dipolar-correlation spectroscopy of solids with frequency-switched Lee–Goldburg homonuclear decoupling, *J. Magn. Reson.* **124,** 516–519 (1997).

111. J. H. van Vleck, The dipolar broadening of magnetic resonance lines in crystals, *Phys. Rev.* **74,** 1168 (1948).

112. W. S. Warren, D. P. Weitekamp, and A. Pines, Theory of selective excitation of multiple-quantum transitions, *J. Chem. Phys.* **73,** 2084–2099 (1980).

113. J. S. Waugh and R. W. Fessenden, Nuclear resonance spectra of hydrocarbons: The free electron model, *J. Am. Chem. Soc.* **79,** 846 (1956).

114. D. P. Weitekamp, Time-domain multiple-quantum NMR, *Adv. Magn. Reson.* **11,** 111 (1983).

115. S. Wirasate, S. Dhumrongvaraporn, D. J. Allen, and H. Ishida, The molecular origin of unusual physical and mechanical properties in novel phenolic materials based on benzoxazine chemistry, *J. Appl. Polym. Sci.* **70,** 1299–1306 (1998).

116. R. Witter, P. Hartmann, J. Vogel, and C. Jäger, Measurements of chain length distributions in calcium phosphate glasses using 2D ^{31}P double quantum NMR, *Solid State Nucl. Magn. Reson.* **13,** 189–200 (1998).